CATALYSTS AND ELECTRODES FOR THE ELECTROREDUCTION OF CARBON DIOXIDE TO USEFUL CHEMICALS

BY

SICHAO MA

DISSERTATION

Submitted in partial fulfillment of the requirements
for the degree of Doctor of Philosophy in Chemistry
in the Graduate College of the
University of Illinois at Urbana-Champaign, 2016

Urbana, Illinois

Doctoral Committee:

Professor Paul J.A. Kenis, Chair
Professor Andrew A. Gewirth
Professor Catherine J. Murphy
Assistant Professor Joaquín Rodríguez-López

Abstract

Industrialization and increasing population have brought the world two major challenges: climate change and increasing energy demands. First, the atmospheric CO_2 level has increased to 400 ppm, and already this high level has been associated with undesirable climate effects such as global warming and an increased occurrence of erratic weather. Second, the world faces challenges in meeting its energy needs due to increasing global population as well as the dwindling resources of fossil fuels on the earth. Various strategies such as switching from fossil fuel derived energy to nuclear energy or renewable energy sources (solar, wind, hydro) need to be pursued to curb the increase in atmospheric CO_2 levels while decreasing our dependence on fossil fuels. However, due to the lack of efficient ways for large-scale energy storage, significant amounts of renewable energy will be wasted when the supply is higher than the actual demand due to its intermittency. A potential strategy that can be employed to help overcome both challenges is the electroreduction of CO_2 into useful feedstock chemicals or fuels such as formic acid, carbon monoxide, hydrocarbons, and alcohols using otherwise wasted large amounts of intermittent excess renewable energy.

Although the electroreduction of CO_2 offers the potential to recycle CO_2 and store intermittent renewable energy, this process is still not economically viable due to insufficient performance levels, specifically due to high overpotentials which reduce energy efficiency, low current densities and low selectivities. Better catalysts that show high activity as well as electrodes that exhibit excellent mass transfer capabilities and electron conductivities are needed. This dissertation reports the development of active and durable catalysts that exhibit low overpotentials

for the electroreduction of CO_2 to products such as CO, C_2H_4 and/or C_2H_5OH. This dissertation will also discuss the roles electrolytes and electrode structures play in the electroreduction of CO_2.

The focus of **Chapters 2** and **3** is on developing better cathode and anode catalysts for the electroreduction of CO_2 to CO. **Chapter 2** reports on the role of support materials on cathode performance. Ag supported on TiO_2 exhibited a twofold higher partial current density for CO than Ag supported on C with the same Ag loading and similar performance compared to unsupported Ag nanoparticles, but at a 2.5 times lower Ag loading. The TiO_2 support material was also found to stabilize a reaction intermediate and serves as a redox electron carrier to assist the CO_2 reduction reaction. **Chapter 3** reports how two forms of IrO_2, dihydrate and non-hydrate, improve system energy efficiency and production rate when used as the anode catalyst. For example, when IrO_2 dihydrate was used as the anode catalyst instead of platinum black, the energy efficiency increased by 40% and the current density showed a 2-fold improvement.

Chapters 4, **5**, and **6** focus on developing active Cu-based cathode catalysts for the electroreduction of CO_2 to C2 chemicals. **Chapter 4** reports the synthesis and application of active Cu nanoparticles with different morphology and composition (amount of surface oxide) for CO_2 reduction in an alkaline electrolyzer. The use of catalysts with large surface roughness results in a high Faradaic efficiency of 46% (only ~30% in most prior work) for the conversion of CO_2 to C2 chemicals with a total current density of ~200 mA cm^{-2} for these C2 products, which, compared to prior work, represents a 10-fold increase in conversion rate at much lower overpotential (only < 0.7 V). The effect of N-containing compounds on the products distribution for the electroreduction of CO_2 on Cu catalysts is discussed in **Chapter 5**. Specifically, 3,5-diamino-1,2,4-triazole (DAT) improves the Faradaic efficiency of C_2H_4 by more than 1.5 fold when used in combinations with a Cu nanoparticle-based electrode. *In-situ* surface enhanced Raman

Spectroscopy (SERS) was applied to elucidate the possible reasons for this improvement. **Chapter 6** describes the design, synthesis and application of CuPd nanoalloys with tunable atomic arrangements (atomically ordered, disordered and phase-separated structures) for the electroreduction of CO_2 to C2 chemicals. The results of electrochemical measurement as well as structural and compositional characterization indicate that the observed differences in selectivities for different products can be attributed predominantly to structural differences in the different catalysts. Also, this work for the first time shows that active sites with neighboring Cu atoms are required for the efficient conversion of CO_2 to C2 chemicals.

Finally, **Chapter 7** describes the improvement in throughput levels for the electroreduction of CO_2 to CO through the optimization of electrode structure and composition. The electrode that incorporates multi-walled carbon nanotubes (MWCNTs) in the catalyst layer achieves high levels of CO production of up to 350 mA cm^{-2} at a high Faradaic efficiency (>95% selective for CO) and an energy efficiency of 45%. This level of performance represents a twofold improvement over the performance achieved with electrodes that lack MWCNTs.

In summary the studies reported in this dissertation provide insight regarding the design and synthesis of active catalysts and electrodes that improve current density (conversion), selectivity and energy efficiency for the electroreduction of CO_2 to different chemical intermediates of value.

Acknowledgments

With outstanding professors, staff and experts, the Illini community has been an inspiring place to pursue research. I would like to express my gratitude to the many people who have helped to make this dissertation possible. First and foremost, I would like to thank my advisor, Professor Paul J.A. Kenis for providing insightful feedback and guidance for my research, and being extremely supportive of the research that I am interested in and would like to pursue. I also would like to thank my committee, Professors Andrew Gewirth, Catherine Murphy, Joaquín Rodríguez-López for the advice and insight they provided.

I would like to thank all Kenis group members for being such great people to work with. First, I would like to thank Dr. Michael Thorson and Dr. Huei-Ru "Molly" Jhong, who demonstrated great patience when providing mentorship. I also would like to thank Byoungsu Kim, Sumit Verma, who I worked most closely with and helped to assume responsibilities for CO_2 subgroup-related affairs. Joseph Whittenberg, Vivek Kumar, and Jeremy Schieferstein joined the same year as I did and I appreciated their comradery in lab and having me involved in ChBE activities. I am also grateful for the other members of the Kenis group for their scientific insight and comradery, particularly, Elizabeth Horstman, Dr. Amit Desai, Dr. Ashtamurthy Pawate, Dr. Matthew Byrne, Dr. Ritika Mohan, Dr. Sachit Goyal, Dr. Sudipto Guha, Dr. Matthew Naughton, Dr. Daria Khvostichenko, Dr. Joshua Tice, Dr. Adam Hollinger, and Dr. Jieqian Zhang. I also would like to thank exchange students that worked with me when they visited UIUC: Gaby Perez, Dr. Yangchun Lan, Dr. Sho Kitano and Lin Liu. Finally, I would like to thank hard working undergraduate researchers, Saman Moniri, Raymond Luo, Jake Gold and Aaron Yu, for their efforts in collecting data.

I have also been fortunate to interact with some wonderful faculty, students, and staff as collaborators both here and at Kyushu University. Without them, much of this work would not have been possible. Professor Andrew Gewirth has been a great mentor during these years and I am grateful for his guidance. His students, Dr. Claire Tornow, Kevin Schmitt and Thao Hoang worked very closely with me and offered a lot of help. I also would like to thank several great scientists and collaborators in Japan: Professors Miho Yamauchi, Masaaki Sadakiyo, Stephen Lyth, Naotoshi Nakashima, and Tsuyohiko Fujigaya at Kyushu University and Professor Teruhisa Ohno at Kyushu Institute of Technology.

I appreciate the generous funding for this work by DOE, Dioxide Materials, the U.S. Air Force, the International Institute for Carbon Neutral Energy Research (WPI-I2CNER, sponsored by the Japanese Ministry of Education, Culture, Sports, Science and Technology), as well as a Fellowship from FMC.

I appreciate my parents for mental support while I am away from home. I especially thank my friends here for making me feel like home.

Table of Contents

Chapter 1*

Introduction

1.1 Global Warming and the Need to Decrease Carbon Dioxide Emission

In the past few decades, the atmospheric carbon dioxide (CO_2) levels have increased drastically (**Figure 1.1**) and are expected to continue to rise. In December 2015, the globally average mole fractions of CO_2 reached 401.85 ppm,[1] which is an increase of 44% compared to pre-industrial levels (pre 1750).[2] These high atmospheric CO_2 levels are mainly attributed to increased human activities such as fossil fuel combustion, cement production and flaring.[3]

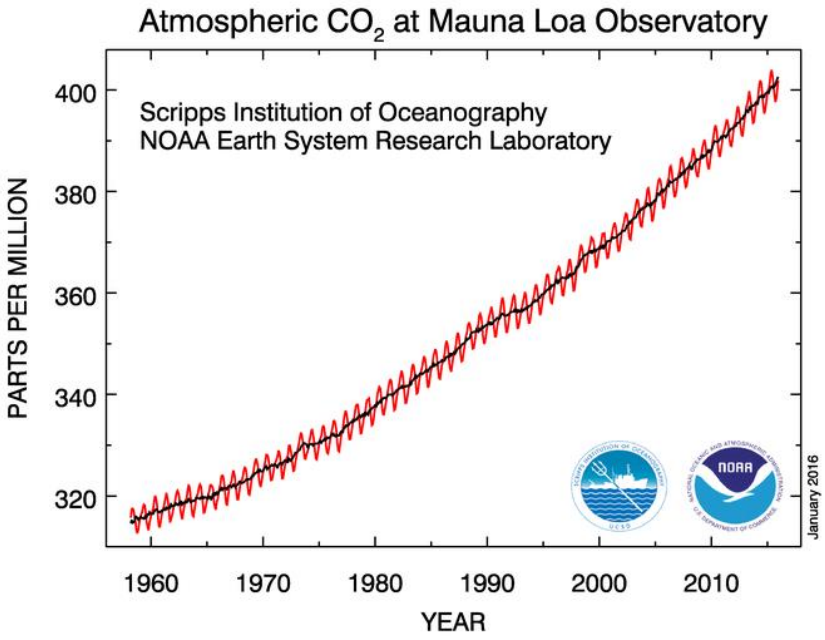

Figure 1.1 Atmospheric CO_2 concentrations from 1960 to present. The red curve represents monthly mean data, while the black curve represents the seasonally corrected data. All the data was measured at Mauna Loa Observatory, Hawaii. Source: National Oceanic & Atmospheric Administration (NOAA), http://www.esrl.noaa.gov/gmd/ccgg/trends/full.html.

* Part of this work has been published: Jhong, H.-R. M., Ma, S. & Kenis, P. J. A. Electrochemical conversion of CO2 to useful chemicals: current status, remaining challenges, and future opportunities. *Curr. Opin. Chem. Eng.* **2**, 191-199, (2013). Copyright 2013. Reproduced with permission from Elsevier.

Carbon dioxide is the most important atmospheric greenhouse gas, which contributes ~65% of radiative forcing among all long-lived greenhouse gases. CO_2 is responsible for ~84% of the increase in radiative forcing from year 2004 to year 2013. Measurement of global surface temperatures over the past hundred years (**Figure 1.2**) indicates that the global climate is warming.[4] As the Intergovernmental Panel on Climate Change (IPCC) states in their 2014 Synthesis Report,[3] the increasing atmospheric concentrations of greenhouse gases are "extremely likely" to have been the dominant cause of the observed warming since the mid-20th century.

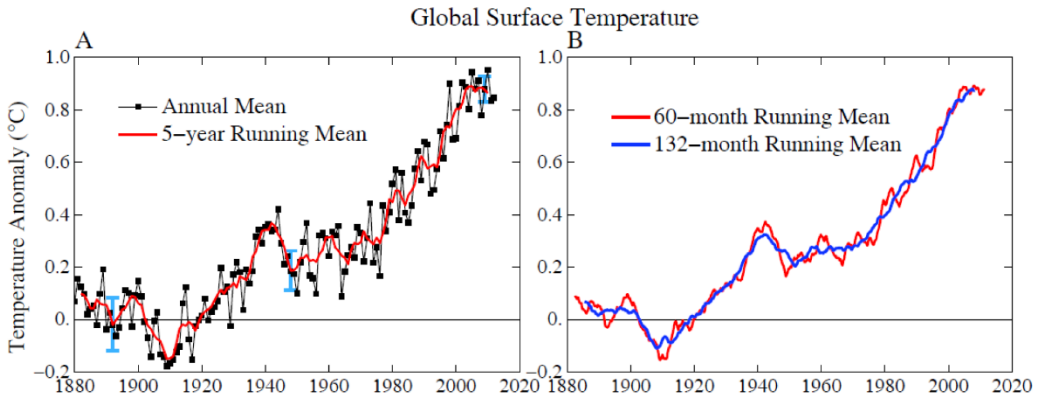

Figure 1.2 Global surface temperatures relative to 1880–1920 mean. Reprinted with permission from ref 4. Copyright 2013 PLOS.

Already this high level of CO_2 impacts the climate and global ecosystems in undesirable ways as is evident from increasing sea levels, shifting climate zones, acidifying oceans, changing wildlife populations, and erratic weather patterns. These facts have caused increased pressure to rapidly decrease carbon emissions to restore Earth's energy and carbon balance.[4] The European Union and IPCC proposed to limit global warming to 2 °C relative to pre-industrial times to minimize deleterious consequences.[5] To curb the rise, and eventually to lower the atmospheric CO_2 levels, multiple approaches are proposed to be applied to reduce CO_2 emissions include switching to energy sources that emit less CO_2 (*e.g.*, natural gas instead of coal), carbon capture

and sequestration from point sources such as power plants, enhancing the energy efficiency of buildings and cars, and the utilization of renewable sources such as solar and wind.[6] Increasing the utilization of CO_2, through both reductive and non-reductive pathways, is also proposed as it can create economic value while helping to decrease atmospheric CO_2 levels.[7] Possible ways to utilize CO_2 as a feedstock for chemical production are shown in **Figure 1.3**. The first group of methods forms products in which carbon keeps its +4 oxidation state: urea, polymeric materials, and inorganic carbonates. The second group aims to form products in which the oxidation state of carbon is reduced to +2 or lower: HCOOH, CO, C_2H_4, CH_3OH, or CH_3CH_2OH. Compared to the first group, formation of products within the second group requires higher energy exchange, which can be provided by strong reducing reagents, electricity, heat and/or radiation.[7]

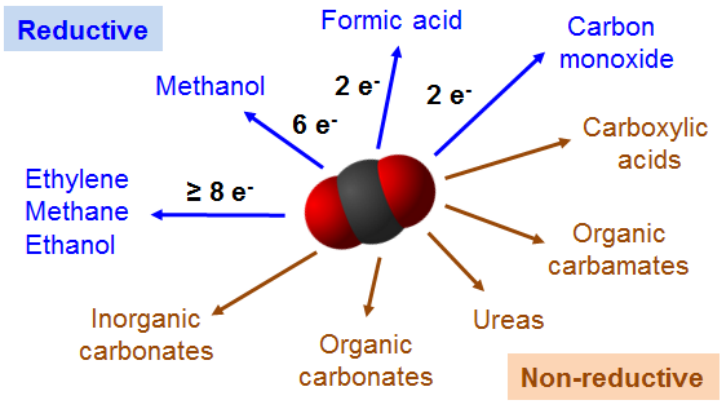

Figure 1.3 Possible ways to utilize CO_2 as a feedstock for chemical production.[7] Redrawn with permission from ref 7. Copyright 2015 RSC.

1.2 Challenges in Energy

Access to reliable and affordable energy has helped push the world towards more economic prosperity and has made human life better. However, as mentioned above, higher levels of prosperity have brought the problem of rising levels of greenhouse gasses to the atmosphere. Economic growth and energy-related emissions are coupled and move in the same direction

(**Figure 1.4**),[8] as more than 80% of the energy we use today are from fossil fuels that emit greenhouse gases (mainly CO_2).

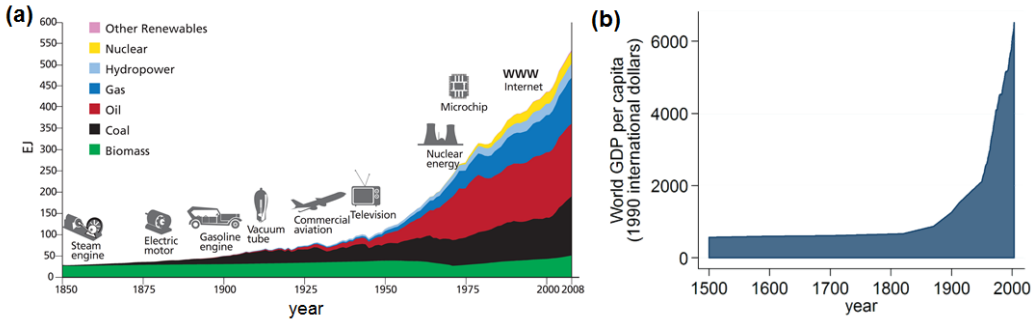

Figure 1.4 (a) Evolution of primary energy shown as absolute contributions by different energy sources (EJ); Reprinted with permission from ref 9. Copyright 2012 International Institute for Applied Systems Analysis. (b) World average GDP per capita 1500 to 2003. Source: https://commons.wikimedia.org/wiki/File:World_GDP_per_capita_1500_to_2003.png. data extracted from Angus Maddison's "World Population, GDP and Per Capita GDP, 1-2003 AD".

With the population continuing to increase, the world will consume much more energy than it does today in the next 20-30 years.[10] The projected world energy consumption in 2040 will be about 40% more than today's level (**Figure 1.5**),[11] with most of the increase from non-Organisation for Economic Co-operation and Development (non-OECD) countries. Therefore, finding ways to supply the rapidly increasing demand for energy while also limiting and/or decreasing carbon emissions is a major global challenge.

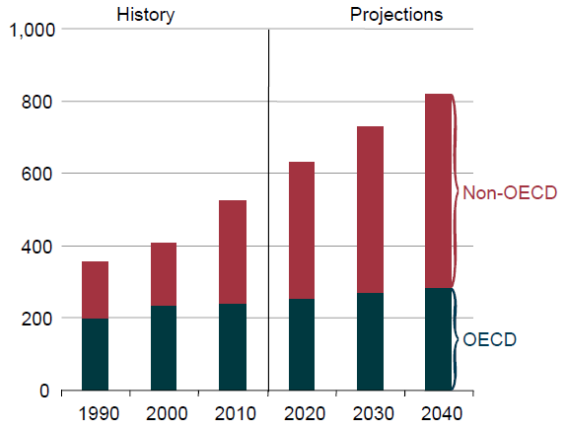

Figure 1.5 World energy consumption (in quadrillion Btu), 1990-2040. Reprinted with permission from ref 11. Copyright 2013 U.S. Energy Information Administration.

In response to the need to meet the increasing energy demand while limiting greenhouse gas emissions, the International Energy Agency (IEA) proposed five energy sector measures: (1) increasing energy efficiency in the industry, building, and transport sectors; (2) progressively reducing the use of the least-efficient coal-fired power plants and banning their construction; (3) increasing investment in renewable energy to $400 billion in 2030; (4) gradually phasing out subsidies to fossil-fuel consumption; and (5) reducing methane emissions from oil and gas production.[8] Many governments have already taken measures to promote these approaches. For example, the United States, the European Union, China and Southeast Asia countries have set new energy performance standards for residential appliances such as refrigerators and air-conditioners to improve energy efficiency; China established a target of phasing out 10 gigawatts (GW) of small thermal power plants by 2020; Several countries have already announced reforms to fossil-fuel consumption subsidies; The United States has set a target to cut methane emissions from the oil and gas sector by 40% to 45% in 2025 relative to the levels of 2012; About $270 billion was invested in renewable energy development in the power sector in 2014 around the world.[8] The global energy-related greenhouse gas emissions reduction achieved by these five policy measures in the Bridge Scenario (The Bridge Scenario depends upon the five proposed measures) relative to the INDC Scenario (Intended Nationally Determined Contributions Scenario: a first assessment of the impact of INDCs national pledges on the energy sector) is shown in **Figure 1.6**. In the INDC Scenario, national pledges have a positive impact in slowing the growth in global energy-related emissions, but emissions will still continue to rise. Effective implementation of the proposed measures in the Bridge Scenario will have a more profound effect on the global greenhouse gas emissions: Global emissions will be 4.8 Gt (or 13%) lower than in the INDC

Scenario by 2030. In the Bridge Scenario, energy related greenhouse gas emissions will peak and then begin to decline by around 2020.[8]

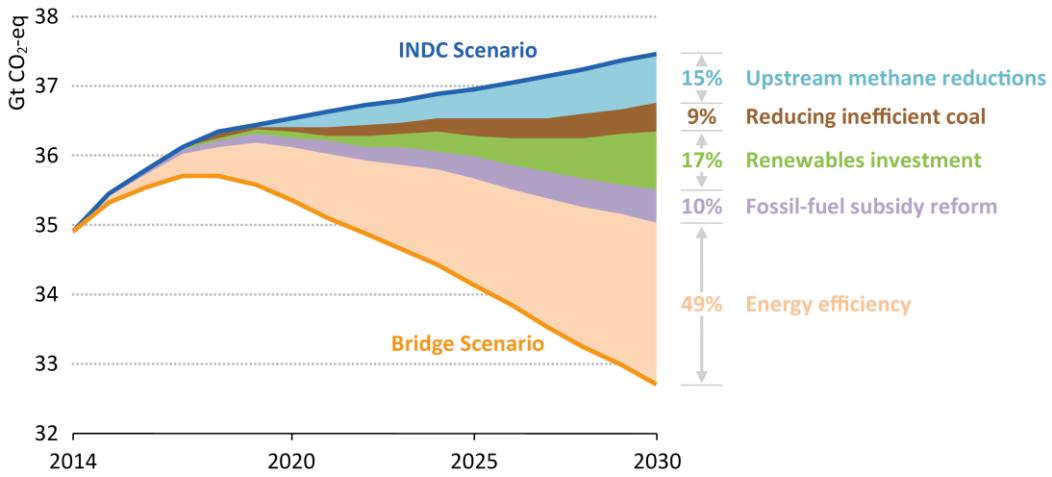

Figure 1.6 Global energy-related greenhouse gas emissions reduction by policy measure in the Bridge Scenario relative to the INDC Scenario. Reprinted with permission from ref 8. Copyright 2015 International Energy Agency.

Among the five measures in the Bridge Scenario, contributions from investment in renewables for reduction of energy-related greenhouse gas emissions will be the second largest. The renewables, especially wind and solar, are becoming increasingly competitive in the market due to cost reduction. The average investment costs for solar panels, has fallen by a factor of more than four over the past few years in China and by a factor of two in the OECD;[8] Wind turbine prices remained well below levels seen several years ago, while the turbine technology have improved significantly.[12] Wind and solar energy production have accounted for more than 60% of the total global renewables-based power capacity additions in 2014.[8] In the US, because federal tax incentives are available for projects that initiated construction by the end of 2014, a further resurgence in new builds of wind turbines is anticipated in both 2015 and 2016.[8] Therefore, further increasing contributions to power capacity from renewable sources such as wind and solar will continue.

However, wind and solar are intermittent sources, and often unpredictable. The electrical grid, by far the largest market for wind and solar energy, is not able to handle the intermittent nature of the rate by which they are produced. Customers still need electricity when the sun is not shining and the wind is not blowing. At times the electricity from wind and solar exceeds actual demand, and in the absence of large scale storage capacity is being wasted. The intermittency of wind and solar energy, therefore, hinders the economic competitiveness of those resources, as they are not necessarily available when they would be of greatest value to the system. As a result, methods for large-scale storage or on-demand utilization of intermittent electricity need to be developed so that lots of solar or wind energy can be stored and/or utilized when the supply is high.

Several approaches such as battery, pumped hydroelectric storage, electrolysis have been proposed to store excess intermittent renewable energy. In these approaches, electricity is converted to some other form of energy such as chemical energy or potential energy. Based on the type of battery used, it costs between 30 – 80 cents to store a kilowatt-hour of electricity.[10] This cost is at least triple the price of electricity, which costs only 10 cents per kilowatt-hour on average in the US. Also, today's batteries have much lower energy density than fossil fuels (about 30-70 times lower). Hydroelectric energy is currently widely used to store excess electricity in mountainous areas, while it cannot be used in flat areas such as the Midwest in the US. Storing electricity in a chemical form through electrolysis adds flexibility as electrolysis can be conducted where excess renewable energy is available, and the products such as hydrogen or liquid fuels can be used as sources for electricity and transportation fuels, or as a feedstock for chemical production.

1.3 Electroreduction of CO_2

Among various electrolysis approaches, the electroreduction of CO_2 into value-added products such as formic acid, CO, hydrocarbons, or alcohols can store on demand excess renewable electricity in a chemical form, and thus at the same time it can help to reduce atmospheric CO_2 levels. **Figure 1.7** summarizes the main concept for the electroreduction of CO_2. If the chemical industry were CO_2-based, the amount of CO_2 that would be consumed yearly is 300 million metric tons.[13] Also, compared to the traditional way of deriving chemicals from fossil fuels, the electroreduction of CO_2 does not rely on fossil fuels and is thus a more sustainable approach as long as it uses electricity from renewable sources or at least from a carbon-neutral source.

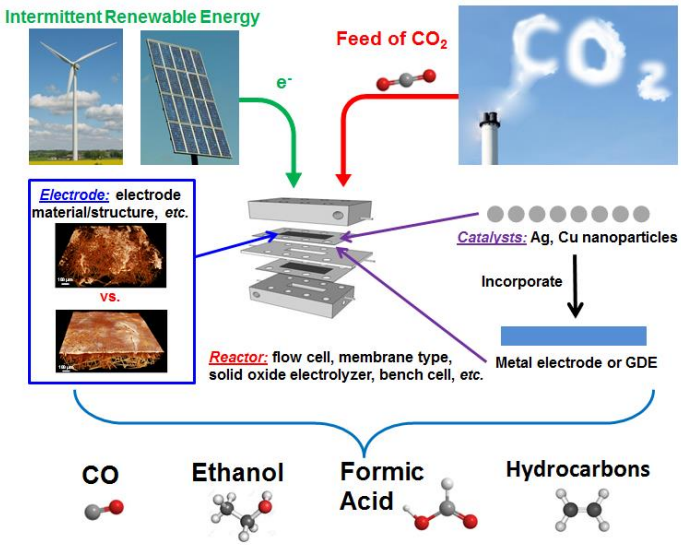

Figure 1.7 Schematic overview of the electroreduction of CO_2. Redraw with permission from ref 14. Copyright 2013 Elsevier.

The electrochemical conversion of CO_2 to other compounds is realized by reducing CO_2 using electrons in the electrical circuit as the driving force for the necessary uphill reactions. In an electrolyzer, CO_2 is reduced on the cathode while a compensating reaction such as the oxygen evolution reaction (OER) takes place on the anode. Half-reactions as well as standard potentials[15]

of the cathode for the electroreduction of CO_2 into major products such as CO, formic acid, methane, ethylene, and ethanol are listed in **Table 1.1**. Another important reaction that happens during the CO_2 reduction process is the hydrogen evolution reaction (HER) when an aqueous solution is used as the electrolyte. The standard electrode potential of hydrogen evolution reaction (HER) is 0 V *vs.* RHE, which is in the similar standard potential ranges for the CO_2 reduction reaction. Therefore, H_2 is often a major byproduct during CO_2 reduction.[16]

Table 1.1 Major half-cell reactions for the electroreduction of CO_2.

Reaction	**E° (V) (vs. RHE)**
$CO_2 + H_2O + 2e^- \rightarrow CO + 2OH^-$	-0.10
$CO_2 + H_2O + 2e^- \rightarrow HCOO^- + OH^-$	-0.02
$CO_2 + 6H_2O + 8e^- \rightarrow CH_4 + 8OH^-$	+0.17
$2CO_2 + 8H_2O + 12e^- \rightarrow C_2H_4 + 12OH^-$	+0.08
$2CO_2 + 9H^+ + 12e^- \rightarrow C_2H_5OH + 3OH^-$	+0.09

The process of CO_2 electrolysis is basically running a fuel cell in reverse; so indeed, many lessons learned over the last five or so decades in the development of catalysts, electrodes and cell configurations for fuel cells do apply also to the development of efficient CO_2 processes, but certain aspects will be very different and will require different optimization strategies. For example, both low-temperature fuel cells and CO_2 electrolysis cells are often limited by cathode performance, so both seek to improve slow cathode kinetics by developing more active catalysts. However, in addition to activity, catalysts for CO_2 reduction need to exhibit high product selectivity so the formation of desired products is heavily favored over unwanted reactions. Moreover, effective removal of products from the catalyst layer to avoid blocking active sites is important in both fuel cells and CO_2 electrolysis cells, but the technical strategies to do so can be very different due to the different nature of products. Specifically, the oxygen reduction reaction

in acidic fuel cells generates water which often leads to water management issues, whereas the CO_2 reduction reaction in CO_2 electrolysis cells often leads to the formation of both gaseous (*e.g.*, CO, H_2) and liquid products and thus effective gas / liquid phase separation is vital.

For electroreduction of CO_2 to be performed in an efficient manner, highly active and durable electrocatalysts for both the cathode (CO_2 reduction reaction) and the anode (O_2 evolution reaction), as well as electrodes and electrolytes that have high conductivity and allow for sufficient mass transport of the reactants and products to/from the catalyst layers are required. Key figures of merit of the process that characterize its performance and thus assist in determining its economic feasibility are (i) the *Energy Efficiency (EE)* – a measure of the overall energy utilization towards the desired product; (ii) the *Current Density (CD)* – a measure of the rate of conversion; (iii) the *Faradaic Efficiency (FE)* – a measure of the selectivity of the process for a given product; (iv) *the catalyst stability*; and (v) *process costs*[17] – including material consumption costs, capital cost and electricity cost. This dissertation will focus on the first three figures of merit (EE, FE, and CD) because currently neither standard protocols for durability tests of catalysts nor cost models for major products exist for electrochemical CO_2 conversion.

The energy efficiency can be calculated using equation 1:

$$\varepsilon_{energetic} = \sum_k \frac{E_k^\circ \varepsilon_{k,Faradaic}}{E_k^\circ + \eta} \qquad (1)$$

where E_k° is the equilibrium cell potential for a certain product. For example, $E^o = E^o_{cathode} - E^o_{anode}$ = -0.10 V - 1.23 V = -1.33 V for converting CO_2 to CO and $E^o = E^o_{cathode} - E^o_{anode}$ = 0 V - 1.23 V = -1.23 V for H_2 evolution). $\varepsilon_{k,Faradaic}$ is the Faradaic efficiency of product *k* and η is the cell overpotential (or the sum of overpotentials on the cathode and anode). From this equation it becomes clear that high energy efficiency is achieved through a combination of high Faradaic

efficiency for the desired product, and low overpotentials on the cathode and anode, because that will lead to a low cell potential. Note that at times researchers use a slightly different approach to determine the energy efficiency of their experimental setup.[18]

The Faradaic efficiency (sometimes also referred to as the current efficiency) for a given product is calculated using equation 2:

$$\varepsilon_{Faradaic} = \frac{z \cdot n \cdot F}{Q} \qquad (2)$$

where z is the number of electrons exchanged (for example, n = 2 for reduction of CO_2 to CO), n the number of moles for a given product, F Faraday's constant (F = 96485 C/mol), and Q the charge passed (C).[15,18,19]

The overall current density, defined as the current at a given cell potential divided by the active cathode electrode area (geometric surface area of the cathode), is a measure of the electrochemical reaction rate (conversion), so it helps determine the electrode area (and thus the electrolyzer size and capital investment) needed to meet the desired rate of producing the product. One can also calculate partial current densities for the individual products formed by multiplying overall current density by the corresponding FE.

1.4 Current Status, Challenges and Future Opportunities of CO_2 Reduction

In addition to providing opportunities to curb atmospheric CO_2 levels and store intermittent renewable energy, the electroreduction of CO_2 also has the potential for economic gains as it produces valuable chemicals or fuels. However, to make this process viable for commercialization, significant improvements in energy efficiency, current density and product selectivity are needed. In this whole process, catalysts, electrodes, electrolytes, as well as reactors (electrolyzers) play important roles in determining the energy efficiency, current density and

product selectivity. (1) Electrocatalysts and (2) electrolytes largely determine kinetics, thereby affecting all the figures of merit; (3) Reactors influence the mass transportation of reactants and products, thereby affecting the current density mostly; (4) Electrodes determine the electron conductivity and mass transportation to/from catalysts, thereby majorly affecting energy efficiency and current density. Current combinations of catalysts, electrodes, electrolytes and reactors have not rendered the electroreduction of CO_2 with similar performance as already commercialized electrolysis technology, *e.g.*, water electrolysis and chlor-alkali process. Therefore, both challenges and opportunities exist within these four areas of research to further improve the viability of CO_2 reduction for being practically applied.

Catalysts

Electrocatalysts are needed to bind and activate CO_2 in order to reduce the high overpotentials typically encountered. Also, catalysts can drive selective formation of desired products. During the past few decades efforts have mostly focused on different metal catalysts and the various products that can be formed using those metals.[20-23] Four distinct classes of metal catalysts have been identified for CO_2 reduction: (1) metals that mainly form formic acid, HCOOH (Pb, Hg, In, Sn, Cd, Tl); (2) metals that mainly form carbon monoxide, CO (Au, Ag, Zn, Pd, Ga); (3) metals that form significant amounts of hydrocarbons such as methane and ethylene (Cu); and (4) metals that mainly form H_2 (Pt, Ni, Fe, Ti).[20] Other potential products formed using metal catalysts include alcohols[24] and oxalic acid[25]. Over the last few years, researchers have also started to study other materials, including metal oxides[26-29], roughened or nanostructured metal catalysts,[30-33] metal organic frameworks (MOF),[34] covalent organic frameworks,[35] pyridine related organic compounds[36,37] as well as organometallic catalysts.[38] The chemistries between the catalyst

and the reactant/intermediates were investigated using either spectroscopic techniques[39,40] or computational approaches such as DFT[41-43] to reveal structure-activity relationships.

Catalysts that simultaneously exhibit low overpotentials (*e.g.*, < -0.2 V) and high current densities (*e.g.*, >100 mA/cm^2) needed for commercial applications are still lacking. The quest for such catalysts could be aided by (i) more fundamental studies focusing on elucidation of reaction mechanisms for distinct catalysts, an area in which reports are few[42,44,45], and (ii) more in-depth modeling efforts, ideally linked directly with experimental work, so pathways for CO_2 reduction on different catalysts can be better understood, which in turn will assist the design and synthesis of novel catalysts that have both low overpotential and high activity for CO_2 reduction reactions. The above-mentioned recent reports in this section on a variety of promising catalysts for CO_2 reduction (MOFs, organometallics, etc.) suggest that significant strides will be made to enhance catalyst activity while reducing overpotential. Such efforts will greatly benefit from fundamental mechanistic studies, as well as modeling of new classes of catalytic materials.

Electrode Structure

Electrodes play a vital role in all devices based on heterogeneous electrochemical reactions, including those for CO_2 conversion. The performance and durability of the reactor is largely determined by the processes occurring at the electrode-electrolyte interface and within the electrode. Maximizing electrode performance, and consequently reactor performance, requires optimizing all of these transport processes that strongly depend on the complex structure of the electrode. Despite their importance, to date only a few efforts have studied the interplay between electrode structure and performance.[18,20,46-48] In early work, Hori *et al.* extensively studied the CO_2 reduction reaction on planar metal electrodes (Cu, Au, Ag, Zn, Pd, Ga, Pb, Hg, In, Sn, Cd, Tl, Ni, Fe, Pt, Ti) at low current densities of about 5 mA/cm^2.[20] Low surface area and low CO_2

concentrations at the electrode surface due to the limited CO_2 solubility in the aqueous electrolytes used limits the performance of such planar electrodes. Recently, Delacourt *et al.* hand- or spray-painted Ag catalyst inks on gas diffusion layers (GDLs) to generate cathodes with a Ag (particle size of 1 µm) loading of 8-10 mg/cm^2.[18] This Ag nanoparticle-covered GDE (cathode) achieved current densities as high as 20 mA/cm^2, in combination with product selectivities for CO and H_2 that are comparable to the findings by Hori *et al.*[20] and Yano *et al.*[46] using similar catalysts (Ag) and electrolytes (0.5 M $KHCO_3$). Our lab recently developed a fully-automated airbrushing method to deposit a very thin, crack free layer with a Ag loading of only 0.75 mg/cm^2.[48] The electrolyzer equipped with this kind of electrode achieved a current density as high as 91 mA/cm^2 in combination with 94% Faradaic efficiency for CO, and 46% energy efficiency. Use of a GDE in combination with optimized catalyst layer deposition methods has led to significant improvement in electrode performance for CO_2 reduction. Further efforts should probably focus on assessing, via experiment and modeling, to what extent the structure and chemical composition of *the catalyst layer* (*e.g.*, pore size and distribution, the choice of binder materials such as Nafion) and *the porous backing layer (e.g.*, porosity, hydrophobicity, layer thickness*)* impact the transport of reactants (sufficient supply of CO_2?) and products (active sites blocked?).

Electrolyte

Electrolytes have been known to affect almost every electrochemical process dating back to the days of Frumkin.[49] The heterogeneous electrochemical reduction of CO_2 employs aqueous electrolytes commonly comprised of alkali cations (*e.g.*, Na^+, K^+), various anions such as halide anions (*e.g.*, Cl^-), bicarbonate (HCO_3^-), or hydroxide (OH^-), and water.[20,50-52] These inorganic salts are often used due to their high conductivities in water. Additionally, the water in aqueous electrolytes provides protons for the necessary electrochemical proton transfer steps involved in

the reaction pathway.[20,42] A number of prior reports have shown that electrolyte choice has profound effects on current density, product selectivity, and energy efficiency in CO_2 reduction.[50] For example, Hori *et al.* reported that cation choice (*i.e.*, Li^+, Na^+, K^+, and Cs^+) for bicarbonate (HCO_3^-) electrolytes significantly impacts the distribution of product formed on copper (Cu) electrodes.[50-52] Hori *et al.* also reported that anion choice (*i.e.*, Cl^-, ClO_4^-, SO_4^-, HCO_3^-, $H_2PO_4^-$), each with different buffer capacities, influences the local pH at the Cu electrode and thus the nature and the amount of products formed.[51] Similar to these findings by Hori *et al*., Wu *et al.* observed significant differences in activity and selectivity of tin (Sn) electrodes when different electrolytes ($KHCO_3$, K_2SO_4, KCl, Na_2SO_4, Cs_2SO_4, $NaHCO_3$, and $CsHCO_3$) are used.[52] Previously, we reported that the size of the cation ($Na^+ < K^+ < Rb^+ < Cs^+$) of the salt used in the electrolyte plays a significant role in CO_2 reduction on silver (Ag) electrodes. Specifically, larger cations favor CO production and suppress H_2 evolution.[53] In summary, these studies show that (i) cation size impacts the propensity for cation adsorption on the electrode surface, which affects the potential of the outer Helmholtz plane (OHP) in the electrical double layer (EDL), and in turn impacts reaction energetics and kinetics; and (ii) the buffer capacity of anions impacts the local pH at the electrode and thus the availability of protons, which in turn affects reaction kinetics. Furthermore, depending on reactor configuration, electrolyte composition may enhance performance by improving the solubility of CO_2, for instance by using ionic liquids[54] instead of aqueous solution, thereby reducing mass transport limitations.

Electrolyzers

No standard experimental setup or methodology for studying electrochemical CO_2 reduction currently exists. Different labs have used a variety of flow cells or electrolyzers for the various studies reported here. Jaramillo and coworkers,[15] as well as our lab,[38,48,53,55] use a

microfluidic flow cell in which the electrodes are separated by a flowing liquid electrolyte, which enables analysis of individual electrode performance by using an external reference electrode. Delacourt *et al.* based their design on an alkaline fuel cell,[18] while Dufek *et al.* used a more traditional electrolyzer design.[56-59] Interestingly, three of these systems exhibit similar behavior when comparing their performance for CO production. Indeed, Dufek *et al.*[56,59] have reported improved reactor performance at elevated temperature and/or pressure. Further optimization of operating conditions (*e.g.*, electrolyzers operated at elevated pressure and temperature) will continue to improve reactor performance in CO_2 reduction. Specifically, multiple labs have reported enhanced current densities in pressurized electrolyzers (*e.g.*, 20 atm).[60,61] For example, Furuya *et al.* reported that a total current density as high as 300-900 mA/cm^2 can be achieved under 20 atm using a pressurized electrolyzer operated with GDEs coated with different metals (Pt, Ag, Cu, Ni, Co, Pd).[60]

1.5 Summary and Thesis Outline

In summary, the electroreduction of CO_2 shows promise to store intermittent renewable energy in the form of chemical bonds and reduce carbon emissions. However, to be used commercially, improvements are needed regarding the present low energy efficiency and current density of the reaction. The purpose of this dissertation is to develop active catalysts and proper electrode structures to improve the current density and selectivity to certain products, thereby improving the energy efficiency for the electroreduction of CO_2. This dissertation will also discuss insights into CO_2 reduction reaction gained through studying the activity of various catalysts with different structures or properties. Hopefully the insight gained will help guide the design of better catalysts and electrodes for this process.

Specifically, Chapters 2, 3 and 7 focus on improving the current density and the energy efficiency for the electroreduction of CO_2 to CO. Chapter 2 presents the use of a support material to lower the Ag-based cathode catalyst loading without sacrificing performance. Chapter 3 discusses how improvements to the anode can drastically improve the prospects of the electrochemical reduction of CO_2. Chapter 7 details the design and application of Ag cathodes with the incorporation of multi-walled carbon nanotubes to improve the current density and energy efficiency. Chapters 4, 5 and 6 mainly focus on developing Cu-related catalysts to improve the production of C2 chemicals (ethylene and ethanol) from CO_2. Chapter 4 explores the application of Cu nanoparticles with different morphologies for the efficient conversion of CO_2 to C2 products. Chapter 5 demonstrates the use of N-containing ligand to improve the selectivity to C2 chemicals on Cu-based catalysts. Chapter 6 discusses the effect of bimetallic alloy structures on the production of C2 chemicals.

1.6 References

1 Tans, P. & Keeling, R. Recent Monthly Average Mauna Loa CO_2. (ESRL Global Monitoring Division Global Greenhouse Gas Reference Network. URLL: http://www.esrl.noaa.gov/gmd/ccgg/trends/, 2015).

2 Astor, Y., Bates, N., Church, M., Coppola, L., Currie, K., González-Dávila, M., Miller, L., Nakano, T. & Wakita, M. WMO Greenhouse Gas Bulletin. 8 (World Meteorological Organization, 2014).

3 Pachauri, R. K. & Meyer, L. Climate Change 2014: Synthesis Report. 151 (IPCC, Geneva, Switzerland, 2014).

4 Hansen, J., Kharecha, P., Sato, M., Masson-Delmotte, V., Ackerman, F., Beerling, D. J., Hearty, P. J., Hoegh-Guldberg, O., Hsu, S.-L., Parmesan, C., Rockstrom, J., Rohling, E. J., Sachs, J., Smith, P., Steffen, K., Van Susteren, L., von Schuckmann, K. & Zachos, J. C. Assessing "Dangerous Climate Change": Required Reduction of Carbon Emissions to Protect Young People, Future Generations and Nature. *PLoS One* **8**, e81648, (2013).

5 Randalls, S. History of the 2°C climate target. *Wiley Interdisciplinary Reviews: Climate Change* **1**, 598-605, (2010).

6 Pacala, S. & Socolow, R. Stabilization Wedges: Solving the Climate Problem for the Next 50 Years with Current Technologies. *Science* **305**, 968-972, (2004).

7 Martin, A. J., Larrazabal, G. O. & Perez-Ramirez, J. Towards sustainable fuels and chemicals through the electrochemical reduction of CO2: lessons from water electrolysis. *Green Chem.* **17**, 5114-5130, (2015).

8 Wanner, B., Kęsicki, F., Hood, C., Baroni, M., Bennett, S., Besson, C., Bouckaert, S., Bromhead, A., Durand-Lasserve, O., El-Laboudy, T., Gould, T., Hashimoto, M., Klingbeil, M., Kurozumi, A., Levina, E., Liu, J., McCoy, S., Olejarnik, P., Selmet, N., Sinopoli, D., Suehiro, S., Trüby, J., Vailles, C., Wilkinson, D., Zazias, G. & Zhang, S. Energy and Climate Change - World Energy Outlook Special Report 2015. 200 (International Energy Agency, Paris, France, 2015).

9 Banerjee, R., Benson, S. M., Bouille, D. H., Brew-Hammond, A., Cherp, A., Coelho, S. T., Emberson, L., Figueroa, M. J. n., Grubler, A., Jaccard, M., Ribeiro, S. K., Karekezi, S., He, K., Larson, E. D., Li, Z., McDade, S., Mytelka, L. K., Pachauri, S., Patwardhan, A., Riahi, K., m, J. R. ö., Rogner, H.-H., Roy, J., Schock, R. N., Sims, R., Smith, K. R., Turkenburg, W. C., rge-Vorsatz, D. Ü., Hippel, F. v. & Yeager, K. *Global Energy Assessment - Toward a Sustainable Future*. (2012).

10 Gates, B. Energy Innovation - Why We Need It and How to Get It. (2015).

11 Conti, J., Holtberg, P., Beamon, J. A., Napolitano, S., Schaal, A. M., Turnure, J. T., Westfall, L., Geagla, A., Grissom, S., Maples, J., Teller, K., Smith, K. A., Staub, J., Ayoub, J., Cheung, C., Eshbaugh, M., Griffin, K., Lou, J., Smith, P., Smith, C. L., Federhen, C. & Wells, P. International Energy Outlook 2013. 312 (U.S. Energy Information Administration, Washington DC, USA, 2013).

12 Wiser, R. & Bolinger, M. 2014 Wind Technologies Market Report. 93 (U.S. Department of Energy, 2015).

13 Scott, A. in *Chem. Eng. News* Vol. 93 7 (American Chemical Society, 2015).

14 Jhong, H.-R. M., Ma, S. & Kenis, P. J. A. Electrochemical conversion of CO_2 to useful chemicals: current status, remaining challenges, and future opportunities. *Curr. Opin. Chem. Eng.* **2**, 191-199, (2013).

15 Kuhl, K. P., Cave, E. R., Abram, D. N. & Jaramillo, T. F. New insights into the electrochemical reduction of carbon dioxide on metallic copper surfaces. *Energy Environ. Sci.* **5**, 7050-7059, (2012).

16 Hori, Y. in *Modern Aspects of Electrochemistry* Vol. 42 *Modern Aspects of Electrochemistry* (eds ConstantinosG Vayenas, RalphE White, & MariaE Gamboa-Aldeco) Ch. 3, 89-189 (Springer New York, 2008).

17 Oloman, C. & Li, H. Electrochemical Processing of Carbon Dioxide. *ChemSusChem* **1**, 385-391, (2008).

18 Delacourt, C., Ridgway, P. L., Kerr, J. B. & Newman, J. Design of an Electrochemical Cell Making Syngas ($CO + H_2$) from CO_2 and H_2O Reduction at Room Temperature. *J. Electrochem. Soc.* **155**, B42-B49, (2008).

19 Wu, J., Risalvato, F. & Zhou, X.-D. Effects of the Electrolyte on Electrochemical Reduction of CO_2 on Sn Electrode. *ECS Trans.* **41**, 49-60, (2012).

20 Hori, Y., Wakebe, H., Tsukamoto, T. & Koga, O. Electrocatalytic Process of CO Selectivity in Electrochemical Reduction of CO_2 at Metal-Electrodes in Aqueous-Media. *Electrochim. Acta* **39**, 1833-1839, (1994).

21 Azuma, M., Hashimoto, K., Hiramoto, M., Watanabe, M. & Sakata, T. Electrochemical Reduction of Carbon-Dioxide on Various Metal-Electrodes in Low-Temperature Aqueous $KHCO_3$ Media. *J. Electrochem. Soc.* **137**, 1772-1778, (1990).

22 Hori, Y., Kikuchi, K. & Suzuki, S. Production of CO and CH_4 in Electrochemical Reduction of CO_2 at Metal-Electrodes in Aqueous Hydrogencarbonate Solution. *Chem. Lett.*, 1695-1698, (1985).
23 Ikeda, S., Takagi, T. & Ito, K. Selective Formation of Formic-Acid, Oxalic-Acid and Carbon-Monoxide by Electrochemical Reduction of Carbon-Dioxide. *Bull. Chem. Soc. Jpn.* **60**, 2517-2522, (1987).
24 Hori, Y. in *Handbook of Fuel Cells* Vol. 2 Ch. 48, 720-733 (John Wiley & Sons, Ltd, 2010).
25 Tomita, Y., Teruya, S., Koga, O. & Hori, Y. Electrochemical reduction of carbon dioxide at a platinum electrode in acetonitrile-water mixtures. *J. Electrochem. Soc.* **147**, 4164-4167, (2000).
26 Chen, Y., Li, C. W. & Kanan, M. W. Aqueous CO_2 Reduction at Very Low Overpotential on Oxide-Derived Au Nanoparticles. *J. Am. Chem. Soc.* **134**, 19969-19972, (2012).
27 Li, C. W. & Kanan, M. W. CO_2 Reduction at Low Overpotential on Cu Electrodes Resulting from the Reduction of Thick Cu_2O Films. *J. Am. Chem. Soc.* **134**, 7231-7234, (2012).
28 Chen, Y. H. & Kanan, M. W. Tin Oxide Dependence of the CO_2 Reduction Efficiency on Tin Electrodes and Enhanced Activity for Tin/Tin Oxide Thin-Film Catalysts. *J. Am. Chem. Soc.* **134**, 1986-1989, (2012).
29 Ren, D., Deng, Y., Handoko, A. D., Chen, C. S., Malkhandi, S. & Yeo, B. S. Selective Electrochemical Reduction of Carbon Dioxide to Ethylene and Ethanol on Copper(I) Oxide Catalysts. *ACS Catal.* **5**, 2814-2821, (2015).
30 Roberts, F. S., Kuhl, K. P. & Nilsson, A. High Selectivity for Ethylene from Carbon Dioxide Reduction over Copper Nanocube Electrocatalysts. *Angew. Chem.* **127**, 5268-5271, (2015).
31 Tang, W., Peterson, A. A., Varela, A. S., Jovanov, Z. P., Bech, L., Durand, W. J., Dahl, S., Norskov, J. K. & Chorkendorff, I. The importance of surface morphology in controlling the selectivity of polycrystalline copper for CO_2 electroreduction. *Phys. Chem. Chem. Phys.* **14**, 76-81, (2012).
32 Lu, Q., Rosen, J., Zhou, Y., Hutchings, G. S., Kimmel, Y. C., Chen, J. G. & Jiao, F. A selective and efficient electrocatalyst for carbon dioxide reduction. *Nat. Commun.* **5**, (2014).
33 Ma, S., Sadakiyo, M., Luo, R., Heima, M., Yamauchi, M. & Kenis, P. J. A. One-step electrosynthesis of ethylene and ethanol from CO_2 in an alkaline electrolyzer. *J. Power Sources* **301**, 219-228, (2016).
34 Hinogami, R., Yotsuhashi, S., Deguchi, M., Zenitani, Y., Hashiba, H. & Yamada, Y. Electrochemical Reduction of Carbon Dioxide Using a Copper Rubeanate Metal Organic Framework. *ECS Electrochemistry Letters* **1**, H17-H19, (2012).
35 Lin, S., Diercks, C. S., Zhang, Y.-B., Kornienko, N., Nichols, E. M., Zhao, Y., Paris, A. R., Kim, D., Yang, P., Yaghi, O. M. & Chang, C. J. Covalent organic frameworks comprising cobalt porphyrins for catalytic CO_2 reduction in water. *Science* **349**, 1208-1213, (2015).
36 Barton Cole, E., Lakkaraju, P. S., Rampulla, D. M., Morris, A. J., Abelev, E. & Bocarsly, A. B. Using a One-Electron Shuttle for the Multielectron Reduction of CO_2 to Methanol: Kinetic, Mechanistic, and Structural Insights. *J. Am. Chem. Soc.* **132**, 11539-11551, (2010).

37 Barton, E. E., Rampulla, D. M. & Bocarsly, A. B. Selective Solar-Driven Reduction of CO_2 to Methanol Using a Catalyzed p-GaP Based Photoelectrochemical Cell. *J. Am. Chem. Soc.* **130**, 6342-6344, (2008).

38 Tornow, C. E., Thorson, M. R., Ma, S., Gewirth, A. A. & Kenis, P. J. A. Nitrogen-Based Catalysts for the Electrochemical Reduction of CO_2 to CO. *J. Am. Chem. Soc.* **134**, 19520-19523, (2012).

39 García Rey, N. & Dlott, D. D. Structural Transition in an Ionic Liquid Controls CO_2 Electrochemical Reduction. *J. Phys. Chem. C* **119**, 20892-20899, (2015).

40 Schmitt, K. G. & Gewirth, A. A. In Situ Surface-Enhanced Raman Spectroscopy of the Electrochemical Reduction of Carbon Dioxide on Silver with 3,5-Diamino-1,2,4-Triazole. *J. Phys. Chem. C* **118**, 17567-17576, (2014).

41 Montoya, J. H., Peterson, A. A. & Nørskov, J. K. Insights into C-C Coupling in CO_2 Electroreduction on Copper Electrodes. *ChemCatChem* **5**, 737-742, (2013).

42 Peterson, A. A., Abild-Pedersen, F., Studt, F., Rossmeisl, J. & Norskov, J. K. How copper catalyzes the electroreduction of carbon dioxide into hydrocarbon fuels. *Energy Environ. Sci.* **3**, 1311-1315, (2010).

43 Peterson, A. A. & Nørskov, J. K. Activity Descriptors for CO_2 Electroreduction to Methane on Transition-Metal Catalysts. *J. Phys. Chem. Lett.* **3**, 251-258, (2012).

44 Chandrasekaran, K. & Bockris, L. O. M. In-situ spectroscopic investigation of adsorbed intermediate radicals in electrochemical reactions: CO_2^- on platinum. *Surf. Sci.* **185**, 495-514, (1987).

45 Schouten, K. J. P., Qin, Z., Gallent, E. P. & Koper, M. T. M. Two Pathways for the Formation of Ethylene in CO Reduction on Single-Crystal Copper Electrodes. *J. Am. Chem. Soc.* **134**, 9864-9867, (2012).

46 Yano, H., Shirai, F., Nakayama, M. & Ogura, K. Electrochemical reduction of CO_2 at three-phase (gas vertical bar liquid vertical bar solid) and two-phase (liquid vertical bar solid) interfaces on Ag electrodes. *J. Electroanal. Chem.* **533**, 113-118, (2002).

47 Yano, H., Shirai, F., Nakayama, M. & Ogura, K. Efficient electrochemical conversion of CO_2 to CO, C_2H_4 and CH_4 at a three-phase interface on a Cu net electrode in acidic solution. *J. Electroanal. Chem.* **519**, 93-100, (2002).

48 Jhong, H.-R. M., Brushett, F. R. & Kenis, P. J. A. The Effects of Catalyst Layer Deposition Methodology on Electrode Performance. *Adv. Energy Mater.* **3**, 589-599, (2013).

49 Frumkin, A. N. Influence of Cation Adsorption on the Kinetics of Electrode Processes. *T Faraday Soc* **55**, 156-167, (1959).

50 Murata, A. & Hori, Y. Product Selectivity Affected by Cationic Species in Electrochemical Reduction of CO_2 and CO at a Cu Electrode. *Bull. Chem. Soc. Jpn.* **64**, 123-127, (1991).

51 Hori, Y., Murata, A. & Takahashi, R. Formation of hydrocarbons in the electrochemical reduction of carbon dioxide at a copper electrode in aqueous solution. *J. Chem. Soc., Faraday Trans. 1* **85**, 2309-2326, (1989).

52 Wu, J., Risalvato, F. G., Ke, F.-S., Pellechia, P. J. & Zhou, X.-D. Electrochemical Reduction of Carbon Dioxide I. Effects of the Electrolyte on the Selectivity and Activity with Sn Electrode. *J. Electrochem. Soc.* **159**, F353-F359, (2012).

53 Thorson, M. R., Siil, K. I. & Kenis, P. J. A. Effect of Cations on the Electrochemical Conversion of CO_2 to CO. *J. Electrochem. Soc.* **160**, F69-F74, (2013).

54 Rosen, B. A., Salehi-Khojin, A., Thorson, M. R., Zhu, W., Whipple, D. T., Kenis, P. J. A. & Masel, R. I. Ionic Liquid–Mediated Selective Conversion of CO_2 to CO at Low Overpotentials. *Science* **334**, 643-644, (2011).

55 Whipple, D. T., Finke, E. C. & Kenis, P. J. A. Microfluidic Reactor for the Electrochemical Reduction of Carbon Dioxide: The Effect of pH. *Electrochem. Solid-State Lett.* **13**, B109-B111, (2010).

56 Dufek, E. J., Lister, T. E., Stone, S. G. & McIlwain, M. E. Operation of a Pressurized System for Continuous Reduction of CO_2. *J. Electrochem. Soc.* **159**, F514-F517, (2012).

57 Dufek, E. J., Lister, T. E. & McIlwain, M. E. Influence of S Contamination on CO_2 Reduction at Ag Electrodes. *J. Electrochem. Soc.* **158**, B1384-B1390, (2011).

58 Dufek, E. J., Lister, T. E. & McIlwain, M. E. Influence of Electrolytes and Membranes on Cell Operation for Syn-Gas Production. *Electrochem. Solid-State Lett.* **15**, B48-B50, (2012).

59 Dufek, E., Lister, T. & McIlwain, M. Bench-scale electrochemical system for generation of CO and syn-gas. *J. Appl. Electrochem.* **41**, 623-631, (2011).

60 Furuya, N., Yamazaki, T. & Shibata, M. High performance Ru-Pd catalysts for CO_2 reduction at gas-diffusion electrodes. *J. Electroanal. Chem.* **431**, 39-41, (1997).

61 Sonoyama, N., Kirii, M. & Sakata, T. Electrochemical reduction of CO_2 at metal-porphyrin supported gas diffusion electrodes under high pressure CO_2. *Electrochem. Commun.* **1**, 213-216, (1999).

Chapter 2*

Titania Supported Silver Catalyst for the Electroreduction of CO_2

2.1 Chapter Overview

While significant research efforts have focused on the exploration of catalysts for electrochemical reduction of CO_2, considerably fewer efforts have studied how support materials for these catalysts affect their performance, including their ability to reduce the overpotential, and/or to increase the catalyst utilization and selectivity. Here Ag nanoparticles supported on carbon black (Ag/C) and on titanium dioxide (Ag/TiO_2) were synthesized. In a flow reactor, 40 wt% Ag/TiO_2 exhibited two-fold higher current density for CO production than 40 wt% Ag/C. Faradaic efficiencies of the 40 wt% Ag/TiO_2 catalyst exceeded 90% with a partial current density for CO of 101 mA cm^{-2}; similar to the performance of unsupported Ag nanoparticle catalysts (AgNP), but at a 2.5 times lower silver loading. A mass activity as high as 2700 $mAmg_{Ag}^{-1}cm^{-2}$ was achieved. In cyclic voltammetry (CV) in a three-electrode cell, Ag/TiO_2 exhibited a lower overpotential for CO_2 reduction than AgNP, which, together with other data, suggests that TiO_2 stabilizes the intermediate and serves as redox electron carrier to assist CO_2 reduction while Ag assists in formation of the final product CO.

2.2 Introduction

The world's increasing energy consumption due to increases in the world population and increased energy consumption in developing parts of the world, is accelerating the depletion of the

* Part of this work has been published: Ma , S., Lan , Y., Perez, G. M. J., Moniri, S. & Kenis , P. J. A. Silver Supported on Titania as an Active Catalyst for Electrochemical Carbon Dioxide Reduction. *ChemSusChem* **7**, 866-874, (2014). Copyright 2014. Reproduced with permission from Wiley.

world's dwindling fossil fuel reserves.[62,63] This increased energy consumption has led to a steady increase in atmospheric CO_2 levels over several decades, which in turn has been linked to undesirable climate change effects. To curb the rise, and eventually to lower the atmospheric CO_2 levels, multiple approaches need to be pursued, because no single approach has the capacity to address this issue by itself.[6] Approaches to reduce CO_2 emissions include switching to energy sources that emit less CO_2 (*e.g.*, natural gas instead of coal), carbon capture and sequestration from point sources such as power plants, enhancing the energy efficiency of buildings and cars, and the utilization of renewable sources such as solar and wind. Potential economic gains provide a natural incentive for the implementation of some of these approaches (*e.g.*, enhancing energy efficiency of buildings and cars), whereas other approaches will require regulation as they can only be implemented at a substantial cost (*e.g.*, carbon capture and underground sequestration). Many renewable power plants (wind, solar, tidal, etc.) have become operational around the world, but due to their intermittent nature these sources can only be used in combination with more conventional, fossil fuel based power plants. Furthermore, to avoid renewable power being wasted when the amount being produced is high, methods for large scale energy storage or on-demand utilization need to be developed.[64,65]

The catalytic conversion of CO_2 into useful chemicals such as intermediates for the synthesis of fuels and polymers using photochemical, electrochemical, thermochemical, or other methods is another promising approach to curb atmospheric CO_2 levels, while at the same time providing the potential for economic gains.[17,24,66-71] More specifically, the electrochemical conversion of CO_2 into value-added products, such as formic acid, carbon monoxide, hydrocarbons, or alcohols can utilize on demand excess energy from renewable energy plants while simultaneously helping to reduce atmospheric CO_2 levels.[72] However, significant

improvements in the efficiency and at times the selectivity of the electrolysis of CO_2 into any of these products are needed for this process to become economically viable.[16,72,73] Most electrocatalysts reported to date exhibit a high overpotential for the desired reaction, which drastically reduces the energy efficiency. Also, conversion rate, as expressed by the observed current density, is still insufficient. Electrocatalysts need to be developed that simultaneously exhibit a low overpotential (thus high energy efficiency), high Faradaic efficiency (high selectivity), and high current density (thus high rate of conversion).[14,72]

Over the past decades multiple metal catalysts have been tested for the production of various products by electrochemical reduction of CO_2.[15,16,21-23,74] For example, Hori *et al.* found that different metal catalysts exhibit selectivity for different products: *i.e.,* metals such as Ag and Au lead to predominantly CO, metals such as Sn lead to formate while Cu leads to the formation of mixtures of hydrocarbons.[20] Here, the conversion of CO_2 to CO is focused in this chapter since the combination of CO and H_2 (syngas) can be converted to liquid fuels through the Fischer-Tropsch process. Although some catalysts are able to produce CO and H_2 at the same time, catalysts that predominantly produce CO are focused because H_2 can be obtained more efficiently (higher system efficiency and current density) from other sources, e.g. water electrolysis, than by co-generating H_2 with CO. Overall, optimizing the electrolysis cell for CO production and supplying H_2 from water electrolysis will be energetically more efficient than co-generation in a single electrolyzer.[72]

Some of the early work indicates that the large overpotential needed for CO_2 reduction mainly stems from the barrier of the initial electron transfer to form a $CO_2^{\bullet-}$ intermediate that is poorly stabilized by most metal surfaces.[24,44] Some approaches to stabilize this intermediate, leading to a lower overpotential have been reported. Recently we reported the use of EMIM-BF_4

(1-Ethyl-3-methylimidazolium tetrafluoro-borate) as a co-catalyst in combination with unsupported Ag nanoparticle-based catalyst to lower the cell overpotential for the electroreduction of CO_2 to CO on silver electrodes to ~0.2 V, although only at low current densities (<5 mA cm^{-2}) and high loading (6.67 mg of Ag per cm^2).[54] Chen *et al.* reduced the overpotential of CO_2 reduction to CO to 140 mV via stabilizing the $CO_2^{\bullet-}$ intermediate on the surfaces of the oxide-derived Au electrodes.[26] With respect to conversion, most studies focusing on electroreduction of CO_2 to CO report current densities in the range of 2 to 118 mA cm^{-2} under ambient condition, and most of these studies use Ag as the cathode catalyst.[14] For example, Dufek *et al.*[59] and Delacourt *et al.*[18] reported partial current densities for CO (j_{co}) of less than 60 $mAcm^{-2}$ at -1.8 V *vs.* Ag/AgCl when operating their respective cells at ambient temperature and pressure. Tornow *et al.* studied nitrogen-based organometallic silver catalysts, which achieved j_{co} as high as 115 $mAcm^{-2}$ while decreasing the Ag loading by a factor of 20.[38] Also, recently we have reported that the performance of Ag catalysts in CO_2 reduction depends on Ag nanoparticle size.[75]

To date significant efforts have focused on the exploration of catalysts, whereas significantly fewer efforts have focused on the study of different catalyst supports. Catalyst supports can have tremendous influence on catalyst performance while simultaneously resulting in lower catalyst loading.[76] For example, in fuel cells, reducing the loading of precious catalysts, especially Pt, while increasing performance and durability, has been a critical step towards improving the commercial viability of this technology.[76] Specifically, support materials have been developed to support and stabilize smaller nanoparticles that are often more active, while enabling better catalyst dispersion and utilization, and providing better electron conduction and mass transport.[76-79]

Titanium dioxide (TiO_2) has been used as a readily available support material and a catalyst for a variety of applications, including as a non-carbonaceous support for Pt in fuel cell electrodes[80] and as a catalyst itself in the photo-reduction of CO_2.[81-84] TiO_2 has been reported to interact strongly with Pt, which increases the Pt catalyst activity, while at the same time increases the stability and durability of Pt catalysts.[76,85,86] TiO_2 can also act as a redox electron carrier to facilitate various reduction reactions including CO_2 conversion.[87-89] Additionally, the TiO_2 surface has been reported to assist in CO_2 adsorption[90-93], thus it may be able to stabilize the $CO_2^{\bullet-}$ intermediate to reduce the overpotential.

Here in this chapter, the use of TiO_2 as a catalyst support for Ag catalysts to improve the reduction of CO_2 to CO will be reported. Previously, Cueto *et al.* observed enhancement of CO_2 and/or H_2O reduction when using Ag particles (~250 nm) that are electrodeposited on a thin film TiO_2 electrode.[94] This work did not report product selectivity, and they did not study the role, if any, of the flat TiO_2 film. In contrast, the study reported here investigates the effect of much smaller, sub-10 nm Ag nanoparticles deposited on 15-30 nm TiO_2 particles on CO_2 electroreduction. Specifically, two types of catalysts: different loadings of Ag catalyst supported on TiO_2 (Ag/TiO_2) and 40 wt% Ag supported on carbon black (Ag/C) were synthesized and characterized. Their electrochemical performance in the reduction of CO_2 to CO was compared with the performance of the well-studied Ag nanoparticle catalysts using an electrochemical flow reactor.[38,55] Through structural characterization and electrochemical experiments, the role of the TiO_2 support in enhancing the catalytic sites, specifically with respect to its ability to maintain the Ag nanoparticles at its most catalytically active size and its ability to stabilize the $CO_2^{\bullet-}$ intermediate, was investigated.

2.3 Experimental

2.3.1 Preparation of Ag/TiO_2 and Ag/C catalysts

The previously reported citrate-protecting method[95,96] was used to obtain the different Ag/TiO_2 catalysts. In contrast to previous reports, the support materials used here (TiO_2 or carbon black) were first mixed with 40 mM $AgNO_3$ (Sigma-Aldrich) aqueous solution to allow for better adsorption of Ag^+ on the support. Sodium citrate (Fisher Chemicals) was then added to stabilize Ag^+ followed by the addition of $NaBH_4$ (Sigma-Aldrich) to reduce Ag^+. Specifically, for the synthesis of 40 wt% Ag/TiO_2, $AgNO_3$ (125.7 mg) was dissolved in Millipore H_2O (18.5 mL), TiO_2 (120 mg, Aeroxide® TiO_2 P25, particle size: 21±5 nm) was added to the solution, followed by stirring for 30 minutes. Subsequently, sodium citrate solution (131 mM, 18.5 mL) was added drop by drop while stirring. The reduction of Ag^+ was achieved by the drop-wise addition of $NaBH_4$ solution (30 mM, 25 mL) with vigorous stirring in an ice-bath. After stirring the solution gently overnight, it was centrifuged, washed and dried in a vacuum oven at 80 °C for 4 hours. The obtained catalyst was wine red in color. Samples with Ag loadings of 5 wt%, 10 wt%, 20 wt%, and 60 wt% were prepared using the same method by changing the amount of TiO_2. For comparison, 40 wt% Ag/C catalyst was synthesized with the same method using Vulcan XC-72R (Carbon Blk Vulcan XC-72R, Fuel Cell Store) as the support.

2.3.2 Physical characterization

The Ag weight percentages of the different catalysts were determined by ICP-OES (PerkinElmer – Optima 2000DV). The samples were digested in a mixture of HNO_3 and HF prior to analysis. Ag particle size and dispersion on the support were examined using TEM (JOEL 2100 CRYO) operated at 200 kV. The TEM sample was prepared by suspending the catalyst in

isopropanol and placing a drop of the suspension onto a holey carbon-coated 200 mesh grid followed by solvent evaporation overnight at room temperature.

2.3.3 Electrochemical characterizations

Electrode preparation: Catalyst inks were prepared by mixing Millipore water (200 μL), catalyst (2 mg), Nafion® solution (2.6 μL, 5 wt%, Fuel Cell Earth), and isopropyl alcohol (200 μL). The inks were then sonicated (Vibra-Cell ultrasonic processor, Sonics & Materials) for 15 minutes and then painted on the microporous layer of Sigracet 35 BC gas diffusion layers (Ion Power) using a paintbrush. All the flow reactor experiments in this study used a 1 mg cm^{-2} cathode catalyst loading on Sigracet 35BC, while all of the anodes used in this study had a 1 mg cm^{-2} Pt loading on Sigracet 35BC.

Electrochemical flow reactor operation: The flow reactor (see *Supporting Information* **Figure 2.6** for a schematic) was operated under ambient condition. A potentiostat (Autolab PGSTAT-30, EcoChemie) operating in steady-state chrono-amperometric mode was used to measure the resulting current as previously reported.[38] For each trial, five cell potential from -2.0 V to -3.0 V, with an interval of 0.25 V was applied to the cell. For each potential, the cell was allowed to reach steady state for 200 s, after which, the gas flowed into a gas chromatograph. The current was averaged for an additional 180 s before stepping to the next potential. The individual electrode potentials were measured using multimeters (AMPROBE 15XP-B) connected to each electrode and a Ag/AgCl reference electrode (RE-5B, BASi) placed in the exit stream. A mass flow controller (MASS-FLO®, MKS instrument) was used to flow CO_2 from a cylinder at 7 SCCM. A syringe pump (PHD 2000, Harvard Apparatus) supplied the 1 M KOH electrolyte at 0.5 mL min^{-1}. Gas products formed on the GDE surface and left through the GDE to the gas stream driven

by vacuum connected to the end of the gas channel. For composition analysis of H_2 and CO, the effluent gas stream flowed directly into a gas chromatograph (Thermo Finnegan Trace GC) operating in the thermal conductivity detection (TCD) mode, with a Carboxen 1000 column (Supelco) and a Helium as the carrier gas at a flow rate of 20 SCCM. The column was held at 150 °C and the TCD detector was held at 200 °C. The only cathode products detected by GC were CO and H_2 when using Ag as the catalyst, consistent with results reported previously.[56,58] Other products that could not be detected by GC may have formed as well, but only in very small amounts (<4% for 40 wt% Ag/TiO_2 and AgNP; <10% for 40 wt% Ag/C). The analysis of these minor products is beyond the scope of this study. After each trial of testing the 40 wt% Ag/TiO_2 and 60 wt% Ag/TiO_2, the catalysts were further characterized using TEM.

Three-Electrode Cell Operation: CV was measured using a standard three-electrode cell, which consisted of a Pt gauze (100 mesh, 99.9% metals basis, Sigma-Aldrich, 25*25 mm^2) counter electrode and a Ag/AgCl reference electrode (RE-5B, BASi), separated from the working electrode by means of a Luggin capillary. The three-electrode cell experiments were carried out using a potentiostat (Autolab PGSTAT302N, EcoChemie). Catalyst inks were prepared using the same method as described above. The catalyst layer for the three electrode cell experiments was prepared as follows: a 5 μL drop of the catalyst ink was deposited (and then dried under flowing Ar) on a rotating disk electrode (Metrohm 6.1204.300), which has a polished (0.05 micron alumina) glassy carbon disk electrode surface (d=3 mm, S=0.07065 cm^2). All CV measurements in this study were conducted in 0.5 M K_2SO_4 at a scan rate of 25 mV s^{-1}.

2.4 Results and Discussion

2.4.1 Composition analysis

Catalysts comprised of different amounts of Ag on TiO_2 support were synthesized, and for comparison, 40 wt% Ag on carbon support was also synthesized, with Vulcan XC-72R being the carbon material. Details on the synthesis of these catalysts were provided in the **Experimental**. **Table 2.1** summarizes values for the actual Ag loading of the synthesized catalysts as obtained using inductively coupled plasma – optical emission spectrometer (ICP-OES). These values are in good agreement with the intended values except for the catalysts with low catalyst loading, which probably can be explained by relatively large loss of catalyst during the washing step since with the larger amount of TiO_2 added, more frequent washing is required.

Table 2.1 Ag composition of the synthesized catalysts.

Sample name	Ag loading (wt%)	
	Intended	Actual
5 wt% Ag/TiO_2	5	1.67
10 wt% Ag/TiO_2	10	5.47
20 wt% Ag/TiO_2	20	18.94
40 wt% Ag/TiO_2	40	38.51
60 wt% Ag/TiO_2	60	54.20
40 wt% Ag/C	40	38.20

2.4.2 Catalyst performance in the flow reactor

2.4.2.1 Performance comparison of different support materials

The performance of the different Ag/TiO_2 and Ag/C catalysts was determined using a previously reported flow reactor.[38,55] 1 M KOH was used as the electrolyte since it has a higher conductivity than other commonly used electrolytes for CO_2 reduction such as K_2SO_4, $KHCO_3$.[58] The geometric area of the electrode was used to calculate current densities. **Figure 2.1a** shows j_{co} as a function of the cathode potential for four different cathode catalysts: 40 wt% Ag/TiO_2, 40

wt% Ag/C, AgNP, and plain TiO_2, which were immobilized on gas diffusion electrodes (GDE) via hand painting at an identical total cathode catalyst loading of 1 mg cm^{-2}. Ag/TiO_2 exhibits better performance than Ag/C. Specifically, at -1.7 V *vs.* Ag/AgCl, j_{co} for 40 wt% Ag/TiO_2 was 60 mA cm^{-2}, while 40 wt% Ag/C reached 28 mA cm^{-2}. So at this cathode potential about twice the amount of CO is produced using TiO_2 rather than carbon black as the support material for the Ag particles. Then, at a cathode potential of -1.8 V *vs.* Ag/AgCl, the j_{co} observed for the 40 wt% Ag/TiO_2 catalysts was about 101 mA cm^{-2}, significantly higher than the approximately 62 mA cm^{-2} reported previously for a commercially available 'Silflon' Ag GDE at the same cathode potential.[58] When comparing the performance observed with 40 wt% Ag/TiO_2 to the prior work by Cueto *et al.* using 250 nm Ag particles on flat TiO_2 films, we observed that 40 wt% Ag/TiO_2 exhibited much higher performance in terms of current density (two orders of magnitude higher) and selectivity for products from CO_2 conversion, although the current density reported by Cueto *et al.* is the sum of CO_2 conversion and H_2O reduction.[94] Also, the current density achieved with 40 wt% Ag/TiO_2 is ~20 times higher compared to our previous work[54], but at a 15-times lower Ag loading: 0.4 *vs.* 6.67 mg of Ag per cm^2. **Figure 2.1a** also shows that the 40 wt% Ag/TiO_2 cathode and the AgNP cathode exhibit very similar performance. This result indicates that the Ag metal content can be drastically reduced without sacrificing performance when using Ag/TiO_2 catalyst, thus improving its commercial viability for CO_2 reduction. The electrochemical surface area (ECSA) measurement of Ag as described in the *supporting information* (SI, section 2.6) indicates that the ECSA of Ag in the 40 wt% Ag/TiO_2 electrode is much lower than the ECSA of Ag in the 40 wt% Ag/C or AgNP electrode, which underscores the important beneficial role of the TiO_2 support in the reduction of CO_2 and suggests the synergistic effect between Ag and TiO_2.

Interestingly, in the low current density regime, the 40 wt% Ag/TiO_2 cathode performed best (highest partial current density for CO), followed by the AgNP and 40 wt% Ag/C cathodes. This increased performance at low current density may be due to the increased adsorption of CO_2 and stabilization of $CO_2^{\bullet-}$ by TiO_2. When plain TiO_2 is used as the cathode catalyst on a GDE (control experiment), no activity for CO production was observed, which confirms that the production of CO in the other experiments stems from the presence of Ag.

Single electrode polarization curves for 40 wt% Ag/TiO_2, 40 wt% Ag/C, and AgNP are shown in **Figure 2.1b**. The anode polarization curves are nearly identical, because the same operating conditions, anode catalyst and catalyst loading were used for all experiments. Therefore, the difference in total current densities can be attributed to differences in cathode performance. Naughton *et al.* developed a method to analyze polarization curves of individual fuel cell electrodes by applying a linear fit in the ohmic region to get a slope R_{ohmic}.[97] A higher R_{ohmic} value indicates a higher electrode resistance.[97] R_{ohmic} contains information about electrical resistances, as well as any contact resistance between electrolyte and electrode, along with any mass transport losses. The R_{ohmic} parameter is not exclusively based on electrical resistance, but rather is the apparent resistance in the ohmic region. Using this method, we found that the lower performance of Ag/C catalyst relative to the Ag/TiO_2 and AgNP catalysts was due to a higher resistance as indicated by a larger R_{ohmic} despite the fact that carbon black has a higher conductivity, which implies that in this case, the R_{ohmic} mainly originates from the contact resistance between electrolyte and electrode as well as mass transport in both electrolyte and gas reactants rather than from the resistance caused by the low conductivity of support materials. Specifically, the carbon black support material is more hydrophobic and porous compared to the TiO_2 support material (see SI **Figure 2.7**), which hampers contact between the Ag particles and the electrolyte. Also, compared

to Ag/C, a thinner catalyst layer could be obtained for the Ag/TiO_2 catalyst at the same Ag loading because TiO_2 has a 2-fold higher density than carbon, thus having improved mass transfer kinetics as previously reported.[80]

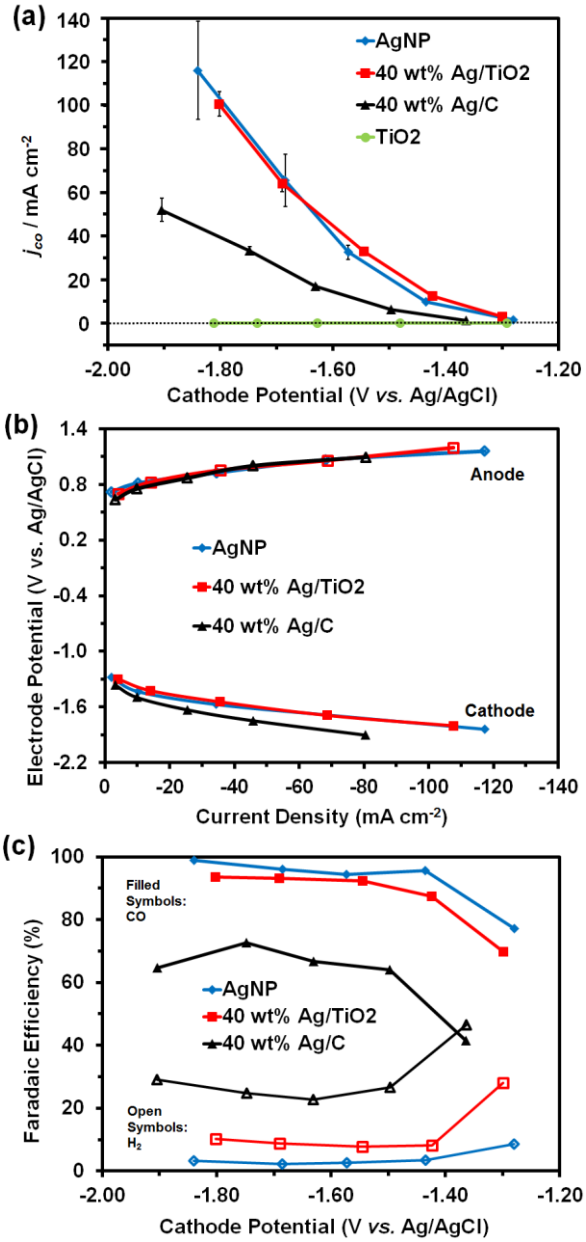

Figure 2.1 (a) Partial current density for CO production using four catalysts: 40 wt% Ag/TiO_2, 40 wt% Ag/C, AgNP and TiO_2; (b) Single electrode polarization curves and (c) Faradaic efficiencies of of 40 wt% Ag/TiO_2, 40 wt% Ag/C and AgNP. The error bars represent the standard deviation of the average of three experiments (N=3). Data collected at room temperature and ambient pressure; electrolyte: 1M KOH; catalyst loading: 1mg cm^{-2}; CO_2 stream: 7 sccm. Reprinted with permission from ChemSusChem 7, 866-874, (2014). Copyright 2013 Wiley.

Figure 2.1c shows the Faradaic efficiencies (see SI for details on the calculation) for CO, the desired product, and H_2, the byproduct as obtained for GDEs covered with 40 wt% Ag/TiO_2, 40 wt% Ag/C, and AgNP catalysts respectively. Among these three catalysts, AgNP achieved the highest Faradaic efficiency for CO: >95%. Ag/TiO_2 achieved a Faradaic efficiency for CO of 93%, while Ag/C achieved only 70% and much larger amounts of the byproduct H_2 were formed. So the low performance (*i.e.*, the low partial current density) exhibited by Ag/C can be explained by its low Faradaic efficiency for CO, in addition to a higher electrode resistance (vide supra).

2.4.2.2 The effect of Ag loading on the performance of Ag/TiO_2

The performance of Ag/TiO_2 catalysts as a function of increasing Ag loading (5 wt%, 10 wt%, 20 wt%, 40 wt%, and 60 wt% Ag/TiO_2) was also studied. **Figure 2.2a and b** show the partial current density and Faradaic efficiency for CO *vs.* the cathode potential for GDEs prepared with these catalysts, while maintaining a constant total catalyst loading of 1 mg cm^{-2}. In general (for the 5-40 wt% samples), the data indicated that the higher the Ag loading, the higher the partial current density and Faradaic efficiency for CO, especially at more negative cathode potentials (from -1.5 V to -1.8 V *vs.* Ag/AgCl). TEM micrographs of the Ag/TiO_2 catalysts with different Ag loading suggest that this trend can be explained by the increased number of Ag particles exposed on the TiO_2 surface (**Figure 2.3)**. Interestingly, the 60 wt% Ag/TiO_2 catalyst did not follow this trend. Its partial current density and Faradaic efficiency for CO were much lower than those observed for the 40 wt% Ag/TiO_2 especially at negative cathode potentials. TEM of the 60 wt% samples suggests that Ag particles are more prone to agglomerate than the 40 wt% sample during reaction (compare **Figure 2.3e** and **e'**, and histograms in **Figure 2.9f** and **2.9g** in the SI) since the Ag particles are more densely arranged on the support in high loading samples, thus

increasing the possibility for aggregation (compare **Figure 2.3e** and **e'**), which could explain the lower performance of the carbon supported Ag catalyst. The other possible reason for the lower performance of the 60 wt% sample is that according to the synergistic effect between Ag and TiO_2 (will introduced later), an optimum silver content, 40 wt% in this work, exists among the different Ag/TiO_2 catalysts. Catalysts with a Ag content higher or lower than 40 wt% exhibit lower performance. Similar trends and explanations have been reported for other supported catalysts, for example for Ag supported on carbon black in fuel cell applications.[96]

One of the main advantages of the Ag/TiO_2 catalysts studied in this paper is their low mass fraction of Ag, thus reducing the amount of precious metal needed. **Figure 2.2c** compares the performance per mass Ag (*i.e.*, the "mass activity") for all catalysts used in this study. For example the mass activity of 5 wt% Ag/TiO_2 was 20-fold higher than that of the commercial AgNP catalyst, and much higher than the mass activity of nitrogen-based Ag catalysts (*e.g.*, Ag pyrazole, AgPz), on which we reported previously with a high mass activity of 1600 mA mg_{Ag}^{-1} cm^{-2} at -1.7 V *vs.* Ag/AgCl.[44] In addition, all Ag/TiO_2 catalysts showed relative high cell energy efficiencies (see SI for details on the calculation). For example, the cell energy efficiency was 65% at a cell potential of -2 V for the 40 wt% Ag/TiO_2 catalyst, compared to only 50% for the 40 wt% Ag/C catalyst and 56% for the AgNP catalyst.

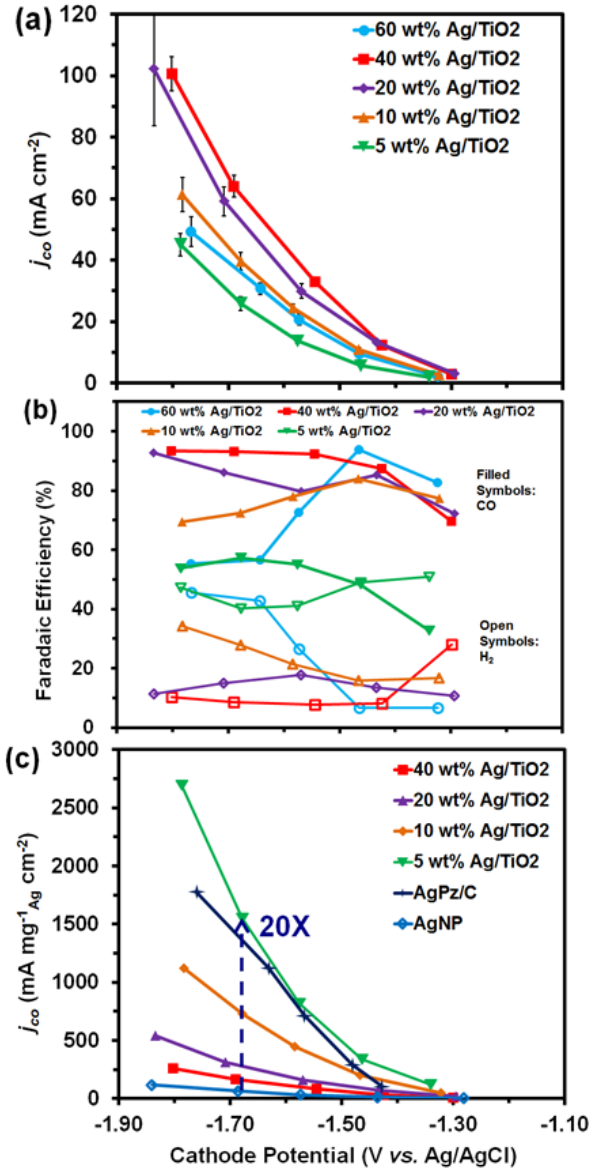

Figure 2.2 (a) Partial current density for CO and (b) Faradaic efficiency of Ag/TiO_2 catalysts with different Ag loading: 5 wt%, 10 wt%, 20 wt%, 40 wt% and 60 wt%; (c) Partial current densities for CO *vs*. cathode potential relative to the cathode silver loading for different catalysts. The error bars represent the standard deviation of the average of three experiments (N=3). Data collected at room temperature and ambient pressure; electrolyte: 1M KOH; catalyst loading: 1mg cm^{-2}; CO_2 stream: 7 sccm. Reprinted with permission from ChemSusChem 7, 866-874, (2014). Copyright 2013 Wiley.

2.4.3 Ag particle size and size distribution

To explain the high performance of the GDEs covered with Ag/TiO_2 catalysts in the flow reactor, we characterized the catalysts with respect to size and size distribution of the nanoparticles

supported by TiO_2 or carbon black both before and after flow reactor tests (**Figure 2.3)**. The histograms of the Ag particle size distribution are shown in **Figure 2.9** in the SI. **Figures 2.3a – e** show that the synthetic method used here yields more uniform and much smaller Ag particles that are at their active size (<10 nm) and dispersed well on the TiO_2, especially when compared to the >200 nm electrodeposited Ag particles reported previously.[94] However, for the Ag/C sample, both small (<10 nm) and large Ag particles (>100 nm) can be found on the carbon black (**Figure 2.3f and Figure 2.3g**). **Figure 2.3d** and **Figure 2.3e** suggest that some of the Ag particles tend to agglomerate to yield larger Ag particles for metal loadings higher than 40 wt%.

Importantly, as shown in **Figure 2.3a – e**, most of the Ag particles in the Ag/TiO_2 catalysts are supported on the surface of TiO_2, while in the Ag/C sample, for those sections with small Ag particles, much fewer Ag particles are exposed on the surface; instead the Ag particles are trapped in deep micropores or recesses, presumably due to the porous nature of carbon support (black dots in red circles in **Figure 2.3f**). Although images from TEM tomography would be more straightforward, the above result is in agreement with previous work.[76] The less exposed nature of the Ag particles in the Ag/C sample makes them less accessible for CO_2 and electrolyte, which, in addition to the presence of agglomerated large Ag particles in the sample, may explain the higher selectivity for CO formation over H_2 evolution (higher Faradaic efficiency for CO) exhibited by, for example, the 40 wt% Ag/TiO_2 catalyst than by the 40 wt% Ag/C catalyst. Although the competing hydrogen evolution reaction can be catalyzed by both exposed carbon and TiO_2, Ag/C exposes a larger surface area of the carbon support to the electrolyte (compared to the surface area of the TiO_2 support exposed in Ag/TiO_2), therefore producing 2-3 times more H_2 than Ag/TiO_2 (**Figure 2.1**).

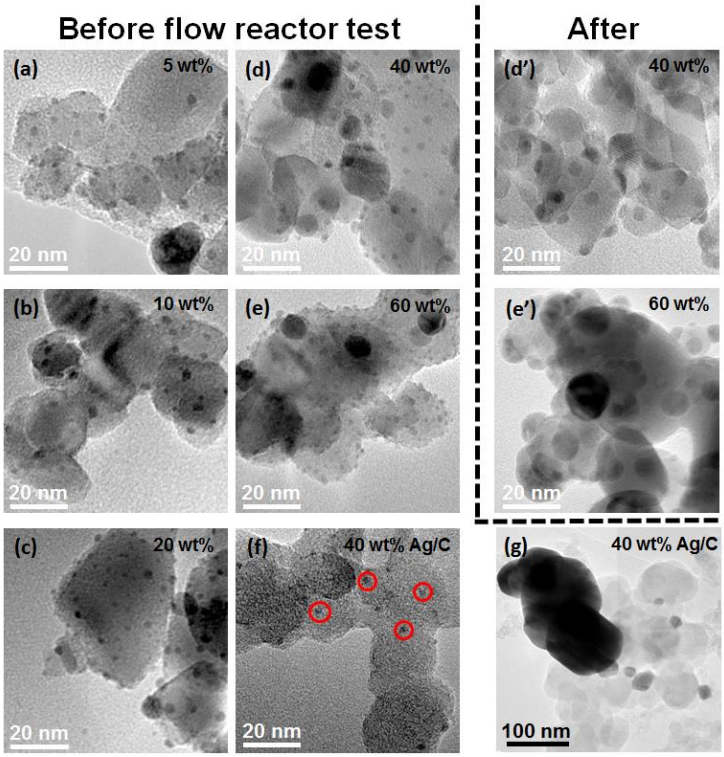

Figure 2.3 TEM images of the synthesized catalysts before flow reactor test: (a) 5 wt% Ag/TiO_2; (b) 10 wt% Ag/TiO_2; (c) 20 wt% Ag/TiO_2; (d) 40 wt% Ag/TiO_2; (e) 60 wt% Ag/TiO_2; (f) 40 wt% Ag/C with larger magnification; (g) 40 wt% Ag/C with smaller magnification; and after flow reactor test: (d') 40 wt% Ag/TiO_2; (e') 60 wt% Ag/TiO_2. Dark spheres or dots are Ag particles; the greyish larger structures are the support materials. The dots in red circles are examples of Ag particles in the pores or recesses of the carbon support. Reprinted with permission from ChemSusChem 7, 866-874, (2014). Copyright 2013 Wiley.

In summary, structural characterization using TEM indicates that the surface of TiO_2 is able to accommodate small and well dispersed Ag particles that are not prone to sintering during experiments for the electrocatalytic conversion of CO_2 to CO. This is in accordance with prior observations, for different catalysts and different reactions, that TiO_2 is able to improve the anchorage of the catalyst nanoparticles on its surface while at the same time reducing agglomeration.[80,85,98]

2.4.4 Catalyst activity in a standard three-electrode cell

The performance towards CO_2 reduction for the Ag/TiO_2 catalyst compared to the AgNP and Ag/C catalysts was also studied using cyclic voltammetry (CV) in a standard three-electrode cell. 0.5 M K_2SO_4, a widely used electrolyte in CO_2 reduction studies[59], was used here. In a standard three-electrode cell KOH would react with CO_2 to form carbonate/bicarbonate, therefore decrease the electrolyte pH significantly (from 13.58 to 9.96) and thus the amount of the active species, molecular CO_2. However, we can use a KOH solution as the electrolyte in the flow reactor because once CO_2 diffuses through the GDE, it reacts at the triple boundary phase[78] to form CO, while the reaction of CO_2 with KOH could be minimized, as reported in prior work.[58] In fact, the flowing electrolyte will refresh the surface and minimize the pH decrease (from 13.65 to 13.48). Therefore, KOH can be used as an electrolyte to increase the electrolyte conductivity in the flow cell, while K_2SO_4 is a better option than KOH in the three-electrode cell. Either CO_2 or Argon gas was bubbled through the electrolyte for 15 minutes prior to CV measurements. As shown in **Figure 2.4a, 2.4b** and **2.4c**, extensive H_2 evolution is observed on both Ag and Ag/TiO_2 electrodes in Ar-saturated electrolyte. However, when using CO_2 saturated electrolyte, different reduction peaks with different onset potential and lower peak current, presumably associated with CO_2 reduction, were observed for both catalysts. The smaller reduction peak current observed when using a CO_2 saturated electrolyte is probably due to inhibition of the hydrogen evolution reaction by the species that adsorb during CO_2 reduction.[16] The Ag/TiO_2 catalyst (**Figure 2.4c**) exhibits a 73 mV lower onset potential for $CO_2^{\bullet-}$ formation (and thus lower overpotential) than the AgNP catalyst **(Figure 2.4a**): respectively -1.189 V and -1.262 V *vs.* Ag/AgCl at i = -0.04 mA, and 102 mV lower onset potential for $CO_2^{\bullet-}$ formation than the Ag/C catalyst. The large overpotential typically observed for CO_2 reduction has been attributed to the barrier of the initial electron transfer

to form a $CO_2^{\bullet-}$ intermediate, which is poorly stabilized by most metal surfaces.[9,25] Thus, the improvement observed here may be due to adsorption and stabilization of $CO_2^{\bullet-}$ on the TiO_2 surface. This may be further proved by the CV study shown in **Figure 2.11a**, in which TiO_2 alone as a catalyst also exhibits a low onset potential: -1.196 V vs. Ag/AgCl, for the conversion of CO_2 to $CO_2^{\bullet-}{}_{ads}$. This observation of earlier onset potential for Ag/TiO_2 is also in agreement with the better performance of the Ag/TiO_2 catalyst compared to the AgNP catalyst in the lower current density regime and compared to the Ag/C catalyst in the whole current density range in the flow reactor test (**Figure 2.1a**). Therefore, both the experiments in the flow reactor and in the standard three-electrode cell with different electrolytes show that Ag/TiO_2 performs better than Ag/C, even pure AgNP.

Interestingly, another reduction peak at around -1.7 V *vs.* Ag/AgCl and two anodic peaks were also observed for the Ag/TiO_2 catalyst compared to the AgNP catalyst. To explain those peaks, Ar was bubbled into the solution for 3 minutes to remove some CO_2 after recording the CV scan in CO_2 saturated electrolyte in **Figure 2.4c**. Bubbling Ar was repeated 4 times and CV measurements were taken each time after Ar was bubbled into the solution. As shown in **Figure 2.4d**, when a relatively large amount of CO_2 was present in the electrolyte, two reductive (I and II) and oxidative peaks (III and IV) were observed. As the amount of CO_2 decreased, intensities of peak I and IV decreased while those of peak III started to increase. The decrease in peak intensity indicates that peak I is related to the direct electrochemical reduction of $CO_{2\ ads}$ to $CO_2^{\bullet-}{}_{ads}$. The similar trend observed for peak IV is probably due to the oxidation of $CO_2^{\bullet-}{}_{ads}$. The other two peaks, II and III, can thus be attributed to the reactions for TiO_2 and Ti (III) species, which indeed can act as a redox electron carrier to facilitate some reactions, including CO_2 reduction.[43,44] In prior work, people reported that the interfacial pH can be quite different from the bulk pH in

unbuffered solutions, thus affecting the reaction rate.[57,58] In this case, buffered solution was not used because the adsorption/desorption peaks from the anions in the buffer solution may interfere with any observed redox species. A similar experiment using TiO_2 without Ag (shown in **Figure 2.11a** in SI) confirms the redox behavior of Ti(IV)/Ti(III) for $CO_{2\ ads}$ reduction to $CO_2^{\bullet-}{}_{ads}$. Direct reduction of CO_2 by TiO_2 is possible, however, the fact that a negligible amount of CO was observed when using only TiO_2, while Ag/TiO_2 is capable of producing a much larger amount of CO in 0.5 M K_2SO_4 electrolyte in the flow reactor (shown in **Figure 2.11b** in SI) indicates that the production of CO requires the presence of Ag on TiO_2.

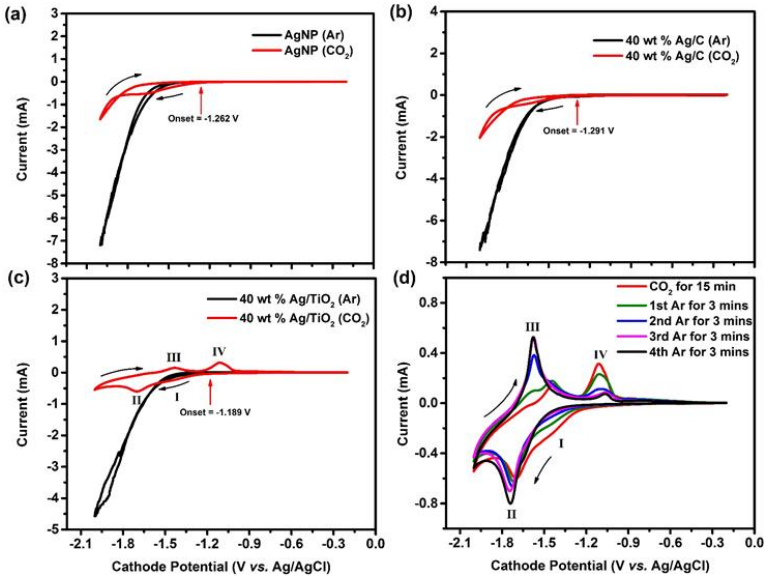

Figure 2.4 Cyclic voltammetry of (a) AgNP catalyst, (b) 40 wt% Ag/C and (c) 40 wt% Ag/TiO_2 catalyst after bubbling Ar (black) or CO_2 (red). The instability in the black curves is probably due to evolution of large amounts of H_2. (d) Cyclic voltammetry of 40 wt% Ag/TiO_2 catalyst after bubbling CO_2 (red) or a number of times of Ar (other colors). All experiments used 0.5 M K_2SO_4 as electrolyte with 25 mV s^{-1} as the scan rate. Reprinted with permission from ChemSusChem 7, 866-874, (2014). Copyright 2013 Wiley.

Figure 2.5 shows a schematic that describes a proposed reaction pathway of the reduction of CO_2 on Ag/TiO_2 catalyst. CO_2 is first adsorbed on TiO_2. At less negative cathode potentials (more positive than the redox potential of Ti(IV)/Ti(III) couple), the adsorbed CO_2 gains one electron from the electrode and converts to $CO_2^{\bullet-}$. Then the produced $CO_2^{\bullet-}$ is adsorbed and

stabilized on the TiO_2 surface, which results in a decrease of the overpotential for this step. At more negative cathode potentials, the Ti(III) species (which has been reported to form upon thermal annealing in a vacuum[47] and is known to facilitate CO_2 adsorption and can act as the active sites for CO_2 photoreduction[59]) is formed by the reduction of TiO_2. Then, the adsorbed CO_2 species is reduced either by one electron from the electrode, or by the produced Ti(III) species to form $CO_2^{\bullet-}{}_{ads}$. The Ti(III) is then oxidized back to TiO_2. This cycle is in agreement with the observed decrease in intensity of anodic peak III in the presence of a relative large amount of CO_2 in the solution, since most of the Ti(III) species are used to reduce CO_2 rather than being oxidized by the electrode on the reverse sweep (peak III). The involvement of these oxygen vacancy Ti(III) species may improve the stabilization of $CO_2^{\bullet-}{}_{ads}$, thereby facilitating this process and increasing the activity of this catalyst to be comparable to AgNP at even lower Ag loading. Once formed, $CO_2^{\bullet-}{}_{ads}$ is further reduced to CO_{ads} under the catalytic influence of Ag in the presence of H_2O. The combination of the observation that the Ag/TiO_2 catalyst was able to produce CO at a lower onset potential than the Ag catalyst, and the observation that TiO_2 alone is not able to produce CO, strongly suggest that the observed enhanced performance can be attributed to a synergistic effect between Ag and TiO_2.

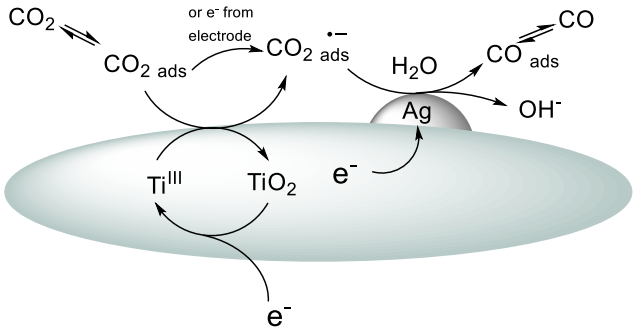

Figure 2.5 A schematic diagram of the proposed pathway for CO_2 reduction to CO on the Ag/TiO_2 catalyst. Reprinted with permission from ChemSusChem 7, 866-874, (2014). Copyright 2013 Wiley.

2.5 Conclusions

In summary, we showed that Ag supported on TiO_2 outperforms Ag supported on carbon black in the reduction of CO_2 to CO, while Ag/TiO_2 performs at a similar absolute level as unsupported Ag nanoparticles with the Faradaic efficiency for CO exceeding 90% and the current density exceeding 100 $mAcm^{-2}$. Compared to carbon black, TiO_2 is a superior support for Ag catalysts for the electrochemical reduction of CO_2 to CO, because: (1) TiO_2 helps to create small, well dispersed Ag particles at their active size (sub-10 nm) on the TiO_2 surface; (2) TiO_2 improves the stability of these Ag particles (minimizes agglomeration during the synthesis); (3) TiO_2 improves CO_2 reduction kinetics, probably via the adsorption and stabilization of the $CO_2^{\bullet-}$ intermediate, which then can react to form CO on adjacent Ag particles. In contrast, Ag particles supported by carbon black are not as well dispersed, not as stable during the synthesis, and do not appear to enhance reaction kinetics.

By using TiO_2 as the support, the Ag loading can be reduced without sacrificing performance towards selective CO production. 40 wt% Ag/TiO_2 is able to produce the same amount of CO as unsupported AgNP, but at a 2.5 times lower silver loading. Furthermore, the 5 wt% Ag/TiO_2 catalyst achieved a mass activity as high as 2700 mA mg_{Ag}^{-1} cm^{-2}. Ag is 5-10 times more expensive than TiO_2, therefore, supporting Ag particles on TiO_2 enhances the promise of these catalyst for the development of an economically viable process for the electrochemical reduction of CO_2 to CO.

We also studied the role of TiO_2 as a support material during the electrochemical reduction of CO_2. Based on CV data, a reaction pathway is proposed that involves the participation of the Ti(IV)/Ti(III) from the support material, by acting as the redox couple and by stabilizing the reaction intermediate. Further research is needed to confirm the proposed reaction pathway. For

example, calculations and spectroscopic experiments could guide these efforts with respect to predicting and confirming the adsorption / stabilization of intermediates and the interactions between metal particles and support materials.

Further studies could also focus on exploring other metal catalysts supported by metal oxide semiconductors such as CeO_2. Such catalyst may be able to modify the adsorption isotherms for the intermediates and be able to further decrease the energy barrier for the electrochemical reduction of CO_2.

2.6 Supporting Information

2.6.1 Schematic of the electrochemical flow reactor

A schematic of the electrochemical flow reactor used in this study is shown in **Figure 2.6**. The flow reactor used in this study is similar to what was reported previously.[1] Stainless steel plates (5.5 x 2.5 cm) served as current collectors, which held the flow reactor together and provided electrical contact between the gas diffusion electrode (GDE) and an external potentiostat (PGSTAT-30, EcoChemie). The potentiostat was connected to the cell *via* banana clips which plugged directly into precisely machined 3/16" holes in the current collectors. One 1.5-mm thick polyether ether ketone (PEEK) spacer with a precisely machined 0.5-cm wide by 2.0-cm long window provided the electrolyte flow fields within the electrochemical reactor. The cathode current collector had a precisely machined 0.5-cm wide by 2.0-cm long by 0.25-cm deep window behind the GDEs to allow for the flow of gases in and out of the reactor. The anode was left open to air allowing oxygen to escape. A squeeze-action toggle plier clamp (McMaster Carr 5062A63) held the cell together.

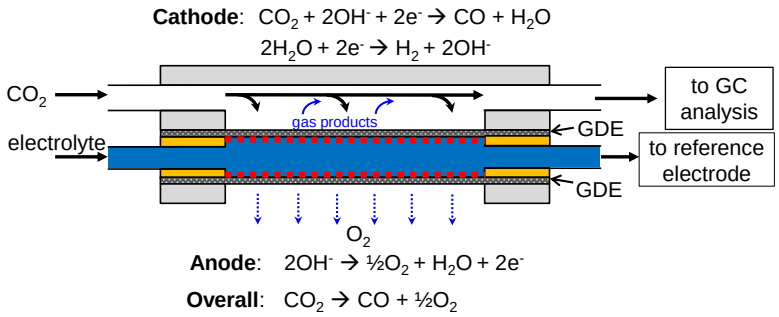

Figure 2.6 Schematic representation of the electrochemical flow reactor used in this study. Reprinted with permission from ChemSusChem 7, 866-874, (2014). Copyright 2013 Wiley.

2.6.2 Calculations for Faradaic efficiency and energy efficiency

The Faradaic efficiency for a specific product and the overall energy efficiency is calculated using the same method as shown in Chapter 1.

2.6.3 Comparison of wettability

Wettability for the cathodes deposited with the 40 wt% Ag/C and 40 wt% Ag/TiO_2 catalysts was qualitatively compared after the electrode preparation step described in the main text. Specifically, after the painting procedure, electrodes were dried overnight under N_2 gas flow. Images that compare the wettability of the two electrodes were taken after dropping 10 µL DI water on the previously dried electrode surface. **Figure 2.7** shows that the catalyst layer with 40 wt% Ag/C is more hydrophobic than the one with 40 wt% Ag/TiO_2. After the flow cell test, the electrodes were washed and dried overnight under a N_2 gas flow. The wettability of Ag/TiO_2 electrode was still better than Ag/C.

Figure 2.7 Image of wettability difference between catalyst layers of 40 wt% Ag/C and 40 wt% Ag/TiO_2. Reprinted with permission from ChemSusChem 7, 866-874, (2014). Copyright 2013 Wiley.

2.6.4 XPS analysis of the 40 wt% Ag/TiO_2 catalyst and Ag nanoparticle

X-ray photoelectron spectroscopy (XPS) experiment was carried out to investigate the electronic properties of the 40 wt% Ag/TiO_2 and Ag nanoparticles. The XPS samples were prepared by the depositing a layer of catalyst powders on one side of double-sided carbon tape (Electron Microscopy Sciences). The other side of the carbon tape is mounted on the XPS sample holder. XPS spectra were collected using a Kratos Axis ULTRA X-ray photoelectron spectrometer with monochromatic Al K excitation, 120 W (120 kV, 10 mA). Data were collected using the hybrid lens setting with the slot aperture (300 x 700 mm^2 analytical area) and charge neutralizer settings of 2.1 A filament current, 2.1 V charge balance and 2V filament bias. Survey spectra were collected as a pass energy of 160 eV and high resolution spectra were collected using a pass energy of 40 eV. The data were fitted with Gaussian-Lorentzian line shapes. The binding energy scale was referenced to the Ag Fermi level.

From the spectra shown in **Figure 2.8**, the binding energy of Ag in Ag/TiO_2 shifted towards higher value compared to Ag nanoparticles, however, this shift in binding energy is within the experimental error of the instrument (±0.2 eV). Therefore, the variation in the Ag electronic structure is insufficient to explain the enhanced activity of Ag/TiO_2 catalyst and the decreased overpotential for CO_2 reduction. That leads to the study of the role TiO_2 plays during the reaction using CV in 3-electrode cell.

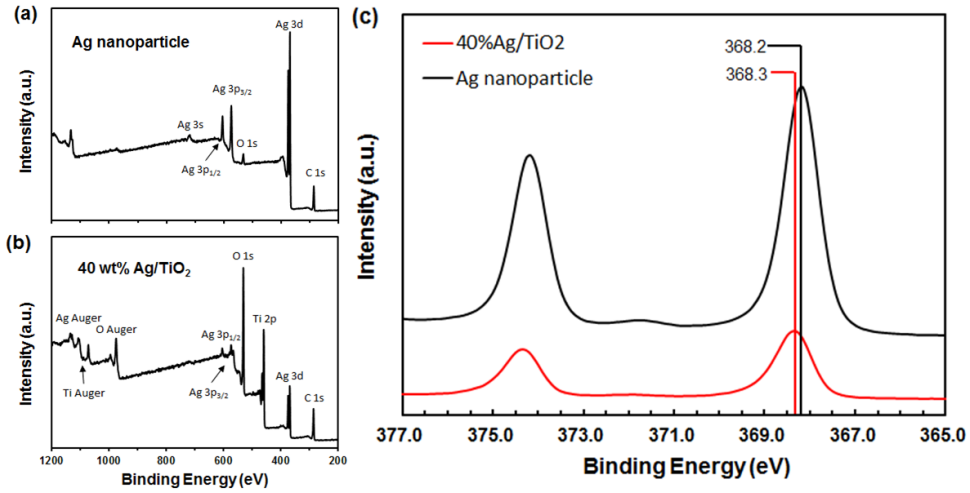

Figure 2.8 XPS survey spectra of (a) Ag nanoparticle, (b) 40 wt% Ag/TiO_2, and (c) high-resolution XPS Ag 3d spectra obtained from Ag nanoparticle (black line) and 40 wt% Ag/TiO_2 (red line). Reprinted with permission from ChemSusChem 7, 866-874, (2014). Copyright 2013 Wiley.

2.6.5 TEM histograms

The average particle size of the commercial AgNP (Sigma-Aldrich) is 70 nm, the particle size distribution of this catalyst can be found in our previous report.[4] TEM histograms of the Ag particle size distribution from the Ag/TiO_2 and Ag/C catalysts are shown in **Figure 2.9**. The average Ag particle size of the Ag/TiO_2 catalysts are below 10 nm, while for the Ag/C catalyst, both small Ag particles (<10 nm) and large Ag particles (>100 nm) are found on the surface of the carbon black support, as evident form the right-skewed distribution. Among Ag/TiO_2 catalysts, larger particles are observed with increasing Ag loading. After the flow cell test, Ag particles tend to agglomerate (shown in **Figure 2.3** in the main text), however, the 60 wt% Ag/TiO_2 sample exhibits more serious agglomeration than the 40 wt% Ag/TiO_2 sample since much larger Ag particles (>50 nm) were formed after reaction.

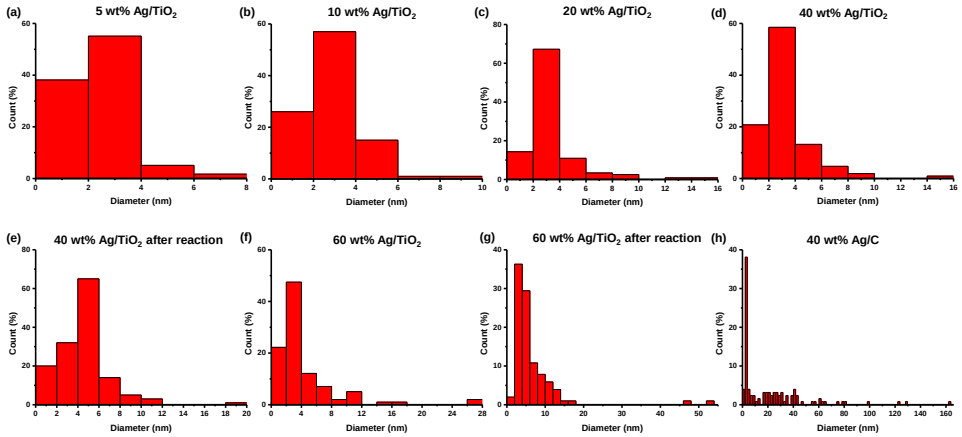

Figure 2.9 TEM histograms of the Ag particle size distribution from (a) 5 wt% Ag/TiO_2; (b) 10 wt% Ag/TiO_2; (c) 20 wt% Ag/TiO_2; (d) 40 wt% Ag/TiO_2; (e) 40 wt% Ag/TiO_2 after reaction; (f) 60 wt% Ag/TiO_2; (g) 60 wt% Ag/TiO_2 after reaction; (h) 40 wt% Ag/C. Reprinted with permission from ChemSusChem 7, 866-874, (2014). Copyright 2013 Wiley.

2.6.6 Measurement of electrochemical active surface area of Ag

The electrochemical active surface area (ECSA) of Ag was performed according to the procedure reported previously.[4-5] The experiment was conducted without removal of oxygen in a 100 mL beaker containing 5 mM $Pb(ClO_4)_2$, 1 mM $HClO_4$ and 0.5 M $NaClO_4$. The working electrode is a hand-painted GDE as described in the "electrode preparation" part in the experimental section. The counter electrode was a 25x25 platinum plate. A cyclic voltammogram was recorded at 10mV/s between -0.60 and 0.1 V *vs.* Ag/AgCl. An example of the under-potential deposition (UPD) lead stripping peak using AgNP catalyst is shown in **Figure 2.10**.

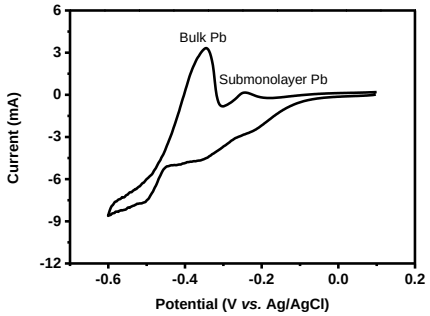

Figure 2.10 Cyclic voltammogram showing the UPD and bulk deposition of Pb onto a AgNP working electrode. Reprinted with permission from ChemSusChem 7, 866-874, (2014). Copyright 2013 Wiley.

The area under the Pb UPD stripping peak at Pb^{2+} concentrations of 5 mM or higher corresponds to a charge of 1.67 x 10^{-3} cm^2 μC^{-1} silver.[5c] Using this constant, the ECSA of Ag in our electrodes was determined from the area of the Pb UPD stripping peak. For AgNP, the area is 3.91 ± 0.23 cm^2; for 40 wt % Ag/TiO_2, the area is 0.52 ± 0.12 cm^2; for 40 wt % Ag/C, the area is 1.37 ± 0.22 cm^2. This measurement shows that the ECSA of Ag in the 40 wt% Ag/TiO_2 electrode is much lower than the ECSA of Ag in the AgNP and 40 wt % Ag/C electrodes. This further underscores the important beneficial role of the TiO_2 support in the reduction of CO_2.

2.6.7 Behavior of TiO_2 in the 3-electrode cell and flow reactor

The results of cyclic voltammetry of bare TiO_2 after bubbling with CO_2 gas (red) or a number of times with Ar gas (other colors) is shown in **Figure 2.11a**. The characteristic peaks and trends for peak transition for TiO_2 are almost the same as those observed for Ag/TiO_2 shown in the main text (**Figure 2.4c**), while the current range is different. This can be explained by the hydrogen evolution reaction being more dominant in the absence of Ag, when the applied potential is more negative than -1.8 V. This result supports the proposed reaction pathway (**Figure 2.5** in the main text), specifically that TiO_2 acts as a redox carrier for the conversion of CO_2 to $CO_2^{\bullet-}$, whereas in the absence of Ag, $CO_2^{\bullet-}$ cannot be further converted to CO. This is further supported by **Figure 2.11b**. In the flow reactor experiment with 0.5 M K_2SO_4 as the electrolyte, TiO_2 did not produce CO, while 40 wt% Ag/TiO_2 produces a relative large amount of CO.

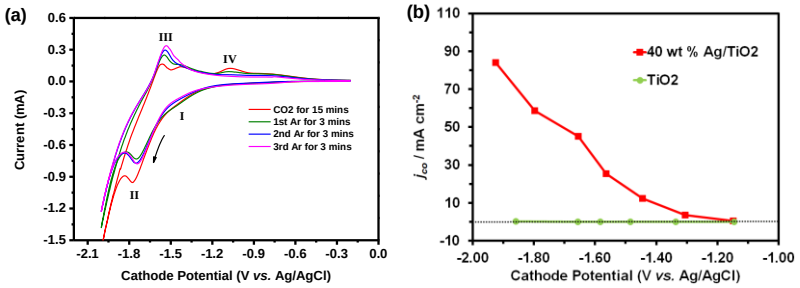

Figure 2.11 (a) Cyclic voltammetry of bare TiO_2 catalyst in a 3-electrode cell after bubbling CO_2 (red) or a number of times of Ar (other colors). Electrolyte: 0.5 M K_2SO_4, scan rate: 25 mV s^{-1}. (b) Partial current density for CO production using 40 wt% Ag/TiO_2 and TiO_2 in the flow reactor. The experiment used 0.5 M K_2SO_4 as electrolyte. Reprinted with permission from ChemSusChem 7, 866-874, (2014). Copyright 2013 Wiley.

2.7 References

1 Bell, A. T. Basic Research Needs, Catalysis for Energy. *Basic Research Needs, Catalysis for Energy*, U.S. Department of Energy: Bethesda, MD, (2008).

2 Taylor, P. Energy Technology Perspectives *Energy Technology Perspectives* International Energy Agency, (2010).

3 Pacala, S. & Socolow, R. Stabilization Wedges: Solving the Climate Problem for the Next 50 Years with Current Technologies. *Science* **305**, 968-972, (2004).

4 Lewis, N. S. Toward Cost-Effective Solar Energy Use. *Science* **315**, 798-801, (2007).

5 Meier, J. C., Katsounaros, I., Galeano, C., Bongard, H. J., Topalov, A. A., Kostka, A., Karschin, A., Schuth, F. & Mayrhofer, K. J. J. Stability investigations of electrocatalysts on the nanoscale. *Energy Environ. Sci.* **5**, 9319-9330, (2012).

6 Gattrell, M., Gupta, N. & Co, A. A review of the aqueous electrochemical reduction of CO_2 to hydrocarbons at copper. *J. Electroanal. Chem.* **594**, 1-19, (2006).

7 Galindo Cifre, P. & Badr, O. Renewable hydrogen utilisation for the production of methanol. *Energy Convers. and Manage.*, **48**, 519-527, (2007).

8 Oloman, C. & Li, H. Electrochemical Processing of Carbon Dioxide. *ChemSusChem* **1**, 385-391, (2008).

9 Hori, Y. in *Handbook of Fuel Cells* Vol. 2 Ch. 48, 720-733 (John Wiley & Sons, Ltd, 2010).

10 Mikkelsen, M., Jorgensen, M. & Krebs, F. C. The teraton challenge. A review of fixation and transformation of carbon dioxide. *Energy Environ. Sci.* **3**, 43-81, (2010).

11 Bensaid, S., Centi, G., Garrone, E., Perathoner, S. & Saracco, G. Towards Artificial Leaves for Solar Hydrogen and Fuels from Carbon Dioxide. *ChemSusChem* **5**, 500-521, (2012).

12 Kumar, B., Llorente, M., Froehlich, J., Dang, T., Sathrum, A. & Kubiak, C. P. Photochemical and Photoelectrochemical Reduction of CO_2. *Annu. Rev. Phys. Chem.* **63**, 541-569, (2012).

13 Dahl, S. & Chorkendorff, I. Solar-fuel generation: Towards practical implementation. *Nat. Mater.* **11**, 100-101, (2012).

14 Whipple, D. T. & Kenis, P. J. A. Prospects of CO2 Utilization via Direct Heterogeneous Electrochemical Reduction. *J. Phys. Chem. Lett.* **1**, 3451-3458, (2010).

15 Hori, Y. in *Modern Aspects of Electrochemistry* Vol. 42 *Modern Aspects of Electrochemistry* (eds ConstantinosG Vayenas, RalphE White, & MariaE Gamboa-Aldeco) Ch. 3, 89-189 (Springer New York, 2008).
16 Centi, G., Quadrelli, E. A. & Perathoner, S. Catalysis for CO_2 conversion: a key technology for rapid introduction of renewable energy in the value chain of chemical industries. *Energy Environ. Sci.* **6**, 1711-1731, (2013).
17 Jhong, H.-R. M., Ma, S. & Kenis, P. J. A. Electrochemical conversion of CO_2 to useful chemicals: current status, remaining challenges, and future opportunities. *Curr. Opin. Chem. Eng.* **2**, 191-199, (2013).
18 Hori, Y., Kikuchi, K. & Suzuki, S. Production of CO and CH_4 in Electrochemical Reduction of CO_2 at Metal-Electrodes in Aqueous Hydrogencarbonate Solution. *Chem. Lett.*, 1695-1698, (1985).
19 Ikeda, S., Takagi, T. & Ito, K. Selective Formation of Formic-Acid, Oxalic-Acid and Carbon-Monoxide by Electrochemical Reduction of Carbon-Dioxide. *Bull. Chem. Soc. Jpn.* **60**, 2517-2522, (1987).
20 Azuma, M., Hashimoto, K., Hiramoto, M., Watanabe, M. & Sakata, T. Electrochemical Reduction of Carbon-Dioxide on Various Metal-Electrodes in Low-Temperature Aqueous $KHCO_3$ Media. *J. Electrochem. Soc.* **137**, 1772-1778, (1990).
21 Agarwal, A. S., Zhai, Y. M., Hill, D. & Sridhar, N. The Electrochemical Reduction of Carbon Dioxide to Formate/Formic Acid: Engineering and Economic Feasibility. *ChemSusChem* **4**, 1301-1310, (2011).
22 Kuhl, K. P., Cave, E. R., Abram, D. N. & Jaramillo, T. F. New insights into the electrochemical reduction of carbon dioxide on metallic copper surfaces. *Energy Environ. Sci.* **5**, 7050-7059, (2012).
23 Hori, Y., Wakebe, H., Tsukamoto, T. & Koga, O. Electrocatalytic Process of CO Selectivity in Electrochemical Reduction of CO2 at Metal-Electrodes in Aqueous-Media. *Electrochim. Acta* **39**, 1833-1839, (1994).
24 Chandrasekaran, K. & Bockris, L. O. M. In-situ spectroscopic investigation of adsorbed intermediate radicals in electrochemical reactions: CO2− on platinum. *Surf. Sci.* **185**, 495-514, (1987).
25 Rosen, B. A., Salehi-Khojin, A., Thorson, M. R., Zhu, W., Whipple, D. T., Kenis, P. J. A. & Masel, R. I. Ionic Liquid–Mediated Selective Conversion of CO_2 to CO at Low Overpotentials. *Science* **334**, 643-644, (2011).
26 Chen, Y., Li, C. W. & Kanan, M. W. Aqueous CO_2 Reduction at Very Low Overpotential on Oxide-Derived Au Nanoparticles. *J. Am. Chem. Soc.* **134**, 19969-19972, (2012).
27 Dufek, E., Lister, T. & McIlwain, M. Bench-scale electrochemical system for generation of CO and syn-gas. *J. Appl. Electrochem.* **41**, 623-631, (2011).
28 Delacourt, C., Ridgway, P. L., Kerr, J. B. & Newman, J. Design of an Electrochemical Cell Making Syngas ($CO + H_2$) from CO_2 and H_2O Reduction at Room Temperature. *J. Electrochem. Soc.* **155**, B42-B49, (2008).
29 Tornow, C. E., Thorson, M. R., Ma, S., Gewirth, A. A. & Kenis, P. J. A. Nitrogen-Based Catalysts for the Electrochemical Reduction of CO_2 to CO. *J. Am. Chem. Soc.* **134**, 19520-19523, (2012).
30 Salehi-Khojin, A., Jhong, H.-R. M., Rosen, B. A., Zhu, W., Ma, S., Kenis, P. J. A. & Masel, R. I. Nanoparticle Silver Catalysts That Show Enhanced Activity for Carbon Dioxide Electrolysis. *J. Phys. Chem. C* **117**, 1627-1632, (2012).

31 Sharma, S. & Pollet, B. G. Support materials for PEMFC and DMFC electrocatalysts—A review. *J. Power Sources* **208**, 96-119, (2012).
32 Wang, X., Hsing, I. M. & Yue, P. L. Electrochemical characterization of binary carbon supported electrode in polymer electrolyte fuel cells. *J. Power Sources* **96**, 282-287, (2001).
33 O'Hayre, R., Barnett, D. M. & Prinz, F. B. The Triple Phase Boundary: A Mathematical Model and Experimental Investigations for Fuel Cells. *J. Electrochem. Soc.* **152**, A439-A444, (2005).
34 Bang, J. H., Han, K., Skrabalak, S. E., Kim, H. & Suslick, K. S. Porous Carbon Supports Prepared by Ultrasonic Spray Pyrolysis for Direct Methanol Fuel Cell Electrodes. *J. Phys. Chem. C* **111**, 10959-10964, (2007).
35 Huang, S.-Y., Ganesan, P., Park, S. & Popov, B. N. Development of a Titanium Dioxide-Supported Platinum Catalyst with Ultrahigh Stability for Polymer Electrolyte Membrane Fuel Cell Applications. *J. Am. Chem. Soc.* **131**, 13898-13899, (2009).
36 Inoue, T., Fujishima, A., Konishi, S. & Honda, K. Photoelectrocatalytic reduction of carbon dioxide in aqueous suspensions of semiconductor powders. *Nature* **277**, 637-638, (1979).
37 Kočí, K., Matějů, K., Obalová, L., Krejčíková, S., Lacný, Z., Plachá, D., Čapek, L., Hospodková, A. & Šolcová, O. Effect of silver doping on the TiO_2 for photocatalytic reduction of CO_2. *Appl. Catal., B* **96**, 239-244, (2010).
38 Li, Y., Wang, W.-N., Zhan, Z., Woo, M.-H., Wu, C.-Y. & Biswas, P. Photocatalytic reduction of CO_2 with H_2O on mesoporous silica supported Cu/TiO_2 catalysts. *Appl. Catal., B* **100**, 386-392, (2010).
39 Li, X., Zhuang, Z., Li, W. & Pan, H. Photocatalytic reduction of CO_2 over noble metal-loaded and nitrogen-doped mesoporous TiO_2. *Appl. Catal., A* **429–430**, 31-38, (2012).
40 Huang, S. Y., Ganesan, P. & Popov, B. N. Titania supported platinum catalyst with high electrocatalytic activity and stability for polymer electrolyte membrane fuel cell. *Appl. Catal., B* **102**, 71-77, (2011).
41 Tauster, S. J. in *Strong Metal-Support Interactions* Vol. 298 *ACS Symposium Series* Ch. 1, 1-9 (American Chemical Society, 1986).
42 Beck, F. & Gabriel, W. Heterogeneous Redox Catalysis on Ti/TiO_2 Cathodes—Reduction of Nitrobenzene. *Angew. Chem. Int. Ed. Engl.* **24**, 771-772, (1985).
43 Ravichandran, C., Kennady, C. J., Chellammal, S., Thangavelu, S. & Anantharaman, P. N. Indirect electroreduction of o-nitrophenol to o-aminophenol on titanium dioxide coated titanium electrodes. *J. Appl. Electrochem.* **21**, 60-63, (1991).
44 Chu, D., Qin, G., Yuan, X., Xu, M., Zheng, P. & Lu, J. Fixation of CO_2 by Electrocatalytic Reduction and Electropolymerization in Ionic Liquid–H2O Solution. *ChemSusChem* **1**, 205-209, (2008).
45 Tanaka, K., Miyahara, K. & Toyoshima, I. Adsorption of carbon dioxide on titanium dioxide and platinum/titanium dioxide studied by x-ray photoelectron spectroscopy and Auger electron spectroscopy. *J. Phys. Chem.* **88**, 3504-3508, (1984).
46 Markovits, A., Fahmi, A. & Minot, C. A theoretical study of CO2 adsorption on TiO_2. *Journal of Molecular Structure: THEOCHEM* **371**, 219-235, (1996).
47 Thompson, T. L., Diwald, O. & Yates, J. T. CO_2 as a Probe for Monitoring the Surface Defects on TiO_2(110)Temperature-Programmed Desorption. *J. Phys. Chem. B* **107**, 11700-11704, (2003).

48 Cueto, L. F., Hirata, G. A. & Sanchez, E. M. Thin-film TiO2 electrode surface characterization upon CO_2 reduction processes. *J. Sol-Gel Sci. Technol.* **37**, 105-109, (2006).
49 Cueto, L. F., Martinez, G. T., Zavala, G. & Sanchez, E. M. Surface Characterization and CO_2 Reduction Using Electrodeposited Silver Particles over TiO_2 Thin Film. *Journal of Nano Research* **9**, 89-100, (2010).
50 Whipple, D. T., Finke, E. C. & Kenis, P. J. A. Microfluidic Reactor for the Electrochemical Reduction of Carbon Dioxide: The Effect of pH. *Electrochem. Solid-State Lett.* **13**, B109-B111, (2010).
51 Guo, J., Hsu, A., Chu, D. & Chen, R. Improving Oxygen Reduction Reaction Activities on Carbon-Supported Ag Nanoparticles in Alkaline Solutions. *J. Phys. Chem. C* **114**, 4324-4330, (2010).
52 Maheswari, S., Sridhar, P. & Pitchumani, S. Carbon-Supported Silver as Cathode Electrocatalyst for Alkaline Polymer Electrolyte Membrane Fuel Cells. *Electrocatal* **3**, 13-21, (2012).
53 Dufek, E. J., Lister, T. E., Stone, S. G. & McIlwain, M. E. Operation of a Pressurized System for Continuous Reduction of CO_2. *J. Electrochem. Soc.* **159**, F514-F517, (2012).
54 Dufek, E. J., Lister, T. E. & McIlwain, M. E. Influence of Electrolytes and Membranes on Cell Operation for Syn-Gas Production. *Electrochem. Solid-State Lett.* **15**, B48-B50, (2012).
55 Naughton, M. S., Moradia, A. A. & Kenis, P. J. A. Quantitative Analysis of Single-Electrode Plots to Understand In-Situ Behavior of Individual Electrodes. *J. Electrochem. Soc.* **159**, B761-B769, (2012).
56 Shih, C.-C. & Chang, J.-R. Pt/C stabilization for catalytic wet-air oxidation: Use of grafted TiO_2. *J. Catal.* **240**, 137-150, (2006).
57 Katsounaros, I., Meier, J. C., Klemm, S. O., Topalov, A. A., Biedermann, P. U., Auinger, M. & Mayrhofer, K. J. J. The effective surface pH during reactions at the solid–liquid interface. *Electrochem. Commun.* **13**, 634-637, (2011).
58 Auinger, M., Katsounaros, I., Meier, J. C., Klemm, S. O., Biedermann, P. U., Topalov, A. A., Rohwerder, M. & Mayrhofer, K. J. J. Near-surface ion distribution and buffer effects during electrochemical reactions. *Phys. Chem. Chem. Phys.* **13**, 16384-16394, (2011).
59 Indrakanti, V. P., Schobert, H. H. & Kubicki, J. D. Quantum Mechanical Modeling of CO_2 Interactions with Irradiated Stoichiometric and Oxygen-Deficient Anatase TiO_2 Surfaces: Implications for the Photocatalytic Reduction of CO_2. *Energy Fuels* **23**, 5247-5256, (2009).

Chapter 3*

Effect of Anode Catalyst on the Electroreduction of CO_2

3.1 Chapter Overview

The electroreduction of CO_2 to CO or other products is one approach to curb the rise in atmospheric CO_2 levels and/or to store excess energy of renewable intermittent sources like solar and wind. To date most efforts have focused on improving cathode catalysis, despite other components such as the anode (oxygen evolution reaction, OER) also being of key importance. Here, we report that dihydrate and non-hydrate forms of IrO_2 as the anode catalyst in alkaline media can achieve onset cell potentials as low as 1.6 V with a cathode overpotential of only 0.02 V, partial current densities for CO as high as 250 mA cm^{-2} (compared to ~130 mA cm^{-2} with a Pt anode), and energy efficiencies as high as 70%. The IrO_2 non-hydrate proved to be much more durable by maintaining more than 90% of its activity after cycling the anode potential over the 0 to 1.0 V *vs.* Ag/AgCl range for over 200 times, whereas the dihydrate lost most of its activity after 19 cycles. Possible causes for these differences are discussed. This work shows that improvements to the anode, so to the OER, can drastically improve the prospects of the electrochemical reduction of CO_2 to useful chemicals.

3.2 Introduction

During the past several decades the atmospheric CO_2 levels have risen steadily, now reaching levels that have started to affect the global climate, as evident from global warming, rising

* Part of this work has been published: Ma, S., Luo, R., Moniri, S., Lan, Y. & Kenis, P. J. A. Efficient Electrochemical Flow System with Improved Anode for the Conversion of CO_2 to CO. *J. Electrochem. Soc.* 161, F1124-F1131, (2014). Copyright 2014. Reproduced with permission from the Electrochemical Society.

sea levels and more erratic weather.[1-3] Multiple strategies, such as carbon capture and sequestration, increasing the energy efficiency of buildings and the transportation sector, and switching to energy sources that emit less CO_2 (*i.e.*, natural gas or renewable source such as solar and wind, instead of coal) need to be employed simultaneously to curb this rise, hopefully leading to lower atmospheric CO_2 levels.[4] Apart from enhancing more efficient use of energy, use of renewable sources such as solar and wind is most desirable as they produce no CO_2.[4] However, both solar and wind are intermittent. Technologies for large scale energy storage or on-demand utilization, both of which are non-trivial at this time, are needed before the energy produced by these renewable sources can be exploited to the fullest extent.[5] Electrochemical reduction of CO_2 into value-added products may represent a means to store excess intermittent renewable energy while simultaneously recycling CO_2, thus assisting in building a low-carbon, or ideally carbon-neutral energy cycle.[6-13] Furthermore, utilizing CO_2 as a starting material for chemical production has the potential to reduce our dependency on fossil fuels.

Among the various products that can be produced by electrochemical reduction of CO_2, CO is attractive due to its versatility as a feedstock (with H_2) for the Fischer-Tropsch process, which enables the synthesis of a variety of chemical products.[14] To date, most studies on the electrochemical reduction of CO_2 to CO have focused on the performance of the cathode, resulting in partial current densities for CO (obtained by multiplying the total current density and the Faradaic efficiency for CO[10]) up to about 120 mA cm^{-2} at applied cell potentials of up to -3 V under ambient conditions, as well as energy efficiencies between 30-70%.[15-25] For example, recently we reported on the development of a N-based Ag complex, which achieved comparable CO current density (110 mA cm^{-2}) as unsupported Ag catalysts, but with a much lower Ag loading.[19] We also studied the activity of Ag catalysts for CO_2 reduction to CO as a function of

particle size and found that Ag catalyst with particle size at around 5 nm exhibits highest activity for CO_2 reduction.[20] Subsequently, we applied TiO_2 as a support to stabilize the Ag particles at a size that is very active, resulting in energy efficiency of 65% at -2 V cell potential and partial current density of 101 mA cm^{-2} at -3 V cell potential.[25] Higher partial current densities (*i.e.*, as high as 300 mA cm^{-2}) for CO only can be achieved under high pressure conditions (>15 atm) with cell potential more negative than -3 V.[26-28] For electrochemical CO_2 reduction to CO to become economically viable, high current densities (well above 200 mA cm^{-2}) need to be achieved simultaneously with overall system energy efficiency over ~50% while operating at ambient conditions.[10,12,13]

The equilibrium cell potential for the electrochemical reduction of CO_2 to CO is -1.33 V, when the oxygen evolution reaction (OER) is the anode reaction.[29] However, a high overpotential is required to drive this process due to sluggish CO_2 reduction on the cathode as previously reported.[10,12,13,30] Previously, the cell overpotential was decreased to less than 0.2 V by using an aqueous solution containing 1-ethyl-3-methylimidazolium tetrafluoroborate (EMIM BF_4) as a co-catalyst,[29] which presumably stabilizes a reaction intermediate.[31] However, the current density achieved with this system was quite low; less than 5 mA cm^{-2}.

While to date overcoming the sluggish reaction kinetics of CO_2 reduction on the cathode has been the main focus, the performance of the anode (OER) also plays a key role in determining overall system efficiency. To date the most widely used anode catalyst in electrochemical CO_2 reduction system has been Pt.[19,22,24,27,29,32-36] Pt, however, does not exhibit outstanding activity for the OER reaction and its performance is hampered by the potential for oxide formation.[37] Some researchers have tried alternative anode catalysts[16] or different anode reaction and anode catalyst combinations (*e.g.*, hydrogen oxidation or Cl_2 formation instead of the OER)[36,38] with mixed

success: the alternative OER catalyst was still not sufficiently active,[16] the setup became more complicated and more expensive chemicals were needed,[36] and more durable electrolyzer materials were needed to withstand the corrosive nature of the Cl_2 product.[38] Other work showed that the two major forms of iridium oxide (IrO_2), hydrate and non-hydrate, are among the most active catalysts for the OER in water electrolyzers due to the much lowered overpotentials compared to Pt or other transition metal oxides,[37,39-41] and differences in physical and chemical properties has been studied.[42-45] However, to date IrO_2 hydrate and non-hydrate have not been studied as anode catalysts in a CO_2 reduction electrolyzer.

Here the use of the hydrate and non-hydrate forms of IrO_2 as anode catalysts in combination with high performance Ag cathodes for the efficient electrochemical reduction of CO_2 to CO in alkaline media will be reported, with the desire to achieve high selectivity and high current density for CO, in combination with high overall system efficiency through reducing overpotential on both the anode and the cathode. Also, the origin of the observed differences in activity and durability between IrO_2 hydrate and non-hydrate forms will be discussed.

3.3 Experimental

3.3.1 Treatment and physical characterization of IrO_2 catalysts

For most experiments, commercially available IrO_2 dihydrate (Premion, 99.99% metal basis, Alfa Aesar) and IrO_2 non-hydrate (Premion, 99.99% metal basis, Alfa Aesar) powders were used as received. To study the cause of the durability differences between IrO_2 dihydrate and non-hydrate, both IrO_2 dihydrate and non-hydrate were calcined in air for 30 min. at different temperatures (250, 350, 450, 550, and 650 °C), using a tube furnace (Lindberg/Blue M, HTF55322A). The morphology of IrO_2 dihydrate catalysts before and after heat treatment were

examined using transmission electron microscopy (TEM, JOEL 2100 CRYO) operated at 200 kV. The TEM sample was prepared by placing a drop of the catalyst suspension in isopropanol onto a holey carbon-coated 200 mesh grid, followed by solvent evaporation. The crystalline structures of the different iridium oxide samples were obtained by X-ray diffraction (XRD) analysis using Siemens-Bruker D5000 diffractometer equipped with a CuKα source, and operated at 40 kV and 30 mA with a scan rate of 1 degree min^{-1}. In parallel these same samples were subjected to electrochemical measurements (see below). The Ir content in the exit electrolyte was determined by using ICP-PES (PerkinElmer-Optima 2000DV).

3.3.2 Electrochemical characterization of IrO_2 catalysts

Electrode preparation: The cathodes were prepared using an air-brush method as previously reported, using unsupported Ag nanoparticles (<100 nm particle size, 99.5% trace metals basis, Sigma-Aldrich).[22] Cathode catalyst inks were prepared by mixing Millipore water (200 μL), Ag catalyst (3.4 mg), Nafion® solution (4.4 μL, 5 wt%, Fuel Cell Earth), and isopropyl alcohol (200 μL). The inks were then sonicated (Vibra-Cell ultrasonic processor, Sonics & Materials) for 15 minutes and air-brushed using the automated air-brushing deposition setup on a gas diffusion layer (GDL, Sigracet 35 BC gas diffusion layers, Ion Power) to create a gas diffusion electrode (GDE) covered with catalyst over a geometric area of 2.5 × 0.8 cm^2. A PTFE spacer with a 2.5 × 0.8 cm^2 window was placed on top of GDL during the deposition process to avoid catalyst being deposited outside of the expected area on the GDL. Since a fraction of the catalyst ended up on the spacer, or was left behind in the air-brush, we determined the actual loading by weighing the GDL before and after deposition. The weight loss was found to be on the order of 50% for the air-brushed cathodes. The anodes were prepared by hand-painting of IrO_2 catalyst

inks comprised of Millipore water (200 μL), IrO_2 catalyst (2.5 mg), Nafion® solution (6.5 μL, 5 wt%, Fuel Cell Earth), and isopropyl alcohol (200 μL). The inks (with IrO_2 dihydrate or non-hydrate) were sonicated for 15 minutes and then each painted on a gas diffusion layer (Sigracet 35 BC) over a geometric area of 1.0×2.5 cm^2 using a paintbrush. The cathodes had a catalyst loading of about 0.9 mg cm^{-2}, while all the anodes had a catalyst loading of 1 mg cm^{-2}.

Electrochemical flow reactor operation: A flow reactor (reported previously [25,34]) in which a liquid electrolyte (here 1 M KOH) flows between the anode and cathode GDEs was used to perform the electrochemical reduction of CO_2 to CO. As in our prior work, a potentiostat (Autolab PGSTAT-30, EcoChemie) was used to control the cell potential in the potentiostatic electrolysis mode.[25] At times we controlled the total current in the galvanostatic electrolysis mode. In the potentiostatic mode, for each potential, the cell was allowed to reach steady state for 200 s, after which the gaseous product stream was analyzed using gas chromatography (Thermo Finnegan Trace GC). The current at a given condition was obtained by averaging the current over 180 s before stepping to the next potential. In the galvanostatic mode, the flow reactor was tested at total current of 10, 20, 40, 70, 100, or 150 mA. The reactor was allowed to reach steady state for about 200 s, after which the individual electrode potentials were recorded using multimeters (AMPROBE 15XP-B) connected to each electrode and a reference electrode (Ag/AgCl; RE-5B, BASi) placed in the electrolyte exit stream. The electrode potentials were corrected for IR drop as previously reported.[46] We found that the IR drop due to cell contact resistance (15 mV) is much smaller than the IR drop due to the resistance of the electrolyte (182 mV) at a cell potential of -3.00 V and associated resulting current of -261 mA (electrolyte resistance = 0.697 Ω). We used the same electrolyte resistance when correcting for IR drop at low current densities, because the electrolyte resistance will continue to be the dominating factor. Similarly, IR drop due to the cell

contact resistance will be much smaller than the IR drop due to the electrolyte at lower currents (see SI, *Supporting Information*, **Section 3.6** for details). For the IR corrected data reported, the cell contact resistance was ignored. The complete calculations for IR drop can be found in the *Supplementary Information* (SI, section 2.6).[47] A mass flow controller (MASS-FLO®, MKS instrument) was used to set the CO_2 (S.J. Smith Welding Supply) flow rate at 7 SCCM. A syringe pump (PHD 2000, Harvard Apparatus) supplied the 1 M KOH (Fisher Scientific, certified ACS pellets) electrolyte at 0.5 mL min^{-1}. The pH of the electrolyte was measured using a calibrated pH meter (Thermo Orion, 9106BNWP). A pressure controller (Cole-Parmer, 00268TC) downstream from the reactor was used to keep the gas pressure in reactor lower than the atmosphere, allowing gas products formed on the catalyst surface of the GDE to leave through the GDE to the gas stream. Periodically, for product analysis, 1 mL of the effluent gas stream was sampled automatically and diverted into a gas chromatograph (Thermo Finnegan Trace GC) operating in the thermal conductivity detection (TCD) mode, with a Carboxen 1000 column (Supelco) and Helium as the carrier gas at a flow rate of 20 SCCM. The column was held at 150 °C and the TCD detector was held at 200 °C. The only cathode products detected by GC were CO and H_2 when using Ag as the catalyst, consistent with results reported previously.[21,28] For experiments conducted in the flow reactor, the onset potential is defined as the lowest cell potential at which we observe CO peak in GC. A fresh cathode was used for each flow reactor test.

Three-Electrode Cell Operation: Cyclic Voltammetry (CV) was performed using a potentiostat (Autolab PGSTAT302N, EcoChemie), and a standard three-electrode cell with 1M KOH as the electrolyte. A catalyst-covered 3-mm glassy carbon disk rotating disk electrode (RDE; Metrohm 6.1204.300) as the working electrode, a Pt gauze (100 mesh, 99.9% metals basis, Sigma-Aldrich, 25*25 mm^2) as the counter electrode, and a Ag/AgCl as the reference electrode (RE-5B,

BASi), separated from the working electrode by means of a Luggin capillary, were used. IrO_2 catalyst ink (4 μL) was deposited on the RDE and then dried under flowing Ar. The inks were prepared using the same method as described above for the GDE anodes. To determine catalyst activity, the potential was scanned from 0 to 0.8 V *vs.* Ag/AgCl at a scan rate of 25 mV s^{-1}, while for the stability test, the potential was continuously cycled between 0 and 1 V *vs.* Ag/AgCl at a scan rate of 100 mV s^{-1}. Ar gas was bubbled through the electrolyte for 15 min prior to all CV measurements. The RDE was rotated at 1600 rpm to eliminate mass transport issues and to remove any bubbles that form on the electrode surface during the experiment. For experiments conducted in a three-electrode cell (CV), the onset potential is defined as the working electrode potential at which the current reaches 0.2 mA.

3.4 Results and Discussion

3.4.1 Overpotential and current density

The performance towards OER activity for the three anode catalysts, IrO_2 dihydrate, IrO_2 non-hydrate, and Pt black was studied using CV in a standard three-electrode cell. Both the IrO_2 dihydrate and IrO_2 non-hydrate catalysts achieved much higher current and significantly lower onset potential (> 0.2 V) for the OER compared to Pt black (**Figure 3.1a**), indicating that these two IrO_2 catalysts (dihydrate and non-hydrate) are more active than Pt black. The IrO_2 dihydrate catalyst performs slightly better: it exhibits a ~50 mV earlier onset potential and a ~4 mA higher current compared to the IrO_2 non-hydrate catalyst.

Next, an electrochemical flow reactor was used to determine whether the high activity of the IrO_2 catalysts observed in the three-electrode cell translates into good performance in an electrolyzer. GDEs with the two IrO_2 catalysts were prepared and compared with a Pt-covered

GDE. The partial current density for CO (j_{co}) as a function of cell potential is shown in **Figure 3.1b** for the systems with these three anode catalysts. The electrolyzer performed significantly better when using one of the IrO_2 catalyst-based GDEs than when using the Pt catalyst-based GDEs. Specifically, at cell potentials of -2.75 V and -3 V, the improvement in j_{co} was more than 100 mA cm^{-2}. At -3 V cell potential, the system using IrO_2 dihydrate as the anode catalyst achieved a j_{co} as high as 250 mA cm^{-2}, which is among the highest partial current density reported to date for the electroreduction of CO_2 to CO at ambient conditions. This level of performance enhances the probability of this technology being transitioned in an economically viable process.[12]

The CV data (**Figure 3.1a**) already indicates that the IrO_2-based anodes exhibit a low OER onset potential. To determine the onset potential for CO_2 reduction of the systems with different anode catalysts on GDEs, the composition of the effluent gas stream of the flow reactor was analyzed with GC for different cell potentials after the flow reactor reached steady state. Whereas no CO production was observed yet at a cell potential of -1.50 V, CO production was observed when applying -1.55 V cell potential (corresponding to an overpotential of only 0.22 V), when using IrO_2 dihydrate as the anode catalyst (**Figure 3.1c**). In comparison, the onset cell potential for CO production was -1.60 V (0.27 V overpotential) and -1.75 V (0.42 V overpotential) when respectively IrO_2 non-hydrate and Pt black were used as the anode catalyst. The overpotential for the system using IrO_2 dihydrate is 0.2 V lower than the system using Pt black as the anode, in agreement with the CV data shown in **Figure 3.1a**. In comparison to previous work where an ionic liquid (EMIM BF_4) containing aqueous electrolyte was used to decrease the cell overpotential to less than 0.2 V,[29] here a similar low cell overpotential (0.22 V) is achieved with an electrolyte that is much cheaper, less viscous (easier operation), and more conductive, resulting in higher throughput (current density).

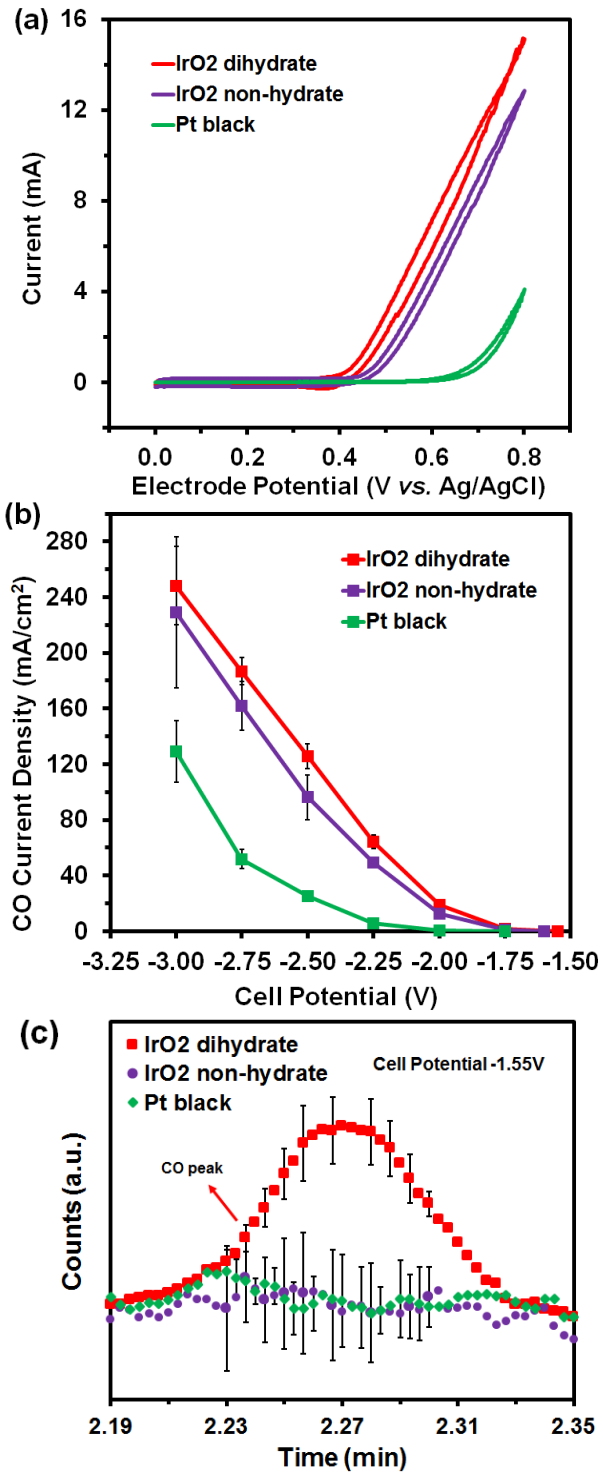

Figure 3.1 (a) CV measurements of IrO_2 dihydrate, IrO_2 non-hydrate and Pt black; (b) Partial current density for CO as a function of cell potential with IrO_2 hydrate, IrO_2 non-hydrate and Pt black as the anode catalysts (data obtained in potentiostatic mode); (c) GC peak at cell potential of -1.55 V applied on the electrochemical flow reactor with 3 different anode catalyst: IrO_2 dihydrate, IrO_2 non-hydrate and Pt black. Reprinted with permission from J. Electrochem. Soc. 161, F1124-F1131, (2014). Copyright 2014 the Electrochemical Society.

The achieved low cell overpotential not only originates from the anode catalyst improvement, but is probably also due to the use of alkaline electrolyte. The standard potential for the cathode reaction

$$H_2O + CO_2 + 2\ e^- \rightarrow CO + 2\ OH^- \qquad 1$$

is calculated as follows: -0.109[7] – 0.0591×pH (pH of 1M KOH is 13.48 from the pH measurement) – 0.209 (correction for reference electrode from SHE to Ag/AgCl) = -1.11 V *vs*. Ag/AgCl. At -1.55 V cell potential with IrO_2 dihydrate as the anode catalyst, the cathode potential was -1.13 V *vs.* Ag/AgCl. This correlates to a cathode overpotential of only 0.02 V, which is the lowest overpotential reported to date for the electrochemical reduction of CO_2 to CO on metal electrodes, lower than those reported for Au oxide derived catalysts in neutral electrolyte.[35] Compared to our prior work in which we used 18 mol% solutions of EMIM BF_4,[29] a much higher current density (129 mA cm^{-2} in this work vs. 3.9 mA cm^{-2} in prior work at -2.5 V cell potential) is obtained when using a Ag cathode and an IrO_2 dihydrate anode in the reactor filled with 1M KOH. Also, to compare the Ag cathode performance in 1M KOH and 1M KCl, we performed potentiostatic measurement in 1M KCl (pH=6.62) using Ag cathode and IrO_2 non-hydrate anode. The results of the above experiment and potentiostatic measurements using 1M KOH in this study, as well as data from prior work[22] were summarized and compared in SI (**Figure 3.5**). As shown in **Figure 3.5a**, by changing the electrolyte (from 1M KCl to 1M KOH), the cathode polarization curves do not shift, while the anode polarization curves shift significantly, by as high as 0.5 V, mainly due to the effect of pH change on the standard potential of OER reaction (**Figure 3.5a**). The standard potential of OER will decrease by 0.0591 × (13.48 – 6.62) = 0.41 V when using 1M KOH instead of 1M KCl. The same is true for the CO_2 reduction to CO. However, the cathode polarization curves do not shift when changing electrolyte from 1M KCl to 1M KOH, indicating that the CO_2

reduction kinetics is improved in the alkaline solution. Therefore, a Ag cathode performs better in 1M KOH compared to 1M KCl as a result of a much lower overpotential in 1M KOH (0.41 V lower). When comparing the Ag cathodes in different electrolytes in **Figure 3.5b** this expected difference of 0.41V due to a change in pH can not be seen, because all are plotted with respect to the Ag/AgCl reference electrode. The 1M KOH alkaline media increases the electrolyte conductivity (compared to $KHCO_3$ and K_2SO_4) [21] and may also improve the CO_2 reduction reaction kinetics due to the suppression of hydrogen evolution reaction by lowering H^+ concentration. Also, on the anode side, IrO_2 catalysts are more active in alkaline media than in other pH environment as previously reported.[44] Therefore, alkaline media not only works better for OER reaction on the anode, but also facilitates the CO_2 reduction reaction on the cathode, making it a highly suitable electrolyte for the electrochemical reduction of CO_2 to CO.

3.4.2 Energy efficiency and current-potential behavior

The energy efficiency of an electrolysis process can be calculated using the following equation as previously reported [12]:

$$\varepsilon_{energetic} = \sum_k \frac{E_k^{\circ}\varepsilon_{k,Faradaic}}{E_k^{\circ} + \eta} = \sum_k \frac{E_k^{\circ}\varepsilon_{k,Faradaic}}{E_k^{\circ} + \eta_{cathode} + \eta_{anode}} \qquad 2$$

where E_k° is the equilibrium cell potential for a certain product, η is the cell overpotential, equal to the sum of the overpotentials from the cathode ($\eta_{cathode}$) and the anode (η_{anode}). In all experiments the two major products are H_2 and CO. No other products, which based on the Faradaic efficiencies for H_2 and CO never totaled to a fraction higher than 5%, were detected. The equilibrium cell potential E^o for converting CO_2 to CO equals $E^o_{cathode} - E^o_{anode}$ = -0.10 V - 1.23 V = -1.33 V and for H_2 evolution E^o equals $E^o_{cathode} - E^o_{anode}$ = 0 V - 1.23 V = -1.23 V. $\varepsilon_{k,Faradaic}$ is

the Faradaic efficiency of product *k* and η is the cell overpotential (*i.e.*, the sum of overpotentials on the cathode and anode).

To study how the system energy efficiency changes when using IrO_2 catalysts (dihydrate or non-hydrate) instead of Pt black, the flow reactor was operated in galvanostatic mode, in which the individual electrode potentials are measured when driving the cell with different currents (from 10 mA to 150 mA). Also note that to confirm the onset potential in potentiostatic mode, at current below 10 mA, cell potential was controlled for the systems with three different anode catalysts. **Table 3.1** summarizes IR-corrected electrode potential and Faradaic efficiency for CO (the desired product), and for H_2 (the byproduct), as obtained for systems using IrO_2 dihydrate, IrO_2 non-hydrate, and Pt black. All cells used the same Ag cathode catalyst, so not surprisingly the three systems with different anode catalysts achieved similar, high Faradaic efficiencies for CO: typically above 90% at the same current density, in agreement with prior studies.[19,25] In contrast, a significant increase in energy efficiency is observed when IrO_2 catalysts are used instead of Pt black (**Figure 3.2a**). Specifically, at a current density of 10 mA cm^{-2}, the system using IrO_2 dihydrate as the anode catalyst achieved an energy efficiency as high as 70%, compared to only 55% when using Pt black as the anode catalyst. Furthermore, when using IrO_2 dihydrate as the anode catalyst, even at a current density as high as 150 mA cm^{-2}, the energy efficiency was above 50%, compared to 39% when Pt black was used as the anode catalyst in this study. Also, the 50% energy efficiency at high current density observed here is higher than what has been reported previously. For example, Yamamoto *et al.* reported an energy efficiency of less than 30%,[16] while Dufek *et al.* reported an energy efficiency less than 40%,[18] both at total current densities of ≥150 mA cm^{-2}. In other studies energy efficiencies exceeding 60% have been reported, but typically at current densities less than 10 mA cm^{-2}.[25,29]

Table 3.1 Faradaic efficiency for CO and H_2 for the experiments running at different currents using 3 anode catalysts: IrO_2 dihydrate, IrO_2 non-hydrate and Pt black (data obtained in galvanostatic mode).

Anode catalyst	Current density (mA/cm^2)	IR corrected potential (V)		Cell Potential (V)	Faradaic efficiency (%)		Energy Efficiency (%)
		Cathode	Anode		CO	H_2	
IrO_2 dihydrate	10	-1.369	0.456	-1.83	90	9	70.89
	20	-1.442	0.484	-1.94	94	5	67.25
	40	-1.525	0.524	-2.08	97	1	62.55
	70	-1.591	0.578	-2.22	99	1	59.85
	100	-1.645	0.658	-2.37	98	1	55.31
	150	-1.751	0.774	-2.63	98	1	50.19
IrO_2 non-hydrate	10	-1.363	0.537	-1.91	88	4	64.19
	20	-1.435	0.571	-2.02	93	1	61.45
	40	-1.531	0.639	-2.20	93	1	56.87
	70	-1.639	0.734	-2.42	95	2	52.91
	100	-1.677	0.804	-2.55	98	2	51.95
	150	-1.768	0.963	-2.84	99	1	46.84
Pt black	10	-1.373	0.752	-2.13	87	1	55.19
	20	-1.448	0.830	-2.29	88	1	51.53
	40	-1.559	0.956	-2.54	89	2	47.20
	70	-1.648	1.111	-2.81	92	2	44.51
	100	-1.715	1.218	-3.00	96	2	43.25
	150	-1.848	1.423	-3.38	97	3	39.14

From the IR-corrected single electrode polarization curves (**Figure 3.2b**) it is clear that the improvements of the overall cell performance (both energy efficiency and current density) can be attributed to the lower overpotentials exhibited by the anodes with IrO_2 catalysts compared to the ones with Pt catalyst. The improvement in anode overpotential was as high as 0.65 V at 150 mA cm^{-2} when IrO_2 dihydrate was used instead of Pt black. To no surprise, with all three systems using similar Ag cathodes, the cathode curves overlap almost completely. In sum, lower cell potentials were obtained by lowering the anode overpotential, which in turn has resulted in high energy efficiencies, even at high current densities.

The IR-corrected single electrode polarization curves (**Figure 3.2b**) also confirm the observations made using CV in a 3-electrode cell (**Figure 3.1a**): that the IrO_2 dihydrate catalyst

exhibits a lower overpotential than the IrO_2 non-hydrate catalyst; in other words the dihydrate is better than the non-hydrate in terms of OER activity. To confirm the behavior of these IrO_2 catalysts under more conventional OER conditions, measurement under Ar-purged condition (flowing Ar instead of CO_2 in the cathode gas chamber during the experiment) was performed in the flow reactor (details shown in Section IV in the *SI*). This result shows that under the Ar flowing condition, IrO_2 dihydrate also performs better than IrO_2 non-hydrate towards the OER. In prior work the higher activity of IrO_2 hydrate compared to IrO_2 non-hydrate is attributed to the higher amount of surface hydroxyl species and highly dispersed amorphous structure of the IrO_2 hydrate, providing higher surface area, microporous morphology and more catalytic sites.[42-45]

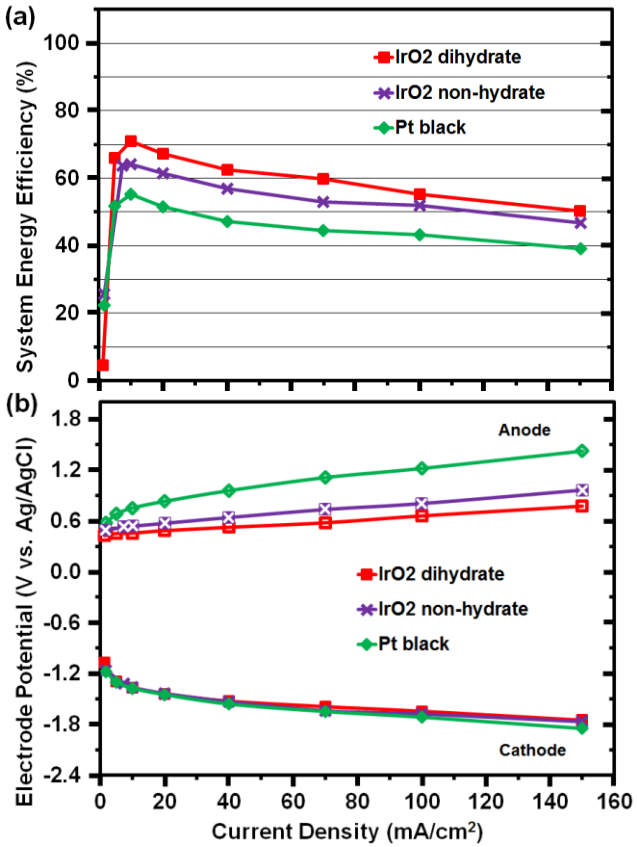

Figure 3.2 (a) Energy efficiency as a function of current density; (b) IR-corrected single electrode polarization curves of the experiments using 3 different anode catalysts: IrO_2 dihydrate, IrO_2 non-hydrate and Pt black (data obtained in galvanostatic mode). Reprinted with permission from J. Electrochem. Soc. 161, F1124-F1131, (2014). Copyright 2014 the Electrochemical Society.

3.4.3 Durability of the IrO_2 catalysts

Although IrO_2 dihydrate exhibits a lower overpotential and thus achieves a higher current density compared to IrO_2 non-hydrate, the durability of these catalysts also needs to be investigated, as this property is of key importance when considering them for applications. Very little has been reported previously on the durability of these catalysts when used in alkaline solution. Here, we performed two different experiments to compare the durability of IrO_2 dihydrate and IrO_2 non-hydrate, one in a 3-electrode cell and one in the flow cell. First, continuous potential cycling (between 0 to 1V vs Ag/AgCl) was performed in a standard 3-electrode cell for both IrO_2 dihydrate and IrO_2 non-hydrate (**Figure 3.3a** and **3.3b).** When using IrO_2 dihydrate, the current decreased significantly in successive cycles, overall from 35.28 mA to 1.78 mA after 19 cycles (**Figure 3.3a**). In contrast, when using IrO_2 non-hydrate, the current only decreased slightly in successive cycles, as evidenced in a drop of less than 2 mA (from 29.24 mA to 27.52 mA) after 200 cycles (**Figure 3.3b**).

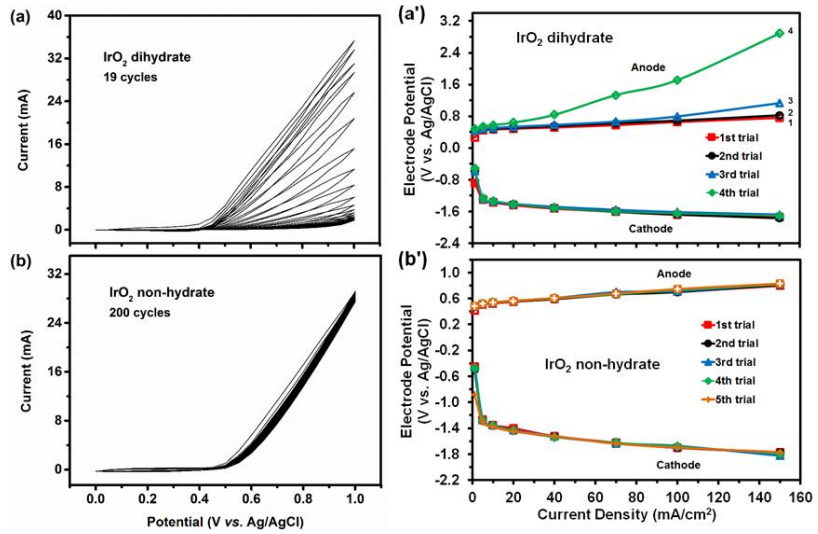

Figure 3.3 Left: Continuous potential cycling conducted in a standard 3-electrode cell for (a) IrO_2 dihydrate, and (b) IrO_2 non-hydrate. Electrolyte: 1M KOH; Scan rate: 100 mV/s; RDE rotating rate: 1600 rpm. Right: IR-corrected single electrode polarization curves for anode durability test conducted in an electrochemical flow reactor for (a') IrO_2 dihydrate, and (b') IrO_2 non-hydrate. Reprinted with permission from J. Electrochem. Soc. 161, F1124-F1131, (2014). Copyright 2014 the Electrochemical Society.

Second, the durability of the two IrO_2 catalysts was also measured in the electrochemical flow reactor. The same anode was used for 4 – 5 trials in the flow reactor, which is operated in galvanostatic mode. The resulted steady state electrode potentials were recorded, and IR-corrected single electrode polarization curves were plotted in **Figure 3.3a'** and **3.3b'**. As shown in **Figure 3.3a'**, the activity of IrO_2 dihydrate towards OER drops significantly after each trail test, while the IrO_2 non-hydrate anode is still as active as the fresh electrode after 5-trial test since the 5 anode polarization curves overlap (**Figure 3.3b'**), which is in good agreement with the results from continuous potential cycling experiment. Therefore, IrO_2 dihydrate is less durable compared to IrO_2 non-hydrate, which is probably due to anodic dissolution during the reaction as reported previously.[39,40,44,48]

In prior work the difference in durability between IrO_2 hydrate and non-hydrate has mainly been attributed to the difference in crystallinity and specific surface area.[42,48] To determine the effect of crystallinity on the durability, XRD patterns of both IrO_2 dihydrate (**Figure 3.4a**) and IrO_2 non-hydrate **(Figure 3.4b**) were collected. This XRD data indicates that both the dihydrate and non-hydrate have a similar amorphous (non-crystalline) structure, so probably not the source of the observed differences in durability. The sharp peaks observed in the XRD patterns of both catalysts are due to the crystalline structure of Ir metal, which is a common component in commercial IrO_2 catalysts.[43] Since Ir will be oxidized to IrO_2 during reaction and both the dihydrate and non-hydrate are comprised of similar amounts of Ir, the presence of Ir (and the associated crystalline peaks in XRD) is assumed not to be the cause of the differences in durability and activity between these two catalysts.

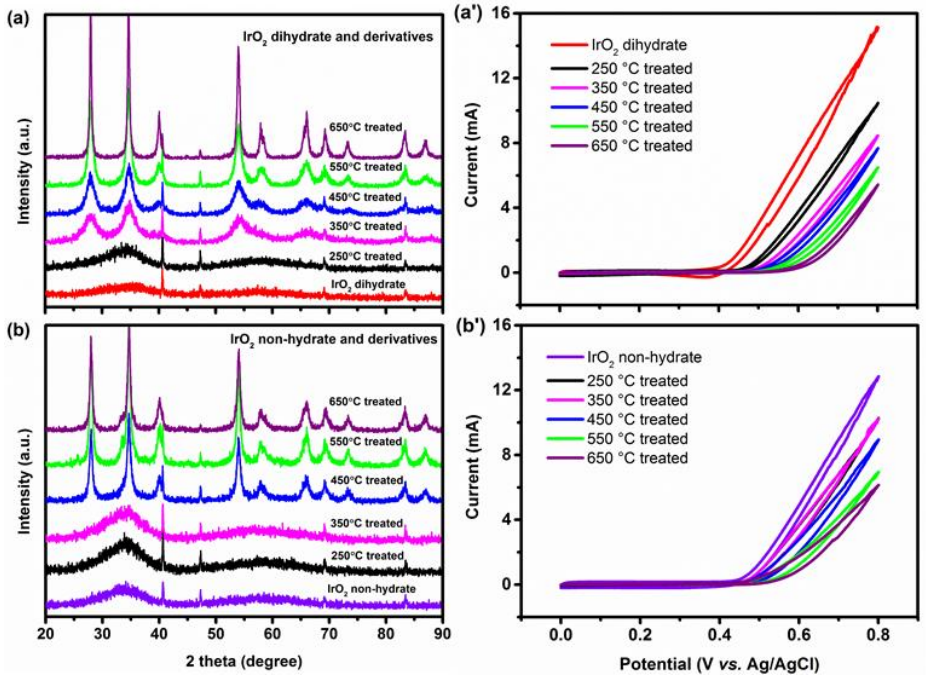

Figure 3.4 Left: XRD analysis of (a) IrO_2 dihydrate, and (b) IrO_2 non-hydrate upon thermal treatment. Right: CV measurements of (a') IrO_2 dihydrate, and (b') IrO_2 non-hydrate after thermal treatment at different temperatures. CV was conducted in 1M KOH at a scan rate of 25 mV/s, with the RDE rotating at 1600 rpm. Reprinted with permission from J. Electrochem. Soc. 161, F1124-F1131, (2014). Copyright 2014 the Electrochemical Society.

Other causes for the observed difference in activity and durability between the two IrO_2 catalysts may originate from the amount of water content or the amount of surface hydroxyl species. To study how water content and surface species density affect catalysts durability, IrO_2 dihydrate and IrO_2 non-hydrate were both heat treated at 250, 350, 450, 550 and 650 ºC (**Figure 3.4a and 3.4b**). Upon gradual calcination of the catalysts, the water content, the coverage with surface hydroxyl species, the morphology, as well as the crystallinity of the catalysts may change, which may help elucidate the connection between structure and electrochemical performance. For IrO_2 dihydrate, the structure changed from amorphous to crystalline at a temperature between 250 and 350 ºC (**Figure 3.4a**), while for IrO_2 non-hydrate, the transition happened between 350 and 450 ºC (**Figure 3.4b**). For both materials, the crystallinity increased when raising the temperature

further, as evidenced by the sharpening of the peaks. The TEM micrographs shown in **Figure 3.6** in the SI suggest that untreated (**Figure 3.6b**) and 250 ºC treated (**Figure 3.6c**) IrO_2 dihydrate have an amorphous structure with irregular particle shape. [47] However, for IrO_2 dihydrate samples treated from 450 ºC to 650 ºC, the particles start to sinter (~10 nm in **Figure 3.6e** to >20 nm in **Figure 3.6g**) and change shape to squares with more crystalline features, while the 350 ºC treated IrO_2 dihydrate sample (**Figure 3.6d**) appears to be in a state between amorphous and crystalline. These morphologies and trends observed in TEM are in agreement with the XRD results shown in **Figure 3.4a**. **Figure 3.4a'** and **3.4b'** show the OER activity for samples of each of the two IrO_2 catalysts after treatment at different temperatures. Heat treatment leads to reduced OER activity for both IrO_2 dihydrate and IrO_2 non-hydrate, probably due to the loss of surface hydroxyl species, and/or a change of the crystalline structure and morphology (especially at temperatures above 350 ºC), leading to the decrease in electrochemical surface area of the catalyst. Further study of the durability of the 250 ºC treated IrO_2 dihydrate sample using continuous potential cycling (same experiment as used in **Figure 3.3a** and **3.3b**) revealed that this sample is remarkably stable: the current dropped only by 12%, from 18.91 mA to 16.80 mA after 200 cycles. In contrast, recall that the untreated IrO_2 dihydrate sample loses more than 90% of its activity after only 19 cycles (**Figure 3.3a**), despite the XRD patterns (**Figure 3.4a**) and TEM micrographs (**Figure 3.6b** and **3.6c**) of the untreated and the 250 ºC treated IrO_2 dihydrate samples being almost identical. This suggests that the difference in durability between the untreated and the 250 ºC treated IrO_2 dihydrate samples is probably due to the differences in water content or surface hydroxyl coverage, rather than due to a change in crystalline structure. Based on the above analysis, along with the observation from TEM (**Figure 3.6a** and **3.6b**) that the 250 ºC treated IrO_2 dihydrate, the untreated IrO_2 non-hydrate, and the dihydrate samples have similar morphology, the differences in activity

and durability among these three IrO_2 catalysts can be attributed mainly to water content and/or surface hydroxyl coverage.

During the past few decades, a large amount of work has been done on OER, and several mechanisms were proposed.[37,44,49-54] Most of the mechanisms proposed for metal oxide catalysts include the formation and subsequent decomposition of higher valent metal oxides.[37,44,49] For example, according to Trassati *et al.*[50], the mechanism would be as follows where S is an active site related to a topological defect on the catalyst:

$$S + OH^- \rightarrow S\text{-}OH + e^- \quad (3)$$

$$S\text{-}OH + OH^- \rightarrow S\text{-}O + H_2O + e^- \quad (4)$$

$$2S\text{-}OH \rightarrow S\text{-}O + S\text{-}H_2O \quad (5)$$

$$S\text{-}O + S\text{-}O \rightarrow O_2 + 2S \quad (6)$$

The Step 3 is followed by the formation of bounded oxide species, which then dissociates to oxygen.[37,49,50] Alternatively, the S-OH bond can be broken slowly to form a peroxide species, which dissociates to the solution (H_2O_2) or stays adsorbed on the surface (S-OOH), before decomposes to O_2.[52,54] Recently, DFT calculations have been reported and suggest that the OER mechanism consists of multiple single-electron charge-transfer steps with the involvement of three adsorbed intermediates: $OH_{(ad)}$, $O_{(ad)}$, and $OOH_{(ad)}$.[49,55,56] When correlating our results to the classic mechanism shown above (Step 3 to 6), we can consider Step 3 and 5 as the rate determining steps (RDS) on porous metal oxide materials such as the IrO_2 dihydrate used here, while Step 3 and 4 can be considered as the RDS on more dense species such as the IrO_2 non-hydrate used in this study. In this mechanism, the surface hydroxyl coverage is closely linked to the number of reaction sites since S-OH is the starting species in Step 4 and 5. More hydroxyls on the catalyst surface represents more reaction sites on the catalysts, which is probably why IrO_2 hydrate has

more reaction sites than IrO_2 non-hydrate as previously reported.[42] When the reaction cycle starts, a higher hydroxyl surface coverage on IrO_2 dihydrate will facilitate Step 4 or 5 without the need to have Step 3 finish. For IrO_2 dihydrate, after faster consumption of hydroxyls, more empty sites will be created compared to IrO_2 non-hydrate, thereby increasing the reaction rate. Therefore, IrO_2 dihydrate initially exhibits a higher current density and lower overpotential because it has a higher hydroxyl surface coverage as well as more reaction sites compared to IrO_2 non-hydrate.[42] However, since hydroxyl species are involved in the oxidation of IrO_2 catalyst during the OER,[37] a higher amount of hydroxyls on the surface will also lead to higher possibility of further oxidation of IrO_2 and subsequent dissolution, lowering the durability of the dihydrate form. Indeed more Ir was detected using inductively coupled plasma optical emission spectroscopy in the electrolyte leaving the reactor when using the dihydrate catalyst (1.70 ppm when using dihydrate compared to 0.35 ppm when using non-hydrate). The results and analysis reported here suggest that further experiments using in-situ spectroscopy in combination with theoretical and/or computational efforts are needed to further unravel the mechanistic aspects of the processes taking place on these electrodes, as also suggested previously.[49]

3.5 Conclusions

In summary, IrO_2-based anode catalysts (a dihydrate and a non-hydrate form) were studied for the oxygen evolution reaction in an electrochemical flow cell for the efficient reduction of CO_2 to CO on Ag cathodes. The use of the dihydrate and non-hydrate forms of IrO_2 instead of Pt black as the anode catalyst in 1M KOH lowered onset cell potential by ~0.2 V to 1.6 V. Also, this configuration produced the highest partial current densities for CO (250 mA cm^{-2}) reported to date under ambient conditions, compared to 130 mA cm^{-2} when Pt black was used as the anode catalyst.

The use of 1 M KOH as the electrolyte helped improve the cathode reaction kinetics, as evidenced by a cathode overpotential of only 0.02 V, which to our knowledge is the lowest overpotential reported to date for the conversion of CO_2 to CO in aqueous media. These improvements result in an energy efficiency as high as 70% at 10 mA cm^{-2} and still >50% at 150 mA cm^{-2}.

While the initial performance of the two forms of IrO_2 catalysts, dihydrate and non-hydrate, was found to be similar, IrO_2 non-hydrate is much more durable (loses less than 10% of activity upon electrochemical cycling) than IrO_2 dihydrate (loses >90% of activity). Based on physical and electrochemical characterization of heat treated samples of the two IrO_2 catalysts, these observed differences can be attributed to differences in their morphology, number of available active sites, and their ability to accommodate surface-bound hydroxyls.

While the use of IrO_2 anodes significantly improved the performance of electrochemical CO_2 conversion in a flow cell, further advances are needed to enhance the applicability of the process, specifically cathodes need to be developed that are able to achieve high energy efficiency (>50%) at much higher current density (>400 mA cm^{-2}) while maintaining high selectivity for a specific product, as well as electrodes that are able to handle the high mass transfer rates of the reactants and products. Further experimental and computational study of the reaction mechanism of CO_2 reduction in alkaline media is needed to understand the improved kinetics and may guide the design of yet better cathode catalysts.

3.6 Supporting Information

3.6.1 IR drop calculations

To calculate the IR drop we used the data at an applied cell potential of -3.00 V (potentiostatic measurement). At this potential, the readings for the cathode and anode from multimeters are -1.990 V and 0.995 V, respectively, and the recorded current is -261 mA.

IR drop due to cell contact resistance:

The difference of the cathode and anode potential (V_{actual}) is calculated to be -2.985 V. Thus, the IR loss which is attributed to cell contact resistance ($IR_{contact}$) equals (-2985) – (-3000) = 15 mV. With the current being -261 mA, $R_{contact}$ is calculated to be 0.057 Ω.

IR drop due to electrolyte resistance:

Based on the specific conductivity of 1M KOH (0.2153 S/cm at 25 °C[57]), and the cell dimensions (1 cm^2 × 0.15 cm), we calculate the electrolyte resistance ($R_{electrolyte}$) to be 0.697 Ω. Therefore, with the current being -261 mA, the IR drop due to electrolyte is 182 mV.

IR correction for the electrodes:

The cathode potentials were IR-corrected by adding half of the $IR_{electrolyte}$ to the cathode readings from the multimeter, while the anode potentials were IR-corrected by subtracting half of the $IR_{electrolyte}$ from the anode readings from the multimeter, following a previously reported protocol.[46]

3.6.2 Comparison of different electrolytes in the flow reactor

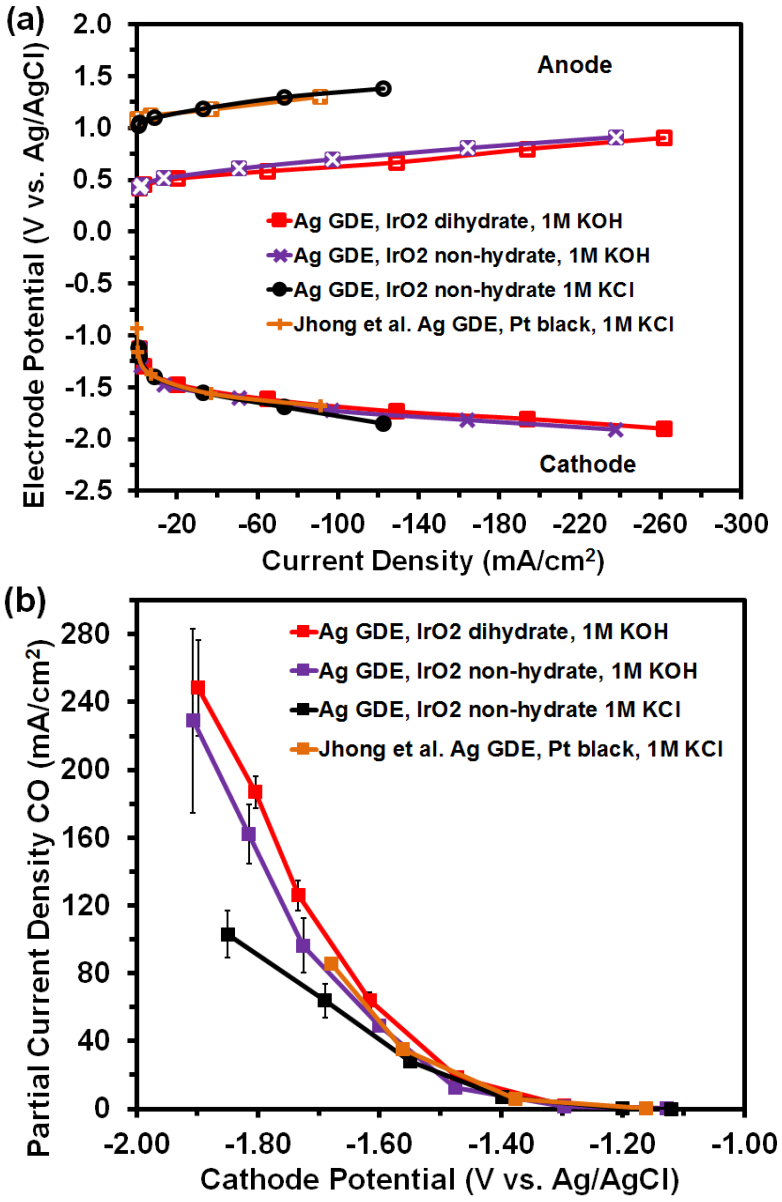

Figure 3.5 (a) Single electrode polarization curves and (b) Partial current density for CO production using a Ag GDE cathode under four different conditions: IrO_2 dihydrate as the anode in 1M KOH, IrO_2 non-hydrate as the anode in 1M KOH, IrO_2 non-hydrate as the anode in 1M KCl, and Pt black as the anode in 1M KCl from prior work [22]. CO_2 stream: 7 sccm. Reprinted with permission from J. Electrochem. Soc. 161, F1124-F1131, (2014). Copyright 2014 the Electrochemical Society.

3.6.3 TEM micrographs of IrO_2 dihydrate catalysts before and after heat treatment

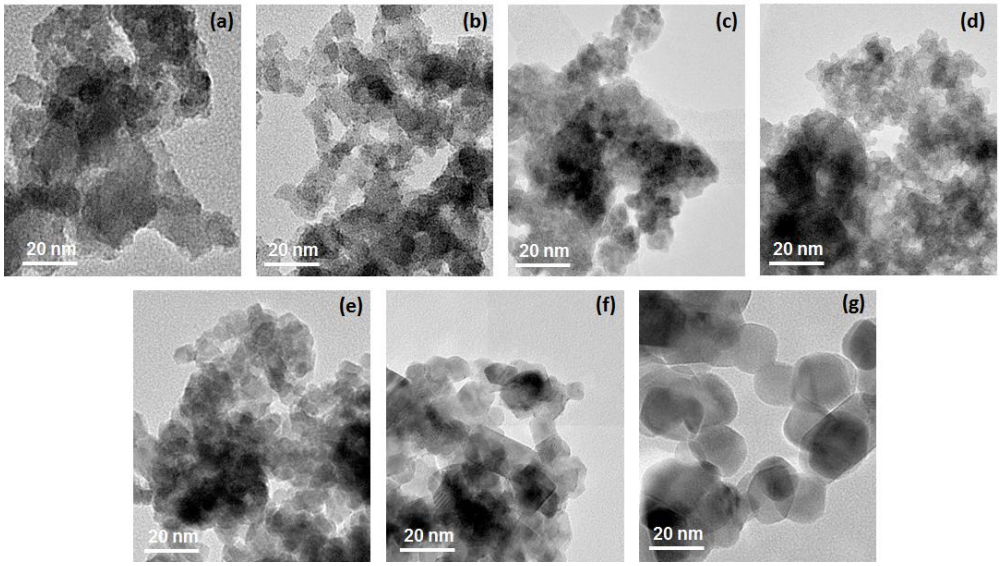

Figure 3.6 TEM micrographs of IrO_2 catalysts before and after heat treatment: (a) IrO_2 non-hydrate without heat treatment; (b) IrO_2 dihydrate without heat treatment; (c) IrO_2 dihydrate after heat treatment at 250 °C ; (d) IrO_2 dihydrate after heat treatment at 350 °C; (e) IrO_2 dihydrate after heat treatment at 450 °C; (f) IrO_2 dihydrate after heat treatment at 550 °C; (g) IrO_2 dihydrate after heat treatment at 650 °C. Reprinted with permission from J. Electrochem. Soc. 161, F1124-F1131, (2014). Copyright 2014 the Electrochemical Society.

3.6.4 OER performance in the flow reactor under Ar-purged condition

Measurements under Ar-purged conditions (flowing Ar instead of CO_2 in the cathode gas chamber during the experiment) were performed in the flow reactor. The electrolyte (1M KOH) was purged with Ar for 15 mins before the experiments. Two IrO_2 catalysts, IrO_2 dihydrate and non-hydrate, were examined. Each anode was first tested under Ar-flowing condition, after which we replaced the cathode with a fresh one and used the same anode for another test under CO_2 flowing condition.

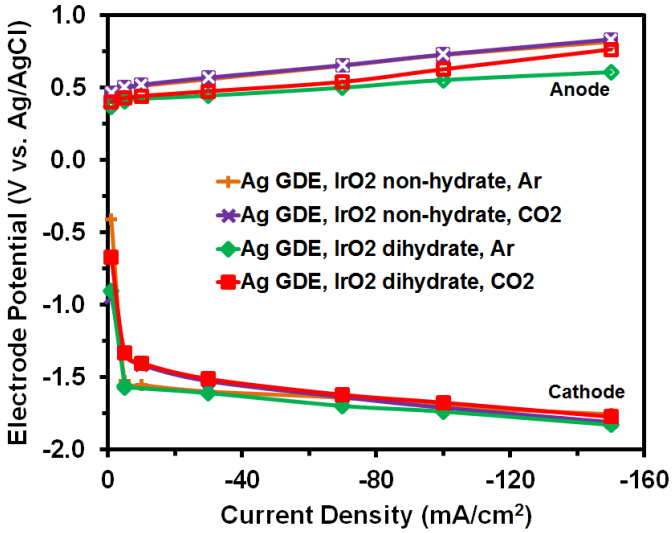

Figure 3.7 IR-corrected single electrode polarization curves of the experiments using 2 different anode catalysts: IrO_2 dihydrate, IrO_2 non-hydrate under different gas flowing conditions on the cathode side. Reprinted with permission from J. Electrochem. Soc. 161, F1124-F1131, (2014). Copyright 2014 the Electrochemical Society.

Under the Ar-flowing condition, IrO_2 dihydrate performs better than IrO_2 non-hydrate for the OER. The performance of IrO_2 dihydrate towards OER decreased under the CO_2 flowing condition. However, for IrO_2 non-hydrate, the OER performance under the Ar-flowing condition and the CO_2 flowing condition is the same. Therefore, flowing Ar or CO_2 on the gas chamber does not affect the OER reaction on the anode. This result is also in good agreement with the observations shown in **Figure 3.3a'** and **Figure 3.3b'** that IrO_2 dihydrate is more durable than IrO_2 non-hydrate.

3.7 References

1 Bell, A. T. Basic Research Needs, Catalysis for Energy. *Basic Research Needs, Catalysis for Energy*, U.S. Department of Energy: Bethesda, MD, (2008).

2 Jacobson, M. Z. Review of solutions to global warming, air pollution, and energy security. *Energy Environ. Sci.* **2**, 148-173, (2009).

3 Taylor, P. Energy Technology Perspectives *Energy Technology Perspectives* International Energy Agency, (2010).

4 Pacala, S. & Socolow, R. Stabilization Wedges: Solving the Climate Problem for the Next 50 Years with Current Technologies. *Science* **305**, 968-972, (2004).

5 Lewis, N. S. Toward Cost-Effective Solar Energy Use. *Science* **315**, 798-801, (2007).
6 Gattrell, M., Gupta, N. & Co, A. A review of the aqueous electrochemical reduction of CO2 to hydrocarbons at copper. *J. Electroanal. Chem.* **594**, 1-19, (2006).
7 Oloman, C. & Li, H. Electrochemical Processing of Carbon Dioxide. *ChemSusChem* **1**, 385-391, (2008).
8 Hori, Y. in *Handbook of Fuel Cells* Vol. 2 Ch. 48, 720-733 (John Wiley & Sons, Ltd, 2010).
9 Mikkelsen, M., Jorgensen, M. & Krebs, F. C. The teraton challenge. A review of fixation and transformation of carbon dioxide. *Energy Environ. Sci.* **3**, 43-81, (2010).
10 Whipple, D. T. & Kenis, P. J. A. Prospects of CO2 Utilization via Direct Heterogeneous Electrochemical Reduction. *J. Phys. Chem. Lett.* **1**, 3451-3458, (2010).
11 Kumar, B., Llorente, M., Froehlich, J., Dang, T., Sathrum, A. & Kubiak, C. P. Photochemical and Photoelectrochemical Reduction of CO_2. *Annu. Rev. Phys. Chem.* **63**, 541-569, (2012).
12 Jhong, H.-R. M., Ma, S. & Kenis, P. J. A. Electrochemical conversion of CO2 to useful chemicals: current status, remaining challenges, and future opportunities. *Curr. Opin. Chem. Eng.* **2**, 191-199, (2013).
13 Appel, A. M., Bercaw, J. E., Bocarsly, A. B., Dobbek, H., DuBois, D. L., Dupuis, M., Ferry, J. G., Fujita, E., Hille, R., Kenis, P. J. A., Kerfeld, C. A., Morris, R. H., Peden, C. H. F., Portis, A. R., Ragsdale, S. W., Rauchfuss, T. B., Reek, J. N. H., Seefeldt, L. C., Thauer, R. K. & Waldrop, G. L. Frontiers, Opportunities, and Challenges in Biochemical and Chemical Catalysis of CO_2 Fixation. *Chem. Rev.* **113**, 6621-6658, (2013).
14 Dry, M. E. The Fischer–Tropsch process: 1950–2000. *Catal. Today* **71**, 227-241, (2002).
15 Hori, Y., Wakebe, H., Tsukamoto, T. & Koga, O. Electrocatalytic Process of CO Selectivity in Electrochemical Reduction of CO_2 at Metal-Electrodes in Aqueous-Media. *Electrochim. Acta* **39**, 1833-1839, (1994).
16 Yamamoto, T., Tryk, D. A., Fujishima, A. & Ohata, H. Production of syngas plus oxygen from CO_2 in a gas-diffusion electrode-based electrolytic cell. *Electrochim. Acta* **47**, 3327-3334, (2002).
17 Delacourt, C., Ridgway, P. L., Kerr, J. B. & Newman, J. Design of an Electrochemical Cell Making Syngas $(CO + H2)$ from CO_2 and H_2O Reduction at Room Temperature. *J. Electrochem. Soc.* **155**, B42-B49, (2008).
18 Dufek, E., Lister, T. & McIlwain, M. Bench-scale electrochemical system for generation of CO and syn-gas. *J. Appl. Electrochem.* **41**, 623-631, (2011).
19 Tornow, C. E., Thorson, M. R., Ma, S., Gewirth, A. A. & Kenis, P. J. A. Nitrogen-Based Catalysts for the Electrochemical Reduction of CO_2 to CO. *J. Am. Chem. Soc.* **134**, 19520-19523, (2012).
20 Salehi-Khojin, A., Jhong, H.-R. M., Rosen, B. A., Zhu, W., Ma, S., Kenis, P. J. A. & Masel, R. I. Nanoparticle Silver Catalysts That Show Enhanced Activity for Carbon Dioxide Electrolysis. *J. Phys. Chem. C* **117**, 1627-1632, (2012).
21 Dufek, E. J., Lister, T. E. & McIlwain, M. E. Influence of Electrolytes and Membranes on Cell Operation for Syn-Gas Production. *Electrochem. Solid-State Lett.* **15**, B48-B50, (2012).
22 Jhong, H.-R. M., Brushett, F. R. & Kenis, P. J. A. The Effects of Catalyst Layer Deposition Methodology on Electrode Performance. *Adv. Energy Mater.* **3**, 589-599, (2013).

23 Thorson, M. R., Siil, K. I. & Kenis, P. J. A. Effect of Cations on the Electrochemical Conversion of CO2 to CO. *J. Electrochem. Soc.* **160**, F69-F74, (2013).
24 Kuhl, K. P., Cave, E. R., Abram, D. N. & Jaramillo, T. F. New insights into the electrochemical reduction of carbon dioxide on metallic copper surfaces. *Energy Environ. Sci.* **5**, 7050-7059, (2012).
25 Ma , S., Lan , Y., Perez, G. M. J., Moniri, S. & Kenis , P. J. A. Silver Supported on Titania as an Active Catalyst for Electrochemical Carbon Dioxide Reduction. *ChemSusChem* **7**, 866-874, (2014).
26 Todoroki, M., Hara, K., Kudo, A. & Sakata, T. Electrochemical reduction of high pressure CO_2 at Pb, Hg and In electrodes in an aqueous $KHCO_3$ solution. *J. Electroanal. Chem.* **394**, 199-203, (1995).
27 Hara, K. & Sakata, T. Large Current Density CO2 Reduction under High Pressure Using Gas Diffusion Electrodes. *Bull. Chem. Soc. Jpn.* **70**, 571-576, (1997).
28 Dufek, E. J., Lister, T. E., Stone, S. G. & McIlwain, M. E. Operation of a Pressurized System for Continuous Reduction of CO_2. *J. Electrochem. Soc.* **159**, F514-F517, (2012).
29 Rosen, B. A., Salehi-Khojin, A., Thorson, M. R., Zhu, W., Whipple, D. T., Kenis, P. J. A. & Masel, R. I. Ionic Liquid–Mediated Selective Conversion of CO_2 to CO at Low Overpotentials. *Science* **334**, 643-644, (2011).
30 Hori, Y. in *Modern Aspects of Electrochemistry* Vol. 42 *Modern Aspects of Electrochemistry* (eds ConstantinosG Vayenas, RalphE White, & MariaE Gamboa-Aldeco) Ch. 3, 89-189 (Springer New York, 2008).
31 Rosen, B. A., Haan, J. L., Mukherjee, P., Braunschweig, B., Zhu, W., Salehi-Khojin, A., Dlott, D. D. & Masel, R. I. In Situ Spectroscopic Examination of a Low Overpotential Pathway for Carbon Dioxide Conversion to Carbon Monoxide. *J. Phys. Chem. C* **116**, 15307-15312, (2012).
32 Furuya, N. & Matsui, K. Electroreduction of carbon dioxide on gas-diffusion electrodes modified by metal phthalocyanines. *Journal of Electroanalytical Chemistry and Interfacial Electrochemistry* **271**, 181-191, (1989).
33 Schwartz, M., Vercauteren, M. E. & Sammells, A. F. Fischer‐Tropsch Electrochemical CO_2 Reduction to Fuels and Chemicals. *J. Electrochem. Soc.* **141**, 3119-3127, (1994).
34 Whipple, D. T., Finke, E. C. & Kenis, P. J. A. Microfluidic Reactor for the Electrochemical Reduction of Carbon Dioxide: The Effect of pH. *Electrochem. Solid-State Lett.* **13**, B109-B111, (2010).
35 Chen, Y., Li, C. W. & Kanan, M. W. Aqueous CO2 Reduction at Very Low Overpotential on Oxide-Derived Au Nanoparticles. *J. Am. Chem. Soc.* **134**, 19969-19972, (2012).
36 Wu, J., Risalvato, F. G., Sharma, P. P., Pellechia, P. J., Ke, F.-S. & Zhou, X.-D. Electrochemical Reduction of Carbon Dioxide: II. Design, Assembly, and Performance of Low Temperature Full Electrochemical Cells. *J. Electrochem. Soc.* **160**, F953-F957, (2013).
37 Park, S., Shao, Y., Liu, J. & Wang, Y. Oxygen electrocatalysts for water electrolyzers and reversible fuel cells: status and perspective. *Energy Environ. Sci.* **5**, 9331-9344, (2012).
38 Lister, T. E. & Dufek, E. J. Chlor-syngas: Coupling of Electrochemical Technologies for Production of Commodity Chemicals. *Energy Fuels* **27**, 4244-4249, (2013).
39 Guerrini, E., Chen, H. & Trasatti, S. Oxygen evolution on aged IrOx /Ti electrodes in alkaline solutions. *J. Solid State Electrochem.* **11**, 939-945, (2007).

40 Carmo, M., Fritz, D. L., Mergel, J. & Stolten, D. A comprehensive review on PEM water electrolysis. *Int. J. Hydrogen Energy* **38**, 4901-4934, (2013).
41 McCrory, C. C. L., Jung, S., Peters, J. C. & Jaramillo, T. F. Benchmarking Heterogeneous Electrocatalysts for the Oxygen Evolution Reaction. *J. Am. Chem. Soc.* **135**, 16977-16987, (2013).
42 Belova, I. D., Varlamova, T. V., Galyamov, B. S., Roginskaya, Y. E., Shifrina, R. R., Prutchenko, S. G., Kaplan, G. I. & Sevostyanov, M. A. The composition, structure and electronic properties of thermally prepared iridium dioxide films. *Mater. Chem. Phys.* **20**, 39-64, (1988).
43 Cruz, J. C., Baglio, V., Siracusano, S., Ornelas, R., Ortiz-Frade, L., Arriaga, L. G., Antonucci, V. & Aricò, A. S. Nanosized IrO_2 electrocatalysts for oxygen evolution reaction in an SPE electrolyzer. *J. Nanopart. Res.* **13**, 1639-1646, (2011).
44 Minguzzi, A., Fan, F.-R. F., Vertova, A., Rondinini, S. & Bard, A. J. Dynamic potential-pH diagrams application to electrocatalysts for water oxidation. *Chem. Sci.* **3**, 217-229, (2012).
45 Elsen, H. A., Monson, C. F. & Majda, M. Effects of Electrodeposition Conditions and Protocol on the Properties of Iridium Oxide pH Sensor Electrodes. *J. Electrochem. Soc.* **156**, F1-F6, (2009).
46 Naughton, M. S., Moradia, A. A. & Kenis, P. J. A. Quantitative Analysis of Single-Electrode Plots to Understand In-Situ Behavior of Individual Electrodes. *J. Electrochem. Soc.* **159**, B761-B769, (2012).
47 Ma, S., Luo, R., Moniri, S., Lan, Y. & Kenis, P. J. A. Efficient electrochemical flow system with improved anode for the conversion of CO_2 to CO. *Supplementary Information*.
48 Song, S., Zhang, H., Ma, X., Shao, Z., Baker, R. T. & Yi, B. Electrochemical investigation of electrocatalysts for the oxygen evolution reaction in PEM water electrolyzers. *Int. J. Hydrogen Energy* **33**, 4955-4961, (2008).
49 Dau, H., Limberg, C., Reier, T., Risch, M., Roggan, S. & Strasser, P. The Mechanism of Water Oxidation: From Electrolysis via Homogeneous to Biological Catalysis. *ChemCatChem* **2**, 724-761, (2010).
50 Lodi, G., Sivieri, E., De Battisti, A. & Trasatti, S. Ruthenium dioxide-based film electrodes. *J. Appl. Electrochem.* **8**, 135-143, (1978).
51 Trasatti, S. Electrocatalysis in the anodic evolution of oxygen and chlorine. *Electrochim. Acta* **29**, 1503-1512, (1984).
52 Bockris, J. O. & Otagawa, T. Mechanism of oxygen evolution on perovskites. *J. Phys. Chem.* **87**, 2960-2971, (1983).
53 Bockris, J. O. M. & Otagawa, T. The Electrocatalysis of Oxygen Evolution on Perovskites. *J. Electrochem. Soc.* **131**, 290-302, (1984).
54 Mehandru, S. P. & Anderson, A. B. Oxygen Evolution on a $SrFeO_3$ Anode: Mechanistic Considerations from Molecular Orbital Theory. *J. Electrochem. Soc.* **136**, 158-166, (1989).
55 Rossmeisl, J., Qu, Z. W., Zhu, H., Kroes, G. J. & Nørskov, J. K. Electrolysis of water on oxide surfaces. *J. Electroanal. Chem.* **607**, 83-89, (2007).
56 Rossmeisl, J., Logadottir, A. & Nørskov, J. K. Electrolysis of water on (oxidized) metal surfaces. *Chem. Phys.* **319**, 178-184, (2005).
57 Gilliam, R. J., Graydon, J. W., Kirk, D. W. & Thorpe, S. J. A review of specific conductivities of potassium hydroxide solutions for various concentrations and temperatures. *Int. J. Hydrogen Energy* **32**, 359-364, (2007).

Chapter 4*

Cu Nanoparticles as Catalyst for Conversion of CO_2 to C2 Products

4.1 Chapter Overview

Electroreduction of CO_2 has potential for storing otherwise wasted intermittent renewable energy, while reducing emission of CO_2 into the atmosphere. Identifying robust and efficient electrocatalysts and associated optimum operating conditions to produce hydrocarbons at high energetic efficiency (low overpotential) remains a challenge. In this study, four Cu nanoparticle catalysts of different morphology and composition (amount of surface oxide) are synthesized and their activities towards CO_2 reduction are characterized in an alkaline electrolyzer. Use of catalysts with large surface roughness results in a combined Faradaic efficiency (46%) for the electroreduction of CO_2 to ethylene and ethanol in combination with current densities of ~200 mA cm^{-2}, a 10-fold increase in performance achieved at much lower overpotential (only < 0.7 V) compared to prior work. Compared to prior work, the high production levels of ethylene and ethanol can be attributed mainly to the use of alkaline electrolyte to improve kinetics and the suppressed evolution of H_2, as well as the application of gas diffusion electrodes covered with active and rough Cu nanoparticles in the electrolyzer. These high performance levels and the gained fundamental understanding on Cu-based catalysts bring electrochemical reduction processes such as presented here closer to practical application.

* Part of this work has been published: Ma, S., Sadakiyo, M., Luo, R., Heima, M., Yamauchi, M. & Kenis, P. J. A. One-step electrosynthesis of ethylene and ethanol from CO_2 in an alkaline electrolyzer. *J. Power Sourc*. 301, 219-228, (2016). Copyright 2016. Reproduced with permission from Elsevier.

4.2 Introduction

Prior work suggests that multiple approaches including switching to renewable energy sources, increasing energy efficiency of buildings, increasing the fuel efficiency of vehicles, and applying underground carbon sequestration need to be implemented at a large scale in order to significantly reduce global CO_2 emissions, which, in turn, may help curb the undesirable effects of climate change.[1-4] Another approach, the electrochemical reduction of CO_2 to various value-added chemicals such as carbon monoxide (CO), formate ($HCOO^-$), methane (CH_4), ethylene (C_2H_4) and alcohols offers promise to suppress CO_2 emissions while it at the same time utilizes excess electrical energy from intermittent renewable sources.[5-8] Of these products, C2 or higher hydrocarbons are preferred over products such as CO because they are either important industrial raw materials or high energy-density fuels.[8,9]

Among the many metal cathode catalysts that have been investigated for reduction of CO_2, Cu is the only metal that catalyzes the production of short hydrocarbons at considerable high Faradaic efficiency (FE).[7-10] However, the overpotentials for hydrocarbon production are usually high (0.7 to 1 V) on Cu electrodes, which reduces the energetic efficiency of the system.[7,11-13] Meanwhile, when using Cu the production rate is quite low under ambient conditions (current density typically less than 35 mA cm^{-2} at cathode potentials positive of –1 V *vs.* RHE).[9,12,14-18] These challenges are mainly due to low catalyst activity as well as lack of ideal electrolysis conditions for this process. More active cathode catalysts as well as optimum electrolysis conditions are needed to make electroreduction of CO_2 a process to be considered as an efficient approach for energy storage from intermittent sources or for the synthesis of chemicals that are used as raw materials at scale.

Recently, significant improvements have been made towards achieving high performance in the reduction of CO_2 on Cu-based electrodes. Several studies have shown that oxide-derived Cu films or cubes exhibit substantial improvement in overpotential and selectivity for CO_2 reduction compared to plain Cu metal catalysts.[12,16,18,19] However, the overpotential for C_2H_4 production is still unacceptably large and the total current densities do not exceed 55 mA cm^{-2} at all applied potentials. A variety of electrolytes has been used, ranging in pH from neutral to alkaline.[20,21] A complication of CO_2 reduction under alkaline conditions is the reaction of KOH with CO_2 to form carbonates. Through the use of CO instead of CO_2 as the reactant, improved selectivity for C_2H_4 or C_2H_5OH formation could be observed under alkaline conditions.[21,22] However, an additional step would be needed to first reduce CO_2 to CO before further reduction of CO, making the whole process more complex while increasing energy consumption. Sammells *et al.* were able to overcome this issue by using a gas diffusion electrode (GDE), covered with Cu particles, to separate a stationary alkaline electrolyte solution (KOH) from the CO_2 reactant.[20] A total current density as high as 400 mA cm^{-2} was obtained to produce a mixture of CH_4 (9.1% FE) and C_2H_4 (69% FE), however, a relatively high cathode potential of -1.98 V *vs.* RHE had to be applied, probably due to the low activity of the Cu particles used.

Here, the efficient electroreduction of CO_2 to C_2H_4 and C_2H_5OH at much lower overpotentials achieved with Cu nanoparticles (CuNPs) with high surface roughness deposited on GDEs in an alkaline flow electrolyzer is reported. Remarkably, Cu catalysts deposited on GDEs exhibited relatively stable performance for four hours under the alkaline condition. Here the effect of morphology (roughness) and the amount of Cu oxides present in the different catalysts on the observed product distribution and current density is investigated. Also, by comparing the performance of the Cu catalysts studied here to the performance of previously reported Cu

catalysts[9,12,14-16,18,23], reasons for the high production of ethylene and ethanol under remarkably mild conditions is elucidated. Based on the observed trends in product distribution a reaction pathway for CO_2 reduction on CuNP catalysts is suggested.

4.3 Experimental

4.3.1 Preparation of CuNP catalysts

Four CuNP catalysts (Cu-1, Cu-2, Cu-3 and Cu-4) were synthesized at an ambient temperature using a solution based method in which solvent composition was varied in the absence or presence of citric acid.[24-26] The reaction solution was prepared by dissolving 3 mmol copper acetate (Wako) in 250 ml solvent. The black precipitates of CuNPs were immediately obtained after the addition of the $NaBH_4$ solution to the reaction solution regardless of the presence of citric acid, an additive known to enhance production of uniform nanoparticles.[27,28] The solvent and additive used for the preparation of each CuNPs are tabulated in **Table 4.1**. Prepared CuNPs were dried in vacuum. For comparison, a commercially available Cu (20–40 nm, Alfa Aesar, Cu-comm) was also used in this study.

Table 4.1 Solvents and additives used for the preparation of Cu nanoparticles.

Samples	Solvent	Additive
Cu-1	2–ethoxyethanol (Wako)	no
Cu-2	water	no
Cu-3	water	citric acid (30 mmol)
Cu-4	2–ethoxyethanol/water (v/v: 50/50)	citric acid (30 mmol)

4.3.2 Physical characterizations

X-ray powder diffraction (XRPD) measurements of the Cu catalysts were performed at room temperature using a Rigaku MiniFlex 600 (λ = 1.54059 Å, Cu-Kα). Lattice constants, crystallite sizes, and weight ratio of each phase in the five samples (Cu-1, Cu-2, Cu-3, Cu-4, and

Cu-comm) were estimated by Rietveld analyses performed using a Topas software package (Bruker AXS Inc.). All patterns were successfully fitted using a combination of simulated patterns for Cu (with the space group of *Fm*-3*m*), Cu_2O (*Pn*-3*m*), and CuO (*C*2/*c*).

X-ray photoelectron spectroscopy (XPS) measurements of the Cu catalysts were performed at ambient temperature using PHI 5000 VersaProbe II (ULVAC-PHI Inc.) with Al-Kα X-ray source.

The morphologies of the Cu samples are examined using transmission electron microscopy (TEM, JOEL 2100 CRYO) operated at 200 kV. The TEM sample was prepared by suspending the catalyst in isopropanol and placing a drop of the suspension onto a holey carbon-coated 200 mesh grid followed by solvent evaporation overnight at room temperature.

4.3.3 Electrolyzer

An electrochemical flow cell reported previously [29-34] is used as the CO_2 electrolyzer. A schematic of the flow cell used in this study is shown in **Figure 4.1**. In this work, an anion exchange membrane (Fumatech®) is inserted between the catholyte and anolyte chamber to prevent the liquid products from diffusing to the anode where they may get oxidized. Stainless steel plates (5.5 × 2.5 cm) serve as current collectors to hold the flow cell together via a squeeze-action toggle plier clamp (McMaster Carr 5062A63) and provide electrical contact between the GDE and an external potentiostat (Autolab, PGSTAT-30, EcoChemie). Two 1.5-mm thick polyether ether ketone (PEEK) spacers with a precisely machined 0.5-cm wide by 2.0-cm long window provide the catholyte and anolyte flow fields, respectively. The cathode current collector has a precisely machined 0.5-cm wide by 2.0-cm long window with 0.5 cm depth behind the GDE to allow for the flow of gases. The anode is open to air, allowing oxygen to escape.

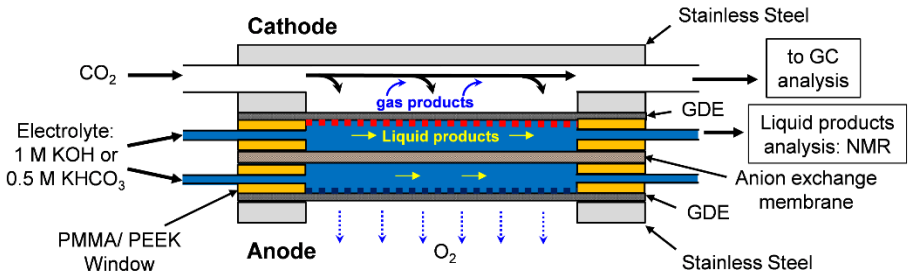

Figure 4.1 Schematic representation of the electrochemical flow cell used in this study. Reprinted with permission from J. Power Sourc. 301, 219-228, (2016). Copyright 2016 Elsevier.

4.3.4 Electrodes preparation

The cathodes were prepared using an air-brush method as previously reported.[33] Cathode catalyst inks were prepared by mixing tetrahydrofuran (200 µL), catalyst (3.4 mg), Nafion® solution (4.4 µL, 5 wt%, Fuel Cell Earth), and isopropyl alcohol (200 µL). The inks were then sonicated (Vibra-Cell ultrasonic processor, Sonics & Materials) for 15 minutes and air-brushed[33] on a gas diffusion layer (GDL, Sigracet 35 BC, Ion Power) to create a GDE covered with catalyst over a geometric area of 2.5 × 0.8 cm^2. A PTFE spacer with a 2.5 × 0.8 cm^2 window was placed on top of GDL during the deposition process to avoid catalyst being deposited outside of the expected area on the GDL. The actual loading was determined by weighing the GDL before and after deposition. The weight loss was found to be on the order of 50% for the air-brushed cathodes since a fraction of the catalyst ended up on the spacer, or was left behind in the air-brush. The anodes were prepared by hand-painting of IrO_2 catalyst inks comprised of Millipore water (200 µL), IrO_2 catalyst (2.5 mg, non-hydrate, Alfa Aesar), Nafion® solution (6.5 µL, 5 wt%, Fuel Cell Earth), and isopropyl alcohol (200 µL) over a geometric area of 1.0 × 2.5 cm^2. Both the cathode and anode loading were determined to be 1.0 ± 0.1 mg cm^{-2}. A fresh cathode was used for each flow cell test.

4.3.5 Electrolysis and product analysis

The flow cell shown in **Figure 4.1** was used to perform the electrolysis of CO_2. A potentiostat (Autolab PGSTAT-30, EcoChemie) was used to control the cell potential (–1.6 V, –1.75 V, –2 V, –2.25 V, –2.5 V, –2.75 V, –3 V, –3.5 V) in the potentiostatic electrolysis mode to measure the activity of each catalyst.[29] For each potential, the cell was allowed to reach steady state, after which the gaseous product stream was analyzed using a gas chromatography (Thermo Finnegan Trace GC). The current at a given condition was obtained by averaging the current over 180 s before stepping to the next potential.

Individual electrode potentials were recorded using multimeters (AMPROBE 15XP-B) connected to each electrode and a reference electrode (Ag/AgCl; RE-5B, BASi) placed in the electrolyte exit stream. 1 M KOH (pH=13.48) or 0.5 M $KHCO_3$ (pH=8.35) was used as the catholyte, while 1 M KOH was used as the anolyte. The measured potentials (*vs.* Ag/AgCl) were converted to the RHE reference scale using E (*vs.* RHE) = E (*vs.* Ag/AgCl) + 0.209 V + 0.0591 V/pH × pH as previously reported.[18,22] The electrode potentials were corrected for iR drop as previously reported.[32,35] A mass flow controller (MASS-FLO®, MKS instrument) was used to set the CO_2 (S.J. Smith Welding Supply) flow rate at 7 SCCM. A syringe pump (PHD 2000, Harvard Apparatus) flowed the electrolyte to minimize boundary layer depletion effects and supply fresh electrolytes thereby helping to maintain the pH on the electrode surface. The flowing stream provides flexibility in operation conditions, minimizes water management issues at the electrodes, and facilitates online sample collection followed by product analysis.[31] The flow rate was set at 0.5 mL min^{-1} when applying cell potentials of –2 to –3.5 V as done previously[31], while a flow rate of 0.1 mL min^{-1} was used for cell potentials between –1.6 and –2 V to increase the concentration of the liquid products at low current density operation conditions. The pH of the electrolyte was

measured using a calibrated pH meter (Thermo Orion, 9106BNWP). A pressure controller (Cole-Parmer, 00268TC) downstream from the cell was used to keep the gas pressure in cell lower than the atmosphere, allowing gas products formed on the catalyst surface of the GDE to leave through the GDE to the gas stream.

Periodically, for product analysis, 1 mL of the effluent gas stream was sampled automatically and diverted into a gas chromatograph (Thermo Finnegan Trace GC) equipped with both the thermal conductivity detection (TCD) and flame ionization detector (FID), with a Carboxen 1000 column (Supelco) and Helium as the carrier gas at a flow rate of 20 SCCM. Meanwhile, the exit catholyte was collected at each applied potential and analyzed using ^{1}H NMR technique reported previously.[17,36,37] 100 µL of the catholyte was mixed with 400 µL D_2O (99.9% deuterium atom, Sigma-Aldrich) and 100 µL of an internal standard consisting of 1.25 mM DMSO (99.98%, Calbiochem) in D_2O. The results presented here are from 32 scans (UI500NB, Varian) after solvent suppression, and processed using the MestReNova software (MestReLab).

For the long-term electrolysis, we controlled the total current in the galvanostatic electrolysis mode. In the galvanostatic mode, the flow cell was tested at total current of –150 mA. Cathode potential was recorded every 15 minutes and products were analyzed every 1 hour.

The onset potential is defined as the lowest cathode potential at which we observe gas products in GC or liquid products from NMR.

The Faradaic efficiency for a specific product is calculated using the same method as shown in Chapter 1. The partial current density for a specific product equals total current density multiplies Faradaic efficiency for this product.

4.3.6 Relative surface roughness measurement

The relative surface roughness factor of each catalyst was determined by the double-layer capacitance[12,38] in a three standard electrode cell with a catalyst-covered 3-mm glassy carbon rotating disk electrode (RDE; Metrohm 6.1204.300) as the working electrode, a Pt gauze (100 mesh, 99.9% metals basis, Sigma-Aldrich, 25*25 mm^2) as the counter electrode, and a Ag/AgCl as the reference electrode (RE-5B, BASi). The cyclic voltammetry (CV) was measured in an Ar-saturated 0.1 M $HClO_4$ aqueous solution. Catalyst ink was prepared using the same method as described above. 4 μL catalyst ink was deposited on the RDE and then dried under flowing Ar. The CV was measured in the potential range of –0.41 to –0.1 V (vs. Ag/AgCl), where only double-layer charging/discharging occurs. The capacitance is the slope from the plot of current density vs. scan rate.

4.4 Results and Discussion

4.4.1 Composition, structure and morphology analysis

XRPD was used to characterize the structure and composition of solid phases formed in the catalysts. The XRPD patterns of the as-synthesized CuNP catalysts Cu-1 to Cu-4 as well as the commercial sample (Cu-comm) are shown in **Figure 4.2a**. All synthesized Cu catalysts are composed of Cu and Cu_2O, but in different relative amounts. The Cu-comm sample also contains a fraction of CuO. The presence of CuO is also evident from the characteristic shake-up peaks at 940 eV and 944 eV [39] in the XPS pattern shown in **Figure 4.2b**. Small shake-up peaks were also found for Cu-2. However, the characteristic peak for CuO is absent in the XRPD pattern for Cu-2, probably because only a very small amount of CuO is present on its surface. Rietveld analysis of the XRPD patterns determined the specific composition and crystallite size of each sample

(results summarized in **Table 4.2,** final fit plots combined in **Figure 4.9** in the SI, *Supporting Information*). Cu-1 and Cu-3 have a lower amount of Cu_2O, while Cu-2 and Cu-4 contain a higher amount of Cu_2O. This result suggests that the use of 2–ethoxyethanol (as used in the synthesis of Cu-1) and citric acid (as used in the synthesis of Cu-3) helps prevent oxidation, while use of a water/2–ethoxyethanol mixture increases the oxidation of Cu. Cu is known to oxidize to Cu_2O under ambient condition[9,39], but the extent of oxidation is affected by the synthetic conditions, as shown in this study. Further analysis of the XRPD data using the Scherrer equation indicates that Cu-3 is composed of smaller crystallites than the other samples, presumably a consequence of the use of citric acid as an additive. In the preparation of Cu-4 citric acid is also used as an additive, resulting in larger crystallites in Cu-4 compared to those in Cu-3. This difference is probably due to the presence of 2–ethoxyethanol in the solvent mixture used for the preparation of Cu-4, with the additional 2–ethoxyethanol decreasing the solubility of citric acid and therefore its dispersion into the solvent during synthesis.

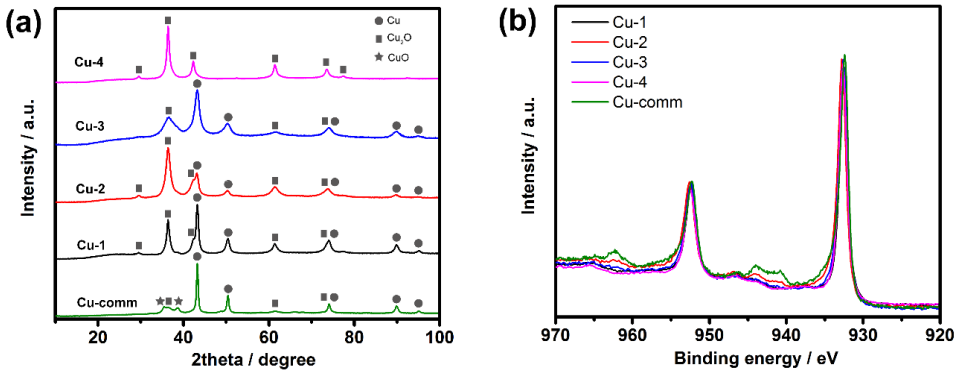

Figure 4.2 (a) XRD patterns of the four synthesized Cu nanoparticles and commercially obtained Cu nanoparticles (Cu-comm); and (b) XPS high resolution scans of the Cu 2p. Reprinted with permission from J. Power Sourc. 301, 219-228, (2016). Copyright 2016 Elsevier.

Table 4.2 Refined parameters of Rietveld analyses for the five samples.

Samples	Lattice parameter (Å)	Crystallite size (nm)	Lattice parameter (Å)	Crystallite size (nm)	R_{wp}	R_p
Cu-1	Cu(fcc): 47.8%		Cu_2O: 52.2%		2.67	1.88
	3.6161 ± 0.0004	15.3 ± 0.2	4.2645 ± 0.0006	10.1 ± 0.1		
Cu-2	Cu(fcc): 13.9%		Cu_2O: 86.1%		2.12	1.64
	3.6251 ± 0.0003	12.3 ± 0.3	4.2705 ± 0.0002	7.2 ± 0.1		
Cu-3	Cu(fcc): 42.8%		Cu_2O: 57.2%		1.94	1.34
	3.6219 ± 0.0009	7.9 ± 0.1	4.242 ± 0.002	3.1 ± 0.1		
Cu-4	Cu(fcc): 2.2%		Cu_2O: 97.8%		2.28	1.64
	3.595 ± 0.003	12.5 ± 2	4.2679 ± 0.0005	11.8 ± 0.1		
Cu-comm	Cu(fcc): 47.6%		Cu_2O: 26.7%		1.88	1.29
	3.6155 ± 0.0002	25.9 ± 0.2	4.2515 ± 0.0009	4.9 ± 0.1		
	CuO: 25.7%					
	a = 4.681 ± 0.003, b = 3.432 ± 0.002, c = 5.133 ±0.004, β = 99.25 ± 0.04°	9.1 ± 0.2				

The morphologies of the five samples were characterized using TEM (**Figure 4.3**). The catalysts exhibited very different morphological features: The Cu-1, Cu-2, and Cu-3 catalysts are comprised of irregular particle shapes with interconnected nanocrystalline networks and grain boundaries, while the Cu-4 and Cu-comm samples mostly feature spherical particles that overlap with each other. TEM histograms of the five Cu catalysts are summarized in **Figure 4.10** in the SI. The particle size of Cu-comm sample is non-uniform, ranging from about 5 nm to 90 nm. In contrast, the particles of the four synthesized catalysts are more uniform and smaller, in the 10–50 nm range. Comparing the TEM results with the XRPD results reveals that the average particle size of Cu-1, Cu-2, and Cu-3 from TEM (~20–30 nm) is significantly bigger than the crystallite size determined from analysis of the XRPD patterns using the Scherrer equation (~5–15 nm). This

discrepancy can probably be attributed to the fact that each particle in Cu-1, Cu-2, and Cu-3 is comprised of several crystallites. For the Cu-comm and Cu-4 samples the particle sizes obtained from TEM are similar to the crystallite sizes obtained from XRPD analysis.

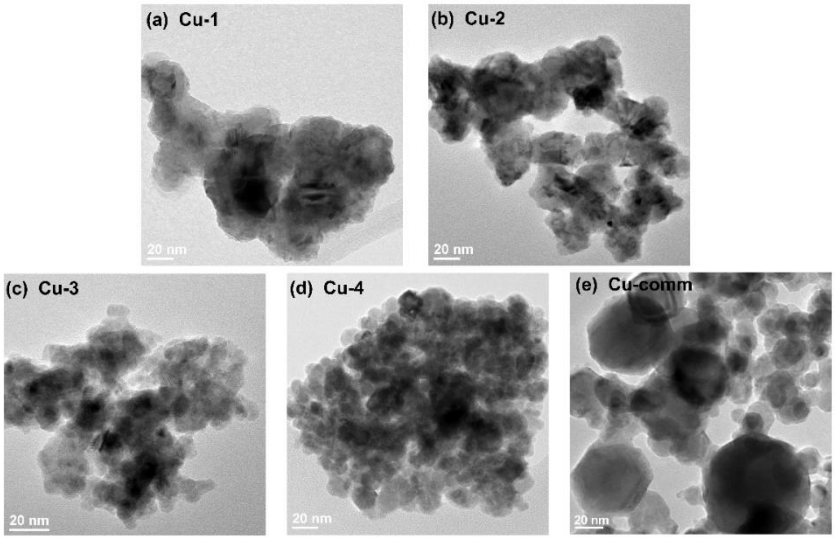

Figure 4.3 TEM micrographs of the Cu catalysts: (a) Cu-1; (b) Cu-2; (c) Cu-3; (d) Cu-4; (e) Cu-comm. Reprinted with permission from J. Power Sourc. 301, 219-228, (2016). Copyright 2016 Elsevier.

The relative surface roughness factor of each catalyst was determined by CV measurement of the double-layer capacitance for each sample. If the surface roughness factor for Cu-comm is assumed to be 1, then the relative surface roughness factors for other Cu catalysts are calculated according to their double-layer capacitances (**Figure 4.11** in the SI). The results of double-layer capacitances as well as the surface roughness factors for all the catalysts (**Table 4.3**) reveal that catalysts Cu-1, 2, 3 have rougher surfaces than catalysts Cu-4 and Cu-comm.

Table 4.3 Capacitance and surface roughness factors for Cu catalysts in this work.

Catalysts	Capacitance (mF)	Surface Roughness Factor
Cu-1	0.57	1.5
Cu-2	0.52	1.4
Cu-3	0.52	1.4
Cu-4	0.43	1.2
Cu-comm	0.37	1

4.4.2 CO_2 electrolysis

The activities of the Cu catalysts towards CO_2 electrolysis were compared in the flow cell described above. Single electrode polarization curves (electrode potentials plotted against the total current density) from each sample measurement are summarized in **Figure 4.4**. All electrode potentials are reported with respect to RHE and are iR-corrected as previously reported.[32] Current densities are calculated based on geometric surface area of the electrode. As shown in **Figure 4.4**, the Cu-1,2,3 catalysts achieve higher total current densities than Cu-4 and Cu-comm, which is in agreement with the measured trends in relative surface roughness: a rougher catalyst surface results in higher total current density.

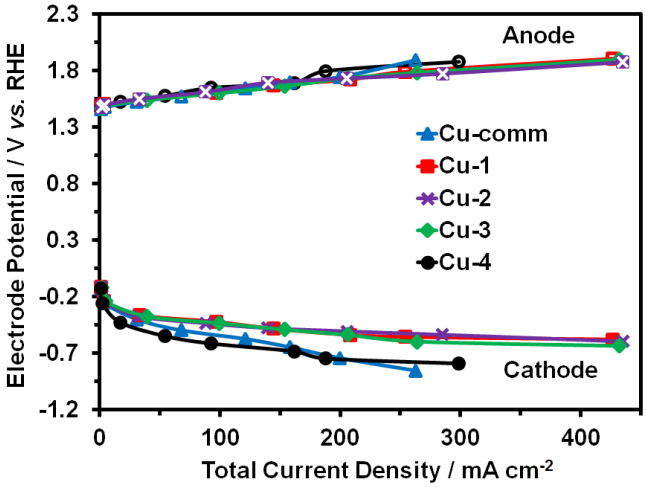

Figure 4.4 iR-corrected single electrode polarization curves of the experiments using five Cu catalysts: Cu-1, Cu-2, Cu-3, Cu-4 and Cu-comm. Electrolyte: 1 M KOH. Reprinted with permission from J. Power Sourc. 301, 219-228, (2016). Copyright 2016 Elsevier.

The FE and partial current density for all major products (CO, H_2, C_2H_4, and C_2H_5OH) using all Cu samples in 1 M KOH are plotted as a function of cathode potential in **Figure 4.5**. **Figure 4.5a** and **4.5c** show that Cu-1, Cu-2, and Cu-3 achieve higher FE for CO and lower FE for H_2 than Cu-4 and Cu-comm. Although Cu-1, Cu-2, and Cu-3 contain different amount of oxides, their FEs for CO and H_2 are almost identical, suggesting that Cu_2O was first reduced to metallic

Cu before CO_2 reduction, similar to previously reported work.[18,19] The effect of the initial amount of oxide in each of the samples on product distribution seems minimal. The differences in selectivity for CO and H_2 observed for the different catalysts probably can be attributed to differences in morphology.

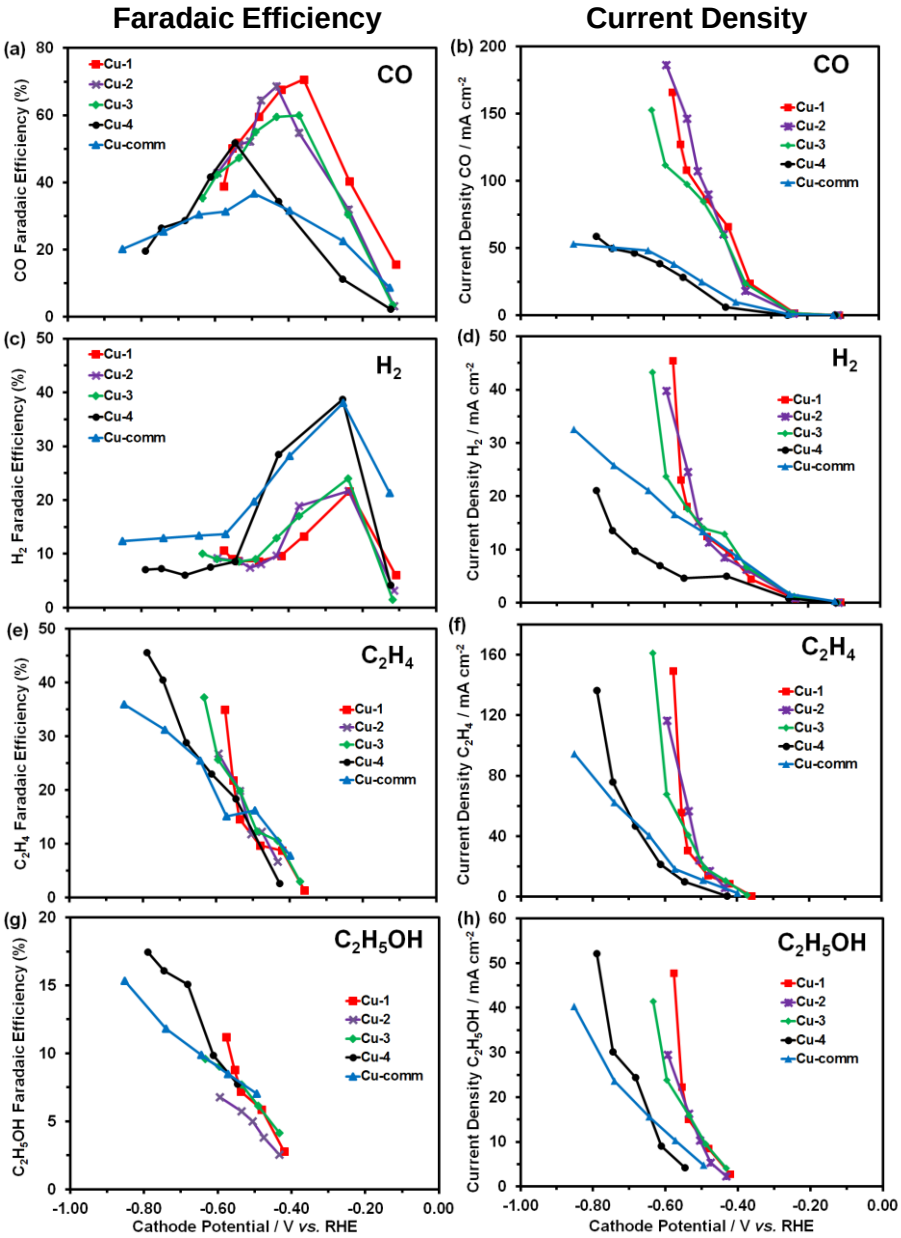

Figure 4.5 Faradaic efficiencies as well as corresponding partial current densities for CO (a,b), H_2 (c,d), C_2H_4 (e,f), and C_2H_5OH (g,h). Electrolyte: 1 M KOH. Each data point represents the average of three measurements. Reprinted with permission from J. Power Sourc. 301, 219-228, (2016). Copyright 2016 Elsevier.

In this study, relatively high FEs and partial current densities for C_2H_4 and C_2H_5OH are achieved at low cathode overpotentials. For all Cu samples, the FEs for C_2H_4 are in the range of 27% to 46% (**Figure 4.5e**), while the FEs for C_2H_5OH are in the range of 7% to 17% (**Figure 4.5g**). The observed significant Faradaic efficiencies for C_2H_4 and C_2H_5OH is probably due to the formation of newly reduced Cu surfaces composed of favorable steps and edges. These steps and edges with under-coordinated Cu atoms are known to be selective for C_2H_4 and C_2H_5OH formation as they promote the adsorption of C1 intermediates and facilitate their dimerization.[9,15,18,19] Compared with polycrystalline Cu foils, rough CuNPs may have a larger concentration of these steps and edges [9], as well as high-index crystal surfaces [7,40], which are favorable for C_2H_4 and C_2H_5OH formation. While similar FEs for C_2H_4 have been reported previously, here these FEs are achieved at overpotentials in the range of 0.66 to 0.87 V, which is at least 0.20 V to 1 V lower than the overpotentials needed to achieve the same FE for C_2H_4 in the aforementioned prior work.[9,14,16,18,20,21,23] The partial current densities for C_2H_4 and C_2H_5OH on the Cu-1 electrode are -150 mA cm^{-2} (**Figure 4.5f**) and -48 mA cm^{-2} (**Figure 4.5h**), respectively, at -0.58 V *vs.* RHE. These values are at least one order of magnitude higher than most previously reported partial current densities for C_2H_4 and C_2H_5OH on Cu electrodes evaluated at similar potentials under ambient conditions.[9,12,14,16-18,23,41] The use of GDEs minimizes CO_2 mass transfer limitations and enables better control of the three-phase interface where the reactions take place. The use of alkaline electrolyte (as opposed to often used neutral electrolytes such as $KHCO_3$ or KCl) minimizes ohmic resistance of the electrolyte. Together, these two factors explain the one order of magnitude improvement in current density. The FEs for C_2H_4 and C_2H_5OH are also similar for all the five Cu catalysts (**Figure 4.5e** and **4.5g**). This is probably due to the formation of similar

amounts of steps and edges with under-coordinated Cu atoms on all five catalysts upon application of the reducing potentials.

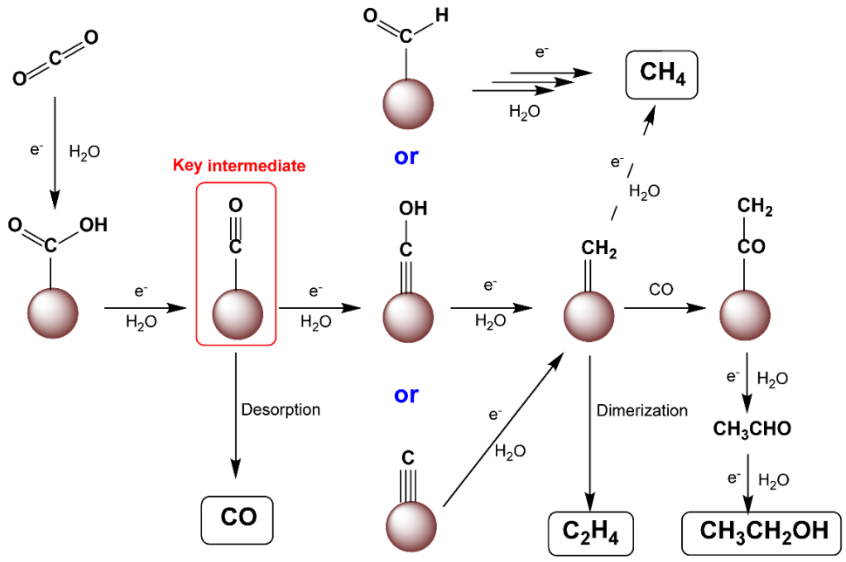

Figure 4.6 Proposed reaction pathway for the CO_2 reduction to various products (mainly C_2H_4 and C_2H_5OH) on Cu nanoparticles. Dashed line with arrows indicates the step that is less likely to happen. Reprinted with permission from J. Power Sourc. 301, 219-228, (2016). Copyright 2016 Elsevier.

For all catalysts, the FE for CO decreased from –0.3 V to –0.5 V, while C_2H_4 and C_2H_5OH started to be produced in the same potential range (**Figure 4.5a, 4.5e,** and **4.5g)**. This trend implies that adsorbed CO is an important intermediate for electroreduction of CO_2 before it is further reduced to hydrocarbons such as C_2H_4 and C_2H_5OH, as suggested previously by others.[7,11,17,42] Based on the high FEs for C2 products observed in this work, as well as information from prior work[17,18,42-44], a possible reaction pathway (**Figure 4.6**) that favors C2 products over CH_4 is proposed. Adsorbed CO is first formed after two steps of proton and electron transfer. Moderately adsorbed CO species then are hydrogenated to adsorbed CHO, COH, or C species, of which CHO is mainly converted to CH_4, while COH and C are mainly converted to C_2H_4 or C_2H_5OH through the dimerization of CH_2 or insertion of CO, respectively. The much lower Faradaic efficiency for

CH_4 (<2%) compared to the Faradaic efficiency for C2 products (~50%) in this study can be explained by the relative low amounts of adsorbed CHO intermediate compared to the amount of adsorbed COH or C intermediates. This proposed pathway lacks direct dimerization of adsorbed CO because prior work suggests that this step is kinetically unfavorable compared with the dimerization of hydrogenated species.[45]

4.4.3 Comparison to prior work

To further study the benefit of alkaline electrolyte, and to allow for better comparison with prior work, we also tested the Cu-1 catalyst using 0.5 M $KHCO_3$ as the catholyte. **Figure 4.7** presents our data obtained using Cu-1 in both 1 M KOH and 0.5 M $KHCO_3$, as well as data sets from previous CO_2 reduction studies that used a Cu-based cathode catalyst.[9,12,14-16,18,23] Most of the previous studies used CuNPs as catalysts in close to neutral electrolytes such as $KHCO_3$, $NaHCO_3$, and $KClO_4$[9,14,15,18,23,46,47], while other studies used oxide-derived Cu materials.[12,16] Specific information on the catalyst, electrolyte and cell configuration in each of the previous reports can be found in **Table 4.4**. An earlier onset is observed for all major products when using Cu-1 in KOH instead of other catalysts and/or electrolytes (**Figure 4.7**). Specifically for hydrocarbon production, Cu-1 exhibits improvements of 140 mV and 80 mV in overpotential for CO_2 reduction to C_2H_4 and C_2H_5OH, respectively, compared to prior data (**Figure 4.7c** and **4.7d**).[12,16] This improvement is probably due to the faster reaction kinetics when using alkaline electrolyte[19,22,32], which is further supported by the fact that conducting the experiment in 0.5 M $KHCO_3$ does not show similar improvements in the onset potential. The FEs observed for H_2 when using Cu-1 in KOH are below 22%, which is much lower than typical levels reported previously (**Figure 4.7b**). However, when using Cu-1 the FEs for H_2 are higher in $KHCO_3$

electrolyte than when using KOH as the electrolyte. This drop in FE for H_2 can be attributed to the much lower H^+ concentration when using alkaline electrolyte.[32] Cu-2, Cu-3, Cu-4 and Cu-comm exhibit similar trends with respect to the suppression of hydrogen evolution when used in $KHCO_3$ *vs.* KOH (data not shown).

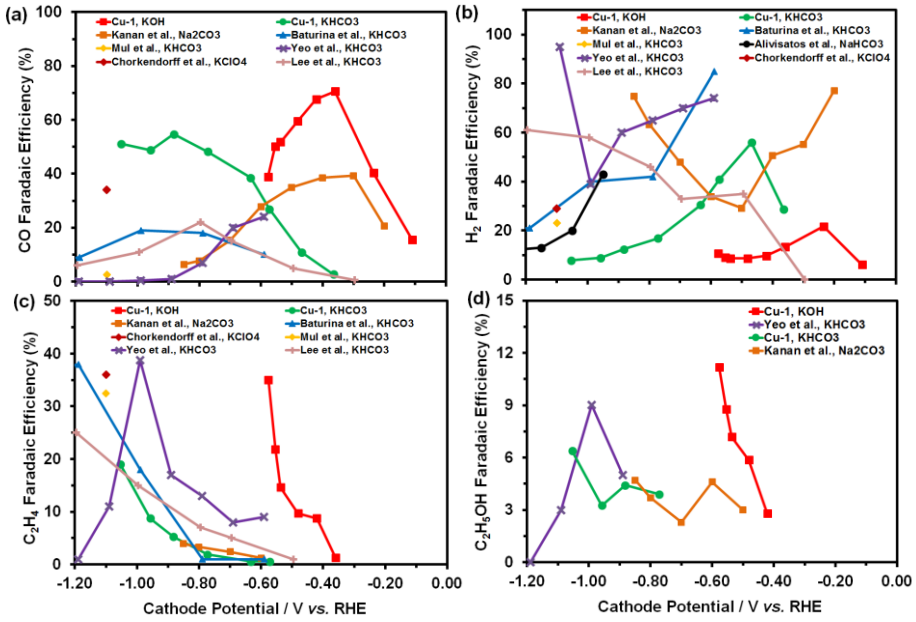

Figure 4.7 The Faradaic efficiencies of this study when using 1 M KOH (red curves) or 0.5 M $KHCO_3$ (green curves) compared to those obtained in prior work using Cu-based cathode catalysts.[9,12,14-16,18,23] Reprinted with permission from J. Power Sourc. 301, 219-228, (2016). Copyright 2016 Elsevier.

Table 4.4 A summary of experimental conditions used in several previous reports of carbon dioxide conversion using copper-based catalysts.

Sample Name	Catalyst	Electrolyte	pH	Cell Configuration	Ref in the main text
Alivisatos *et al.*, $NaHCO_3$	Cu nanoparticle	0.1 M $NaHCO_3$	6.8	Two compartment flow cell	15
Baturina *et al.*, $KHCO_3$	Cu nanoparticle	0.1 M $KHCO_3$	6.8	Standard RDE set-up	23
Chorkendorff *et al.*, $KClO_4$	Cu nanoparticle	0.1 M $KClO_4$	6	Standard 3-electrode cell	9
Kanan *et al.*, Na_2CO_3	Cu_2O derived electrode	0.5 M Na_2CO_3	7.2	Two compartment cell	12
Yeo *et al.*, $KHCO_3$	Cu_2O derived films	0.1 M $KHCO_3$	6.8	Two compartment cell	18
Mul *et al.*, $KHCO_3$	Cu nanoparticle	0.1 M $KHCO_3$	6.8	Standard 3-electrode cell	14
Lee *et al.*, $KHCO_3$	Cu_2O/Cu	0.5 M $KHCO_3$	N.P.	H-type electrolytic cell	16

4.4.4 Durability measurement

The durability of the Cu-1 and the Cu-comm catalysts was also compared under electrolysis conditions (galvanostatic mode, at a constant current of –150 mA). **Figure 4.8** indicates that the cathode potential remains stable for both catalysts over 4-hr electrolysis test. Similarly, only very small changes in product distribution were observed. This data suggest that both Cu-1 and Cu-comm exhibit significant stability under electrolysis conditions, but longer experiments are needed to determine their durability over extended periods of time.

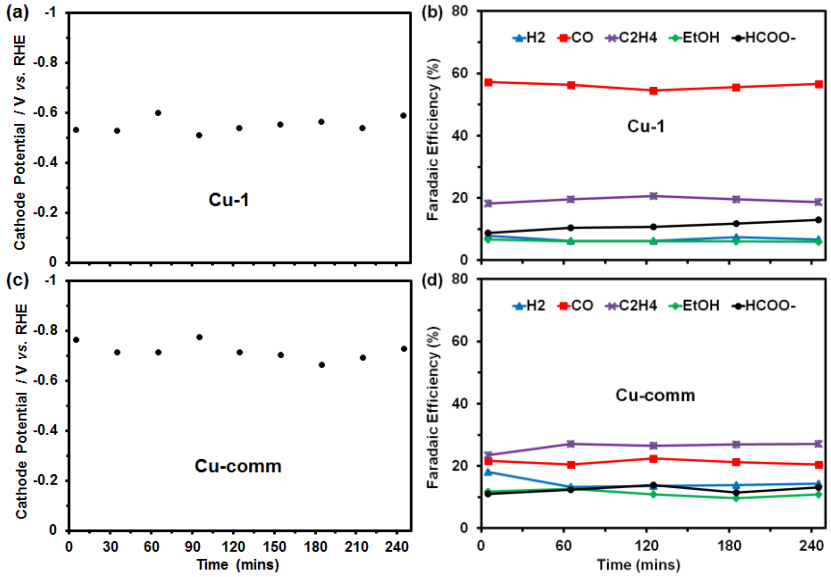

Figure 4.8 (a), (c) Cathode potential and (b), (d) Faradaic efficiency as a function of time when using Cu-1 or Cu-comm as the catalyst in a galvanostatic experiment (current kept contestant at –150 mA) over a total of 4 hours. Reprinted with permission from J. Power Sourc. 301, 219-228, (2016). Copyright 2016 Elsevier.

4.5 Conclusions

In summary, high conversion of CO_2 to C_2H_4 and C_2H_5OH using active CuNP catalysts in a single alkaline electrolyzer is reported in this work. Compared to prior studies, significantly higher partial current densities for C_2H_4 (as high as –150 mA cm^{-2}) and C_2H_5OH (as high as –48 mA cm^{-2}) in combination with lower overpotentials (at least 140 mV lower for C_2H_4 production

and 80 mV lower for C_2H_5OH production) were obtained for the Cu-1 catalyst in alkaline electrolyte. The high current densities are attributed to the use of GDEs covered with high surface roughness Cu catalysts and the use of alkaline electrolyte in the flow cell (lower ohmic resistance), while the decreased overpotential is attributed to the use of active CuNP catalysts in combination with improved kinetics due to the alkaline pH.

Catalyst morphology rather than the amount of surface oxide affects the product distribution. However, whether reconstructing of the catalyst upon applying a reducing potential[48] plays a role in this system is unclear. Further investigations using *in situ* microscopic techniques would potentially reveal structural transformation of the CuNPs under electrolysis conditions. Also, further mechanistic studies, both in an experimental and computational context, could further elucidate the reaction mechanisms and differences in kinetics associated with use of alkaline electrolyte.

4.6 Supporting Information

4.6.1 Fit Rietveld plots for XRPD patterns

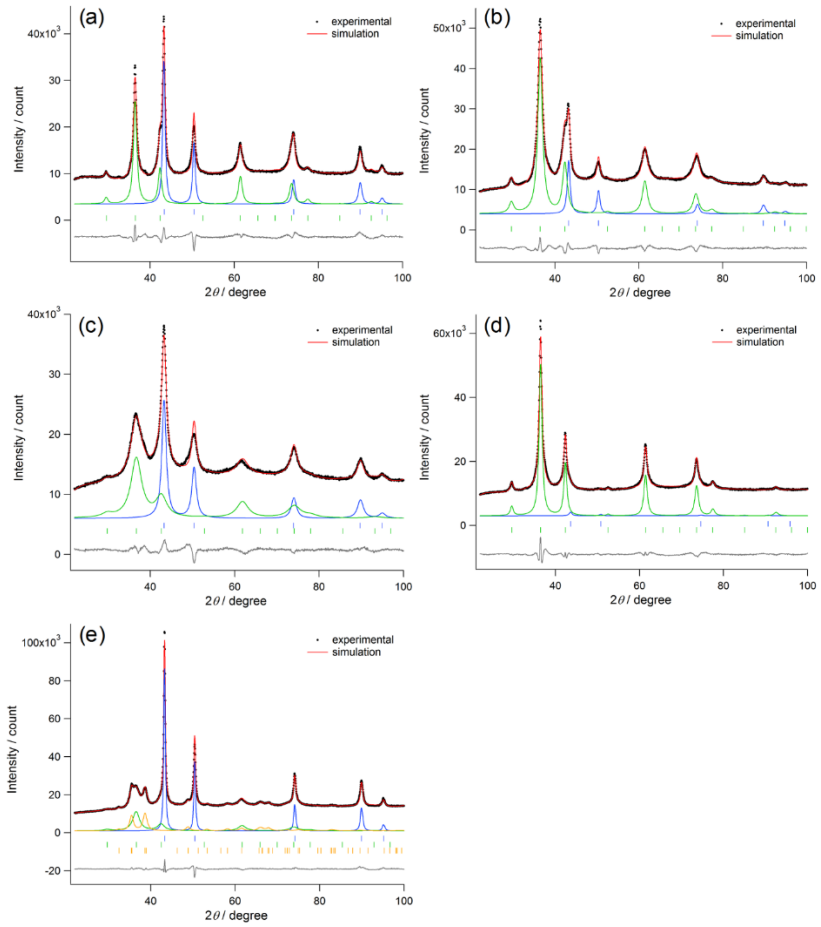

Figure 4.9 Final Rietveld plots for (a) Cu-1, (b) Cu-2, (c) Cu-3, (d) Cu-4, and (e) Cu-comm. Blue, green, and orange colors correspond to the components of simulated patterns for Cu, Cu_2O, and CuO, respectively. Reprinted with permission from J. Power Sourc. 301, 219-228, (2016). Copyright 2016 Elsevier.

4.6.2 TEM histograms

TEM histograms of the Cu particle size distribution from the five Cu samples are shown in **Figure 4.10**. The average Cu particle size of the Cu-1, Cu-2, Cu-3, Cu-4 and Cu-comm catalysts is 26.4 nm, 26.2 nm, 22.8 nm, 15.2 nm, and 25.6 nm, respectively. Both small Cu particles (<20 nm) and large Cu particles (>60 nm) are found in the Cu-comm sample, while for Cu-1,2,3,4 samples, particle size is below 50 nm.

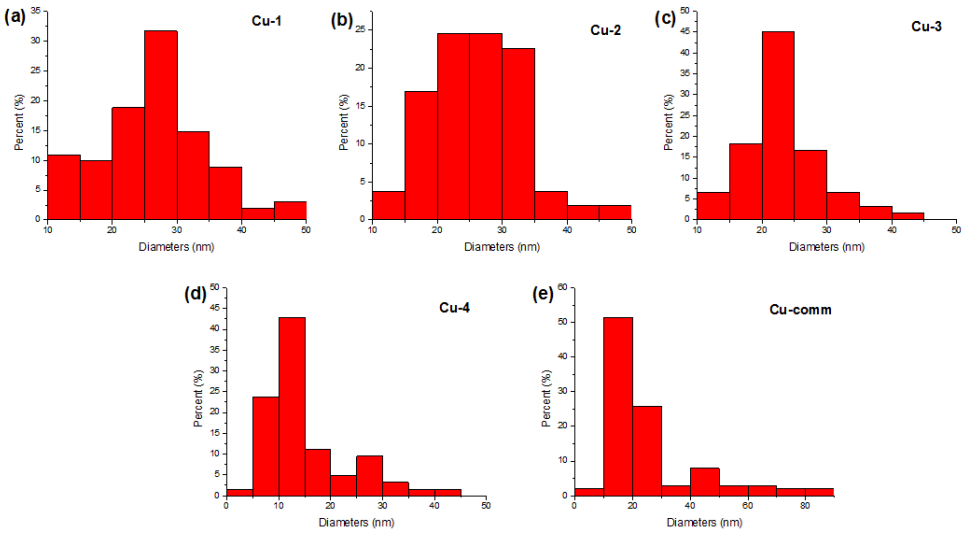

Figure 4.10 TEM histograms of the Cu particle size distribution from (a) Cu-1; (b) Cu-2; (c) Cu-3; (d) Cu-4; (e) Cu-comm. Reprinted with permission from J. Power Sourc. 301, 219-228, (2016). Copyright 2016 Elsevier.

4.6.3 Capacitance determination

Plots of double-layer charge/discharge current density *vs.* scan rate for all five Cu samples.

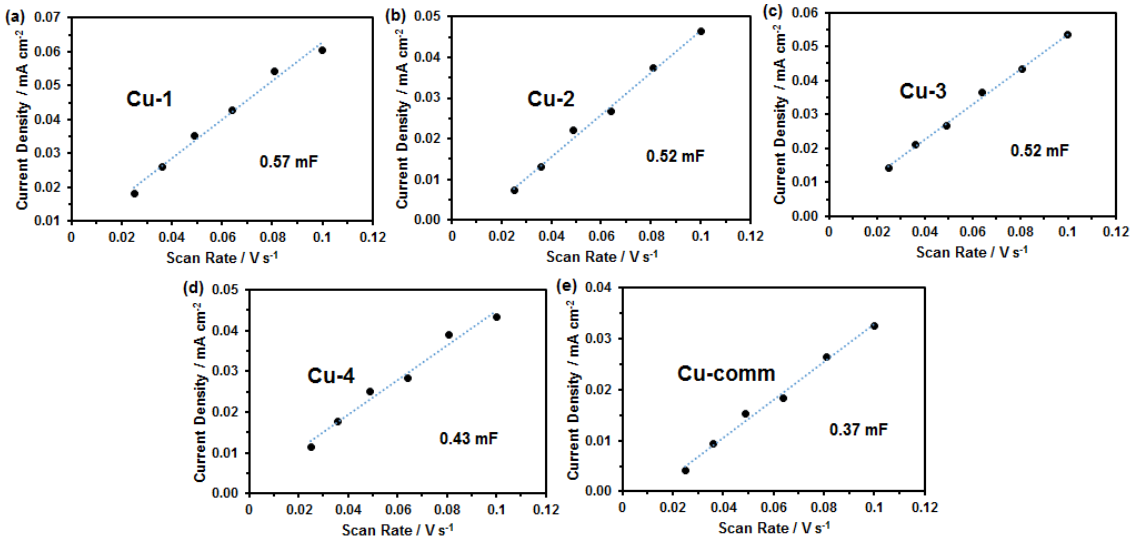

Figure 4.11 Double-layer charge/discharge current density vs. scan rate for various Cu catalysts: (a) Cu-1; (b) Cu-2; (c) Cu-3; (d) Cu-4; (e) Cu-comm. Reprinted with permission from J. Power Sourc. 301, 219-228, (2016). Copyright 2016 Elsevier.

4.7 References

1 Pacala, S. & Socolow, R. Stabilization Wedges: Solving the Climate Problem for the Next 50 Years with Current Technologies. *Science* **305**, 968-972, (2004).

2 Taylor, P. Energy Technology Perspectives *Energy Technology Perspectives* International Energy Agency, (2010).

3 Matsumoto, T., Sadakiyo, M., Ooi, M. L., Kitano, S., Yamamoto, T., Matsumura, S., Kato, K., Takeguchi, T. & Yamauchi, M. CO_2-Free Power Generation on an Iron Group Nanoalloy Catalyst via Selective Oxidation of Ethylene Glycol to Oxalic Acid in Alkaline Media. *Sci. Rep.* **4**, (2014).

4 Watanabe, R., Yamauchi, M., Sadakiyo, M., Abe, R. & Takeguchi, T. CO_2-free electric power circulation via direct charge and discharge using the glycolic acid/oxalic acid redox couple. *Energy Environ. Sci.*, (2015).

5 Jhong, H.-R. M., Ma, S. & Kenis, P. J. A. Electrochemical conversion of CO_2 to useful chemicals: current status, remaining challenges, and future opportunities. *Curr. Opin. Chem. Eng.* **2**, 191-199, (2013).

6 Whipple, D. T. & Kenis, P. J. A. Prospects of CO_2 Utilization via Direct Heterogeneous Electrochemical Reduction. *J. Phys. Chem. Lett.* **1**, 3451-3458, (2010).

7 Hori, Y. in *Modern Aspects of Electrochemistry* Vol. 42 *Modern Aspects of Electrochemistry* (eds ConstantinosG Vayenas, RalphE White, & MariaE Gamboa-Aldeco) Ch. 3, 89-189 (Springer New York, 2008).

8 Gattrell, M., Gupta, N. & Co, A. A review of the aqueous electrochemical reduction of CO_2 to hydrocarbons at copper. *J. Electroanal. Chem.* **594**, 1-19, (2006).

9 Tang, W., Peterson, A. A., Varela, A. S., Jovanov, Z. P., Bech, L., Durand, W. J., Dahl, S., Norskov, J. K. & Chorkendorff, I. The importance of surface morphology in controlling the selectivity of polycrystalline copper for CO_2 electroreduction. *Phys. Chem. Chem. Phys.* **14**, 76-81, (2012).

10 Hori, Y., Wakebe, H., Tsukamoto, T. & Koga, O. Electrocatalytic Process of CO Selectivity in Electrochemical Reduction of CO_2 at Metal-Electrodes in Aqueous-Media. *Electrochim. Acta* **39**, 1833-1839, (1994).

11 Peterson, A. A., Abild-Pedersen, F., Studt, F., Rossmeisl, J. & Norskov, J. K. How copper catalyzes the electroreduction of carbon dioxide into hydrocarbon fuels. *Energy Environ. Sci.* **3**, 1311-1315, (2010).

12 Li, C. W. & Kanan, M. W. CO_2 Reduction at Low Overpotential on Cu Electrodes Resulting from the Reduction of Thick Cu_2O Films. *J. Am. Chem. Soc.* **134**, 7231-7234, (2012).

13 Reske, R., Mistry, H., Behafarid, F., Roldan Cuenya, B. & Strasser, P. Particle Size Effects in the Catalytic Electroreduction of CO_2 on Cu Nanoparticles. *J. Am. Chem. Soc.* **136**, 6978-6986, (2014).

14 Kas, R., Kortlever, R., Milbrat, A., Koper, M. T. M., Mul, G. & Baltrusaitis, J. Electrochemical CO_2 reduction on Cu_2O-derived copper nanoparticles: controlling the catalytic selectivity of hydrocarbons. *Phys. Chem. Chem. Phys.* **16**, 12194-12201, (2014).

15 Manthiram, K., Beberwyck, B. J. & Alivisatos, A. P. Enhanced Electrochemical Methanation of Carbon Dioxide with a Dispersible Nanoscale Copper Catalyst. *J. Am. Chem. Soc.* **136**, 13319-13325, (2014).

16 Kim, D., Lee, S., Ocon, J. D., Jeong, B., Lee, J. K. & Lee, J. Insights into an autonomously formed oxygen-evacuated Cu_2O electrode for the selective production of C_2H_4 from CO_2. *Phys. Chem. Chem. Phys.* **17**, 824-830, (2015).

17 Kuhl, K. P., Cave, E. R., Abram, D. N. & Jaramillo, T. F. New insights into the electrochemical reduction of carbon dioxide on metallic copper surfaces. *Energy Environ. Sci.* **5**, 7050-7059, (2012).

18 Ren, D., Deng, Y., Handoko, A. D., Chen, C. S., Malkhandi, S. & Yeo, B. S. Selective Electrochemical Reduction of Carbon Dioxide to Ethylene and Ethanol on Copper(I) Oxide Catalysts. *ACS Catal.* **5**, 2814-2821, (2015).

19 Roberts, F. S., Kuhl, K. P. & Nilsson, A. High Selectivity for Ethylene from Carbon Dioxide Reduction over Copper Nanocube Electrocatalysts. *Angew. Chem.* **127**, 5268-5271, (2015).

20 Cook, R. L., MacDuff, R. C. & Sammells, A. F. High Rate Gas Phase CO_2 Reduction to Ethylene and Methane Using Gas Diffusion Electrodes. *J. Electrochem. Soc.* **137**, 607-608, (1990).

21 Hori, Y., Murata, A. & Takahashi, R. Formation of hydrocarbons in the electrochemical reduction of carbon dioxide at a copper electrode in aqueous solution. *J. Chem. Soc., Faraday Trans. 1* **85**, 2309-2326, (1989).

22 Li, C. W., Ciston, J. & Kanan, M. W. Electroreduction of carbon monoxide to liquid fuel on oxide-derived nanocrystalline copper. *Nature* **508**, 504-507, (2014).

23 Baturina, O. A., Lu, Q., Padilla, M. A., Xin, L., Li, W., Serov, A., Artyushkova, K., Atanassov, P., Xu, F., Epshteyn, A., Brintlinger, T., Schuette, M. & Collins, G. E. CO_2 Electroreduction to Hydrocarbons on Carbon-Supported Cu Nanoparticles. *ACS Catal.* **4**, 3682-3695, (2014).

24 Yamauchi, M. & Tsukuda, T. Production of an ordered (B2) CuPd nanoalloy by low-temperature annealing under hydrogen atmosphere. *Dalton Trans.* **40**, 4842-4845, (2011).

25 Yamauchi, M., Okubo, K., Tsukuda, T., Kato, K., Takata, M. & Takeda, S. Hydrogen-induced structural transformation of AuCu nanoalloys probed by synchrotron X-ray diffraction techniques. *Nanoscale* **6**, 4067-4071, (2014).

26 Bradley, J. S., Via, G. H., Bonneviot, L. & Hill, E. W. Infrared and EXAFS Study of Compositional Effects in Nanoscale Colloidal Palladium−Copper Alloys. *Chem. Mater.* **8**, 1895-1903, (1996).

27 Maheswari, S., Sridhar, P. & Pitchumani, S. Carbon-Supported Silver as Cathode Electrocatalyst for Alkaline Polymer Electrolyte Membrane Fuel Cells. *Electrocatal* **3**, 13-21, (2012).

28 Guo, J., Hsu, A., Chu, D. & Chen, R. Improving Oxygen Reduction Reaction Activities on Carbon-Supported Ag Nanoparticles in Alkaline Solutions. *J. Phys. Chem. C* **114**, 4324-4330, (2010).

29 Ma , S., Lan , Y., Perez, G. M. J., Moniri, S. & Kenis , P. J. A. Silver Supported on Titania as an Active Catalyst for Electrochemical Carbon Dioxide Reduction. *ChemSusChem* **7**, 866-874, (2014).

30 Tornow, C. E., Thorson, M. R., Ma, S., Gewirth, A. A. & Kenis, P. J. A. Nitrogen-Based Catalysts for the Electrochemical Reduction of CO_2 to CO. *J. Am. Chem. Soc.* **134**, 19520-19523, (2012).

31 Whipple, D. T., Finke, E. C. & Kenis, P. J. A. Microfluidic Reactor for the Electrochemical Reduction of Carbon Dioxide: The Effect of pH. *Electrochem. Solid-State Lett.* **13**, B109-B111, (2010).

32 Ma, S., Luo, R., Moniri, S., Lan, Y. & Kenis, P. J. A. Efficient Electrochemical Flow System with Improved Anode for the Conversion of CO_2 to CO. *J. Electrochem. Soc.* **161**, F1124-F1131, (2014).

33 Jhong, H.-R. M., Brushett, F. R. & Kenis, P. J. A. The Effects of Catalyst Layer Deposition Methodology on Electrode Performance. *Adv. Energy Mater.* **3**, 589-599, (2013).

34 Thorson, M. R., Siil, K. I. & Kenis, P. J. A. Effect of Cations on the Electrochemical Conversion of CO_2 to CO. *J. Electrochem. Soc.* **160**, F69-F74, (2013).

35 Naughton, M. S., Moradia, A. A. & Kenis, P. J. A. Quantitative Analysis of Single-Electrode Plots to Understand In-Situ Behavior of Individual Electrodes. *J. Electrochem. Soc.* **159**, B761-B769, (2012).

36 Wu, J., Risalvato, F. G., Sharma, P. P., Pellechia, P. J., Ke, F.-S. & Zhou, X.-D. Electrochemical Reduction of Carbon Dioxide: II. Design, Assembly, and Performance of Low Temperature Full Electrochemical Cells. *J. Electrochem. Soc.* **160**, F953-F957, (2013).

37 Chen, C. S., Handoko, A. D., Wan, J. H., Ma, L., Ren, D. & Yeo, B. S. Stable and selective electrochemical reduction of carbon dioxide to ethylene on copper mesocrystals. *Catal. Sci. Technol.* **5**, 161-168, (2015).

38 Fan, M., Bai, Z., Zhang, Q., Ma, C., Zhou, X.-D. & Qiao, J. Aqueous CO_2 reduction on morphology controlled CuxO nanocatalysts at low overpotential. *RSC Advances* **4**, 44583-44591, (2014).

39 Yin, M., Wu, C.-K., Lou, Y., Burda, C., Koberstein, J. T., Zhu, Y. & O'Brien, S. Copper Oxide Nanocrystals. *J. Am. Chem. Soc.* **127**, 9506-9511, (2005).

40 Hori, Y., Takahashi, I., Koga, O. & Hoshi, N. Selective Formation of C2 Compounds from Electrochemical Reduction of CO_2 at a Series of Copper Single Crystal Electrodes. *J. Phys. Chem. B* **106**, 15-17, (2001).

41 Sen, S., Liu, D. & Palmore, G. T. R. Electrochemical Reduction of CO_2 at Copper Nanofoams. *ACS Catal.* **4**, 3091-3095, (2014).

42 Schouten, K. J. P., Kwon, Y., van der Ham, C. J. M., Qin, Z. & Koper, M. T. M. A new mechanism for the selectivity to C1 and C2 species in the electrochemical reduction of carbon dioxide on copper electrodes. *Chem. Sci.* **2**, 1902-1909, (2011).

43 Hori, Y., Takahashi, R., Yoshinami, Y. & Murata, A. Electrochemical Reduction of CO at a Copper Electrode. *J. Phys. Chem. B* **101**, 7075-7081, (1997).

44 Kas, R., Kortlever, R., Yılmaz, H., Koper, M. T. M. & Mul, G. Manipulating the Hydrocarbon Selectivity of Copper Nanoparticles in CO_2 Electroreduction by Process Conditions. *ChemElectroChem* **2**, 354-358, (2015).

45 Montoya, J. H., Peterson, A. A. & Nørskov, J. K. Insights into C-C Coupling in CO_2 Electroreduction on Copper Electrodes. *ChemCatChem* **5**, 737-742, (2013).

46 Lan, Y., Gai, C., Kenis, P. J. A. & Lu, J. Electrochemical Reduction of Carbon Dioxide on Cu/CuO Core/Shell Catalysts. *ChemElectroChem* **1**, 1577-1582, (2014).

47 Qiao, J., Fan, M., Fu, Y., Bai, Z., Ma, C., Liu, Y. & Zhou, X.-D. Highly-active copper oxide/copper electrocatalysts induced from hierarchical copper oxide nanospheres for carbon dioxide reduction reaction. *Electrochim. Acta* **153**, 559-565, (2015).

48 Lange, K. J., Sui, P.-C. & Djilali, N. Pore Scale Simulation of Transport and Electrochemical Reactions in Reconstructed PEMFC Catalyst Layers. *J. Electrochem. Soc.* **157**, B1434-B1442, (2010).

Chapter 5*

N-containing Compound for Efficient Reduction of CO_2 to Ethylene

5.1 Chapter Overview

Electrochemical conversion of CO_2 to value-added chemicals has the potential to reduce CO_2 emissions, store otherwise-wasted intermittent renewable energy, and create economic value. Cu is the only known metal catalyst able to reduce CO_2 to hydrocarbons at fairly high Faradaic efficiencies (FEs). However, the FE for C_2H_4 is usually lower than 35%. Finding approaches to increase the FE for the useful C_2H_4 remains a challenge. In this study, four different N-containing ligands are incorporated in Cu electrodes to study how N-containing ligands affect the FE for C_2H_4. We found that the addition of 3,5-diamino-1,2,4-triazole (DAT) into the Cu electrodes exhibits more than 2-fold improvement in the FE for C_2H_4. The FE for C_2H_4 is as high as 56%, and the partial current density for C_2H_4 is as high as 190 mA cm^{-2} at a cathode potential of only 0.84 V_{RHE}. *In situ* Surface-Enhanced Raman Spectroscopy of a Cu electrode in the presence of DAT showed that the addition of DAT induces bending in chemisorbed CO (a necessary precursor for ethylene), blocks adsorption of ethanol and formate species, and provides observable quantities of surface adsorbed ethylene. Overall, this study shows that the incorporation of N-containing ligands in the electrode affects the product distribution for CO_2 reduction on Cu catalysts, therefore providing new insights to design electrocatalysts that improve the selectivity of C_2H_4.

* Adapted with permission from Ma, S.; Schmitt, K. G.; Liu, L.; Chen, R. Y.; Ishihara, T.; Kenis, P. J. A.; Gewirth, A. A. Improved Conversion of CO_2 to C_2H_4 by Electrolysis on Cu with 3,5-Diamino-1,2,4-Triazole. In preparation 2016. This work is performed in collaboration with the Gewirth Group at UIUC, specifically with Kevin G. Schmitt and with Lin Liu (an exchange student from Kyushu University). Collaborator Kevin Schmitt contributed the data presented in Figures 5.5-5.13, Table 5.2, and Table 5.3.

5.2 Introduction

In the past few decades, atmospheric CO_2 levels have increased drastically and reached 400 ppm due to increased human activities and global population, leading to undesired impacts such as global warming, sea level rise, and more erratic weather.[1] Multiple approaches such as switching to renewable energy, enhancing the energy efficiency of buildings and cars, and capturing carbon from point sources have been proposed to curb the rise, and eventually lower atmospheric CO_2 levels.[2] Additionally, the electroreduction of CO_2 to other value-added chemicals provides a pathway to reduce CO_2 emissions and at the same time store otherwise-wasted intermittent renewable electricity in the form of chemical energy.[3-6]

Among various metal catalysts for the electroreduction of CO_2, Cu is the only catalyst explored to be able to reduce CO_2 to ethylene (C_2H_4) at considerable Faradaic efficiencies.[6] However, the Faradaic efficiency of C_2H_4 is still around 30% when using Cu catalysts, which hampers the practical application of this technique. Developing catalysts to improve the selectivity of C_2H_4 at low overpotentials (< 1 V) is necessary to make this process economically viable. Previously, Hori *et al.* found that a single crystal Cu(911) surface could achieve a C_2H_4 FE of 51% at -0.96 V_{RHE}.[7] However, these single crystal electrodes are usually difficult to manufacture and have low surface areas, and thereby are unsuitable for practical applications.[8] Highly dispersed Cu nanoparticles are much better suited for electrolyzer-type applications.[8] Chorkendorff *et al.* reported that Cu nanoparticle covered electrode shows better selectivity to ethylene compared with an electropolished Cu electrode and an argon-sputtered Cu electrode.[9,10] However, the highest FE for C_2H_4 is still around 35% at -1.1 V_{RHE}. Therefore, methods to further improve the FE for C_2H_4 when using Cu nanoparticles are needed. Previously, N-containing electrolytes or solid-state materials have been reported to act as co-catalysts or even catalysts directly to improve the reaction

kinetics and selectivity for a specific product.[11-17] Surface-enhanced Raman spectroscopy (SERS) has been previously used to improve understanding of the CO_2 reduction pathways on Au and Ag electrodes.[13,18] The inclusion of specific nitrogen-containing ligands as additives in the electrolyte was found to improve catalysis for both metals, but by different mechanisms. Like these metals, metallic Cu also has surface plasmon resonance that is excited by visible-wavelength light and can be easily nanostructured. Therefore, SERS is an ideal technique to obtain structural information about CO_2 reduction intermediates, products, and ligands at the Cu surface.

Here, inspired by prior work, N-containing compounds were incorporated into Cu nanoparticle (CuNP) based electrodes to improve the selectivity for C_2H_4. SERS was employed to help correlate mechanistic changes in product formation, particularly the improvement in FE for C_2H_4, to structural changes of Cu surface adsorbates.

5.3 Experimental

5.3.1 Preparation of electrodes composed of Cu nanoparticles and N-containing ligands

Anode gas diffusion electrodes (GDEs) were prepared using a hand-painting method as previously reported.[19] IrO_2 (non-hydrate, Alfa Aesar) was used as the anode catalyst. Anode catalyst inks used for anodes were prepared by mixing Millipore water (200 μL), IrO_2 catalyst (5 mg), Nafion solution (6.5μL, 5 wt%, Fuel Cell Earth) and isopropyl alcohol (200 μL, Macron Fine Chemicals). The mixture was sonicated for 15 mins and painted using a painting brush on a gas diffusion layer (GDL, Sigracet 35BC). The anode loading was determined to be 1.5 ± 0.1 mg cm^{-2}.

The CuNP GDE (control electrode) was prepared by depositing CuNP catalyst ink onto a GDL. The copper nanoparticles (CuNPs) catalyst inks used for cathodes were prepared by mixing

Millipore water (200 μL), CuNPs (5 mg, 20–40 nm, 99.9%, metal basis, Alfa Aesar), Nafion solution (13.0 μL, 5 wt%, Fuel Cell Earth) and isopropyl alcohol (200 μL). The above mixture was sonicated for 15 mins and deposited on a GDL using an automated air-brushing setup as reported previously.[20] The Cu catalyst loading was determined to be 1.1 mg cm^{-2}.

The N-containing ligand-incorporated GDEs were prepared by depositing a mixed catalyst ink of CuNPs and corresponding ligand onto a GDL. The CuNP-DAT (3,5-diamino-1,2,4-triazole, Sigma-Aldrich, 98%), CuNP-PZ (pyrazole, Sigma-Aldrich, 98%) and CuNP-TRZ (1,2,4-triazole, Sigma-Aldrich, 98%) inks were prepared by adding a DAT solution (solvent: mixture of V_{H2O}/V_{IPA}=1/1), a PZ solution (solvent: mixture of V_{H2O}/V_{IPA}=1/1) and a TRZ solution (solvent: mixture of V_{H2O}/V_{IPA}=1/1) into a CuNP ink, respectively. The molar ratio of DAT to CuNPs, PZ to CuNPs and TRZ to CuNPs were controlled at 1:1. The mixture of ligand solution and CuNPs ink was sonicated for another 15mins and then air-brushed onto the GDL. The final loading of Cu on CuNP-DAT, CuNP-PZ, and CuNP-TRZ electrodes was determined to be 1.0 ± 0.1 mg cm^{-2}.

5.3.2 Physical characterization

X-ray photoelectron spectroscopy (XPS) measurements of the Cu catalysts were performed at ambient temperature using Kratos Axis Ultra (Manchester, UK) with a monochromatic Al-Kα X-ray source. GDEs of CuNP-DAT, CuNP-PZ, and CuNP-TRZ before and after flow cell test were characterized directly using XPS. Survey spectra as well as high resolution spectra of Cu 2p and N 1s were obtained. Survey spectra were collected at a pass energy of 160 eV and high resolution spectra were collected using a pass energy of 40 eV. The binding energy of the main C1s peak is adjusted to 284.5 eV.

Scanning electron microscopy (SEM, Hitachi S-4700) was used to observe the surface of GDEs before and after flow cell test. The SEM was operated at 10.0 kV, 15 μA and a working distance of 6.0 mm.

In situ SERS measurements were made using a previously described spectrometer system and 3-electrode cell.[13] The excitation laser was a 632.8 nm He-Ne laser (Meredith Instruments), and the spectral resolution was estimated between 6-7 cm^{-1}. For these experiments, the working electrode was a manually polished polycrystalline Cu disk that was roughened for SERS activity by redox cycling in 0.1 M KCl (≥99.0%, Sigma-Aldrich), as previously described.[21] The counter electrode was Cu wire, and the reference electrode was a "no leak" Ag/AgCl electrode (3.4 M KCl, eDAQ). The potential of this reference was measured against a normal hydrogen electrode prior to each experiment, and the applied potential values are reported with respect to the reversible hydrogen electrode (RHE) based on conversion using the solution pH. For each *in situ* SERS experiment, the potential was stepped in 50 mV increments every 30 s, and an accumulated Raman spectrum was simultaneously acquired from thirty 1 s acquisitions. For clarity, the spectra are shown in each figure at 100 mV increments in the cathodic scan direction, from approximately 0.5 V to -1.0 V *vs.* RHE.

1 M $KHCO_3$ (≥99.5% trace metals basis, Sigma-Aldrich) solutions were prepared with 18.2 MΩ•cm Milli-Q water (Millipore). For control trials without CO_2 using 1 M KOH electrolyte , a saturating quantity of $Ca(OH)_2$ (99.995% trace metals basis, Aldrich) was added to bind excess atmospheric CO_2 as insoluble $CaCO_3$ solid.[22] This was added to the $KHCO_3$ solutions as well to maintain similarity between the two solutions. $HClO_4$ (Ultrex II Ultrapure Reagent, J. T. Baker) was added to the control solutions without CO_2 to provide pH similarity as well (approx. 7.8). For electrolytes containing 3,5-diamino-1,2,4 triazole (DAT, 98%, Aldrich), the DAT concentration

was 10 mM. Each solution was sparged with CO_2 or Ar for at least 30 minutes before use, and was continuously bubbled into the cell during experiments.

5.3.3 CO_2 electrolysis operation and product analysis

The electrochemical flow cell we described previously[23] was used to carry out the CO_2 electrolysis. An anion exchange membrane (Fumatech®) is inserted between the catholyte and anolyte chamber to prevent the liquid products from diffusing to the anode where they may get oxidized. A mass flow controller (MASS-FLO®, MKS instrument) was used to control the CO_2 (S.J. Smith Welding Supply) flow rate at 7 SCCM. A syringe pump (PHD 2000, Harvard Apparatus) was used to control the flow rate of the electrolyte (1 M KOH, pH=13.48). The flow rate was set at 0.5 mL min^{-1} when applying cell potentials of –2.25 V to –3.5 V, while a flow rate of 0.1 mL min^{-1} was used for cell potentials between –1.6 and –2 V to increase the concentration of the liquid products at low current density operation conditions as previously described.[23] A pressure controller (Cole-Parmer, 00268TC) was used to maintain a low gas pressure downstream of the cell, allowing gas products formed on the catalyst surface of the GDE to leave through the GDE to the gas stream. A potentiostat (Autolab PGSTAT-30, EcoChemie) was used to control the cell potential (–1.6 V, –1.75 V, –2 V, –2.25 V, –2.5 V, –2.75 V, –3 V, -3.5 V) in potentiostatic electrolysis mode to measure the performance of each GDE. For each potential, the cell was allowed to reach steady state before the products were collected for analysis. Gaseous products were analyzed using a gas chromatography (Thermo Finnegan Trace GC) equipped with both thermal conductivity detector (TCD) and flame ionization detector (FID). A triple injection was used to average the gaseous product peaks. The liquid products were collected at the exit stream of the electrolyte chamber and analyzed using ^1H NMR technique as reported previously.[24-

[26] 100 μL of the catholyte was mixed with 400 μL D_2O (99.9% deuterium atom, Sigma-Aldrich) and 100 μL of an internal standard consisting of 1.25 mM DMSO (99.98%, Calbiochem) in D_2O. The results presented here are from 32 scans (UI500NB, Varian) after solvent suppression, and processed using the MestReNova software (MestReLab).

Individual electrode potentials were recorded using multimeters (AMPROBE 15XP-B) connected to each electrode and a reference electrode (Ag/AgCl; RE-5B, BASi) placed in the electrolyte exit stream. The measured potentials (*vs.* Ag/AgCl) were converted to the RHE scale using E (*vs.* RHE) = E (*vs.* Ag/AgCl) + 0.209 V + 0.0591 V/pH × pH as previously reported.[24,25] The electrode potentials were corrected for iR drop as previously reported.[18,26]

The onset potential is defined as the lowest cathode potential at which we observe gas products in GC or liquid products from NMR.

The Faradaic efficiency for a specific product is calculated using the same approach as described in Chapter 1. The partial current density for a specific product equals total current density multiplies Faradaic efficiency for this product.

For the durability test, we controlled the total current in the galvanostatic electrolysis mode, in which the flow cell was operated at a total current of –150 mA. Cathode potentials and products were recorded and analyzed every 30 mins at a starting point of 35 mins.

5.4 Results and Discussion

5.4.1 Flow cell electrolysis

Three N-incorporated GDEs: CuNP-DAT, CuNP-PZ, and CuNP-TRZ were prepared by simply mixing CuNP with N-containing ligands (DAT: 3,5-diamino-1,2,4-triazole, PZ: pyrazole, TRZ: 1,2,4-triazole) during the catalyst deposition step (see Experimental section for details). The

activities towards CO_2 electrolysis of the N-incorporated GDEs as well as the GDE with only CuNP were measured in an electrochemical flow reactor as we reported previously.[23] The electrolysis of CO_2 on different electrodes was conducted potentiostatically, in which the overall cell potential was controlled. -3.5 V was the most negative cell potential applied in this study as more negative potentials would produce a large amount of gaseous products in the electrolyte chamber and easily cause flooding of the electrode due to unbalanced gas-liquid pressure.

Figure 5.1 compares the Faradaic efficiencies (FEs) for various major CO_2 reduction products (CO, $HCOO^-$, C_2H_4, C_2H_5OH) when different electrodes were used. For CuNP, the FEs for CO (2-17%), $HCOO^-$ (3-16%), C_2H_4 (0-26%), C_2H_5OH (0-18%) from -0.1 to -1.0 V_{RHE} are similar to previously reported work,[9,26] but at lower overpotentials, likely as a consequence of the use of an alkaline electrolyte that improves reaction kinetics and the use of GDEs that improve mass transfer as described in prior work.[23]

The incorporation of N-containing ligands into the Cu electrode affects the selectivity for different products. Specifically, compared with the CuNP electrode, the electrodes incorporated with N-containing compounds exhibit higher FE for CO (**Figure 5.1a**), but lower FE for $HCOO^-$ (**Figure 5.1b**), which indicates that N-containing compounds may act to inhibit the conversion of CO_2 to $HCOO^-$. Previously, we reported that N-containing compounds may act as co-catalysts to improve the activity of Ag for the CO_2 conversion to CO through promoting weaker CO adsorption.[12,13] Here, the improvement in CO FE after incorporating N-containing compounds into the CuNP electrodes may also stem from changes to Cu-CO interactions by co-adsorbed ligands (as evidenced by SERS results, vide infra).. The proposed formation mechanisms of CO and $HCOO^-$ occur through different reaction pathways, therefore the increase in selectivity for CO may lead to the decrease in selectivity for $HCOO^-$, or vice versa.[6,30] The SERS data also show

adsorption of the DAT ligand, which displaces $HCOO^-$ at the surface. This direct surface blocking may cause the loss of $HCOO^-$ FE.

CuNP-DAT exhibits the highest FE for C_2H_4 (**Figure 5.1c**). At only -0.84 V_{RHE}, the CuNP-DAT achieves a C_2H_4 FE of 56%, which is about 2-fold higher than other electrodes at similar potentials. For example, CuNP only achieves a C_2H_4 FE of 25% at a cathode potential of -0.85 V_{RHE}, whereas CuNP-PZ achieves a C_2H_4 FE of 28% at a cathode potential of -0.80 V_{RHE}, and CuNP-TRZ achieves a C_2H_4 FE of 28% at a cathode potential of -0.88 V_{RHE}. The lower CO FE that was observed in **Figure 5.1a** for CuNP-DAT compared with other N-incorporated electrodes is probably due to the improved conversion of adsorbed CO to C_2H_4. Previously, Sammells *et al*. has reported that a Cu-powder based GDE achieved a C_2H_4 FE of 67%, albeit at a very negative potential of -1.7 V_{RHE}.[31] Mul *et al*.[10] and Chorkendorff *et al*.[9] reported C_2H_4 FEs of 33% and 35% at -1.1 V_{RHE} when using Cu nanoparticles prepared with two different methods. Hori *et al.* reported a C_2H_4 FE of 51% at -0.96 V_{RHE} on a single crystal Cu(911) surface.[7] Compared with these prior research efforts, the C_2H_4 FE level achieved by CuNP-DAT is among the highest, but at the lowest overpotentials.

Figure 5.1d shows that the C_2H_5OH FEs are similar for all electrodes. Usually, a high FE for C_2H_4 will result in a high FE for C_2H_5OH as the production of C_2H_4 and C_2H_5OH is thought to occur through the same C-C coupling pathway.[32,33] However, the high FE for C_2H_4 exhibited by the Cu-DAT electrode does not result in appreciable increased C_2H_5OH production, due to competitive surface adsorption of DAT (vide infra).

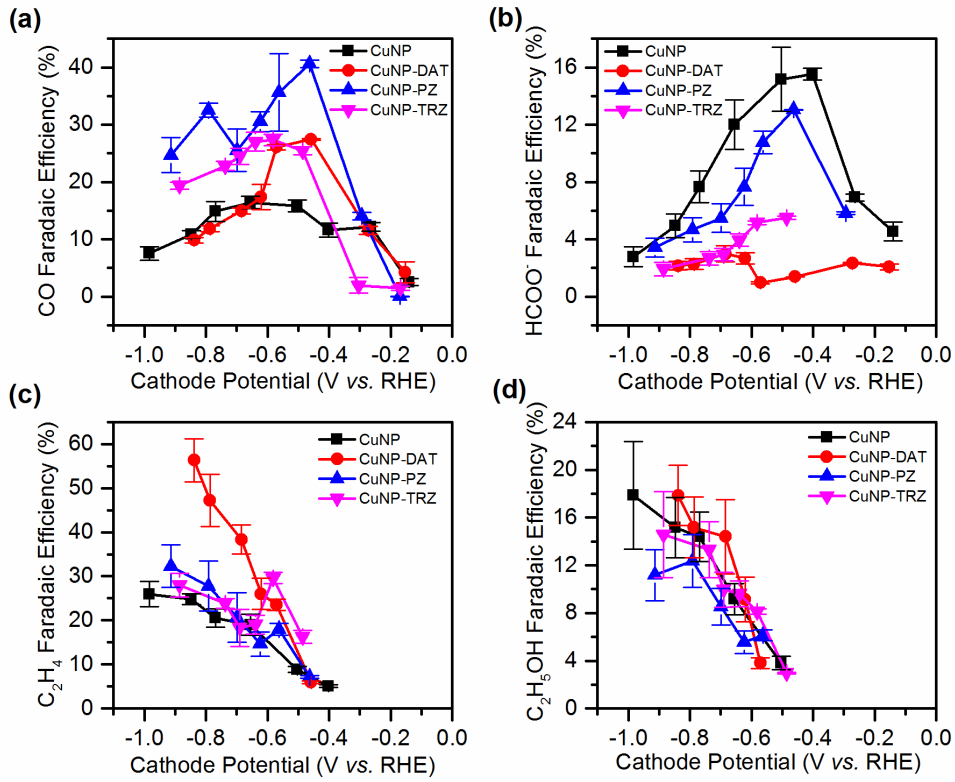

Figure 5.1 Faradaic efficiencies for (a) CO, (b) $HCOO^-$, (c) C_2H_4, and (d) C_2H_5OH using the CuNP electrode and the CuNP electrodes with different N-containing ligands incorporated (CuNP-DAT, CuNP-PZ, CuNP-TRZ).

The incorporation of N-containing compounds improves the total current density at cathode potentials more negative than -0.6 V_{RHE} (Supporting Information, SI, **Figure 5.9**), indicating increased overall rate in the presence of N-containing compounds, especially DAT. The origin of this behavior is likely increased roughness of the electrode following reduction of surface oxides in the presence of DAT (SI, **Figure 5.10**). It is shown that DAT utilized as a deposition additive results in an exceptionally rough (and electrocatalytically active) surface for other electrocatalytic processes.[34]

The partial current densities for various major products, obtained by multiplying the total current density by the product Faradaic efficiency, are shown in **Figure 5.2**. **Figure 5.2** shows a trend similar to that seen in **Figure 5.1**: electrodes incorporated with N-containing ligands exhibit

higher partial current density for CO (**Figure 5.2a**), but lower partial current density for $HCOO^-$ (**Figure 5.2b**) compared with the CuNP electrode. The CuNP-DAT exhibits a partial current density for C_2H_4 production as high as 190 mA cm^{-2} at 0.84 V_{RHE}, which is about two to three-fold higher than other the other electrodes (**Figure 5.2c**). This high level of current density for C_2H_4 is at least one order of magnitude higher than most previously reported partial current densities for C_2H_4 on Cu electrodes evaluated at similar potentials under ambient conditions[9,10,26,27,35] and is similar to the case when more active CuNPs were used on GDEs in an electrochemical flow reactor as we reported previously.[23] The partial current density for C_2H_5OH for CuNP-DAT is slightly higher than for other electrodes (**Figure 5.2d**) despite the similar C_2H_5OH FEs of all the electrodes, which is due to the higher total current density achieved by CuNP-DAT.

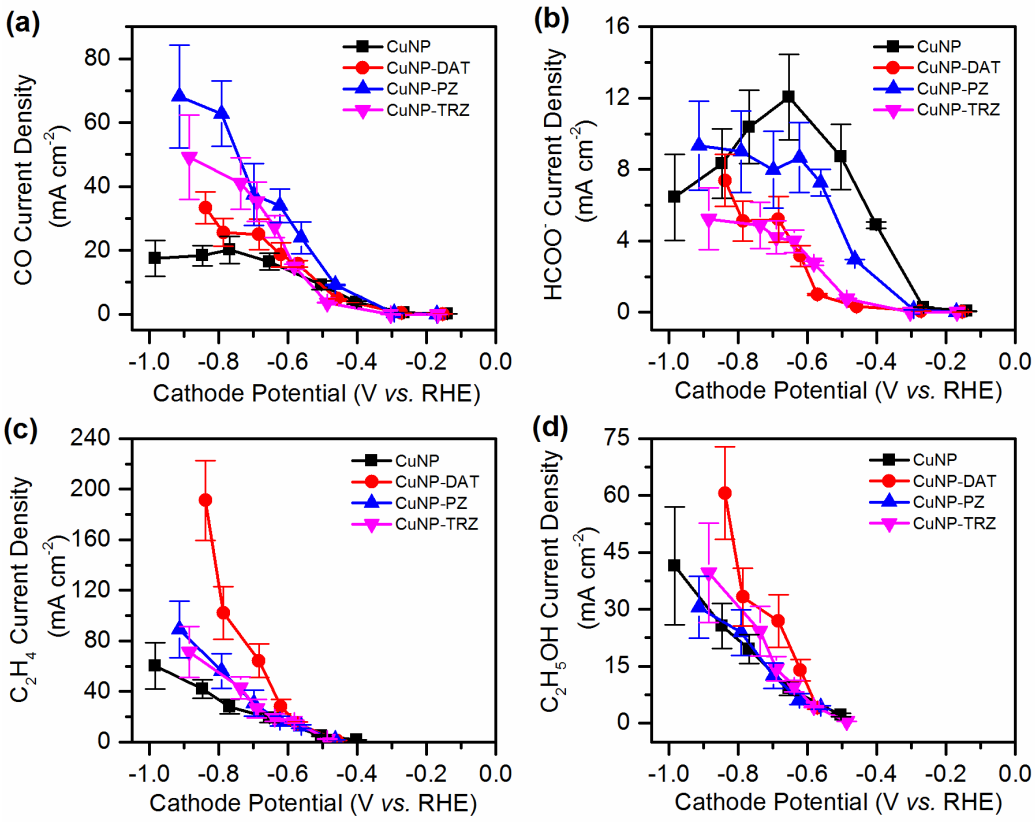

Figure 5.2 Partial current densities for (a) CO, (b) $HCOO^-$, (c) C_2H_4, and (d) C_2H_5OH using CuNPs and CuNPs with different ligands incorporated on electrodes.

Figure 5.3 reports on the durability of the CuNP-DAT electrode under galvanostatic electrolysis conditions (constant current of -150 mA). As shown in **Figure 5.3a**, the cathode potential increased slightly over the 275-min durability test. The FE for CO, C_2H_4 and C_2H_5OH decreased slightly, while the FE for H_2 and $HCOO^-$ increased slightly (**Figure 5.3b**). This change may be due to leaching of some DAT from the electrode surface or incorporation of DAT into the cracks of the electrode, leading to the activity more similar to that exhibited by the bare CuNP electrode (**Figure 5.1**). In particular, the bare CuNP electrode exhibits decreased conversion of CO to C_2 products and increased CO production.

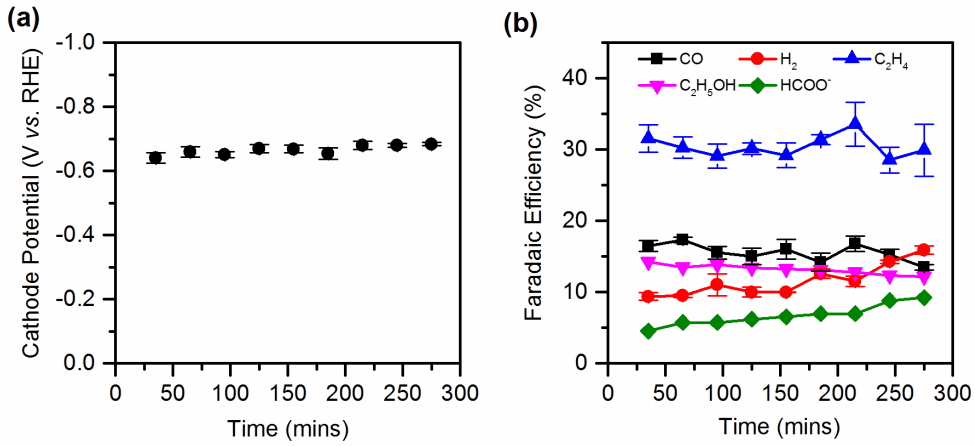

Figure 5.3 (a) Cathode potential and (b) Faradaic efficiency as a function of time when using the Cu-DAT cathode in a galvanostatic experiment (current kept contestant at –150 mA) over a total of 275 minutes.

X-ray Photoelectron Spectroscopy (XPS) was used to analyze the oxidation states of the different electrodes. **Figure 5.4** shows the XPS spectra of CuNP, CuNP-DAT, CuNP-PZ and CuNP-TRZ before CO_2 electrolysis. As shown in **Figure 5.4**, Cu(0)/Cu(I) and Cu(II) exist on the surface of all the electrodes. Adding PZ into the CuNP electrode does not cause any obvious changes in Cu 2p peaks, while adding TRZ or DAT into the CuNP electrode increased the ratio of Cu(II) $2p_{3/2}$ (~935 eV) peak intensity to Cu(0)/Cu(I) $2p_{1/2}$ (953 eV) and $2p_{3/2}$ (932 eV) peak intensities. This observation indicates that DAT forms a stable complex with Cu(II) species,[36-38]

which facilitates the oxidation of Cu(0)/Cu(I) species to Cu (II). The XPS spectra for all electrodes after the electrolysis do not show much difference as compared with the XPS spectra before the electrolysis (data not shown), indicating that Cu(0) formed in situ was oxidized to Cu(I) and Cu(II) when exposed to air after the electrolysis.[9,27] The similar XPS spectra of CuNP-TRZ and CuNP-DAT also explain why CuNP-TRZ rather than CuNP-PZ performs more similarly to CuNP-DAT in terms of Faradaic efficiencies and partial current densities for CO, $HCOO^-$ and C_2H_4. The N concentration on different electrodes before and after the CO_2 electrolysis was analyzed and summarized in **Table 5.1**. For all the N-containing electrodes, the surface N content decreased after the electrolysis, indicating that N-containing compounds leached from the electrode surface, which is in good agreement with the durability results shown in **Figure 5.3**.

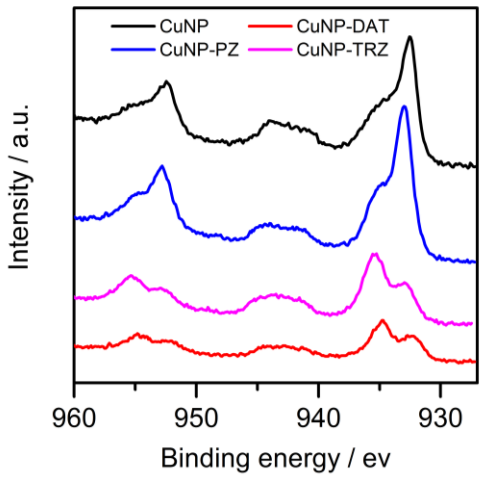

Figure 5.4 High resolution XPS spectra of Cu 2p peaks for different electrodes: CuNP, CuNP-DAT, CuNP-PZ and CuNP-TRZ.

Table 5.1 N content before and after the CO_2 electrolysis from XPS analysis.

Sample	***Remain-N / Original-N***
CuNP-DAT	35.42%
CuNP-PZ	65.85%
CuNP-TRZ	67.02%

5.4.2 SERS identification of surface species

5.4.2.1 CO

Figure 5.5a shows the SER spectra obtained from a solution containing CO_2-sat'd 1 M $KHCO_3$ + sat'd $Ca(OH)_2$ at different applied potentials. At positive potentials, the figure shows the presence of bands at 526 and 624 cm^{-1} (peaks 4 and 5) indicating the presence of Cu_2O.[39] When the potential is decreased, this oxide is reduced near 0.3 V and a new band appears with a significant Stark shift near 364 cm^{-1} (peak 3). This band is associated with the Cu-O stretch associated with adsorbed formate,[40] as will be discussed in the following section. With further reduction to about -0.5 V, new bands appear near 279 and 360 cm^{-1} (peaks 1 and 2) arising from adsorbed CO on Cu. The 279 cm^{-1} band represents the frustrated rotation mode of Cu-CO, and 360 cm^{-1} is the Cu-CO stretch.[41] **Figure 5.5b** shows the corresponding SER spectra for the internal C-O stretching mode. Four bands are observed at 2021, 2063, 2079, and 2093 cm^{-1}, (peaks 6-9, respectively) all of which increase in intensity with applied cathodic potential beyond -0.3 V. These peaks are associated with linear adsorption of CO to atop surface sites.[42] These peaks are consistent with C-O stretching on Cu surfaces previously observed by vibrational spectroscopy,[43-45] although the specific crystalline arrangement of the adsorption sites is unclear. The wide bandwidths and significant peak overlap likely reflects a high degree of disorder on the rough polycrystalline Cu electrode.[46]

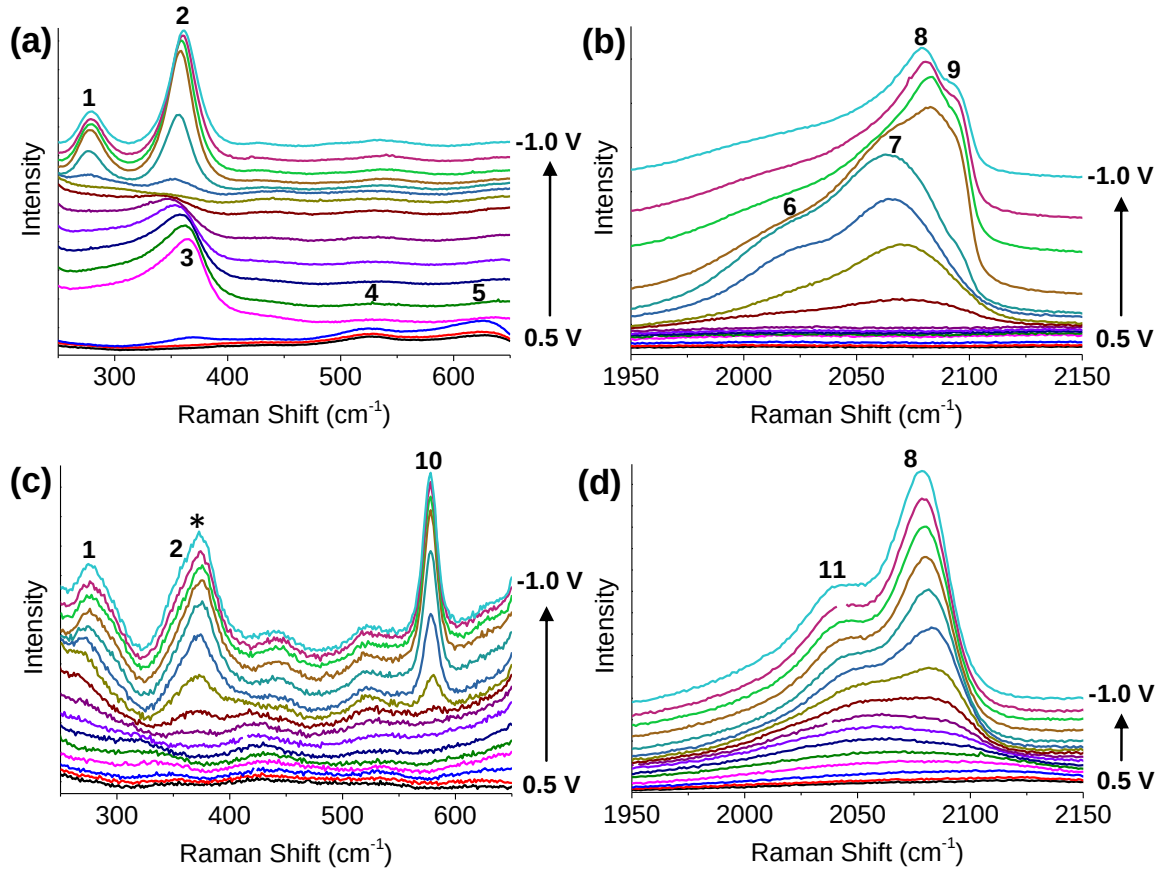

Figure 5.5 *In situ* SER spectra of CO_2 reduction at the Cu electrode surface during cathodic polarization in the Cu-CO [(a) and (c)] and internal C-O [(b) and (d)] stretching regions. The electrolytes were 1 M $KHCO_3$ + sat'd $Ca(OH)_2$ [(a) and (b)] + 10 mM DAT [(c) and (d)]. * denotes modes assigned to DAT. Peak assignments are given in **Table 5.2**.

Table 5.2 Raman mode assignments. ν = stretch, δ = bend, ρ = rock, ω = wag.

Peak	Raman Shift (cm^{-1})	Species	Mode Assignment	Reference
1	279	CO	frustrated ρ(Cu-CO)	41
2	352-360	CO	ν(Cu-CO)	41
3	343-364	$HCOO^-$	ν(Cu-O)	40
4	526	Cu_2O	ν(Cu-O)	39
5	624	Cu_2O	ν(Cu-O)	39
6	2021	CO	ν(C-O)	42-46
7	2063	CO	ν(C-O)	42-46
8	2079	CO	ν(C-O)	42-46
9	2093	CO	ν(C-O)	42-46
10	578	CO	δ(Cu-C-O)	47,48
11	2044	CO	ν(C-O)	42-46
12	691-704	$HCOO^-$	δ(OCO)	49-51
13	745	$HCOO^-$	δ(OCO)	49-51

Table 5.2 (cont.)

14	823	$C_2H_5O_{ads}$	ν_s(C-C) + ν_a(C-O)	50,51
15	845	$C_2H_5O_{ads}$	ν_s(C-C) + ν_a(C-O)	50,51
16	1002	$intermediate_{ads}$	undetermined	45
17	1014	HCO_3^-	ν(C-OH)	52
18	1042	$C_2H_5O_{ads}$	ν_a(C-C) + ν_a(C-O)	53
19	1071	$C_2H_5O_{ads}$	$\rho(CH_3)$ + ν(C-O)	53
20	1129	$intermediate_{ads}$	undetermined	45
21	1297	$intermediate_{ads}$	undetermined	45
22	1359-1378	$HCOO^-$	ν_s(C-O)	49-51
23	1522-1557	$HCOO^-$	ν_a(C-O)	51,54,55
24	1673-1687	HCOOH	ν(C=O)	51,54,55
25	1438	$intermediate_{ads}$	δ(C-H)	56
26	1456	$intermediate_{ads}$	δ(C-H)	56
27	1550	$intermediate_{ads}$	ν(C--O)	56
28	1600	$intermediate_{ads}$	ν(C=C)	56
29	949	C_2H_4	$\omega(CH_2)$	57
30	1258	C_2H_4	$\delta(CH_2)$	57
31	1441	C_2H_4	$\delta(CH_2)$	57,58
32	1530	C_2H_4	ν(C=C)	57,58
33	1645-1654	$intermediate_{ads}$	ν(C=C)	56
34	2850	$C_2H_5O_{ads}$	$\nu_s(CH_2)$	59
35	2873	$HCOO^-$	ν(C-H)	51
36	2903	$C_2H_5O_{ads}$	$\nu_a(CH_3)$	59
37	2930	$HCOO^-$	combination	51
38	2959	$C_2H_5O_{ads}$	$\nu_a(CH_3)$	59

Figures 5.5c and 5.5d shows the corresponding SER spectra obtained from a solution containing CO_2-sat'd 1 M $KHCO_3$ + sat'd $Ca(OH)_2$ + 10 mM DAT. To distinguish peaks in these spectra that result from CO_2 reduction processes from peaks attributable to DAT, control experiments in CO_2-free 1 M KOH + sat'd $Ca(OH)_2$ + 10 mM DAT + $HClO_4$ (to adjust pH ≈ 7.8) were also performed. **Figure 5.11** in the SI includes the experimental spectra for these trials with peak identification of the DAT modes, which are listed in **Table 5.9** in the SI. **Figure 5.12** in the SI compares the SER spectra obtained with and without CO_2 at 0.5 V and -1 V against spectra of complexed AgDAT and neat DAT. AgDAT was used instead of CuDAT because the Raman

spectra of neat samples of prepared CuDAT powder demonstrated too much fluorescence to be a useful standard for comparison. These figures show that at high potentials, DAT adsorbs at the copper surface as a coordination complex of CuDAT. The complete assignment of CuDAT vibrational modes is beyond the scope of this work. As the potential is lowered, DAT dissociates from the Cu surface, but remains close to the surface as a free or physisorbed molecule. This contrasts with DAT behavior on Ag surfaces, where more cathodic potentials resulted in lower DAT peak intensity as DAT was increasingly desorbed.[13]

In **Figure 5.5c**, the peaks associated with Cu_2O and adsorbed formate are now absent, suggesting blockage by competitive adsorption of DAT at these potentials as a Cu-DAT complex (see **Figure 5.12** in the SI). When the potential is lowered beyond -0.3 V, three prominent peaks are observed at 276, 373, and 578 cm^{-1}. Peak 1 (276 cm^{-1}) remains as the Cu-CO frustrated rotation mode from adsorbed CO. The peak at 373 cm^{-1} results from DAT, but the Cu-CO stretching mode (peak 2, 360 cm^{-1}) is likely subsumed beneath this peak as a left shoulder.[41] Peak 10 (578 cm^{-1}) is a new peak that is observed only when the solution contains both CO_2 and DAT. This peak may be assigned to a bending mode of adsorbed CO. Infrared spectroscopy of several metal carbonyl complexes have revealed M-C-O bending vibrations between 468-682 cm^{-1}.[47] Hydrogen bonding by distal histidine to Fe-CO adducts in myoglobin is known to induce Fe-C-O bending vibrations near 570 cm^{-1}.[48] It is possible that hydrogen bonding by DAT, which is observed to remain at the surface even at large cathodic potentials (**Figure 5.11** in the SI), could induce Cu-C-O bending in surface adsorbed CO in a similar fashion.

Figure 5.5d shows spectra obtained for the internal C-O stretching vibration in the presence of DAT. Where four distinct vibration modes were observed without DAT (**Figure 5.5b**), only two bands are now present near 2044 and 2079 cm^{-1}. The peak at 2044 cm^{-1} lies in-between

peaks 6 and 7 in **Figure 5.5b**, and has been given its own assignment as peak 11. The 2079 cm^{-1} peak is in excellent agreement with peak 8 without DAT, and likely results from the same species.

5.4.2.2 $HCOO^-$

Figures 5.6a and 5.6b display the SER spectra obtained from CO_2-sat'd 1 M $KHCO_3$ + sat'd $Ca(OH)_2$ solutions in the intermediate frequency regions. In **Figure 5.6a**, the only major peak (peak 17, 1014 cm^{-1}) at 0.5 V is the C-OH stretch of bicarbonate in the electrolyte.[52] At slightly lower potential, peaks 12, 13, and 22 (691-704, 745, 1359-1378 cm^{-1}, respectively) may be assigned to vibrations from produced formate. These modes correspond to the OCO bending (12-13) and C-O sym. stretching (22) vibrations in adsorbed $HCOO^-$.[49-51] Similar to the Cu-formate stretch observed in **Figure 5.5a**, these modes appear at 0.2 V and their intensities decrease gradually as the potential is lowered. The C-O-O rocking mode expected near 1070 cm^{-1} may be present,[50] but is overshadowed by a very intense peak at the same frequency assignable to adsorbed ethoxy (discussed in the next section). In **Figure 5.6b**, peaks 23 (1522-1557 cm^{-1}) and 24 (1673-1687) also indicate the presence of formate, where 23 is the asy. C-O stretch and 24 represents the C=O stretch in formic acid ligated to a copper surface through the carbonyl.[51,54,55] These formate-related bands also near 0.2 V and gradually decrease in intensity with applied cathodic potential. Notably, many of the observed formate modes possess significant Stark shifts. The large influence of applied potential on vibration frequency suggests direct interaction with the Cu surface.

Figures 5.6c and 5.6d show the corresponding spectra in the presence of DAT. In these figures, most observed bands are assigned to DAT (see **Figure 5.11** in the SI). Formate-related peaks (12, 13, 22, 23, 24) are notably absent. While it is possible for some of these peaks to be

merely subsumed underneath overlapping DAT modes, the decreased FE for $HCOO^-$ (see **Figure 5.1b**) suggests that $HCOO^-$ production is strongly inhibited by adsorption of the DAT. Moreover, peak 3 (Cu-formate stretching, **Figure 5.5a**) is also absent when DAT is added (**Figure 5.5c**).

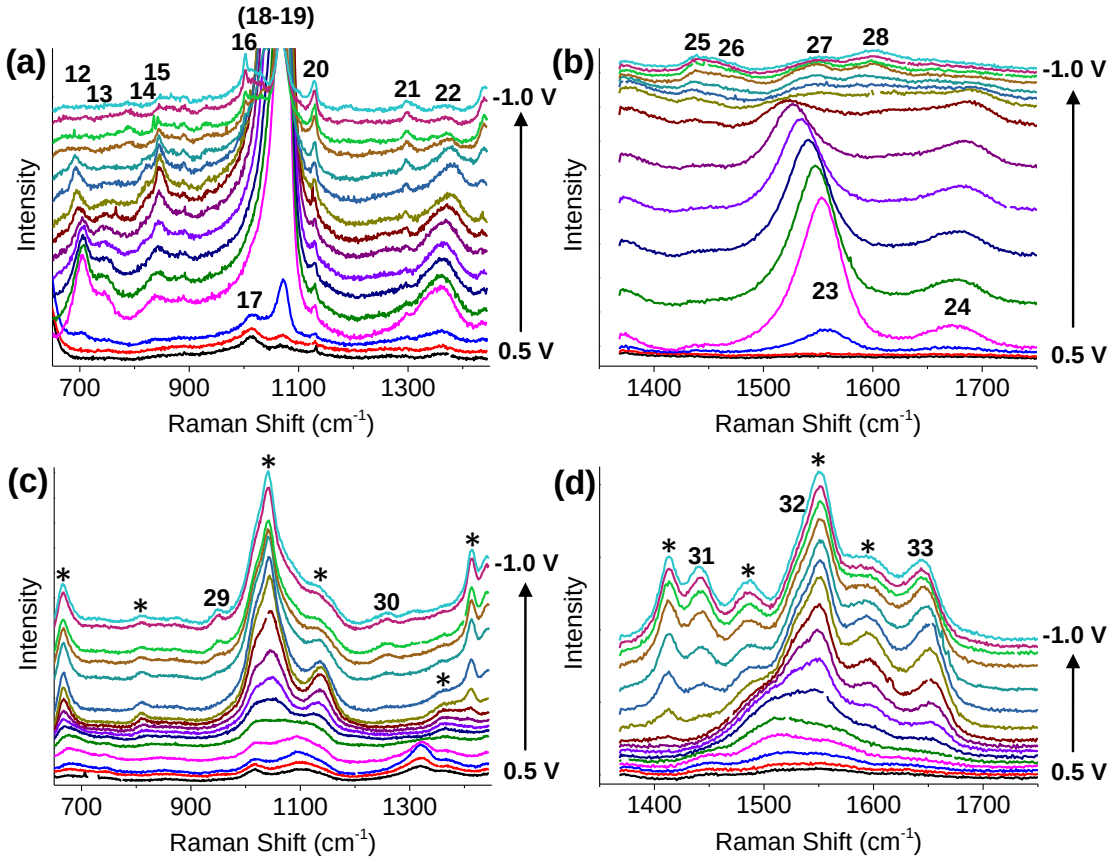

Figure 5.6 *In situ* SER spectra of CO_2 reduction at the Cu electrode surface during cathodic polarization in the regions of formate and ethoxy vibrations. The electrolytes were 1 M $KHCO_3$ + sat'd $Ca(OH)_2$ [(a) and (b)] + 10 mM DAT [(c) and (d)]. * denotes modes assigned to DAT. Peak assignments are given in **Table 5.2**.

5.4.2.3 C_2H_5OH

Figure 5.6a also contains several other SERS peaks in addition to those already assigned to formate. These are assigned to vibrations of adsorbed ethoxy, as an intermediate in the production of ethanol. The most intense peaks near 1042 and 1070 cm^{-1} (18 and 19, respectively) are cropped in **Figure 5.6a** so that the other bands may be seen, but they are presented in full in

Figure 5.13 in the SI. These broad bands likely result from asy. C-C + C-O stretching (18) and CH_3 rocking + C-O stretching vibrations (19) in surface-adsorbed ethoxy.[53] The smaller peaks at 823 and 845 cm^{-1} peaks (14 and 15, respectively) may also be associated with ethoxy, as they display growth and decay in their intensities similar to the larger peaks 18 and 19. These modes are tentatively assigned to the C-C + C-O sym. stretching in adsorbed ethoxy, with significant redshifting from the observed frequency on Cu(100) in UHV studies near 870 cm^{-1} perhaps due to influences of solvent and a polycrystalline substrate.[59,60] These four ethoxy-related modes demonstrate peak intensity growth from 0.2 V to -0.3 V, followed by decay until approximately -0.8 V.

In addition, **Figure 5.6a** has three smaller bands observed at 1002, 1129, and 1297 cm^{-1} (peaks 16, 20, 21, respectively) and for which specific vibrational assignments are unclear. However, these peaks are among those previously observed by SERS of CO_2 reduction on Cu, that were assigned to an intermediate species with C-H, C=O, and C=C bonds.[45] In **Figure 5.6b**, concurrent bands appear at 1438, 1456, 1550, and 1600 cm^{-1} (peaks 25-28). These peaks exhibit similar intensity growth with cathodic potential, and their frequencies coincide with the frequencies expected for C-H bends, C--O stretches, and C=C stretches.[56] The relative intensities of all these peaks generally increase with cathodic potential, with the greatest intensity occurring at the most negative potentials between -0.5 and -1 V. Taken together, these seven peaks likely represent surface-bound intermediates that, like CO, have greater quantity and/or stability at negative potentials where formate and ethoxy are largely desorbed.

5.4.2.4 C_2H_4

Figures 5.6c and **5.6d** again demonstrate that the adsorption of DAT displaces the major bands of formate, ethoxy, and other intermediates. However, a few new bands are now apparent in presence of DAT, but which are not ascribed to DAT modes. Previous studies of vibrational spectroscopy of ethylene adsorption indicate that these modes may result from adsorbed ethylene or ethylene-like intermediates on Cu.[57,58,61] Peak 29 (949 cm^{-1}) likely represents a CH_2 wagging mode, and peak 30 (1258 cm^{-1}) represents the CH_2 scissor bend in chemisorbed C_2H_4.[57] These two peaks appear near -0.5 to -0.6 V and increase in intensity with cathodic potential. Likewise, peaks 31, 32, and 33 in **Figure 5.6d** also demonstrate increased growth with cathodic potential. However, these bands possess higher intensity and can be observed with onsets as early as 0 V. Peak 31 (1441 cm^{-1}) is assigned to the CH_2 scissor bend in physisorbed C_2H_4, and peak 32 (1530 cm^{-1}) denotes a C=C stretch.[57,58] Finally, peak 33 (1645-1654) appears at a higher frequency than expected for even free gaseous ethylene (1623 cm^{-1}),[62] suggesting that this band may be produced by an intermediate species containing C=C bonds which has not been fully reduced.[56]

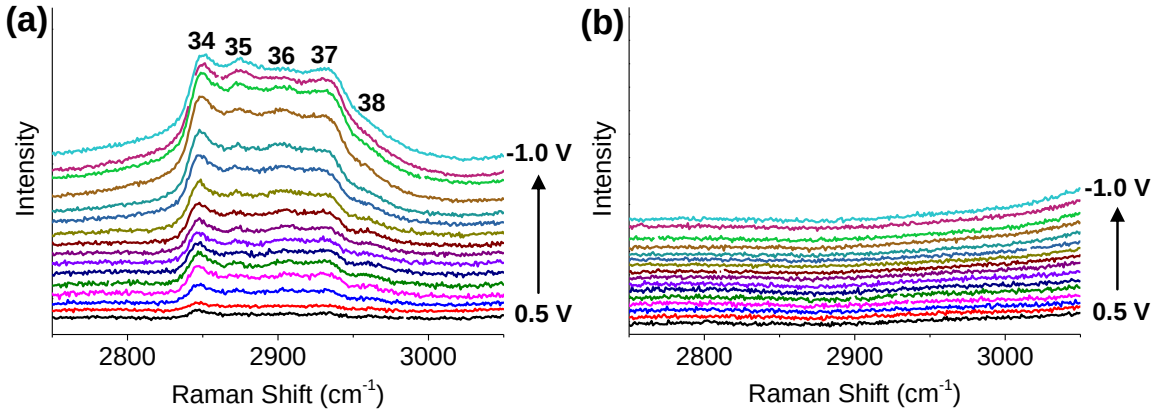

Figure 5.7 *In situ* SER spectra of CO_2 reduction at the Cu electrode surface during cathodic polarization in the C-H stretching region. The electrolyte was 1 M $KHCO_3$ + sat'd $Ca(OH)_2$ (a) and 1 M $KHCO_3$ + sat'd $Ca(OH)_2$ + 10 mM DAT (b). Peak assignments are given in **Table 5.2**.

Figure 5.7a shows the SER spectra in the region of C-H stretching vibrations for the CO_2-sat'd solution containing 1 M $KHCO_3$ + sat'd $Ca(OH)_2$ without DAT. Multiple C-H stretching modes are present with a large degree of peak overlap. We tentatively assign three peaks (34, 36, and 38) to the vibrational modes in adsorbed ethoxy (2850 cm^{-1} CH_2 sym. str., 2903 cm^{-1} CH_3 sym. str., and 2959 cm^{-1} CH_3 asy. str., respectively)[59] and two peaks (35 and 37) to adsorbed formate (2873 cm^{-1} C-H stretch, and 2930 cm^{-1} combination mode, respectively).[51] However, there may unidentified intermediate species contributing peak intensity in this region as well. These peaks show increased intensity with applied cathodic current, suggesting increasing formation of CH-containing products at larger overpotentials. This steady increase in intensity differs from the potential dependence observed for most other lower frequency modes, possibly indicating differences in molecular orientation or transitions from chemisorption to physisorption at very negative potentials.

Figure 5.7b shows the corresponding spectra in the presence of 10 mM DAT. Here, there are no observable C-H stretching modes at any applied potential. The competing adsorption of DAT at these potentials (vide supra) likely inhibits significant adsorption of formate or ethoxy species. Therefore, the addition of DAT may promote the formation of ethylene, which is able to leave the surface more quickly, over ethanol, which would remain on the surface during multiple proton and electron transfer steps.[30]

5.4.3 Discussion

The combination of GC and SERS techniques provides a robust method with which to study the product distribution of the CO_2 reduction reaction and the influence of DAT. In the absence of DAT, the SER spectra above show selective adsorption of CO_2-reduction species which

demonstrate significant dependence on the Cu electrode potential. **Figure 5.8** shows how the normalized Raman intensity changes with potential for each observable product or intermediate. For clarity, one peak is chosen to represent each class of surface species.

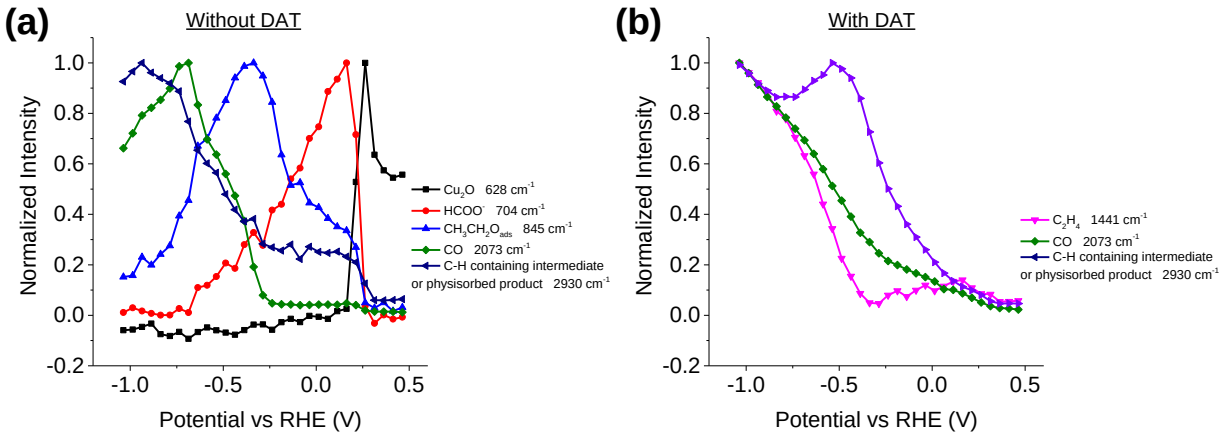

Figure 5.8 Baseline-corrected, relative SERS intensity as a function of cathodic scan potential for CO_2 reduction species. The electrolyte was 1 M $KHCO_3$ + sat'd $Ca(OH)_2$ (a) and 1 M $KHCO_3$ + sat'd $Ca(OH)_2$ + 10 mM DAT (b).

Figure 5.8a shows that near 0.5 V, the predominant surface species is Cu_2O. The oxide is soon removed as the potential is decreased near 0.25 V, allowing for CO_2 surface adsorption and reduction. Between 0.25 V and -0.2 V, chemisorbed formate is the major products. Further reduction between 0 and -0.5 V shifts the majority species to ethoxy, and the onset of significant CO adsorption begins at -0.3 V. The intensity of adsorbed CO then increases until approx. -0.7 V, and decreases slightly until -1 V. The intensities of C-H stretching modes that represent physisorbed ethanol/formate products and/or reduction intermediates rises with cathodic potential below 0.25 V, and increases significantly with the increase of CO intensity. This change in product speciation with changing potential is consistent with that observed in the GC results (vide supra). Formate is preferentially produced at lesser overpotentials, and ethanol and ethylene are preferred at larger overpotentials. However, at the most negative potentials, these species are displaced by

significant adsorption of CO, which is both an intermediate to these three species and the fourth major product.

Figure 5.8b shows that only ethylene and CO modes are observed in the in the presence of DAT. The lack of ethoxy and formate associated modes between approx. 0.2 and -0.7 V suggests that strong Cu-DAT coordination is capable of blocking adsorption of these CO_2 reduction products.

There are several possible ways in which DAT could catalyze the formation of ethylene. The appearance of Cu-C-O bending and the alteration of C-O stretching vibrations in the presence of DAT suggest that DAT influences the geometric and/or electronic environment around adsorbed CO. This effect could influence the rate of C-C coupling processes, which has been proposed as the rate determining step for the generation of ethylene and ethanol.[30] Formation of ethylene from adsorbed CO requires at least two fewer coupled proton-electron transfer steps relative to ethanol. Thus, residence time of adsorbed species on the surface must be higher in the case of ethanol relative to ethylene. Competitive adsorption of DAT for surface sites may therefore favor ethylene production over ethanol.

Moreover, by inhibiting the production of formate by competitive adsorption, DAT may also remove $HCOO^-$ as a source of influence over distribution of later products. It has been previously observed that formic acid can catalyze certain reactions that may be influential during CO_2 reduction, such as ketene hydrolysis[63] and keto-enol tautomerizations.[64] The presence of formic acid might affect the surface-bound reduction intermediates,[30] and alter the overall product distribution. By strongly inhibiting the generation of formate, DAT could then indirectly influence the formation rate and amount of various products. The improvement in the rate of ethylene production by DAT relative to PZ or TRZ reflects the weaker adsorption of DAT on the Cu surface,

and the ability of the DAT molecule to leave open sites where ethylene production may occur. **Table 5.1** shows that both PZ and TRZ are more strongly adsorbed and consequently lead to preferential CO production relative to ethylene.

5.5 Conclusions

In summary, this work studies how three different nitrogen-containing compounds affect the product distribution for the electroreduction of CO_2 on Cu-based electrodes. Compared to other N-containing compounds such as PZ and TRZ, DAT exhibit significant improvement in the selectivity to ethylene. The Faradaic efficiency for ethylene on the DAT incorporated electrode is more than twofold higher than the Faradaic efficiency achieved on other electrodes. The partial current density for ethylene is as high as 190 mA cm^{-2} with a Faradaic efficiency of 56% at only -0.8 V_{RHE}. *In situ* surface-enhanced Raman spectroscopy indicates that the improved selectivity for ethylene with incorporated DAT is due to competition for surface adsorption sites between DAT and ethoxy and formate, as well as influencing the surface adsorption of CO. Inducing Cu-CO bending may help to achieve faster kinetics of C-C coupling, a key step in the formation of C_2 products.

5.6 Supporting Information

5.6.1 Single electrode polarization curve

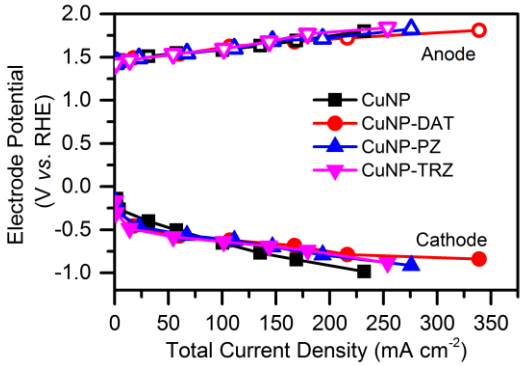

Figure 5.9 Single electrode polarization curves of the experiments using four Cu electrodes: CuNP, CuNP-DAT, CuNP-PZ and CuNP-TRZ.

5.6.2 SEM images of electrodes before and after the flow cell test

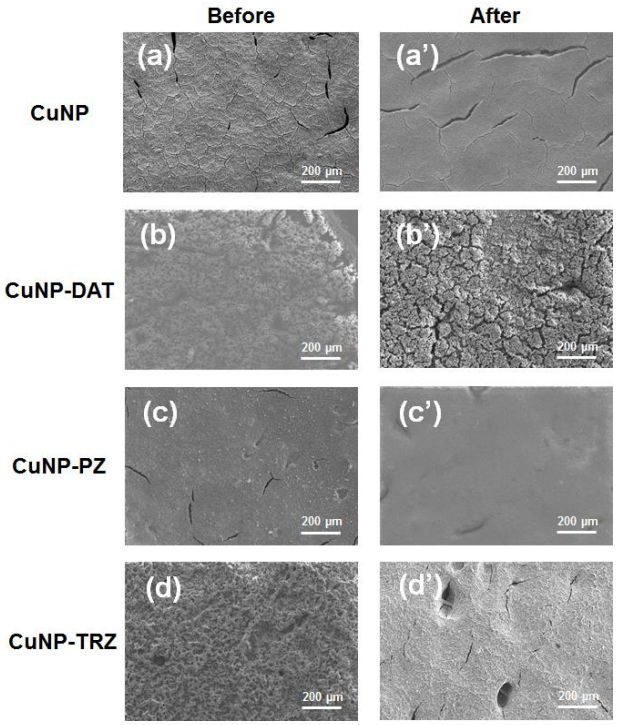

Figure 5.10 SEM images for CuNP, CuNP-DAT, CuNP-PZ and CuNP-TRZ electrodes before and after flow cell test.

5.6.3 In situ SERS of DAT without CO_2

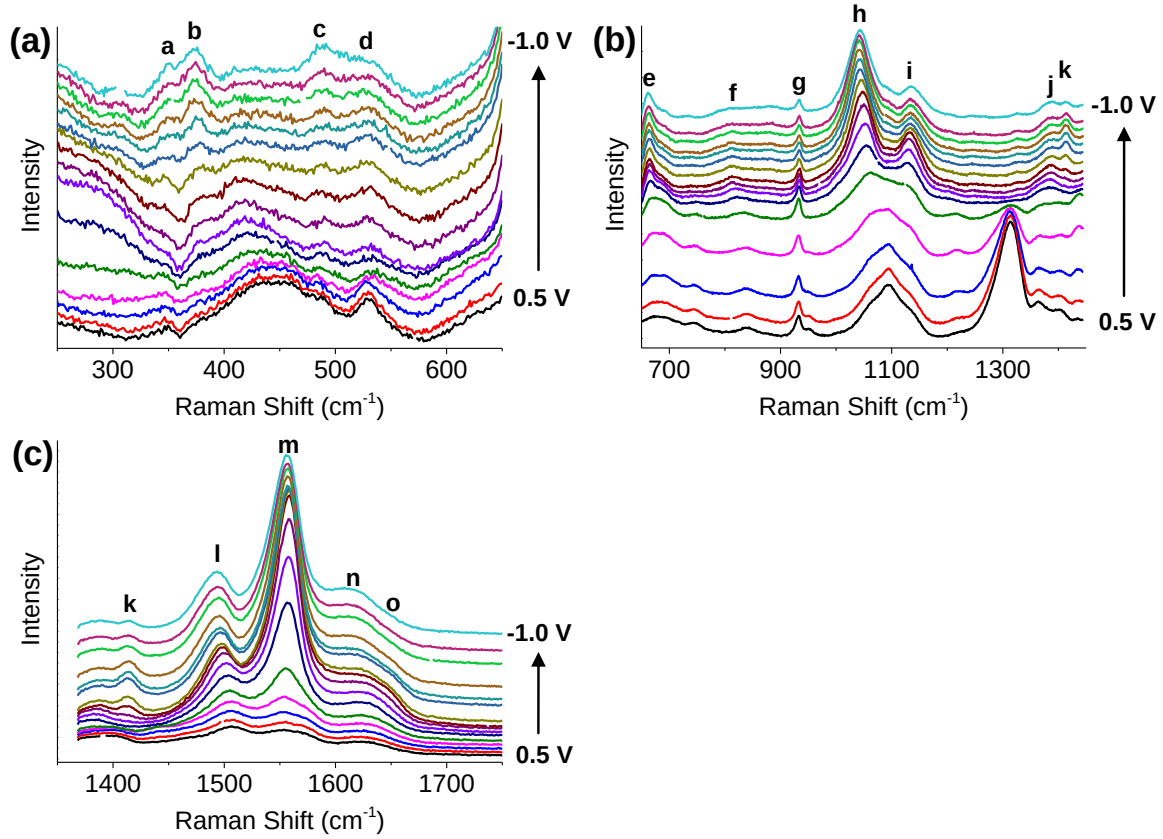

Figure 5.11 *In situ* SER spectra of the Cu electrode surface during cathodic polarization in the absence of CO_2 for regions of (a) low, (b) middle, and (c) high Raman shift values. The electrolyte was Ar-purged 1 M KOH + sat'd $Ca(OH)_2$ + 10 mM DAT + $HClO_4$ (to adjust pH ≈ 7.8).

5.6.4 In situ SERS of DAT without CO_2

Table 5.3 Raman mode assignments. ν = stretch, δ = in-plane deformation, γ = out-of-plane deformation τ = torsion, ρ = rock, ω = wag.

Peak	Raman Shift (cm^{-1})		Assignment	References
	DAT	ClO_4^-		
a	349		δ(C-NH_2) + τ(NH_2)	[1]
b	376		δ(C-NH_2) + τ(NH_2)	[1]
c	489		γ(C-NH_2)	[1]
d	531		δ(C-NH_2)	[1]

Table 5.3 (cont.)

e	662		$\omega(NH_2)$	1
f	811		δ(ring)	1
g		934	$\nu(ClO_4^-)$	2
h	1043		ν(ring) + δ(ring)	1,3,4
i	1135		$\rho(NH_2)$ + ν(ring)	1
j	1388		δ(N-H)	1
k	1415		ν(ring)	1,4
l	1494		ν(ring) + ν(C-NH_2)	1,3,4
m	1557		ν(ring) + ν(C-NH_2)	1,4
n	1614		$\delta(NH_2)$	1,4,5
o	1645		$\delta(NH_2)$	1,4

5.6.5 In situ SERS of DAT without CO_2

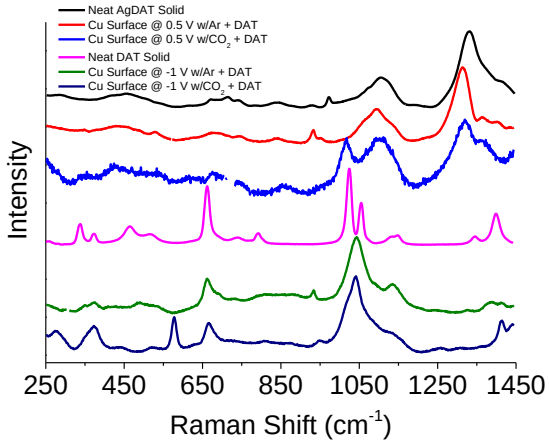

Figure 5.12 Normal ex situ and surface-enhanced in situ Raman spectra of DAT metal complexes (black, red, and blue lines) and of free DAT (pink, green, and navy).

5.6.6 In situ SERS of adsorbed ethoxy peaks with full intensity

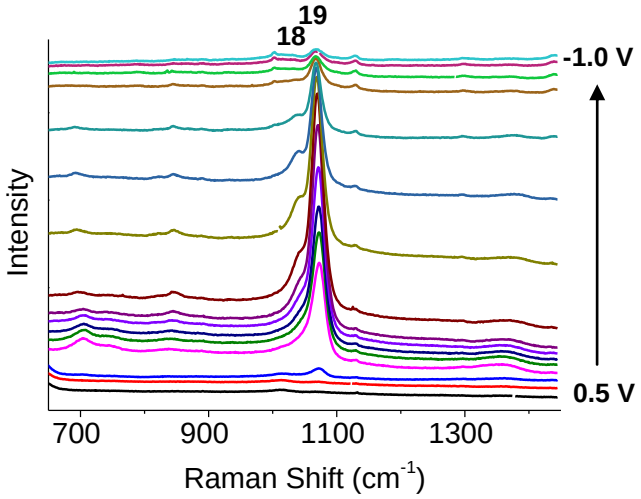

Figure 5.13 *In situ* SER spectra of CO_2 reduction at the Cu electrode surface during cathodic polarization in the region of ethoxy vibrations. The electrolyte was 1 M $KHCO_3$ + sat'd $Ca(OH)_2$.

5.7 References

1 Pachauri, R. K.; Meyer, L. *Climate Change 2014: Synthesis Report*, IPCC, 2014.

2 Pacala, S.; Socolow, R. *Science* **2004**, *305*, 968.

3 Appel, A. M.; Bercaw, J. E.; Bocarsly, A. B.; Dobbek, H.; DuBois, D. L.; Dupuis, M.; Ferry, J. G.; Fujita, E.; Hille, R.; Kenis, P. J. A.; Kerfeld, C. A.; Morris, R. H.; Peden, C. H. F.; Portis, A. R.; Ragsdale, S. W.; Rauchfuss, T. B.; Reek, J. N. H.; Seefeldt, L. C.; Thauer, R. K.; Waldrop, G. L. *Chem. Rev.* **2013**, *113*, 6621.

4 Jhong, H.-R. M.; Ma, S.; Kenis, P. J. A. *Curr. Opin. Chem. Eng.* **2013**, *2*, 191.

5 Whipple, D. T.; Finke, E. C.; Kenis, P. J. A. *Electrochem. Solid-State Lett.* **2010**, *13*, B109.

6 Hori, Y. In *Modern Aspects of Electrochemistry*; Vayenas, C., White, R., Gamboa-Aldeco, M., Eds.; Springer New York: 2008; Vol. 42, p 89.

7 Hori, Y.; Takahashi, I.; Koga, O.; Hoshi, N. *J. Mol. Catal. A: Chem.* **2003**, *199*, 39.

8 Manthiram, K.; Beberwyck, B. J.; Alivisatos, A. P. *J. Am. Chem. Soc.* **2014**, *136*, 13319.

9 Tang, W.; Peterson, A. A.; Varela, A. S.; Jovanov, Z. P.; Bech, L.; Durand, W. J.; Dahl, S.; Norskov, J. K.; Chorkendorff, I. *Phys. Chem. Chem. Phys.* **2012**, *14*, 76.

10 Kas, R.; Kortlever, R.; Milbrat, A.; Koper, M. T. M.; Mul, G.; Baltrusaitis, J. *Phys. Chem. Chem. Phys.* **2014**, *16*, 12194.

11 Rosen, B. A.; Salehi-Khojin, A.; Thorson, M. R.; Zhu, W.; Whipple, D. T.; Kenis, P. J. A.; Masel, R. I. *Science* **2011**, *334*, 643.

12 Tornow, C. E.; Thorson, M. R.; Ma, S.; Gewirth, A. A.; Kenis, P. J. A. *J. Am. Chem. Soc.* **2012**, *134*, 19520.

13 Schmitt, K. G.; Gewirth, A. A. *J. Phys. Chem. C* **2014**, *118*, 17567.

14 Zhang, S.; Kang, P.; Ubnoske, S.; Brennaman, M. K.; Song, N.; House, R. L.; Glass, J. T.; Meyer, T. J. *J. Am. Chem. Soc.* **2014**, *136*, 7845.

15 Varela, A. S.; Ranjbar Sahraie, N.; Steinberg, J.; Ju, W.; Oh, H.-S.; Strasser, P. *Angew. Chem. Int. Ed.* **2015**, *54*, 10758.
16 Chai, G.-L.; Guo, Z.-X. *Chem. Sci.* **2016**, *7*, 1268.
17 Barton Cole, E.; Lakkaraju, P. S.; Rampulla, D. M.; Morris, A. J.; Abelev, E.; Bocarsly, A. B. *J. Am. Chem. Soc.* **2010**, *132*, 11539.
18 Oberst, J. L.; Jhong, H.-R. M.; Kenis, P. J. A.; Gewirth, A. A. *Journal of Solid State Electrochemistry* **2015**, *20*, 1149.
19 Ma, S.; Luo, R.; Moniri, S.; Lan, Y.; Kenis, P. J. A. *J. Electrochem. Soc.* **2014**, *161*, F1124.
20 Jhong, H.-R. M.; Brushett, F. R.; Kenis, P. J. A. *Adv. Energy Mater.* **2013**, *3*, 589.
21 Feng, Z. V.; Li, X.; Gewirth, A. A. *The Journal of Physical Chemistry B* **2003**, *107*, 9415.
22 Mahojey, M. R.; Howard, M. W.; Cooney, R. P. *Chemical Physics Letters* **1980**, *71*, 59.
23 Ma, S.; Sadakiyo, M.; Luo, R.; Heima, M.; Yamauchi, M.; Kenis, P. J. A. *J. Power Sources* **2016**, *301*, 219.
24 Wu, J.; Risalvato, F. G.; Sharma, P. P.; Pellechia, P. J.; Ke, F.-S.; Zhou, X.-D. *J. Electrochem. Soc.* **2013**, *160*, F953.
25 Chen, C. S.; Handoko, A. D.; Wan, J. H.; Ma, L.; Ren, D.; Yeo, B. S. *Catal. Sci. Technol.* **2015**, *5*, 161.
26 Kuhl, K. P.; Cave, E. R.; Abram, D. N.; Jaramillo, T. F. *Energy Environ. Sci.* **2012**, *5*, 7050.
27 Ren, D.; Deng, Y.; Handoko, A. D.; Chen, C. S.; Malkhandi, S.; Yeo, B. S. *ACS Catal.* **2015**, *5*, 2814.
28 Li, C. W.; Ciston, J.; Kanan, M. W. *Nature* **2014**, *508*, 504.
29 Naughton, M. S.; Moradia, A. A.; Kenis, P. J. A. *J. Electrochem. Soc.* **2012**, *159*, B761.
30 Kortlever, R.; Shen, J.; Schouten, K. J. P.; Calle-Vallejo, F.; Koper, M. T. M. *J. Phys. Chem. Lett.* **2015**, *6*, 4073.
31 Cook, R. L.; MacDuff, R. C.; Sammells, A. F. *J. Electrochem. Soc.* **1990**, *137*, 607.
32 Luo, W.; Nie, X.; Janik, M. J.; Asthagiri, A. *ACS Catalysis* **2016**, *6*, 219.
33 Calle-Vallejo, F.; Koper, M. T. M. *Angew. Chem.* **2013**, *125*, 7423.
34 Hoang, T. T. H.; Gewirth, A. A. *ACS Catal.* **2016**, *6*, 1159.
35 Lee, S.; Kim, D.; Lee, J. *Angew. Chem. Int. Ed.* **2015**, *54*, 14701.
36 Bing, Y.; Liu, H.; Zhang, L.; Ghosh, D.; Zhang, J. *Chem. Soc. Rev.* **2010**, *39*, 2184.
37 Aznar, E.; Ferrer, S.; Borrás, J.; Lloret, F.; Liu-González, M.; Rodríguez-Prieto, H.; García-Granda, S. *European Journal of Inorganic Chemistry* **2006**, *2006*, 5115.
38 Thorum, M. S.; Yadav, J.; Gewirth, A. A. *Angew. Chem. Int. Ed.* **2009**, *48*, 165.
39 Chan, H. Y. H.; Takoudis, C. G.; Weaver, M. J. *The Journal of Physical Chemistry B* **1999**, *103*, 357.
40 Carter, R. O.; Poindexter, B. D.; Weber, W. H. *Vibrational Spectroscopy* **1991**, *2*, 125.
41 Akemann, W.; Otto, A. *Surface Science* **1993**, *287*, 104.
42 Marek, G.; Andreas, E.; Jürgen, H. *Journal of Physics: Condensed Matter* **2004**, *16*, 1141.
43 Hori, Y.; Koga, O.; Yamazaki, H.; Matsuo, T. *Electrochimica Acta* **1995**, *40*, 2617.
44 Oda, I.; Ogasawara, H.; Ito, M. *Langmuir* **1996**, *12*, 1094.
45 Batista, E. A.; Temperini, M. L. A. *Journal of Electroanalytical Chemistry* **2009**, *629*, 158.

46 Smith, B. D.; Irish, D. E.; Kedzierzawski, P.; Augustynski, J. *Journal of The Electrochemical Society* **1997**, *144*, 4288.
47 Adams, D. M. *Journal of the Chemical Society (Resumed)* **1964**, 1771.
48 Spiro, T. G.; Kozlowski, P. M. *Accounts of Chemical Research* **2001**, *34*, 137.
49 Gomes, J. R. B.; Gomes, J. A. N. F. *Surface Science* **1999**, *432*, 279.
50 Ito, K.; Bernstein, H. J. *Canadian Journal of Chemistry* **1956**, *34*, 170.
51 Pohl, M.; Pieck, A.; Hanewinkel, C.; Otto, A. *Journal of Raman Spectroscopy* **1996**, *27*, 805.
52 Davis, A. R.; Oliver, B. G. *Journal of Solution Chemistry*, *1*, 329.
53 Andersson, M. P.; Uvdal, P. *Surface Science* **2004**, *549*, 87.
54 Millar, G. J.; Rochester, C. H.; Waugh, K. C. *Journal of the Chemical Society, Faraday Transactions* **1991**, *87*, 1491.
55 Millar, G. J.; Newton, D.; Bowmaker, G. A.; Cooney, R. P. *Appl. Spectrosc.* **1994**, *48*, 827.
56 Lin-Vien, D.; Colthup, N. B.; Fateley, W. G.; Grasselli, J. G. **1991**.
57 Siemes, C.; Bruckbauer, A.; Goussev, A.; Otto, A.; Sinther, M.; Pucci, A. *Journal of Raman Spectroscopy* **2001**, *32*, 231.
58 Patterson, M. L.; Weaver, M. J. *The Journal of Physical Chemistry* **1985**, *89*, 1331.
59 Ásmundsson, R.; Uvdal, P.; MacKerell, A. D. *The Journal of Chemical Physics* **2000**, *113*, 1258.
60 Ásmundsson, R.; Uvdal, P. *Surface Science* **1999**, *442*, L1013.
61 Sinther, M.; Pucci, A.; Otto, A.; Priebe, A.; Diez, S.; Fahsold, G. *physica status solidi (a)* **2001**, *188*, 1471.
62 Magnotti, G.; Kc, U.; Varghese, P. L.; Barlow, R. S. *Journal of Quantitative Spectroscopy and Radiative Transfer* **2015**, *163*, 80.
63 Louie, M. K.; Francisco, J. S.; Verdicchio, M.; Klippenstein, S. J.; Sinha, A. *The Journal of Physical Chemistry A* **2015**, *119*, 4347.
64 da Silva, G. *Angewandte Chemie International Edition* **2010**, *49*, 7523.

Chapter 6*

Bimetallic CuPd Catalysts for the Electroreduction of CO_2

6.1 Chapter Overview

Electrochemical conversion of CO_2 holds promise for utilization of CO_2 as a carbon feedstock and for storage of intermittent renewable energy. Presently Cu is the only metallic electrocatalyst known to reduce CO_2 to appreciable amounts of hydrocarbons, but often a wide range of products such as CO, $HCOO^-$ and H_2 are formed as well. Better catalysts that exhibit high activity and especially high selectivity for specific products, such as valuable C2 hydrocarbons or oxygenates are needed. Here a range of bimetallic Cu-Pd catalysts with ordered, disordered, and phase-separated atomic arrangements (Cu_{at}:Pd_{at}=1:1), as well as two additional disordered arrangements (Cu3Pd and CuPd3 with Cu_{at}:Pd_{at}=3:1 and 1:3) are studied to determine key factors needed to achieve high selectivity for C1 or C2 chemicals in CO_2 reduction. When compared with the disordered and phase-separated CuPd catalysts, the ordered CuPd catalyst, which has *d*-band centers at higher energies than the other two catalysts, exhibits the highest selectivity for C1 products (>80%). This result suggests that the change in electronic structure induced by the alternating Cu-Pd structure enhances C1 selectivity. The phase-separated CuPd and Cu3Pd achieve higher selectivity (>60%) for C2 chemicals than CuPd3 and ordered CuPd, which suggests that the probability of dimerization of C1 intermediates is higher on surfaces with neighboring Cu atoms. These results imply that geometric effects are key in determining the

* This work was performed in collaboration with the Yamauchi Group at Kyushu University, specifically with Dr. Masaaki Sadakiyo, Minako Heima, and Prof. Miho Yamauchi.

selectivity of bimetallic Cu-Pd catalysts. This insight may benefit the design of catalytic surfaces that further improve activity and selectivity for CO_2 reduction.

6.2 Introduction

Atmospheric CO_2 levels recently have reached 400 ppm, and are expected to continue to rise. This increase in CO_2 levels has been associated with undesirable climate effects such as global warming, rising sea levels, and more erratic weather patterns. A variety of strategies (*e.g.*, switching to renewable energy sources, enhancing the energy efficiency of buildings and cars, and capturing carbon from point sources) need to be pursued to reduce CO_2 emissions, and thereby curb the increase in atmospheric CO_2 levels.[1] Another promising strategy that can be employed to help address the issue of high atmospheric CO_2 levels is the electrochemical reduction of CO_2 to useful intermediates or fuels such as formic acid, carbon monoxide, hydrocarbons, and alcohols.[2-5] This process can be driven by the vast amounts of intermittent excess electricity that are becoming available with the rapid increase in the number of solar and wind power plants coming online in many countries.

Although the electroreduction of CO_2 to value-added products has promise, the high overpotential of this reaction and low activity of the currently known catalysts still hampers this process from becoming close to commercialization. Cu is the only catalyst known to electrochemically convert CO_2 to hydrocarbons and/or oxygenates, but it also produces other products such as CO, $HCOO^-$, and H_2 at fairly high Faradaic efficiencies (FEs).[6] The FEs for the useful C2 chemicals (ethylene, ethanol, *etc.*) are usually below 30%, with the overpotentials for the production of these usually being high (0.7 to 1 V), resulting in low overall energetic efficiency. Intensive research efforts, both experimental (nanostructured Cu catalyst,[7] oxide-derived Cu catalyst,[8-10] and *etc.*) and theoretical (key intermediates,[11] different reaction pathways,[12,13] and

etc.), have focused on improving the overpotential and selectivity of Cu catalysts for the electroreduction of CO_2 to a specific product. However, the observed Faradaic efficiencies for C2 chemicals are typically below 40%. Norskov *et al.* suggested developing bimetallic Cu-based catalysts to break the scaling relationship and stabilize the reaction intermediate to lower the overpotential.[14] Recently, experimentalists have started to develop various Cu-based bimetallic catalysts such as Au-Cu nanoparticles,[15] polymer-supported CuPd nanoalloys,[16] and Au@Cu core@shell nanoparticles[17] for CO_2 reduction. However, among these studies, only few focused on the production of C2 chemicals, which can only be produced on Cu catalysts. Also, these reports only studied the effect of composition (ratio of two different metals). To date the lack of bimetallic catalysts with well-defined arrangement of respective metal atoms have prevented study of the effect of structure (different mixing patterns of two elements) on product distribution. The synthesis of bimetallic catalysts with well-defined elemental arrangements is the major challenge that needs to be conquered.

In this work, we report on the synthesis and characterization of bimetallic Cu-Pd catalysts with different elemental arrangements (ordered, disordered, phase-separated, schematic illustration shown in **Figure 1a**) and different atomic ratios (1:3 to 3:1) to study the effect of structure and composition on catalyst activity and selectivity for CO_2 reduction. Possible active sites for the production of C2 chemicals and CH_4 are proposed based on the electrochemical analysis of the performance of these bimetallic catalysts.

6.3 Experimental

6.3.1 Synthetic procedures for all Cu-Pd bimetallic samples

Preparation of solid-solution type CuPd, Cu3Pd and CuPd3: Solid-solution type CuPd alloys, *i.e.*, disordered types, were produced by reducing a mixture of palladium (II) acetate and copper (II) acetate (with molar ratio of Cu(II):Pd(II)=1:1) using $NaBH_4$. An acetone solution of palladium acetate (1.5 mmol) was mixed into the solution of 2-ethoxyethanol including copper acetate (1.5 mmol). An aqueous solution of $NaBH_4$ was added into the alcoholic solution at ambient temperature and the mixture was stirred for 5 min. The color of the solution immediately changed to brown black after the addition, indicating the formation of alloy. The synthesized alloy was collected by filtering and washing with water ten times and ethanol twice and dried under vacuum. Cu3Pd and CuPd3 alloys were synthesized in an analogous way using a solution containing metal species with concentrations corresponding to the final composition. *Preparation of ordered CuPd:* The disordered CuPd nanoalloy was annealed under 0.1 MPa H_2 while increasing temperature up to 573 K for the acceleration of atomic displacement into the formation of an ordered phase. *Preparation of phase-separated CuPd:* A mixed solution of 10 ml acetone solution of palladium acetate (1.5 mmol) and 250 ml 2-ethoxy ethanol was stirred at 393 K for 30 min and cooled to room temperature. After 20 ml aqueous solution of copper acetate (1.5 mmol) was mixed with the reaction solution including Pd species, 20 ml aqueous solution including $NaBH_4$ (30 mmol) was added with stirring. Precipitates were collected by filtration and washed with water ten times and ethanol twice. *Preparation of Cu nanoparticles:* Copper (II) acetate (3 mmol) was dissolved into 250 mL 2-ethoxyethanol. After vigorous stirring with bubbling Ar for 30 minutes, 20 ml aqueous solution of $NaBH_4$ (30 mmol) was added dropwise to the copper solution and the mixed solution was stirred for 5 minutes at ambient temperature. The resultant

black precipitate was collected by filtration and washed with water three times and ethanol twice. The precipitate was then dried. *Preparation of Pd nanoparticles:* 30 ml aqueous solution including $NaBH_4$ (30 mmol) was added to a mixed solution of 30 ml acetone solution of palladium acetate (3.0 mmol) and 250 ml 2-ethoxyethanol at room temperature. After the 5 min stirring, precipitates were collected by filtration and washed with water ten times and ethanol twice. The precipitate was then dried.

6.3.2 Physical characterizations

SEM-EDS analysis was performed using JEOL JSM-IT100 operated at 18 kV. XRD measurements of all the catalysts were performed at room temperature using a Rigaku MiniFlex 600 (λ = 1.54059 Å, Cu-Kα). All samples were scanned from 10 degree to 100 degree with a step of 0.05 and a scan rate of 0.5 degree min^{-1}. TEM images of all samples were taken using JEOL 2100 CRYO operated at 200 kV. The TEM sample was prepared by placing several drops of catalyst suspension in isopropanol onto a holey carbon-coated 200 mesh grid followed by solvent evaporation overnight at room temperature. The HAADF-STEM images and STEM-EDS data were corrected using JEOL ARM200F microscope operated at 200 kV. XPS core-level and valance band spectra as well as X-ray-induced Auger spectra were collected using a Kratos Axis ULTRA X-ray photoelectron spectrometer with monochromatic Al Kα excitation, 210 W (14kV, 15 mA). Data were collected using the hybrid lens setting with the slot aperture (300 x 700 μm^2 analysis area) and charge neutralizer settings of 1.8 A filament current, 3.25 V charge balance and 1 V filament bias. Survey spectra were collected using a pass energy of 160 eV and high resolution core-level and valance band spectra were collected using a pass energy of 40 eV. The binding energy scale was referenced to the aliphatic C 1s line at 285.0 eV. In order to enhance d-band

intensity of the metallic nanoparticles, the signal from the Nafion® support was subtracted from the X-ray-induced valence band spectra. This was accomplished by collecting a valence band spectrum from a sample containing only the support and then fitting the spectrum with a set of Gaussian-Lorentzian curves. Next, the composite intensity of the fitted curves was normalized to spectra of the metallic nanoparticles using the characteristic features of the Nafion® support found between 18 – 10 eV. The normalized composite intensity of the support was then subtracted from that of the spectra of the metallic nanoparticles. The d-band center value was determined using a numeric integration over the range of 8 – 0 eV, placing the center at the mean value of the integrated area in a method similar to previous reported work.[15]

6.3.3 Electrode preparation

The cathodes were prepared using an air-brush deposition method.[18] Cathode catalyst inks were prepared by mixing tetrahydrofuran (200 μL), catalyst (5.0 mg), Nafion® solution (6.5 μL), and isopropyl alcohol (200 μL) in a glass vial. The inks were then sonicated (Vibra-Cell ultrasonic processor, Sonics & Materials) for 20 minutes and air-brushed on a GDL to create a GDE covered with catalyst over a geometric area of 5.0×0.8 cm^2. A PTFE spacer with a 5.0×0.8 cm^2 window was placed on top of GDL during the deposition process to avoid catalyst being deposited outside of the expected area on the GDL. The actual loading was determined by weighing the GDL before and after deposition. About 3 vials of catalyst ink were used to obtain a catalyst loading of 1.0 ± 0.1 mg cm^{-2}. The weight loss was found to be on the order of 40% for the air-brushed cathodes since a fraction of the catalyst ended up on the spacer, or was left behind in the air-brush. The anodes were prepared by hand-painting of IrO_2 catalyst inks comprised of water (200 μL), IrO_2 catalyst (5 mg, non-hydrate, Alfa Aesar), Nafion® solution (13 μL, 5 wt%, Fuel Cell Earth), and

isopropyl alcohol (200 μL) over a geometric area of 1.0 × 2.5 cm^2. The anode loading was determined to be 1.5 ± 0.1 mg cm^{-2}. A fresh cathode was used for each flow cell test.

6.3.4 CO_2 electrolysis and product analysis

An electrochemical flow cell reported previously is used as the electrolyzer for CO_2 reduction. An AEM is inserted between the catholyte and anolyte chamber to prevent the liquid products from diffusing to the anode where they may get oxidized. A mass flow controller (MASS-FLO®, MKS instrument) was used to set the CO_2 (S.J. Smith Welding Supply) flow rate at 7 SCCM. A syringe pump (PHD 2000, Harvard Apparatus) flowed 1 M KOH (pH=13.48) as the electrolyte to minimize boundary layer depletion effects and supply fresh electrolytes thereby helping to maintain the pH on the electrode surface. The flowing stream provides flexibility in operation conditions, minimizes water management issues at the electrodes, and facilitates online sample collection followed by product analysis.[4] The cell potential (–1.6 V, –1.75 V, –2 V, –2.25 V, –2.5 V, –2.75 V, –3 V, –3.5 V) is controlled by a potentiostat (Autolab PGSTAT-30, EcoChemie) in the potentiostatic electrolysis mode. The electrolyte flow rate was set at 0.5 mL min^{-1} when applying cell potentials of –2 to –3.5 V as done previously[4], while a flow rate of 0.1 mL min^{-1} was used for cell potentials between –1.6 and –2 V to increase the concentration of the liquid products at low current density operation conditions. Individual electrode potentials were recorded using multimeters (AMPROBE 15XP-B) connected to each electrode and a reference electrode (Ag/AgCl; RE-5B, BASi) placed in the electrolyte exit stream. The measured potentials (*vs.* Ag/AgCl) were converted to the RHE reference scale using E (*vs.* RHE) = E (*vs.* Ag/AgCl) + 0.209 V + 0.0591 V/pH × pH as previously reported.[9,19] The electrode potentials were corrected for iR drop as previously reported.[20,21] A pressure controller (Cole-Parmer, 00268TC) downstream

from the cell was used to keep the gas pressure in cell lower than the atmosphere, allowing gas products formed on the catalyst surface of the GDE to leave through the GDE to the gas stream.

Periodically, for product analysis, 1 mL of the effluent gas stream was sampled automatically and diverted into a GC (Thermo Finnegan Trace GC) equipped with both the thermal conductivity detection (TCD) and flame ionization detector (FID) after the cell reaches steady state. Meanwhile, the exit catholyte was collected at each applied potential and analyzed using ^{1}H NMR technique reported previously.[6,22,23] 100 μL of the catholyte was mixed with 400 μL D_2O (99.9% deuterium atom, Sigma-Aldrich) and 100 μL of an internal standard consisting of 1.25 mM DMSO (99.98%, Calbiochem) in D_2O. The results presented here are from 32 scans (UI500NB, Varian) after solvent suppression, and processed using the MestReNova software (MestReLab).

The Faradaic efficiency for a specific product is calculated using the same method as shown in Chapter 1. The partial current density for a specific product equals total current density multiplies Faradaic efficiency for this product.

6.4 Results and Discussion

The preparation of the samples studied, a solid-solution type CuPd alloy (disordered sample, Cu_{at}:Pd_{at}=1:1), an ordered CuPd alloy (Cu_{at}:Pd_{at}=1:1), a phase-separated (PhaseSep) CuPd sample (Cu_{at}:Pd_{at}=1:1), as well as a Cu3Pd sample (Cu_{at}:Pd_{at}=3:1) and a CuPd3 sample (Cu_{at}:Pd_{at}=1:3), is described in detail in the Experimental Section shown above. The composition of these samples was examined using scanning electron microscope equipped with energy dispersive X-ray spectroscopy (SEM-EDS). The measured atomic ratios of the various synthesized CuPd samples are summarized in **Table 6.1** in the SI.

The structure of the bimetallic Cu-Pd samples was first characterized using X-ray diffraction (XRD). From the XRD pattern (**Figure 6.1b**) it is evident that the ordered and disordered samples form homogeneous structures. The XRD pattern of the ordered CuPd sample fits well with an ordered B2 structure (**Figure 6.5a** in the SI) in which alternatively arranged Cu and Pd atoms reside on neighboring sites in a bcc-based lattice, as previously reported.[24] The disordered CuPd sample shows a broad single peak around 2θ = 42°, which is likely due to a diffraction from the (011) plane in a bcc-based structure. However, the peaks at higher angles do not match a bcc structure (**Figure 6.5b** in the SI), implying low crystallinity of this sample. The absence of the characteristic peak of the ordered B2 structure around 2θ = 30° ((001) plane) suggests that the Cu and Pd atoms form a disordered structure in this sample. XRD data also reveals that the sample we will refer to as phase-separated is composed of three separate phases: fcc-type Cu, Cu_2O, and fcc-type Pd (**Figure 6.5c** in the SI).

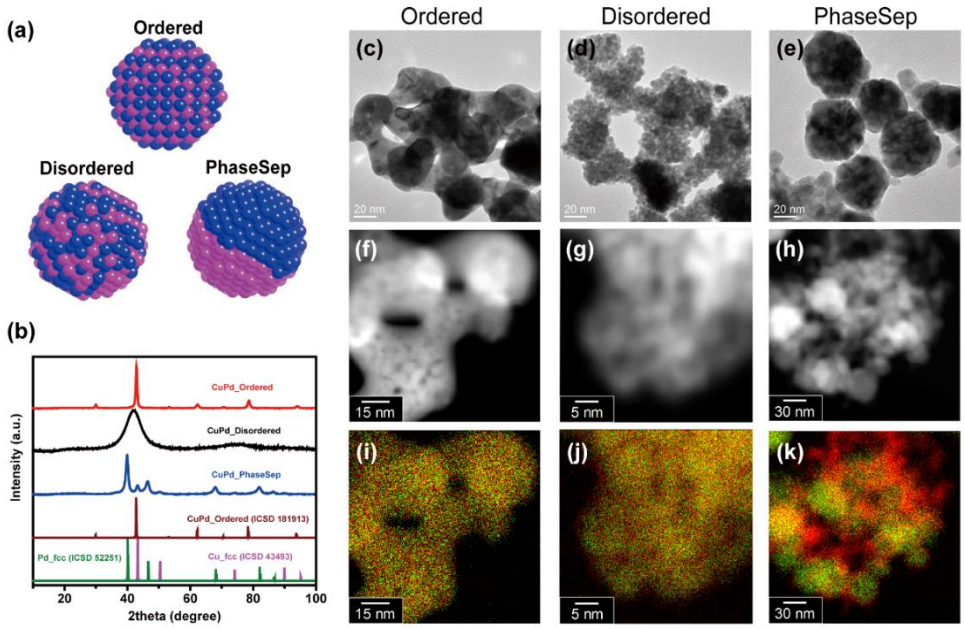

Figure 6.1 Physical characterization of bimetallic Cu-Pd catalysts with different atomic mixing patterns: ordered, disordered, and phase-separated. (a) Schematic illustration of prepared CuPd nanoalloys with different structures; (b) XRD patterns of prepared CuPd nanoalloys as well as previously reported Cu, Pd and CuPd alloys; (c), (d), (e) High-resolution TEM images; (f), (g), (h) HAADF-STEM images; (i), (j), (k) Combined EDS elemental maps of Cu (red) and Pd (green).

High-resolution transmission electron microscope (HR-TEM) measurements showed that three CuPd alloys indeed have different morphologies and particle sizes (**Figure 6.1c-e**): the ordered sample consists of interconnected crystalline features with a particle size of ~50 nm; the disordered sample consists of uniform spheres with a particle size of ~5 nm; the phase-separated sample consists of two different aggregates with distinct morphologies: (1) spherical particles ~50 nm in size, and (2) an interconnected structure with smaller particles ~20 nm in size.

The chemical microstructure of these three different CuPd alloys was also examined using scanning transmission electron microscope combined with EDS (STEM-EDS) to yield high-angle annular dark-field STEM (HAADF-STEM) images and STEM-EDS maps of the alloys **(Figure 6.1f-k**). Similar morphologies as shown in the HR-TEM images were evident from the HAADF-STEM images, however, clear differences in the elemental distributions were observed. The EDS mapping of the ordered sample (**Figure 6.1i**) shows that Cu (red) and Pd (green) atoms are homogeneously mixed and distributed, forming an ordered intermetallic structure. Large domains composed of only Cu or Pd throughout the disordered alloy particles could not be found (**Figure 6.1j**). XRD data indicates that this sample has a solid-solution type alloy structure that contains small domains of Cu atoms due to its disordered character (**Figure 6.1a)**. In contrast, the EDS mapping of the phase-separated sample exhibits separate phases of Cu and Pd elements, within each phase most of the neighboring sites are from the same element (**Figure 6.1k**). In summary, these STEM-EDS results are in good agreement with the XRD results; we successfully obtained ordered, disordered, and phase-separated mixing patterns in the samples.

X-ray photoemission spectroscopy (XPS) results combined with Auger spectra (**Figure 6.6** in the SI) show that different valence states of Cu exist on the surface of the different bimetallic Cu-Pd samples due to the differences in their elemental arrangement. Note, however, that the

initial amount of Cu oxides on the surface does not affect the product distribution significantly in the electroreduction of CO_2, as previously reported.[25]

To evaluate activities of catalysts for CO_2 reduction, each bimetallic Cu-Pd catalyst was deposited onto a gas diffusion layer to form a gas diffusion electrode (GDE), which was assembled in a flow reactor that we reported previously.[25] The electrolysis was performed in a 1 M KOH electrolyte in potentiostatic mode under ambient conditions. Gas-phase and liquid-phase products were analyzed by gas chromatography (GC) and nuclear magnetic resonance (NMR) spectroscopy, respectively. **Figure 6.7** shows the single electrode polarization curves of the ordered, disordered and phase-separated samples. The phase-separated sample achieves the highest total current density (CD) of 370 mA cm^{-2}, while the ordered sample has the lowest total CD, indicating that the phase-separated sample exhibit the highest overall production rate among these three samples.

Figure 6.2a-d show Faradaic efficiencies (FEs) as a function of cathode potential for each of the major products using the ordered, disordered and phase-separated CuPd samples. At cathode potentials more positive than -0.3 V_{RHE}, the CO FE is almost the same for all three samples; while at cathode potentials more negative than -0.3 V_{RHE}, where C2 chemicals start to be produced, the ordered CuPd exhibits the highest CO FE, and the phase-separated CuPd achieves the lowest CO FE (**Figure 6.2a**). However, for C2 chemicals, the phase-separated CuPd exhibits the highest FE (up to 63%, among the highest reported values for C2 production reported in the literature[25]), and the ordered CuPd has the lowest C2 FE (<5%, **Figure 6.2c** and **6.2d**). The phase-separated CuPd has a higher FE for CH_4 compared to the FEs observed for ordered or disordered CuPd alloys (**Figure 6.2b**). This result is in agreement with prior experimental[16] and theoretical studies[14] reporting that alloying Cu with an element with a high oxygen affinity improves the FE for CH_4. Although the ordered CuPd has more alternating Cu-Pd sites than the disordered CuPd,

the higher CH_4 FE observed for the disordered sample may be due to a higher surface coverage of the intermediate. All the above observations indicate that (1) CO is an important precursor for C2 chemicals production;[12,19] and (2) the phase-separated CuPd catalyst converts adsorbed CO to C2 chemicals more easily than the ordered CuPd catalyst, with the latter converting adsorbed CO more easily to CH_4 than the phase-separated catalyst.

Linking mixing patterns of the catalysts with the trend in FE for C2 products, the catalyst structure with dominant neighboring Cu atoms (phase-separated sample in this study) is suspected to favor conversion of CO_2 to C2 chemicals, while the structure with intermetallic mixing patterns (the ordered sample in this study) favors conversion of CO_2 to CH_4. Specifically, in the phase-separated structure, due to the neighboring feature of Cu atoms which may allow for the favorable molecular distance and small steric hindrance, adjacently adsorbed CO will be easily dimerized to COCOH intermediate. The COCOH intermediate will then be mainly converted to C2 products, with only a small portion decomposes and converting to CH_4. While in the ordered structure, Cu-Pd intermetallic structures are majorly present. The adsorbed CO on a Cu atom tends to form CHO intermediate with the oxygen atom partially adsorbed on the Pd atom, which stabilizes the adsorption of the CHO intermediate and favors the further production of CH_4, as predicted from prior theoretical studies[14]. Therefore, the dimerization of adsorbed CO, a key step for the production of C2 chemicals, may be preferred on the sites with neighboring Cu atoms. Our observations also indicate that the formation of CH_4 and C2 chemicals proceeds through different reaction pathways as proposed previously.[13]

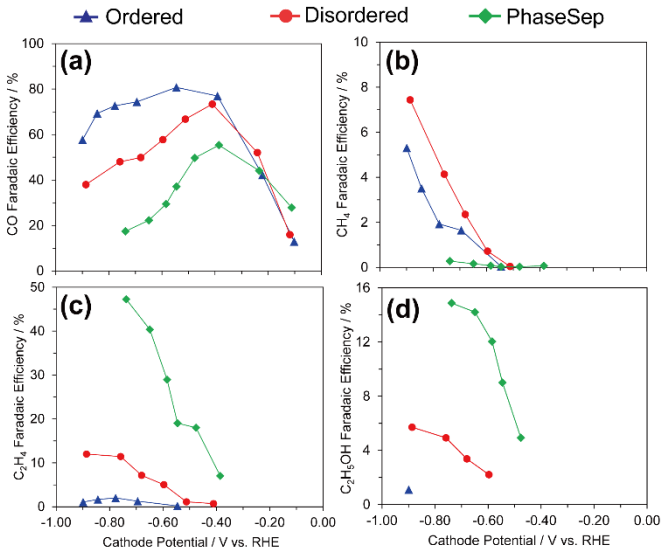

Figure 6.2 Faradaic efficiencies for (a) CO; (b) CH_4; (c) C_2H_4; (d) C_2H_5OH for bimetallic Cu-Pd catalysts with different mixing patterns: ordered, disordered, and phase-separated.

The effect of composition on catalyst activity and selectivity was also studied. Two samples with different Cu:Pd ratios for the disordered structure: Cu3Pd (Cu_{at}:Pd_{at}=3:1) and CuPd3 (Cu_{at}:Pd_{at}=1:3) were prepared. The HR-TEM data (**Figure 6.8** in the SI) shows that the morphologies of Cu3Pd and CuPd3 resemble the disordered CuPd sample. The crystalline structure of Cu3Pd is similar to that of the disordered CuPd sample, with some shoulder peaks around 35-40˚ indicating the existence of oxides, while the crystalline structure of CuPd3 resembles that of fcc-type Pd (**Figure 6.9** in the SI). Next, electrochemical characterization was performed: The FEs for various products using these two samples, as well as the disordered CuPd sample, Cu nanoparticles (Cu-1 data from prior work under the same condition[25]) and Pd nanoparticles are provided in **Figure 6.3** in the SI. As the concentration of Cu increases from Pd, CuPd3, CuPd, to Cu3Pd and Cu, the FEs for C2 products increase. This observation further supports the idea that the dimerization of adsorbed CO to form C2 chemicals may be preferred on the sites with neighboring Cu atoms. The CH_4 FEs for both Cu3Pd and CuPd3 are lower than that for the disordered CuPd, probably due to the lower amount of Cu-Pd intermetallic sites within

these two samples compared to the disordered CuPd. Since Cu3Pd and CuPd3 have a similar morphology as the disordered CuPd sample, their differences in FEs for C2 chemicals indicate that the difference in morphologies among the samples probably is not the major cause for the observed differences in performance for the different catalyst structures shown in **Figure 6.2**.

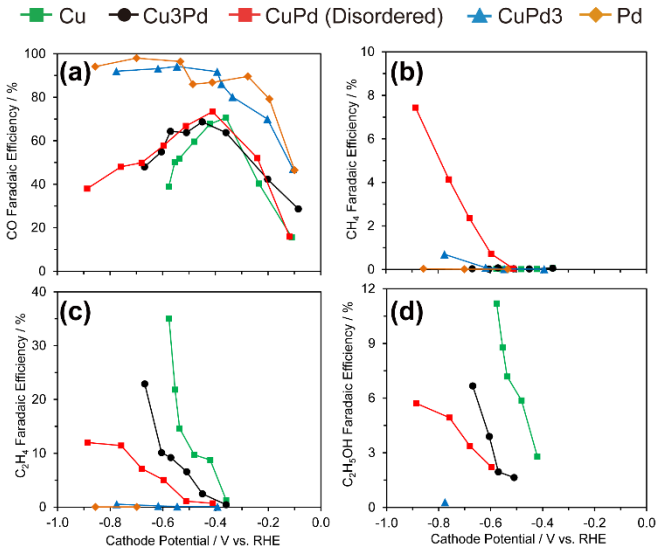

Figure 6.3 Faradaic efficiencies for (a) CO; (b) CH_4; (c) C_2H_4; (d) C_2H_5OH for catalysts with different Cu:Pd ratios: Cu, Cu3Pd, CuPd, CuPd3, and Pd.

We also suspect that electronic effects induced after mixing Cu with Pd may cause some of the observed differences in FEs for various products. To confirm this possibility, surface valence band photoemission spectra of the ordered, disordered, and phase-separated samples, as well as Cu nanoparticles and Pd nanoparticles were collected (**Figure 6.4**). The spectra reveal that the *d*-band centers, which relates to the electronic structure of the catalysts as well as the binding energy of intermediates with the catalyst surface,[15] are similar for the disordered sample (3.70 ± 0.10 eV), phase-separated sample (3.67 ± 0.10 eV), and the Cu sample (3.71 ± 0.10 eV), but are different from the *d*-band centers of the ordered sample (3.39 ± 0.10 eV) and the Pd sample (3.42 ± 0.10 eV). Considering the high selectivity for CO and CH_4 production observed for the ordered CuPd and Pd catalysts, we conclude that the change of *d*-band center after alloying Cu with Pd

mainly enhances the selectivity for C1 products by changing the adsorption energy of the CO intermediate. Despite the observed difference in FEs for C2 chemicals for the disordered, phase-separated and Cu samples, the fact that the d-band centers of these samples are similar indicates that geometric/structural effects, and not electronic effects, are the major cause for the observed differences in catalytic activity for C2 production among these bimetallic catalysts.

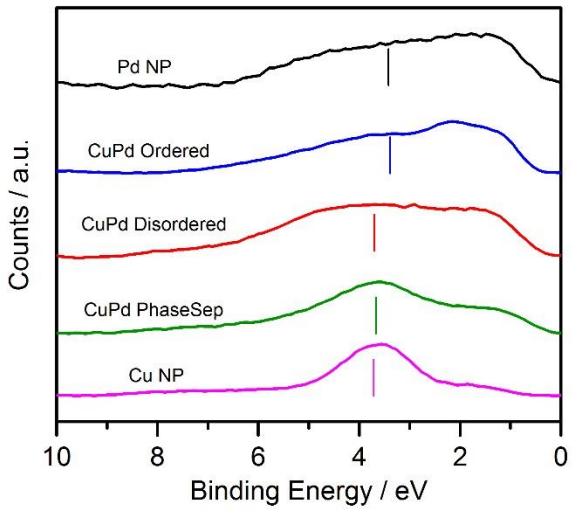

Figure 6.4 Surface valence band photoemission spectra of CuPd nanoalloys. All the spectra are background corrected. The vertical line indicates the d-band center of each sample.

6.5 Conclusions

In summary, through the synthesis and characterization of bimetallic Cu-Pd catalysts with different elemental mixing patterns and compositions, we demonstrate that mixing patterns of the two components play an important role in determining each catalyst's activity and selectivity. The sample that features neighboring Cu atoms (phase-separated) favors production of C2 products, while the sample that features the alternating Cu-Pd arrangement favors the production of CH_4. This finding provides insight to further design proper Cu-related catalysts for the conversion of CO_2 to desired products. Computational studies on determining the actual number of Cu atoms within the active site for the production of C2 chemicals would be desired in the future.

6.6 Supporting Information

Table 6.1. Actual Cu:Pd atomic ratios in various CuPd samples.

Sample Name	Actual Cu:Pd Atomic Ratio
Ordered CuPd	50.9:49.1
Disordered CuPd	51.1:48.9
PhaseSep CuPd	51.3:48.7
Cu3Pd	75.2:24.8
CuPd3	24.9:75.1

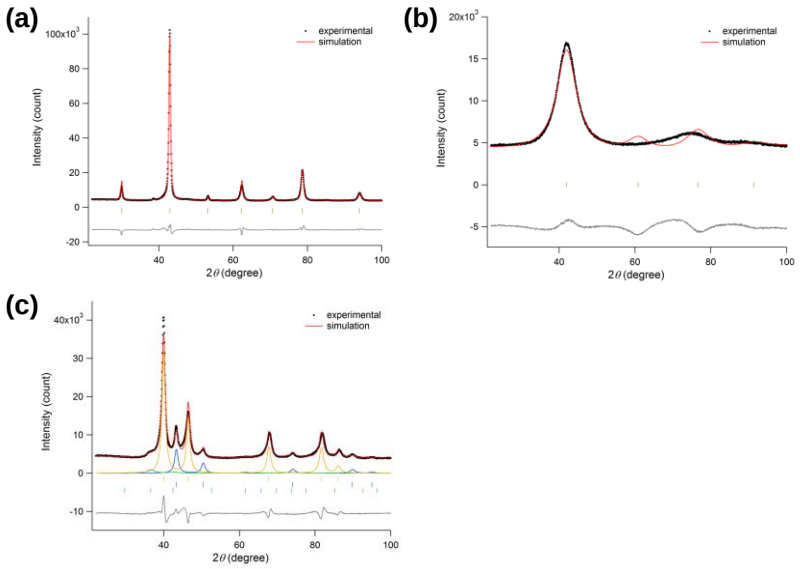

Figure 6.5 Rietveld refinement analysis of CuPd nanoalloys. a, Final Rietveld plot of the ordered-B2 CuPd alloy (*Pm-3m*, a = 2.9806(1) Å, R_p = 4.10%, R_{wp} = 5.90%). b, The XRPD data of the disordered sample fitted by bcc structure (peaks of (002) (~60.8°) and (211) (~76.5°) planes are not assignable to the experimental data). c, Final Rietveld plot of the Phase-Separated sample (orange color: Pd-fcc, a = 3.9104(2) Å; blue color: Cu-fcc, a = 3.619(1) Å, green color: Cu_2O (*Pn-3m*), a = 4.260(10) Å; R_p = 4.46%, R_{wp} = 6.25%). Mol fractions of Pd and Cu (Cu-fcc and Cu_2O) elements were estimated to be 54% and 46%, respectively.

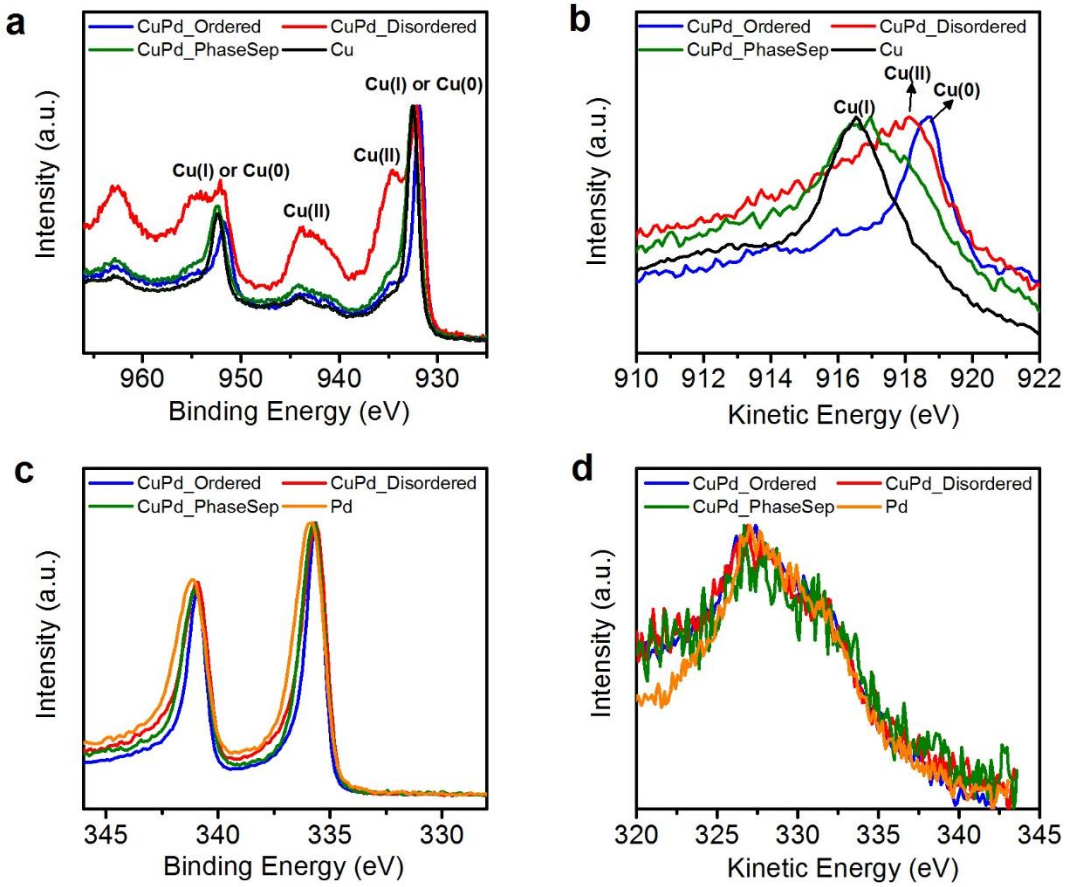

Figure 6.6 High resolution XPS and Auger spectra for ordered CuPd, Disordered CuPd, PhaseSep CuPd, Cu and Pd. a, High resolution XPS spectrum of Cu2p. b, High resolution Auger spectrum of Cu LMM. c, High resolution XPS spectrum of Pd3d. d, High resolution Auger spectrum of Pd MVV.

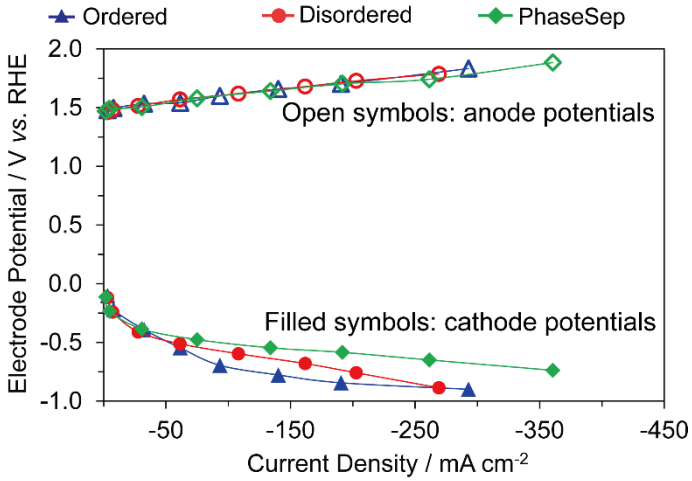

Figure 6.7 Single electrode polarization curves for bimetallic CuPd catalysts with different mixing patterns: ordered, disordered, and phase-separated.

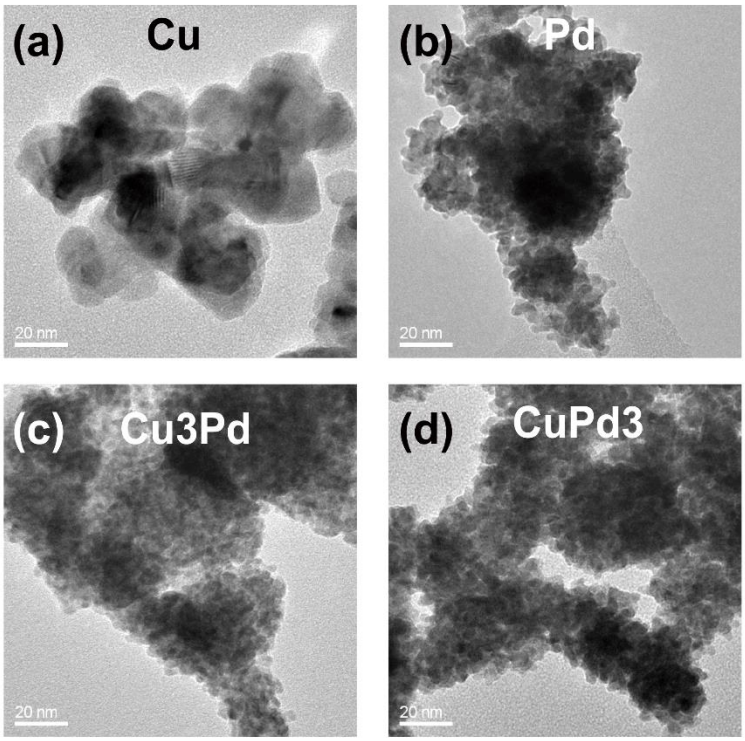

Figure 6.8 TEM micrograph of (a) Cu; (b) Pd; (c) Cu3Pd1; and (d) Cu1Pd3.

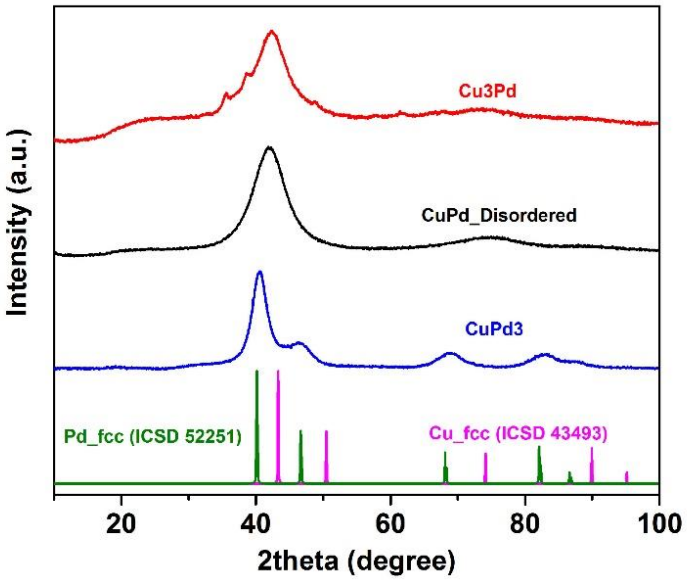

Figure 6.9 XRD patterns of CuPd samples with different Cu:Pd ratios.

6.7 References

1 Pacala, S. & Socolow, R. Stabilization Wedges: Solving the Climate Problem for the Next 50 Years with Current Technologies. *Science* **305**, 968-972, (2004).

2 Appel, A. M., Bercaw, J. E., Bocarsly, A. B., Dobbek, H., DuBois, D. L., Dupuis, M., Ferry, J. G., Fujita, E., Hille, R., Kenis, P. J. A., Kerfeld, C. A., Morris, R. H., Peden, C. H. F., Portis, A. R., Ragsdale, S. W., Rauchfuss, T. B., Reek, J. N. H., Seefeldt, L. C., Thauer, R. K. & Waldrop, G. L. Frontiers, Opportunities, and Challenges in Biochemical and Chemical Catalysis of CO2 Fixation. *Chem. Rev.* **113**, 6621-6658, (2013).

3 Jhong, H.-R. M., Ma, S. & Kenis, P. J. A. Electrochemical conversion of CO2 to useful chemicals: current status, remaining challenges, and future opportunities. *Curr. Opin. Chem. Eng.* **2**, 191-199, (2013).

4 Whipple, D. T., Finke, E. C. & Kenis, P. J. A. Microfluidic Reactor for the Electrochemical Reduction of Carbon Dioxide: The Effect of pH. *Electrochem. Solid-State Lett.* **13**, B109-B111, (2010).

5 Hori, Y. in *Modern Aspects of Electrochemistry* Vol. 42 *Modern Aspects of Electrochemistry* (eds ConstantinosG Vayenas, RalphE White, & MariaE Gamboa-Aldeco) Ch. 3, 89-189 (Springer New York, 2008).

6 Kuhl, K. P., Cave, E. R., Abram, D. N. & Jaramillo, T. F. New insights into the electrochemical reduction of carbon dioxide on metallic copper surfaces. *Energy Environ. Sci.* **5**, 7050-7059, (2012).

7 Roberts, F. S., Kuhl, K. P. & Nilsson, A. High Selectivity for Ethylene from Carbon Dioxide Reduction over Copper Nanocube Electrocatalysts. *Angew. Chem.* **127**, 5268-5271, (2015).

8 Li, C. W. & Kanan, M. W. CO2 Reduction at Low Overpotential on Cu Electrodes Resulting from the Reduction of Thick Cu2O Films. *J. Am. Chem. Soc.* **134**, 7231-7234, (2012).

9 Ren, D., Deng, Y., Handoko, A. D., Chen, C. S., Malkhandi, S. & Yeo, B. S. Selective Electrochemical Reduction of Carbon Dioxide to Ethylene and Ethanol on Copper(I) Oxide Catalysts. *ACS Catal.* **5**, 2814-2821, (2015).

10 Kas, R., Kortlever, R., Milbrat, A., Koper, M. T. M., Mul, G. & Baltrusaitis, J. Electrochemical CO2 reduction on Cu2O-derived copper nanoparticles: controlling the catalytic selectivity of hydrocarbons. *Phys. Chem. Chem. Phys.* **16**, 12194-12201, (2014).

11 Peterson, A. A., Abild-Pedersen, F., Studt, F., Rossmeisl, J. & Norskov, J. K. How copper catalyzes the electroreduction of carbon dioxide into hydrocarbon fuels. *Energy Environ. Sci.* **3**, 1311-1315, (2010).

12 Calle-Vallejo, F. & Koper, M. T. M. Theoretical Considerations on the Electroreduction of CO to C2 Species on Cu(100) Electrodes. *Angew. Chem.* **125**, 7423-7426, (2013).

13 Schouten, K. J. P., Kwon, Y., van der Ham, C. J. M., Qin, Z. & Koper, M. T. M. A new mechanism for the selectivity to C1 and C2 species in the electrochemical reduction of carbon dioxide on copper electrodes. *Chem. Sci.* **2**, 1902-1909, (2011).

14 Peterson, A. A. & Nørskov, J. K. Activity Descriptors for CO2 Electroreduction to Methane on Transition-Metal Catalysts. *J. Phys. Chem. Lett.* **3**, 251-258, (2012).

15 Kim, D., Resasco, J., Yu, Y., Asiri, A. M. & Yang, P. Synergistic geometric and electronic effects for electrochemical reduction of carbon dioxide using gold–copper bimetallic nanoparticles. *Nat Commun* **5**, (2014).

16 Zhang, S., Kang, P., Bakir, M., Lapides, A. M., Dares, C. J. & Meyer, T. J. Polymer-supported CuPd nanoalloy as a synergistic catalyst for electrocatalytic reduction of carbon dioxide to methane. *Proc. Natl. Acad. Sci.* **112**, 15809-15814, (2015).
17 Monzo, J., Malewski, Y., Kortlever, R., Vidal-Iglesias, F. J., Solla-Gullon, J., Koper, M. T. M. & Rodriguez, P. Enhanced electrocatalytic activity of Au@Cu core@shell nanoparticles towards CO2 reduction. *Journal of Materials Chemistry A* **3**, 23690-23698, (2015).
18 Jhong, H.-R. M., Brushett, F. R. & Kenis, P. J. A. The Effects of Catalyst Layer Deposition Methodology on Electrode Performance. *Adv. Energy Mater.* **3**, 589-599, (2013).
19 Li, C. W., Ciston, J. & Kanan, M. W. Electroreduction of carbon monoxide to liquid fuel on oxide-derived nanocrystalline copper. *Nature* **508**, 504-507, (2014).
20 Naughton, M. S., Moradia, A. A. & Kenis, P. J. A. Quantitative Analysis of Single-Electrode Plots to Understand In-Situ Behavior of Individual Electrodes. *J. Electrochem. Soc.* **159**, B761-B769, (2012).
21 Ma, S., Luo, R., Moniri, S., Lan, Y. & Kenis, P. J. A. Efficient Electrochemical Flow System with Improved Anode for the Conversion of CO2 to CO. *J. Electrochem. Soc.* **161**, F1124-F1131, (2014).
22 Wu, J., Risalvato, F. G., Sharma, P. P., Pellechia, P. J., Ke, F.-S. & Zhou, X.-D. Electrochemical Reduction of Carbon Dioxide: II. Design, Assembly, and Performance of Low Temperature Full Electrochemical Cells. *J. Electrochem. Soc.* **160**, F953-F957, (2013).
23 Chen, C. S., Handoko, A. D., Wan, J. H., Ma, L., Ren, D. & Yeo, B. S. Stable and selective electrochemical reduction of carbon dioxide to ethylene on copper mesocrystals. *Catal. Sci. Technol.* **5**, 161-168, (2015).
24 Yamauchi, M. & Tsukuda, T. Production of an ordered (B2) CuPd nanoalloy by low-temperature annealing under hydrogen atmosphere. *Dalton Trans.* **40**, 4842-4845, (2011).
25 Ma, S., Sadakiyo, M., Luo, R., Heima, M., Yamauchi, M. & Kenis, P. J. A. One-step electrosynthesis of ethylene and ethanol from CO2 in an alkaline electrolyzer. *J. Power Sources* **301**, 219-228, (2016).

Chapter 7*

The Effect of Catalyst Layer Structure on CO_2 Reduction

7.1 Chapter Overview

Over the last few decades significant progress has been made in the development of catalysts for efficient and selective electroreduction of CO_2. These improvements in catalyst performance have been of the extent that identifying electrodes of optimum structure and composition has become key to further improve throughput levels in the electrolysis of CO_2 to CO. Here two gas diffusion electrodes in which multi-walled carbon nanotubes (MWCNT) have been incorporated in the catalyst layer are reported: (i) a "mixed" catalyst layer in which the Ag nanoparticle catalyst and MWCNTs are homogeneously distributed; and (ii) a "layered" catalyst layer comprised of a layer of MWCNTs covered with a layer of Ag catalyst. Both approaches improve performance in the electroreduction of CO_2 compared to electrodes that lack MWCNTs. The "mixed" layer performed best: an electrolyzer operated at a cell potential of -3 V using 1 M KOH as the electrolyte yielded unprecedented high levels of CO production of up to 350 mA cm^{-2} at high Faradaic efficiency (>95% selective for CO) and an energy efficiency of 45% under the same condition. Electrochemical impedance spectroscopy measurements indicate that the observed differences in electrode performance can be attributed to a lower charge transfer resistance in the "mixed" catalyst layer. This study shows that a simple modification of structure and composition of gas diffusion electrodes, *i.e.* incorporation of MWCNTs in the catalyst layer,

* Part of this work has been published: Ma, S., Luo, R., Gold, J.I., Yu, A.Z., Kim, B. & Kenis, P. J. A. Carbon nanotube containing Ag catalyst layers for efficient and selective reduction of carbon dioxide. *J. Mater. Chem. A*, 4, 8573-8578, (2016).

has a profound beneficial effect on their performance in electrocatalytic conversion of CO_2, while allowing for a lower precious metal catalyst loading.

7.2 Introduction

Current global atmospheric CO_2 levels are approximately 400 ppm and are expected to continue to rise. Already these levels impact the climate in undesirable ways as is evident from increasing sea levels, shifting climate zones, and erratic weather patterns.[1] Combined implementation of multiple approaches at a large scale such as switching to renewable energy sources, increasing the energy efficiency of buildings and vehicles, and applying underground carbon sequestration are suggested in order to significantly reduce global CO_2 emissions.[2,3] Electrochemical reduction of CO_2 to various value-added chemicals or intermediates such as carbon monoxide (CO), formate ($HCOO^-$), methane (CH_4), ethylene (C_2H_4) and alcohols is another approach that offers promise to reduce CO_2 emissions.[4-8] At the same time CO_2 electroreduction can utilize excess electrical energy from intermittent renewable sources.[4,5,9] Among the different possible products, CO is an important intermediate for the large scale production of liquid fuels through the Fischer-Tropsch process.[10]

Silver (Ag) is one of the state-of-the-art metal catalysts for electrochemically conversion of CO_2 to CO at high selectivity and current density.[4,6,11,12] Significant research efforts have been devoted to the exploration of novel Ag-based catalysts, such as organometallic Ag catalysts[13], nanostructured Ag catalysts[14,15], Ag particles with different particle sizes[16], and supported Ag catalysts[17], to improve the energy efficiency and throughput (current density) of the process. However, much fewer studies have focused on the composition and/or structure of the associated electrode, properties that are key to maximizing performance of the catalyst on the electrode. In

several studies, the electrode is a metal foil[12], or is composed of metal particles deposited on substrates such as glassy carbon electrodes in a standard three-electrode cell[16,18] or gas diffusion layers (GDL) to form a gas diffusion electrode (GDE) for an electrolyzer[17,19-21]. Use of a GDE typically improves mass transport to and from the gas-liquid-catalyst interface[22], which is particularly important for electrochemical CO_2 conversion given the low solubility of CO_2 in water.[6] However, the electron transfer barrier between the catalyst layer and substrate, as well as the electron transfer barrier within the catalyst layer, such as deposited Ag nanoparticles (AgNPs), may limit the availability of accessible catalytic sites.

Since their discovery in 1991[23], carbon nanotubes have been recognized as a class of carbon materials with interesting properties for a broad range of applications.[24] Carbon nanotubes are porous and hydrophobic, which helps to facilitate gas transport; they are mechanically stable and extremely conductive, and are reported to have electronic interaction with catalytically active species, and thus potentially suitable as support materials for electrocatalysts.[24] The rapid development of chemical vapor deposition has enabled large scale production of multi-walled carbon nanotubes (MWCNTs) at reduced cost, and thus their potential use in cost effective applications.[24,25] Several studies have already shown that the use of carbon nanotubes as the catalyst support improves metal nanoparticle catalytic performance in fuel cell applications.[24,26,27] However, to date only little research has focused on use of carbon nanotubes in electrodes for CO_2 reduction to improve metal catalyst performance.

Here, how the CO_2 reduction reaction can be improved by incorporating MWCNTs into the catalyst layer of a AgNP-based GDE is reported, either in a "layered" or "mixed" fashion, compared to AgNP-based GDEs that lack MWCNTs in the catalyst layer. The reasons for the observed differences in performance are elucidated using electrochemical impedance spectroscopy

(EIS). It is also shown that a smaller amount of precious AgNPs is needed to achieve similar performance levels when incorporating MWCNTs in the catalyst layer.

7.3 Experimental

7.3.1 Electrode preparation

The catalyst layer was deposited on gas diffusion layers (GDLs) using an air-brush method.[20] For ES1, the procedure is the same as previously reported.[19] For ES2, a MWCNT layer was first deposited on a GDL, then a layer of AgNPs was deposited on top of the MWCNT layer. For ES3, AgNPs and MWCNTs were first mixed and dispersed in a vial with proper amount of solvents before air-brushing the resulted ink onto the GDL. For the preparation of AgNP ink, 5 mg AgNPs were dispersed in the mixture of H_2O (200 μL), Nafion® solution (6.5 μL, 5 wt%, Fuel Cell Earth), and isopropyl alcohol (200 μL). However, the preparation of MWCNTs-containing ink is slightly different due to the difficulty in dispersing MWCNTs. Specifically, every 6 mg of MWCNTs or the mixture of AgNPs and MWCNTs were dispersed in the mixture of tetrahydrofuran (400 μL), Nafion® solution (8 μL), and isopropyl alcohol (1600 μL). All the prepared inks were then sonicated (Vibra-Cell ultrasonic processor, Sonics & Materials) for 15 minutes and air-brushed on a GDL (Sigracet 35 BC, Ion Power) over a geometric area of 2.5 × 0.8 cm^2. A PTFE spacer was placed on top of GDL during the deposition process to avoid catalyst being deposited outside of the expected area on the GDL. The actual loading was determined by the mass difference of the GDL before and after deposition. The weight loss was found to be on the order of 50-60% for the air-brushed cathodes since a fraction of the catalyst ended up on the spacer, or was left behind in the air-brush. The anodes were prepared by hand-painting of IrO_2 catalyst inks composed of Millipore water (200 μL), IrO_2 catalyst (5 mg, non-hydrate, Alfa Aesar),

Nafion® solution (13 μL), and isopropyl alcohol (200 μL) over a geometric area of 1.0 × 2.5 cm^2. Both the cathode loading was determined to be 1.0 ± 0.1 mg cm^{-2}, while the anode loading was determined to be 1.5 ± 0.1 mg cm^{-2}.

7.3.2 CO_2 electrolysis operation and product analysis

The electrochemical flow cell that we reported previously[13,17,19] was used to carry out the electrochemical reaction. A mass flow controller (MASS-FLO®, MKS instrument) was used to control the CO_2 (S.J. Smith Welding Supply) flow rate at 7 SCCM. A syringe pump (PHD 2000, Harvard Apparatus) flowed the electrolyte (1 M KOH, pH=13.48) at a flow rate of 0.5 mL min^{-1} between the cathode and anode. A pressure controller (Cole-Parmer, 00268TC) was used to keep the low gas pressure in the downstream of the cell, allowing gas products formed on the catalyst surface of the GDE to leave through the GDE to the gas stream. A potentiostat (Autolab PGSTAT-30, EcoChemie) was used to control the cell potential (–1.6 V, –1.75 V, –2 V, –2.25 V, –2.5 V, –2.75 V, –3 V) in the potentiostatic electrolysis mode to measure the performance of each GDE. The highest potential that we applied is -3 V because at potentials more negative of -3 V, serious flooding will happen due to the serious gas bubbling, causing unbalanced pressure between the electrolyte chamber and the gas chamber. For each potential, the cell was allowed to reach steady state before the gaseous product stream was analyzed using a gas chromatography (Thermo Finnegan Trace GC) equipped with the thermal conductivity detector (TCD). 1 mL of the effluent gas stream was sampled automatically and diverted into the GC with a Carboxen 1000 column (Supelco) and Helium as the carrier gas at a flow rate of 20 SCCM. A triple injection was used to average the gaseous product peaks. The current at a given condition was obtained by averaging the current over 180 s after the gas analysis was started.

Individual electrode potentials were recorded using multimeters (AMPROBE 15XP-B) connected to each electrode and a reference electrode (Ag/AgCl; RE-5B, BASi) placed in the electrolyte exit stream. The measured potentials (*vs.* Ag/AgCl) were converted to the RHE scale using E (*vs.* RHE) = E (*vs.* Ag/AgCl) + 0.209 V + 0.0591 V/pH × pH as previously reported.[28,29] The electrode potentials were corrected for iR drop as previously reported.[19,30]

The Faradaic efficiency for a specific product is calculated using the same method as shown in Chapter 1. The partial current density for a specific product equals total current density multiplies Faradaic efficiency for this product.

Since CO is major product in this study, the energy efficiency for CO is used for comparison. The energy efficiency can be calculated using the following equation:

$$\varepsilon_{energetic} = \sum_{k} \frac{E_k^{\circ} \varepsilon_{k,Faradaic}}{E_k^{\circ} + \eta}$$

Where: E_k^o = the equilibrium cell potential for CO

$\varepsilon_{k,Faradaic}$ = the Faradaic efficiency of CO

η = the cell overpotential

In this case, $E_k^o + \eta$ also equals to the applied cell potential. For converting CO_2 to CO, $E_{CO}^o = E^o_{cathode} - E^o_{anode}$ = -0.10 V[31] - 1.23 V = -1.33 V.

7.3.3 Electrochemical impedance spectroscopy

Electrochemical impedance spectroscopy was performed on the flow cell using the FRA32M module of the potentiostat (Autolab PGSTAT-30, EcoChemie). The spectrum was recorded in a potentiostatic mode at a cell potential of -2.00 V. Higher potentials were not used since a significant amount of noise in the low frequency range was obtained due to gas bubbling at the GDE. Moreover, at lower cell potentials a better understanding of kinetics can be obtained.

All the conditions (CO_2 gas flow rate, back pressure, electrolyte flow rate, etc.) are the same as described above. 100 different frequencies (range: 10 kHz to 0.1 Hz) were used to scan the system in a logarithmic step. The single sine wave mode was used for the sweep with a wave amplitude of 10 mV. A simplified Randles equivalent circuit without the Warburg element (W) was used to simulate this data.[32-34] The double layer capacitance (C_{dl}) was replaced with the constant phase element (Q) to approximate the non-ideal behavior of a porous electrode. The high frequency intercept on the Nyquist plot represents the ohmic resistance of the cell (R_{cell}), which includes the contact resistance and the electrolyte resistance. The diameter of the semi-circle represents the reaction charge transfer resistance (R_{ct}).

7.4 Results and Discussion

Three different electrode structures, as illustrated in **Figure 7.1**, were investigated in this work. Electrode Structure 1 (ES1) is comprised of a layer of AgNPs deposited directly on a GDL (most commonly used approach); Electrode Structure 2 is composed of an AgNP layer on top of a MWCNT layer deposited on a GDL (ES2 or "layered"); Electrode Structure 3 is comprised of a layer of a uniform mixture of AgNPs and MWCNTs deposited on a GDL (ES3 or "mixed"). The total mass of the catalyst layer (the mass of catalyst + MWCNT) was kept constant at 1 mg cm^{-2}. Therefore, the Ag loading is 1 mg cm^{-2} for ES1 and 0.5 mg cm^{-2} for ES2, while in ES3, the Ag loading varies with the Ag-to-MWCNT ratio used: For the 1:1 Ag/MWCNT sample, the Ag loading is 0.5 mg cm^{-2}; for the 1:4 Ag/MWCNT sample, the Ag loading is 0.2 mg cm^{-2}; and for the 1:9 Ag/MWCNT sample, the Ag loading is 0.1 mg cm^{-2}. For comparison, ES1-type electrodes were also created with respective Ag loadings of 0.1, 0.2, and 0.5 mg cm^{-2}.

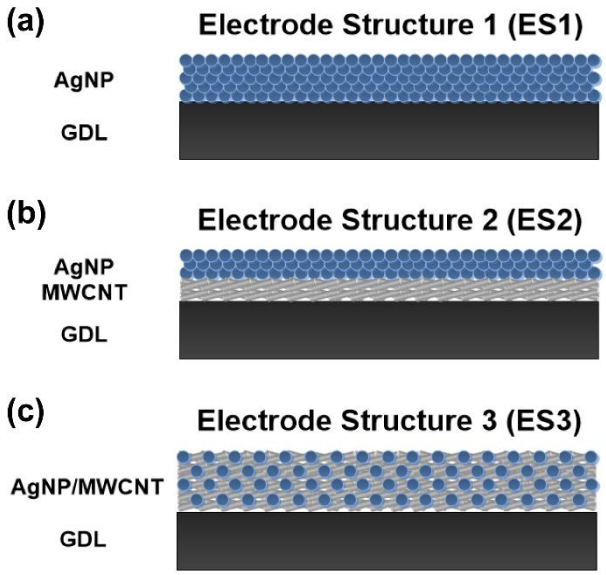

Figure 7.1 Three electrode structures that were applied in this work: Electrode Structure 1 (ES1) is comprised of a layer of AgNPs deposited directly on a gas diffusion layer (GDL); Electrode Structure 2 (ES2, "layered") is composed of an AgNP layer on top of a MWCNT layer deposited on a GDL; Electrode Structure 3 (ES3, "mixed") is comprised of a layer of a uniform mixture of AgNPs and MWCNTs deposited on a GDL. Not drawn to scale.

Top-down views of the surface of the different GDEs obtained by scanning electron microscopy (SEM) are shown in **Figure 7.2**. ES1 and ES2 exhibit similar morphologies as expected, since the top layer of both GDEs is composed of AgNPs. On both surfaces of ES1 and ES2, Ag nanoparticles agglomerated into bigger chunks. In contrast, agglomeration of Ag nanoparticles is not as evident on the surface of ES3. The Ag agglomerates that are visible seem to be in close contact with the MWCNTs and are distributed uniformly within the MWCNTs.

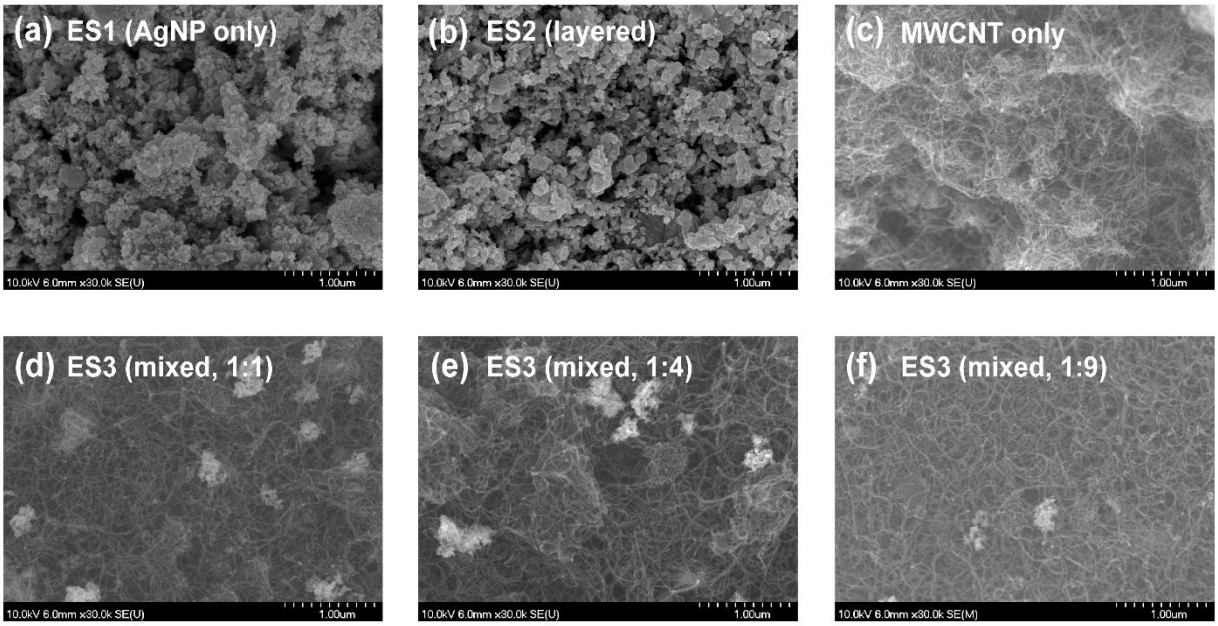

Figure 7.2 SEM characterization of the surface of different electrode structures: (a) ES1 (AgNPs layer only); (b) ES2 (AgNPs layer on top of a MWCNT; "layered"); (c) control electrode with only MWCNT on the surface; (d) (e) (f) ES3 (catalyst layer comprised of AgNPs and MWCNT; "mixed"; in different ratios: 1:1, 1:4, and 1:9).

The electrochemical performance of the GDEs with different electrode structures was examined using an electrochemical flow reactor that we have reported on previously.[17,19,35] In brief, an alkaline electrolyte flows between cathode and anode GDEs and refreshes the electrode surface with ions, while CO_2 gas diffuses through the GDE and reacts at the triple boundary of gas phase, electrode and electrolyte to form CO. This flow cell based on GDEs separated by a flowing electrolyte minimizes mass transfer limitations, improves throughput, and allows for tailoring of the conditions at the catalyst surface through the composition of the electrolyte. As before, the products of the electrochemical reduction of CO_2 in the gaseous effluent can be analyzed using a gas chromatography (GC) equipped with a thermal conductivity detector. The only gaseous cathode products detected were CO and H_2, which is consistent with our previous work when using Ag catalysts.[17,19] Other products such as methane may have formed as well,[12] but in quantities that

are below the detection limit of the GC. The geometric area of the electrode was used to calculate current densities. **Figure 7.3a** shows the partial current density for CO (j_{co}) as a function of cathode potential for GDEs with different electrode structures: ES1, ES2 ("layered", Ag/MWCNT=1:1), and ES3 ("mixed", Ag/MWCNT=1:1). Also, to determine the activity of MWCNT for CO_2 reduction to CO in the absence of AgNPs, a GDE covered with MWCNT only was tested. The GDE with ES2 achieves a higher j_{co} than the GDE with ES1, the typical catalyst layer structure used in prior work.[17,19] The improvement in j_{co} after adding a layer of MWCNT between the Ag layer and GDL probably can be attributed to the increased charge transfer between the Ag layer the GDL substrate. The GDE with ES3 achieves the highest j_{co} among all GDEs tested: a j_{co} as high as 338 mA cm^{-2} at a cathode potential of –0.77 V *vs*. RHE. This performance level represents a more than 2-fold increase compared to the performance achieved by ES1, which exhibited the highest performance under the same condition in prior studies (*e.g.*, 164 mA cm^{-2} at a cathode potential of –0.81 V *vs*. RHE).[19] Also, ES3 exhibits a higher j_{co} than ES2, indicating that the approach to truly integrate the MWCNT within the catalyst layer ("mixed" instead of "layered") positively affects the performance. In the "mixed" configuration (ES3), the AgNPs only exhibit minimal agglomeration and are more uniformly distributed than in ES2 as mentioned above (**Figure 7.2c, 7.2d, 7.2e** *vs.* **Figure 7.2b**). Furthermore, increased contact between the Ag nanoparticles and the MWCNTs in the "mixed" structure of ES3 compared to the "layered" structure in ES2, is expected to minimize charge transfer resistance within the catalyst layer.

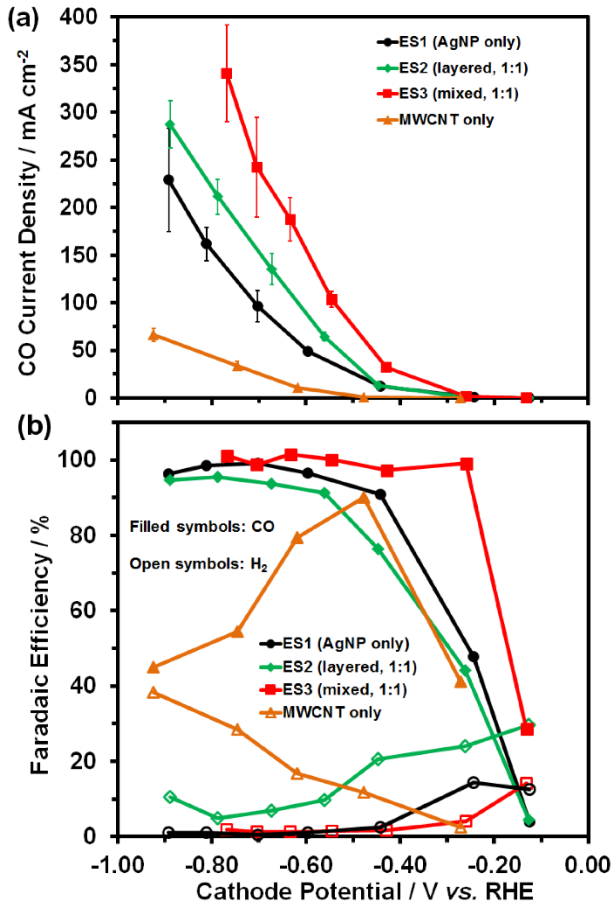

Figure 7.3 (a) Partial current density for CO and (b) Faradaic efficiencies for CO and H_2 as a function of cathode potential for electrodes with different structures: ES1 (AgNP only), ES2 (AgNP layer on top of a MWCNT layer; "layered"; Ag/MWCNT ratio of 1:1), ES3 (catalyst layer comprised of AgNPs and MWCNT; "mixed"; Ag/MWCNT ratio of 1:1), and a control electrode (MWCNT layer only). The total catalyst layer loading (Ag + MWCNT mass) for all electrodes is 1 mg cm^{-2}.

The GDEs with "mixed" and "layered" structures also exhibit a significantly higher Ag utilization than the GDE with only AgNPs in the catalyst layer (ES1). The Ag loading in ES2 and the ES3 with the Ag/MWCNT ratio of 1:1 (0.5 mg cm^{-2}) is only half of the Ag loading in ES1 (1 mg cm^{-2}), while the j_{co} achieved using ES2 and ES3 is about 2 times higher than when using ES1. In contrast, decreasing the Ag loading to 0.1 mg cm^{-2}, 0.2 mg cm^{-2} or 0.5 mg cm^{-2} in ES1 results in lower j_{co} compared to the ES1 electrode with the Ag loading of 1.0 mg cm^{-2} (shown in **Figure**

7.4), which further indicates that incorporating MWCNT into the catalyst layer improves accessibility of active sites of the Ag catalysts.

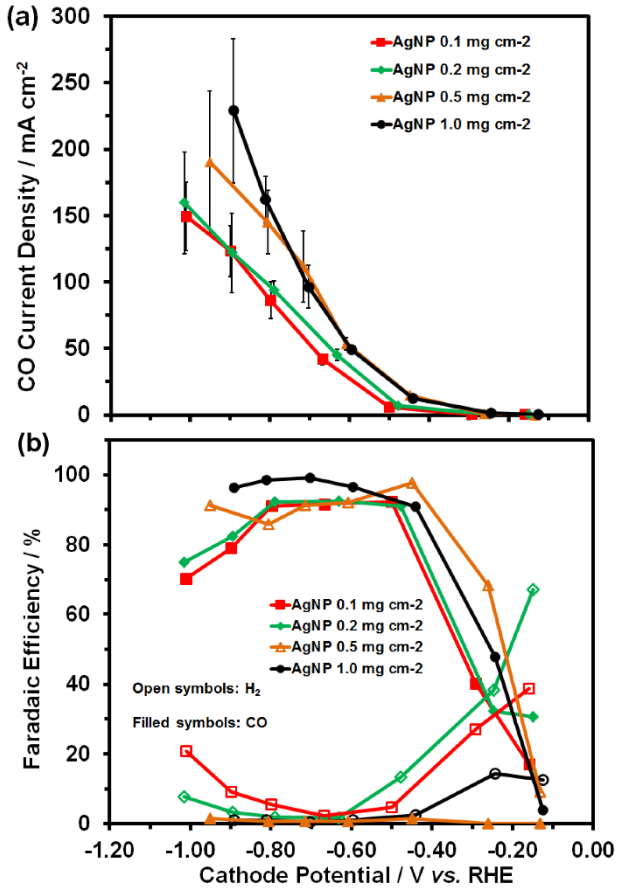

Figure 7.4 (a) Partial current density for CO and (b) Faradaic efficiencies for CO and H_2 as a function of cathode potential for the ES1 electrodes (AgNP only) with different Ag loadings: 0.1 mg cm^{-2}, 0.2 mg cm^{-2}, 0.5 mg cm^{-2}, and 1.0 mg cm^{-2}.

Figure 7.3b shows the Faradaic efficiencies as a function of cathode potentials for GDEs with different electrode structures. At low overpotentials, ES3 exhibits the highest Faradaic efficiency (=selectivity) for CO among all GDEs, indicating that the improved charge transfer between Ag and MWCNT increases the activity for Ag to reduce CO_2 to CO. At high overpotentials, all the GDEs with AgNPs in the catalyst layer exhibit a j_{CO} on the order of 200 mA cm^{-2} (**Figure 7.3a**) and all exhibit similar high Faradaic efficiencies for CO (>90%, **Figure 7.3b**).

In contrast, the electrode covered only with MWCNTs (no Ag catalyst) exhibits a much lower j_{co} (< 100 mA cm^{-2}, **Figure 7.3a**), and a lower Faradaic efficiency for CO of only 50%. Therefore, the improvement achieved when mixing MWCNT and Ag nanoparticles is not due to the activity of MWCNT, but probably due to the enhanced charge transfer within the catalyst layer (*vide infra*), thereby increasing the Ag catalyst utilization.

ES3 ("mixed"), the electrode structure that exhibits the highest performance, was used as a model to study how the ratio of Ag to MWCNT affects the electrochemical performance. Ag-to-MWCNT ratios of 1:1, 1:4, and 1:9 were used, resulting in Ag loadings of 0.5, 0.2, and 0.1 mg cm^{-2}, respectively. The results of CO_2 electrolysis using these three electrodes as well as ES1 (Ag loading of 1 mg cm^{-2}) are shown in **Figure 7.5**. The ES3 electrodes with Ag loadings of 0.5 and 0.2 mg cm^{-2} achieve similar j_{co} levels as high as 340 mA cm^{-2}, while the ES3 with Ag loading of 0.1 mg cm^{-2} exhibits a lower maximum j_{co} of 200 mA cm^{-2}. *At low overpotentials* (more positive than -0.8 V_{RHE}), the j_{co} for the ES3 electrode with a Ag loading of 0.1 mg cm^{-2} is higher than the j_{co} for ES1, whereas at high overpotentials (more negative than -0.8 V_{RHE}), the ES3 electrode with a Ag loading of 0.1 mg cm^{-2} performs less well than the ES1 electrode. This observation can be attributed to the relative low Faradaic efficiency for CO when using the electrode with a Ag loading of 0.1 mg cm^{-2} compared to the other electrodes (**Figure 7.5b**). The GDE with Ag loading of 0.1 mg cm^{-2} (**Figure 7.5b**) and the GDE with only MWCNT in the catalyst layer (**Figure 7.3b**) showed a similar trend in the Faradaic Efficiencies for CO in that it drops for both electrodes at high overpotentials. In summary, when the AgNP/MWCNT ratio in the electrode is below 1:4, its performance becomes more similar to the GDE covered with MWCNT only (no Ag catalyst). In this study, the ES3 electrode with the AgNP/MWCNT ratio of 1:4 has the optimum Ag loading since it achieves the highest j_{co} (350 mA cm^{-2}) at a Ag loading of only 0.2 mg cm^{-2}. This

corresponds to a mass activity of 1750 mA cm^{-2} mg^{-1} compared to 800 mA cm^{-2} mg^{-1} for the ES1 electrode with a Ag loading of 0.2 mg cm^{-2} (**Figure 7.4**).

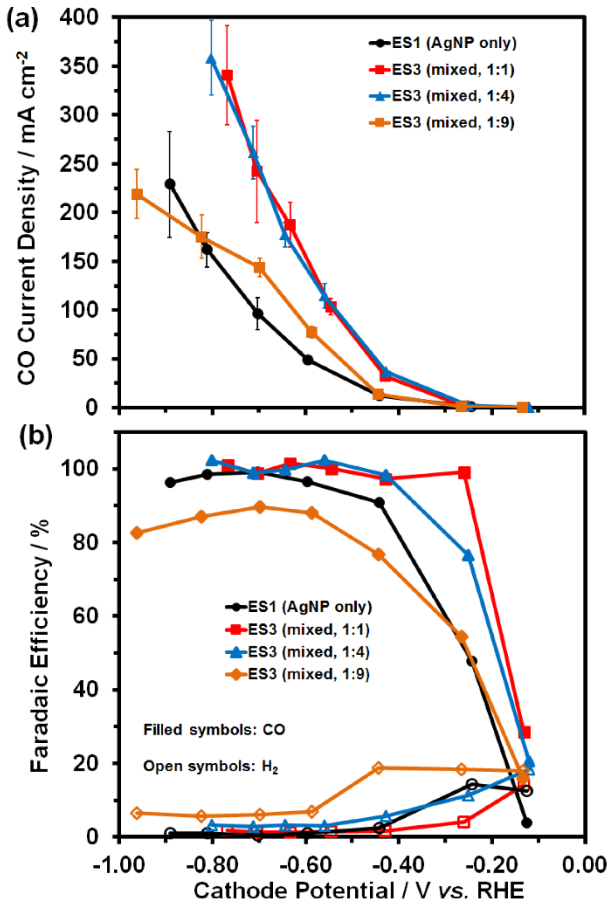

Figure 7.5 (a) Partial current density for CO and (b) Faradaic efficiencies for CO and H_2 as a function of cathode potential for the ES1 electrode (AgNP only) and ES3 electrodes ("mixed" catalyst layer; AgNPs and MWCNT ratios of 1:1, 1:4, and 1:9). The total catalyst layer loading (Ag + MWCNT mass) is 1 mg cm^{-2}.

To determine how electrode structure and Ag loading within the catalyst layer affect electrode performance, electrochemical impedance spectroscopy (EIS) was used to measure the ohmic resistance (R_{cell}) and charge resistance (R_{ct}) of electrolysis cells composed of an IrO_2 anode and cathodes with different electrode structures and Ag/MWCNT ratios. The experimental data was fitted using the Boukamp model as previously reported.[33,36] In EIS the potentiostatic mode was used at a cell potential of -2.00 V. The ohmic resistance of the cell (R_{cell}, the left intercept of

the hemi-circle with the x-axis) is almost the same for cells with different cathodes (**Figure 7.6**). The slight differences in R_{cell} are probably due to differences in contact resistance between each assembled cell. The charge transfer resistance of the cell (R_{ct}, the right intercept of the hemi-circle with the x-axis) varies significantly when different cathodes were used. Specifically, the R_{ct} of the ES3 electrodes with Ag/MWCNT ratios of 1:1 and 1:4 is much smaller than the R_{ct} of the ES1 electrode, the ES2 electrode, and the ES3 electrode with a Ag/MWCNT ratio of 1:9. Also, the R_{ct} values of the ES2 and the ES3 electrodes are generally smaller than the R_{ct} value of the ES1 electrode. These results are in good agreement with the results shown in **Figure 7.3a**, where the ES3 electrodes with Ag/MWCNT ratios of 1:1 and 1:4 exhibit higher j_{co} levels than the ES1 electrode, the ES2 electrode, and the ES3 electrode with a Ag/MWCNT ratio of 1:9. These results indicate that the approach to incorporate MWCNT into the catalyst layer affects charge transfer resistance within the catalyst layer: The electrodes with "mixed" structure and optimum Ag/MWCNT ratios (1:1 and 1:4) exhibit a higher charge transfer rate than the electrodes with a "layered" structure; therefore the former facilitates the catalytic conversion of CO_2 to CO better.

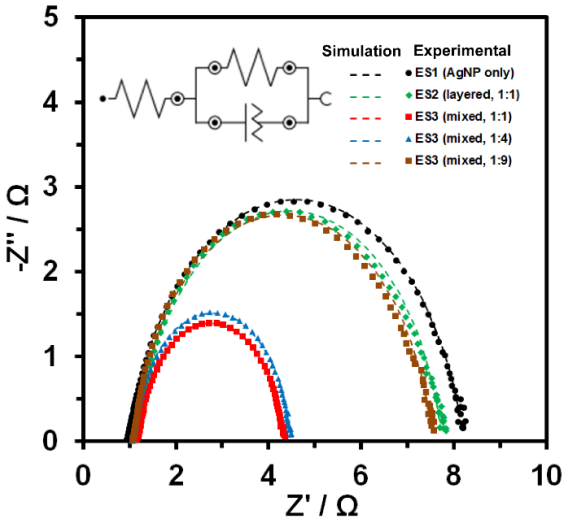

Figure 7.6 Nyquist plot obtained via electrochemical impedance spectroscopy at a cell potential of -2.00 V for cells with different electrodes. The symbols represent experimental data while the dashed lines (under the symbols due to excellent fit) represent simulated curves using the Boukamp model.[36]

The improvement in the partial current densities for CO production after incorporating MWCNT in the catalyst layers of the electrodes also leads to an increase in energy efficiency (calculated using a method described earlier[4]). **Figure 7.7** compares energy efficiency as a function of current density for cells using the different cathodes studied here. The ES2 electrode and the ES3 electrodes achieve higher energy efficiencies than the ES1 electrode. For the ES3 electrode with a Ag/MWCNT ratio of 1:4, the energy efficiency is still at 45.4 % even at the highest current density of 350 mA cm^{-2}. In our prior work, 45% energy efficiency was also achieved but at a lower j_{co} of 250 mA cm^{-2} using an ES1-type Ag electrode in 1M KOH.[37] So the ES3 electrode studied here achieves a similar energy efficiency at a significantly higher current density. Indeed, a high overall energy efficiency in combination with high rates of CO_2 conversion will be essential for this type of electrolysis technology being transitioned to an economically viable process. Based on the same prior work that focused on optimizing electrolyte composition,[37] the ES3 electrode studied here may perform even better when using 3M (instead of 1M) KOH as the electrolyte.

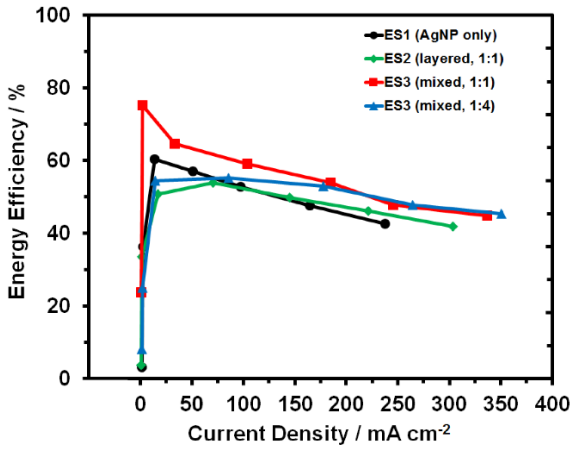

Figure 7.7 Energy efficiency as a function of current density for CO_2 electrolysis cells using different electrodes: ES1 electrode (AgNP only), ES2 electrode ("layered", 1:1) and ES3 electrodes ("mixed"; Ag/MWCNT ratio 1:1 or 1:4). The total catalyst layer loading (Ag + MWCNT mass) is 1 mg cm^{-2}.

7.5 Conclusions

In summary, a significant level of improvement in the conversion of CO_2 to CO through electrode structure modifications is reported here, specifically through incorporation of MWCNTs into the Ag catalyst layer of gas diffusion electrodes. Electrodes with uniformly mixed Ag and MWCNT as its catalyst layer exhibit higher current density (350 mA cm^{-2}), than electrodes in which the catalyst layer is comprised of a Ag layer on top of a MWCNT layer (280 mA cm^{-2}). Both types of electrodes with MWCNTs incorporated in their catalyst layer show higher performance than GDEs that lack MWCNTs (230 mA cm^{-2} at same operation conditions but at a lower Ag loading). EIS measurements indicate that the observed improvement in current density upon the incorporation of MWCNTs is due to a decrease in charge transfer resistance within the catalyst layer.

This work demonstrates that optimization of the electrode, here the composition and structure of the cathode catalyst layer, leads to improvement in CO_2 electrolysis performance. The high current density of 350 mA cm^{-2} observed for the "mixed" electrode ES3 (one of the highest values reported in the literature to date) holds promise for developing this electrolysis technology further, especially when considering the high energy efficiency of 45% at which this CO_2 conversion rate is achieved. Further optimization of electrodes with respect to the composition and structure of components other than the catalyst layer, *i.e.*, the microporous layer and the macroporous layer, may be necessary to further increase the performance, thereby bringing this technology closer to becoming an economical viable process for CO_2 mitigation and/or utilization.

7.6 References

1 Hansen, J., Kharecha, P., Sato, M., Masson-Delmotte, V., Ackerman, F., Beerling, D. J., Hearty, P. J., Hoegh-Guldberg, O., Hsu, S.-L., Parmesan, C., Rockstrom, J., Rohling, E. J.,

Sachs, J., Smith, P., Steffen, K., Van Susteren, L., von Schuckmann, K. & Zachos, J. C. Assessing "Dangerous Climate Change": Required Reduction of Carbon Emissions to Protect Young People, Future Generations and Nature. *PLoS One* **8**, e81648, (2013).

2 Pacala, S. & Socolow, R. Stabilization Wedges: Solving the Climate Problem for the Next 50 Years with Current Technologies. *Science* **305**, 968-972, (2004).

3 Taylor, P. Energy Technology Perspectives *Energy Technology Perspectives* International Energy Agency, (2010).

4 Jhong, H.-R. M., Ma, S. & Kenis, P. J. A. Electrochemical conversion of CO_2 to useful chemicals: current status, remaining challenges, and future opportunities. *Curr. Opin. Chem. Eng.* **2**, 191-199, (2013).

5 Whipple, D. T. & Kenis, P. J. A. Prospects of CO_2 Utilization via Direct Heterogeneous Electrochemical Reduction. *J. Phys. Chem. Lett.* **1**, 3451-3458, (2010).

6 Hori, Y. in *Modern Aspects of Electrochemistry* Vol. 42 *Modern Aspects of Electrochemistry* (eds ConstantinosG Vayenas, RalphE White, & MariaE Gamboa-Aldeco) Ch. 3, 89-189 (Springer New York, 2008).

7 Gattrell, M., Gupta, N. & Co, A. A review of the aqueous electrochemical reduction of CO_2 to hydrocarbons at copper. *J. Electroanal. Chem.* **594**, 1-19, (2006).

8 Appel, A. M., Bercaw, J. E., Bocarsly, A. B., Dobbek, H., DuBois, D. L., Dupuis, M., Ferry, J. G., Fujita, E., Hille, R., Kenis, P. J. A., Kerfeld, C. A., Morris, R. H., Peden, C. H. F., Portis, A. R., Ragsdale, S. W., Rauchfuss, T. B., Reek, J. N. H., Seefeldt, L. C., Thauer, R. K. & Waldrop, G. L. Frontiers, Opportunities, and Challenges in Biochemical and Chemical Catalysis of CO_2 Fixation. *Chem. Rev.* **113**, 6621-6658, (2013).

9 Martin, A. J., Larrazabal, G. O. & Perez-Ramirez, J. Towards sustainable fuels and chemicals through the electrochemical reduction of CO_2: lessons from water electrolysis. *Green Chem.* **17**, 5114-5130, (2015).

10 Dry, M. E. The Fischer–Tropsch process: 1950–2000. *Catal. Today* **71**, 227-241, (2002).

11 Hori, Y., Wakebe, H., Tsukamoto, T. & Koga, O. Electrocatalytic Process of CO Selectivity in Electrochemical Reduction of CO_2 at Metal-Electrodes in Aqueous-Media. *Electrochim. Acta* **39**, 1833-1839, (1994).

12 Hatsukade, T., Kuhl, K. P., Cave, E. R., Abram, D. N. & Jaramillo, T. F. Insights into the electrocatalytic reduction of CO_2 on metallic silver surfaces. *Phys. Chem. Chem. Phys.* **16**, 13814-13819, (2014).

13 Tornow, C. E., Thorson, M. R., Ma, S., Gewirth, A. A. & Kenis, P. J. A. Nitrogen-Based Catalysts for the Electrochemical Reduction of CO_2 to CO. *J. Am. Chem. Soc.* **134**, 19520-19523, (2012).

14 Lu, Q., Rosen, J., Zhou, Y., Hutchings, G. S., Kimmel, Y. C., Chen, J. G. & Jiao, F. A selective and efficient electrocatalyst for carbon dioxide reduction. *Nat. Commun.* **5**, (2014).

15 Jee, M. S., Jeon, H. S., Kim, C., Lee, H., Koh, J. H., Cho, J., Min, B. K. & Hwang, Y. J. Enhancement in carbon dioxide activity and stability on nanostructured silver electrode and the role of oxygen. *Appl. Catal., B* **180**, 372-378, (2016).

16 Salehi-Khojin, A., Jhong, H.-R. M., Rosen, B. A., Zhu, W., Ma, S., Kenis, P. J. A. & Masel, R. I. Nanoparticle Silver Catalysts That Show Enhanced Activity for Carbon Dioxide Electrolysis. *J. Phys. Chem. C* **117**, 1627-1632, (2012).

17 Ma , S., Lan , Y., Perez, G. M. J., Moniri, S. & Kenis , P. J. A. Silver Supported on Titania as an Active Catalyst for Electrochemical Carbon Dioxide Reduction. *ChemSusChem* **7**, 866-874, (2014).

18 Mistry, H., Reske, R., Zeng, Z., Zhao, Z.-J., Greeley, J., Strasser, P. & Cuenya, B. R. Exceptional Size-Dependent Activity Enhancement in the Electroreduction of CO_2 over Au Nanoparticles. *J. Am. Chem. Soc.* **136**, 16473-16476, (2014).
19 Ma, S., Luo, R., Moniri, S., Lan, Y. & Kenis, P. J. A. Efficient Electrochemical Flow System with Improved Anode for the Conversion of CO_2 to CO. *J. Electrochem. Soc.* **161**, F1124-F1131, (2014).
20 Jhong, H.-R. M., Brushett, F. R. & Kenis, P. J. A. The Effects of Catalyst Layer Deposition Methodology on Electrode Performance. *Adv. Energy Mater.* **3**, 589-599, (2013).
21 Kang, P., Zhang, S., Meyer, T. J. & Brookhart, M. Rapid Selective Electrocatalytic Reduction of Carbon Dioxide to Formate by an Iridium Pincer Catalyst Immobilized on Carbon Nanotube Electrodes. *Angew. Chem. Int. Ed.* **53**, 8709-8713, (2014).
22 O'Hayre, R., Barnett, D. M. & Prinz, F. B. The Triple Phase Boundary: A Mathematical Model and Experimental Investigations for Fuel Cells. *J. Electrochem. Soc.* **152**, A439-A444, (2005).
23 Iijima, S. Helical microtubules of graphitic carbon. *Nature* **354**, 56-58, (1991).
24 Melchionna, M., Marchesan, S., Prato, M. & Fornasiero, P. Carbon nanotubes and catalysis: the many facets of a successful marriage. *Catal. Sci. Technol.* **5**, 3859-3875, (2015).
25 Tessonnier, J.-P., Becker, M., Xia, W., Girgsdies, F., Blume, R., Yao, L., Su, D. S., Muhler, M. & Schlögl, R. Spinel-Type Cobalt–Manganese-Based Mixed Oxide as Sacrificial Catalyst for the High-Yield Production of Homogeneous Carbon Nanotubes. *ChemCatChem* **2**, 1559-1561, (2010).
26 Kongkanand, A., Kuwabata, S., Girishkumar, G. & Kamat, P. Single-Wall Carbon Nanotubes Supported Platinum Nanoparticles with Improved Electrocatalytic Activity for Oxygen Reduction Reaction. *Langmuir* **22**, 2392-2396, (2006).
27 Wu, G. & Xu, B.-Q. Carbon nanotube supported Pt electrodes for methanol oxidation: A comparison between multi- and single-walled carbon nanotubes. *J. Power Sources* **174**, 148-158, (2007).
28 Ren, D., Deng, Y., Handoko, A. D., Chen, C. S., Malkhandi, S. & Yeo, B. S. Selective Electrochemical Reduction of Carbon Dioxide to Ethylene and Ethanol on Copper(I) Oxide Catalysts. *ACS Catal.* **5**, 2814-2821, (2015).
29 Li, C. W., Ciston, J. & Kanan, M. W. Electroreduction of carbon monoxide to liquid fuel on oxide-derived nanocrystalline copper. *Nature* **508**, 504-507, (2014).
30 Naughton, M. S., Moradia, A. A. & Kenis, P. J. A. Quantitative Analysis of Single-Electrode Plots to Understand In-Situ Behavior of Individual Electrodes. *J. Electrochem. Soc.* **159**, B761-B769, (2012).
31 Hori, Y. in *Handbook of Fuel Cells* Vol. 2 Ch. 48, 720-733 (John Wiley & Sons, Ltd, 2010).
32 Sambandam, S., Valluri, V., Chanmanee, W., de Tacconi, N., Wampler, W., Lin, W.-Y., Carlson, T., Ramani, V. & Rajeshwar, K. Platinum-carbon black-titanium dioxide nanocomposite electrocatalysts for fuel cell applications. *J Chem Sci* **121**, 655-664, (2009).
33 Giorgi, L., Pozio, A., Bracchini, C., Giorgi, R. & Turtù, S. H_2 and H_2/CO oxidation mechanism on Pt/C, Ru/C and Pt–Ru/C electrocatalysts. *J. Appl. Electrochem.* **31**, 325-334, (2001).
34 Yuan, X., Wang, H., Colin Sun, J. & Zhang, J. AC impedance technique in PEM fuel cell diagnosis—A review. *Int. J. Hydrogen Energy* **32**, 4365-4380, (2007).

35 Whipple, D. T., Finke, E. C. & Kenis, P. J. A. Microfluidic Reactor for the Electrochemical Reduction of Carbon Dioxide: The Effect of pH. *Electrochem. Solid-State Lett.* **13**, B109-B111, (2010).
36 Boukamp, B. A. A Nonlinear Least Squares Fit procedure for analysis of immittance data of electrochemical systems. *Solid State Ionics* **20**, 31-44, (1986).
37 Verma, S., Lu, X., Ma, S., Masel, R. I. & Kenis, P. J. A. The effect of electrolyte composition on the electroreduction of CO_2 to CO on Ag based gas diffusion electrodes. *Phys. Chem. Chem. Phys.* **18**, 7075-7084, (2016).

Chapter 8

Conclusions and Future Directions

The challenges of global climate change and increasing global energy demands are daunting. Multiple approaches are needed to curb CO_2 emissions, while maximizing the utilization of alternative energy sources. The electroreduction of CO_2 into value-added products offers the potential to store intermittent renewable energy, and at the same time it helps to reduce atmospheric CO_2 emissions. The process of electroreduction of CO_2 is still not commercially available, mainly due to the lack of suitable catalysts. Current catalysts exhibit high overpotentials which reduce energy efficiency, low current densities (reaction rate), and low selectivity. To overcome these challenges, more active catalysts and more durable electrodes that allow for excellent mass transfer and exhibit sufficient electron conductivity are needed.

This dissertation mainly describes several studies undertaken to develop active and durable catalysts that exhibit low overpotentials for the electroreduction of CO_2 to products such as CO, ethylene (C_2H_4) and/or ethanol (C_2H_5OH), as well as the role the electrolyte and electrode structure play in these processes. Chapter 2 reports the use of TiO_2 as a support material for Ag nanoparticle catalysts for the reduction of CO_2 to CO, including the role TiO_2 plays in the reaction pathway. Chapter 3 reports how a better anode catalyst results in a twofold increase in current density and a ~0.5 V decrease in overall cell potential. Chapter 4 reports the synthesis and characterization of Cu nanoparticle-based GDEs, resulting in high levels of ethylene and ethanol production in an alkaline electrolyte. Chapter 5 describes how the selectivity to ethylene improves significantly by adding N-containing compounds into the Cu nanoparticle-based electrodes. Chapter 6 explores possible active sites for the conversion of CO_2 to C2 products using CuPd nanoalloys with different

atomic arrangements. Chapter 7 studies how the optimization of the electrode, including the composition and structure of the cathode catalyst layer, leads to improvements in current density for CO_2 electrolysis. Together, these studies present a number of more active catalysts and optimized electrodes that help make the electroreduction of CO_2 a more economically viable process, but further progress is needed.

Looking forward, present performance levels and lack of detailed mechanistic understanding of CO_2 reduction provide several avenues for future research: (1) How the metal nanoparticles (Au, Ag, Cu, etc.) transform during the actual catalytic condition is still unknown for the CO_2 reduction reaction. *In-situ* TEM observation of metal nanoparticles in the electrolyte while under the electric potential will be helpful to identify actual surface features during the reaction. (2) Results in Chapter 5 already show that N-containing compounds such as DAT help improve the selectivity for ethylene production on Cu catalysts. However, DAT partially dissolves in the electrolyte. Finding a way to chemically bind DAT to the catalyst support may help stabilize DAT on the electrode surface and therefore improve the long term performance of the corresponding electrodes. (3) We found that neighboring Cu atoms are favorable for CO_2 conversion to C2 chemicals in Chapter 6. Developing core/shell alloy catalysts with Cu as the shell would help to maintain the ensemble feature of Cu atoms while the other element (in the core) could tune the properties of the resulting alloy, thus forming a new catalyst with suitable surface adsorption energy for certain reaction intermediates to improve the selectivity to C2 chemicals. (4) The durability of catalysts for CO_2 reduction is seldom reported due to the lack of standard testing protocols and the flooding of GDEs. Future work on improving water management capabilities of GDEs will help avoid the flooding issue on GDEs, thereby making the measurement of catalysts' durability easier.